Strahlverluststudien an Siliziumstreifendetektormodulen für das CMS Experiment

Manuel Fahrer

Zur Erlangung des akademischen Grades eines
Doktors der Naturwissenschaften
von der Fakultät für Physik der
Universität Karlsruhe (TH)

genehmigte

Dissertation

von

Dipl. Phys. Manuel Fahrer

aus Calw

Karlsruhe, 27. Juni 2006

Tag der mündlichen Prüfung: 14. Juli 2006
Referent: Prof. Dr. Thomas Müller
Korreferent: Prof. Dr. Günter Quast

Zusammenfassung

Das Standardmodell der Teilchenphysik beschreibt die elementaren Bestandteile der Materie und drei ihrer fundamentalen Wechselwirkungen. Es ist bei Energien bis zu 200GeV erfolgreich getestet worden. Bei höheren Energien erwartet man die Entdeckung des letzten fehlenden Teilchens dieses Modells, des Higgs-Bosons, sowie von Teilchen außerhalb davon. Der im Bau befindliche Große Hadronen-Beschleuniger (LHC) wird das Verständnis des Standardmodells vertiefen sowie neue Physik auf einer Energieskala von bis zu 1TeV erschließen.

Die hohe Luminosität des LHC wird benötigt, um die geringen Wechselwirkungsquerschnitte bei hohen Energien zu kompensieren. Allerdings hat dies zwei nachteilige Konsequenzen:

Einerseits verlangt der daraus resultierende große hadronische Untergrund nach strahlungsharten Detektoren mit hoher Granularität. Insbesondere der Silizium-Spurdetektor des CMS-Experiments ist mit einer hohen Belegungsdichte konfrontiert und benötigt deshalb eine hervorragende Ortsauflösung, um den besonderen Anforderungen an die Signatur des vielversprechendsten Zerfallskanals eines leichten Higgs-Bosons in ein $b\bar{b}$-Paar zu genügen.

Andererseits wird die hohe Luminosität mit einer sehr großen Strahlenergie erkauft, was nach einer sicheren Monitorierung, Reinigung und kontrollierten Vernichtung des Strahls verlangt. Obwohl es große Anstrengungen beim Schutz von Maschine und Experimenten vor Strahlverlusten gibt, können solche, die von einem Versagen des Strahlabbruchsystems selbst hervorgerufen werden, nicht mit letzter Gewissheit ausgeschlossen werden. Die Auswirkungen eines solchen Strahlverlustes auf den CMS Spurdetektor bzw. seine kleinste Einheit, das *Modul*, wurden in dieser Arbeit untersucht.

Ein Modul besteht aus einem oder zwei Silizium-Streifensensoren, einem sog. *Hybriden*, welcher die analoge Streifenauslese beherbergt und einem einfachen Filter- und Puffer-Schaltkreis in der Hochspannungsversorgungsleitung der Sensoren. Bei einem Silizium-Streifensensor handelt es sich um ein n-dotiertes Volumen, welches mithilfe von implantierten p-Streifen und einer Hochspannung in Sperrrichtung von freien Ladungsträgern verarmt wird. Ionisierende Strahlung erzeugt bei ihrem Durchgang durch das sensitive Volumen Elektron-Loch-Paare, welche im Feld der Raumladungen getrennt werden und an das entsprechende Ende des Sensors driften. Die zu den p-Streifen driftenden Löcher erzeugen kapazitiv ein Ladungs-Signal in den auf einem Dielektrikum über den p-Streifen parallel angebrachten Aluminium-Streifen (siehe Abb. 1).

Im ersten Strahlverlust-Experiment sollte die Frage nach dem Überleben von Modulen und seinen Komponenten beantwortet werden. Drei Sensoren, zwei komplette Module sowie ein Auslese-Hybrid wurden am CERN Proton Synchrotron mit einzelnen Protonpaketen beschossen und das Zeitverhalten von Betriebsparametern, insbesondere die Hochspannung am Sensor, die Spannung an der dielektrischen Schicht sowie der komplette Strom durch den Sensor während des Ereignisses gemessen. Ferner wurden fast alle getesteten Komponenten im Labor vor- und nach-qualifiziert. Diese beiden Datensätze sollten im Falle von Beschädigungen einen Hinweis auf die Ursache geben. Ein Resultat ist in Abb. 2 für einen der Sensoren dargestellt und zeigt, daß die Spannung an der bei solchen Ereignissen potentiell am meisten gefährdeten Sensorkomponente, dem Dielektrikum, weit unter dem spezifizierten Maximum liegt. Die Standardqualifikation eines Moduls im Labor nach dem Experiment sowie ein Langzeittest mit kosmischen Myonen verliefen sehr erfolgreich und beweisen dessen Unversehrtheit.

In der zweiten experimentellen Strahlverluststudie im Labor mithilfe einer IR LED Matrix wurden mehrere Sensoren getestet, um eine statistische Aussage über die Belastbarkeit

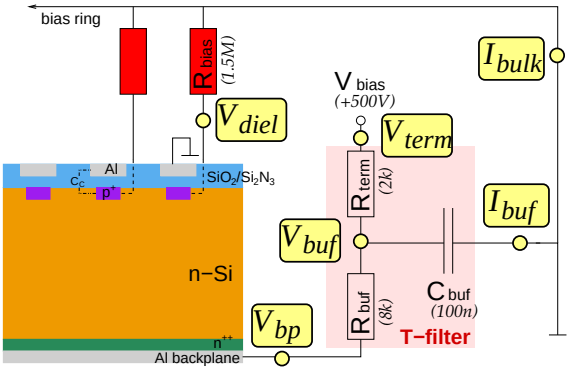

Abbildung 1: Schematische Darstellung eines Siliziumstreifen-Sensors und seines Schaltkreises. *Die Messgößen im Schaltkreis sind mit Markern versehen und zeigen das Messprogramm während der Laborstudien. Der Filter in der Hochspannungsleitung ("T-Filter") spielt die entscheidende Rolle beim Verständnis der Vorgänge.*

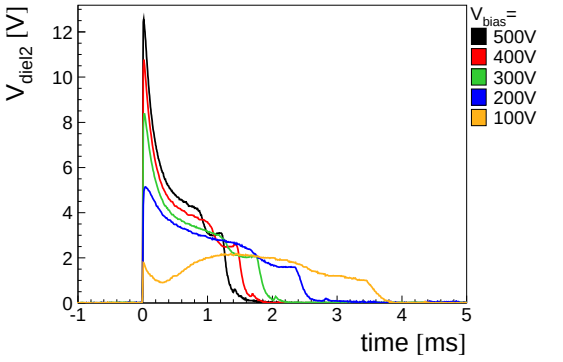

Abbildung 2: Spannung am Dielektrikum in Abhängigkeit der Zeit für verschiedene Sensorspannungen. *Diese Daten wurden beim Test am CERN PS gewonnen und zeigen, dass Sensoren bei Strahlverlusten nicht gefährdet sind. Die Spannungswerte bleiben weit unter dem spezifizierten Maximum von 120V.*

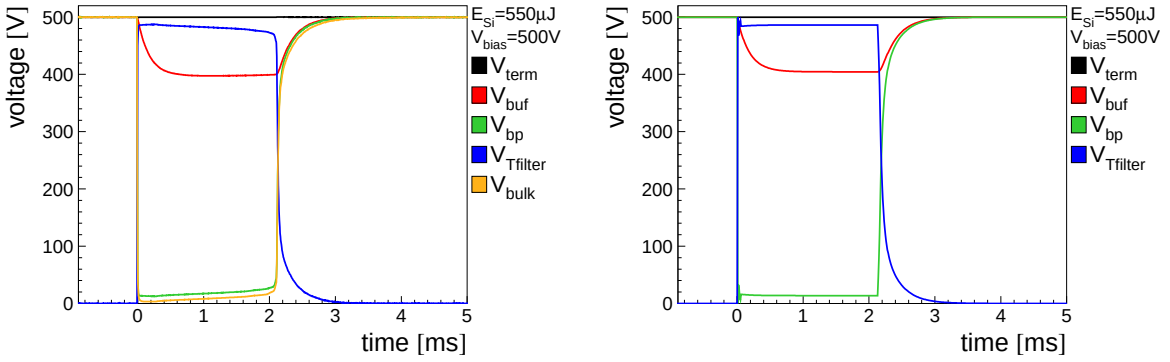

a. Messung

b. Simulation

Abbildung 3: Spannungsabfall an verschiedenen Modulkomponenten in Abhängigkeit der Zeit. *Diese Messung wurde im Labor mithilfe einer IR LED Matrix durchgeführt und zeigt die Konsistenz von Daten (links) und Modell (rechts). Ferner beweist sie, daß der Sensor in diesem Messaufbau vor der anliegenden Hochspannung* V_{term} *hauptsächlich von zum Moduldesign gehörenden Widerständen geschützt wird* ($V_{Tfilter}$)*, sodass am Sensor selbst der geringste Teil der Spannung abfällt* (V_{bp} *und* V_{bulk}).

verschiedener Sensortypen treffen zu können. Ferner sollte der Mechanismus geklärt werden, durch welchen die Sensoren geschützt sind. Dies wurde erreicht durch eine Erweiterung und Verfeinerung des Messprogramms. Die Studie führte zu einem detailierten physikalischen und elektrischen Verständnis der Vorgänge im Sensor bei einem Strahlverlust. Das Resultat in Abb. 3 zeigt, dass der Sensor in dieser als am schlimmsten angenommenen Messanordnung vor hohen Spannungen hauptsächlich durch die Widerstände des Filters in der Hochspannungszuleitung geschützt ist. Der größte Teil der Eingangsspannung V_{term} wird dort ($V_{Tfilter}$) absorbiert, sodass an Sensorrückseite (V_{bp}) und Sensorbulk (sensitiven Sensorvolumen, V_{bulk}) nur noch ein geringer Bruchteil der anliegenden Spannung abfallen. Außerdem zeigt die Schaltkreissimulation eine exzellente Übereinstimmung mit den Messdaten, was beweist, dass das entwickelte einfache Modell sehr aussagekräftig ist.

In einem weiteren Experiment im Labor wurde untersucht, wo die Belastbarkeitsgrenze

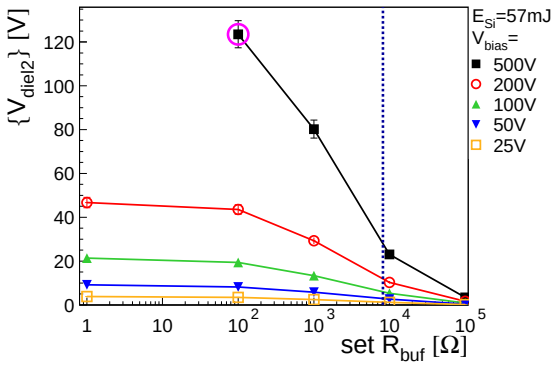

Abbildung 4: Maximalspannung am Dielektrikum in Abhängigkeit von Puffer-Widerstand und Sensorspannung. *Die Daten stammen vom Lasertest im Labor und demonstrieren die Belastbarkeitsgrenze des Moduldesigns. Der hervorgehobene Punkt markiert die Extremalbedingungen für den sicheren Betrieb des Sensors.*

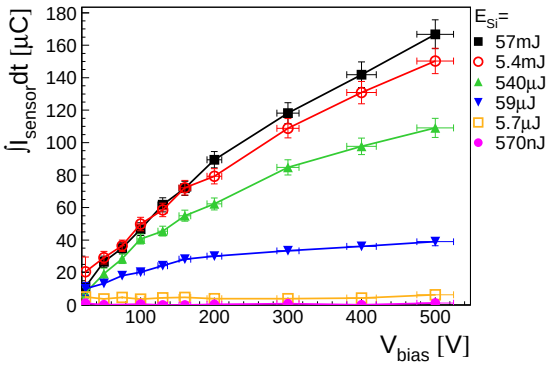

Abbildung 5: Durch den Sensor geflossene Ladung über Sensorspannung und Energie pro Schuss. *Diese Daten stammen vom Lasertest im Labor und zeigen, dass das Moduldesign unempfindlich ist gegen die Erhöhung der Schuss-Energie. Die Verzehnfachung der Energie von 5 auf 50mJ bewirkt eine Zunahme der Ladung um nur 10%.*

des Moduldesigns liegt. Dabei wurden vier Sensoren einem hoch intensiven, gepulsten und aufgeweiteten IR Laserstrahl ausgesetzt und dieselben Sensorparameter wie im LED-Test während der Laser-Schüsse aufgezeichnet. Dabei wurden wesentliche Elemente des Moduldesigns, genauer gesagt, die Komponenten des Hochspannungsfilters, systematisch zu Werten hin verändert, die für den Sensor als immer gefährlicher angenommen wurden. Ein Resultat ist in Abb. 4 dargestellt. Die Spannung am Dielektrikum erreicht potentiell immer gefährlichere Werte bei Reduktion der Widerstände des HV-Filters. Bei ca. 1/100 des Design-Wertes war letztmalig ein sicherer Betrieb möglich. Bei Werten darunter wurde der Sensor zerstört. Ein weiteres wichtiges Resultat dieses Tests war der Gewinn eines qualitativen Verständnisses für die Verhältnisse bei hohen Pulsenergien. Abb. 5 zeigt die vom Sensor durchflossene Ladung in Abhängigkeit von Pulsenergie und Sensorspannung. Eine Erhöhung der Pulsenergie von 5mJ auf 50mJ bewirkte eine Vergrößerung der Ladung um nur 10%. Dies lässt sich mit hohen Rekombinationsverlusten im zusammengebrochenen Feld des Sensors erklären und beweist, dass das Moduldesign unempfindlich gegenüber sehr hochenergetischen Schüssen ist.

Beam Loss Studies on Silicon Strip Detector Modules for the CMS Experiment

PhD Thesis

by

Manuel Fahrer

Faculty for Physics
University of Karlsruhe (TH)
June 27, 2006

Supervisor: Prof. Dr. Thomas Müller,
Second Supervisor: Prof. Dr. Günter Quast,
Institut für Experimentelle Kernphysik, University of Karlsruhe (TH)

Contents

1 Abstract

The common theory of particle physics, the so called Standard Model (SM), describes the elementary constituents of matter and three of their fundamental interactions. Up to now it is successfully tested at energies up to 200GeV. The last particle of the Standard Model that still has to be discovered, the Higgs-boson, and even particles beyond the SM, are expected to be found at higher energies. The Large Hadron Collider (LHC) will provide comprehension to standard model physics and new physics on the scale up to 1TeV.

The high luminosity of the LHC is needed to compensate low interaction cross sections at high energies. But it has two disadvantageous consequences.

On the one hand, the resulting large hadronic background demands for radiation hard detectors with high granularity. In particular, the full silicon tracker of the Compact Muon Solenoid (CMS) experiment has to deal with a high occupancy and thus must have an excellent resolution to be prepared for the signature of the most promissing decay channel of a light Higgs into $b\bar{b}$.

On the other hand, the large luminosity is bought by means of a very high beam energy asking for save beam monitoring, cleaning and dumping. Although there will be great effort in protecting machine and experiments from beam losses, they cannot be excluded with last assurance. The impact of a beam loss to the CMS tracking detector has been investigated in this thesis.

Chapter 2 introduces the reader more detailed into the basics of this thesis concerning machine, beam dump system and silicon detectors. Chapter 3 presents the smallest subdetector of the CMS silicon strip tracker, the *module*. A description is given, its design is justified and its performance is briefly summarized. Chapter 4 motivates the need of beam loss studies in detail. The problem of particle fluxes induced by beam losses is discussed as well as the expected impact to modules. The fundamental questions motivating the beam loss tests are formulated.

In the following three sections, the experimental beam loss studies are presented. In Chapter 5, the first study at CERN PS with several modules and components exposed to a high intensive short proton bunch is reported. Measurement program and setup introduced here are the basis for the other two tests. Raw and evaluated data obtained from the online readout of sensor parameters is presented. These results are discussed in detail as well as the lab qualification of the tested devices. In Chapter 6, several sensors are exposed to a high intensive IR LED array within the scope of a lab study. Construction and energy calibration of the LED array are described extensively as well as the used data analysis package. Many new measured dynamical parameters are introduced. The results lead to a detailed physical and electrical comprehension of the processes occuring during such events. If possible, the data is confronted with an appropriate SPICE simulation. In the following Chapter 7, four sensors are exposed to a high intensive and enlarged IR laser beam. Sever damages to sensors due to the modification of the module's components are observed yielding in the knowledge of the safety margin of the final module design.

2 Introduction

An overview of the technical aspects of the Large Hadron Collider (LHC) is given with an emphasis on the beam abort system as main motivation of this thesis. Then, the physics objectives of the LHC and its four experiments are briefly introduced. The Compact Muon Solenoid (CMS) experiment is described in greater detail. The physical basis of silicon sensors, which are the fundamental part of the CMS tracking detector, is provided.

2.1 The Large Hadron Collider

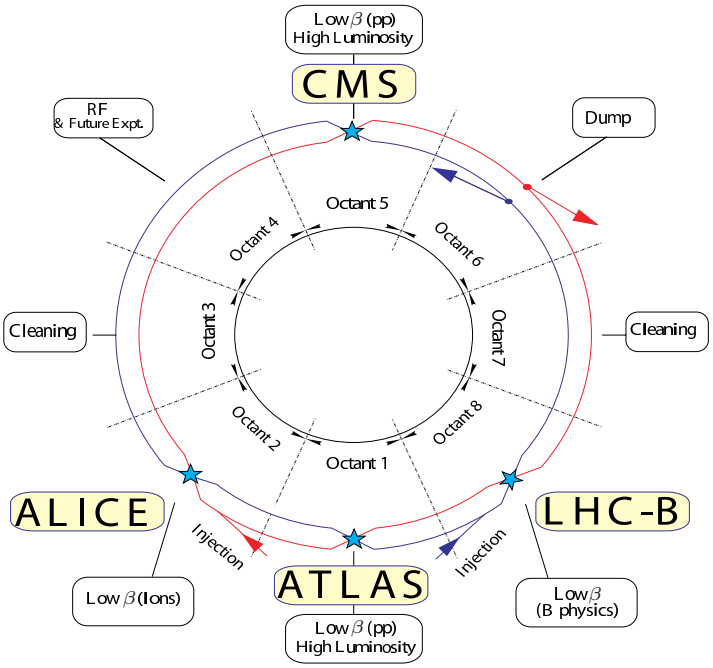

Figure 2.1: Layout of the LHC [LHC05].

The LHC will be a proton-proton-collider with the largest center of mass energy ($\sqrt{s} = 14$TeV) ever reached. The collisions take place at four interaction points where the experiments are setup (Fig. 2.1). ATLAS and CMS are general purpose detectors whose main objectives are the search for new particles completing the Standard Model (SM) as well as going beyond it. The two other experiments are optimised for special purposes. LHCb will investigate the physics of B-mesons and ALICE is dedicated to studies of hadronic matter by means of heavy ion collisions.

The LHC ring stores $b = 2808$ bunches with $N_{1/2} = 1.15 \times 10^{11}$ protons each. The RMS beam size at the interaction points 1 and 5 is $\sigma_{x/y} = 16.7\mu$m. With a circumfence of U = 26.65km, the revolution frequency is $f = c/U = 11.25$kHz. With a geometric luminosity reduction factor of $F^f = 0.836$ due to a non zero crossing angle of both beams, this results into a design luminosity of

$$\mathcal{L} = \frac{1}{4\pi} \frac{bfN_1N_2}{\sigma_x\sigma_y} F^f \approx \frac{1 \times 10^{34}}{cm^2 s}. \tag{2.1}$$

This large luminosity is necessary to compensate lower cross sections at higher energies.

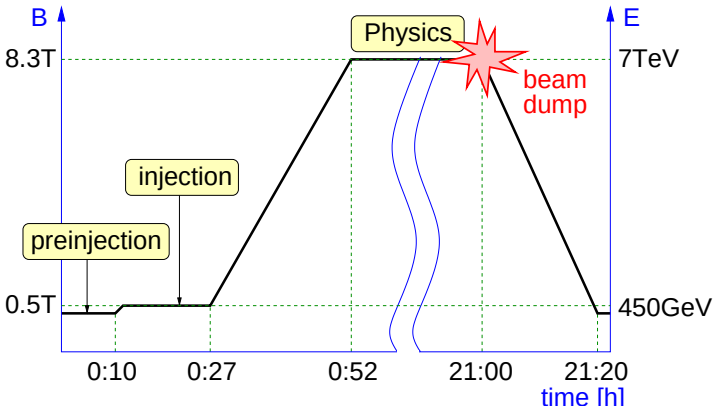

Figure 2.2: Baseline cycle of the LHC (after [LHC05]). *The protons enter the LHC at an energy of 450GeV. The total injection phase takes about 25 minutes. The duration of the following acceleration phase is downward limited by the magnetic field ramp up to the full strength of 8T and lasts other 25 minutes. A physics run at 7TeV lasts about 10 to 20 hours. Then, the beam is dumped in one circulation and the down-ramping of the magnets starts.*

The total cross section σ_{tot} is calculated by means of luminosity integration over time. Together with the production cross section of a special particle σ_{p}, this gives the expected number $\mathrm{N_p}$ of observed particles of this type during integration time.

$$\sigma_{tot}^{-1} = \int \mathcal{L}\, dt \tag{2.2}$$

$$N_p = \frac{\sigma_p}{\sigma_{tot}} \tag{2.3}$$

The TOTEM experiment will measure the total cross section and will also provide an absolute calibration of the machine luminosity [TOT04].

The efficient use of the acceleration facility and its experiments not only depends on the luminosity but also on its operation load. It is given by the machines and experiments maintenance time periods and intervals and by the duty cycle of the accelerator. A schematic of the latter one is shown in Fig. 2.2. The protons enter the LHC at an energy of 450GeV. The total injection phase takes about 25 minutes. The duration of the following acceleration phase is downward limited by the magnetic field ramp up to the full strength of 8T and lasts other 25 minutes. A physics run at 7TeV lasts about 10 to 20 hours (not shown in the figure). Then, the beam is dumped in one circulation. To enable the re-fill of the beam-line, the magnets are ramped down within 20 minutes to the injection strength of about 0.5T corresponding to the injection energy.

2.1.1 Beam Dumping System

Although "acceptable" beam dump failures will not damage the machine equipment, an impact of an *unsynchronized beam abort* on the tracking detector of the neighboured experiment (CMS) is likely and thus has been simulated in [H+99] and experimentally studied in this thesis. The detailed motivation is given in the dedicated Chapter 4 on Page 36.

In this section, an overview on the beam dumping system is given, and in the following one the types of possible failures. But firstly, the existance of a beam dump is motivated in the following paragraphs.

Due to unavoidable imperfections, there are continuous proton losses along the beam pipe reducing the luminosity with time. Therefore, the remaining beam must be dumped and re-filled from time to time. Given the very large stored energy of one LHC beam of 300MJ, the dumping system must meet extremely high reliability criteria, which condition the overall and detailed design [LHC05] (see Fig. 2.3 on the next page). It is placed in Octant 6, and provides the loss-free fast-extraction of the beam from each collider ring in one turn, its dilution and

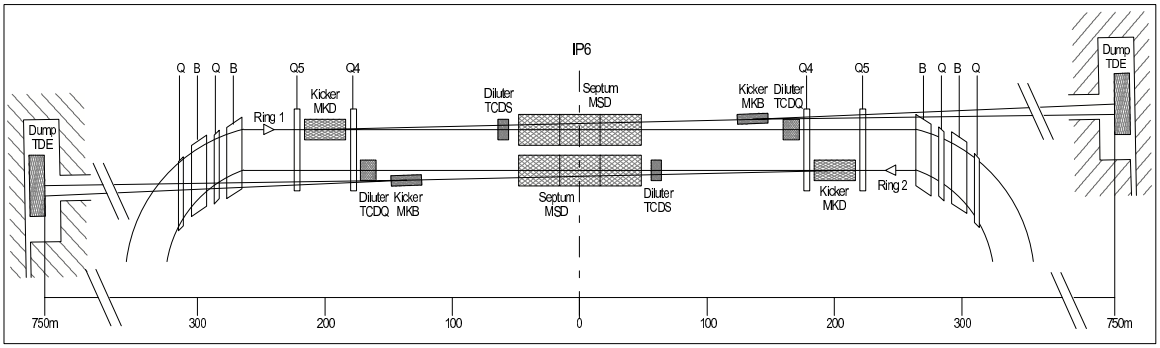

Figure 2.3: Layout of the LHC beam dumping system [LHC05].

the transportation to an external absorber block. The extraction system consists of 15 kicker magnets deviating the bunches from their original direction of motion and several dilution kicker magnets to open up the beam to an e-shaped spot of $40 \times 40\text{cm}^2$ on the absorber block, 950m away from the first kicker modules. The absorber block consists of polycrystalline graphite having a high melting point and best thermal shock resistance. The loss-free beam extraction requires a particle-free gap in the beam, the so called *abort gap* (3.17μs), during which the field of the extraction kicker magnets can rise to their nominal value (3μs). They hold their maximum strength of 0.34T with overshoots of only 5% for at least one turn (90μs).

The beam dumping system must be able to accept beams with well-controlled parameters (e.g. during a planned abort at the end of a physics run) and also beams with off-normal parameters (e.g. as arising from an equipment failure or beam instability).

2.1.2 Accidental Beam Losses

Regular *slow* beam losses are unavoidable and occur continuously during machine operation. Collimators and apertures along the beam pipe absorb almost all lost protons. But irregular or *accidental*, so called *fast* beam losses respectively are most probably caused by failures in the LHC magnet powering system or by magnet quenches [Brü01]. Beam loss monitors together with the beam interlock system avoid sever damages to machine and experiments by requesting a beam dump in such cases. But faults within the beam dumping system, so called *one-turn failures*, will cause *ultra-fast beam losses* [Sch03]. They could lead to damages to the dumping system itself, to the machine or to the experiments, due to full or partial loss of the beam onto machine components.

So called "acceptable" or design beam dump failures are expected to occur about once per year. They are considered in the design and the load calculations of dedicated machine systems, in particular the collimators. They may result in a loss of efficiency for operation but should not result in machine equipment damage.

- At an asynchronous dump (also called *unsynchronized abort* [H^+99, M^+99]), one of the kicker modules pre-fires followed by a re-triggering of the other ones, *or* all kicker magnets reach their full strength not synchronized with the abort gap.

- One extraction kicker module is missing. But a correct beam dump can be performed with only 14 functioning modules.

- Missing diluting kickers can cause a longer cool-down period of the dump block leading to a delay of the machine re-fill.

- The system is self-triggered causing an unwanted but synchronous beam abort.

Total system failures are expected once in about 100 years [LHC05] and are called "unacceptable" or beyond design fault cases.

- The kicker magnets do not fire when a dump request is made by another system (e.g. the beam loss system). This potentially catastrophic failure could be caused by an undetected fault of the beam interlock system or by problems in trigger signal transmission or reception.

- Only 13 or fewer of the 15 extraction kicker magnets are pulsing correctly resulting in equipment damage dependent on the number of failing kickers.

- The dump system receives the wrong energy information, caused by an error in the beam energy system. An error of only a few percent is sufficient to cause severe equipment damage.

- Magnetic fields of kicker magnets out of tolerance by more than 1% can cause beam losses or damages.

- All diluting kickers missing will cause damages to the dump block depending on the beam energy.

The above mentioned low failure rate makes such kind of beam loss very unlikely during the ten years of LHC operation. It is based on the use of high quality components and introducing redundancy for the most critical elements.

2.1.3 Beam Loss Protection

The machine and its experiments are protected from uncontrolled, *accidental* beam losses by several protection systems [S$^+$02]. *Collimators* arranged tightly arround the beam pipe catch protons with too large momentum deviation. Ionization chambers installed close to the collimators and other aperture limitations monitor the flux of secondary particles continuously (*beam loss monitor*). In case of an equipment failure (power supply or magnet quench), beam losses could then be detected within one turn. After the interlock system triggers the beam dump system, the beam could be dumped within about three turns.

Protection mechanisms of the CMS experiment from beam dump failures and the most probable *unsynchronized beam abort* in particular have been proposed [M$^+$99, M$^+$01]. Movable shadow collimators consisting of very tight jaws are placed in IP6 downstream of the abort system. Simulations predict a reduction of the peak particle flux in IP5 by six orders of magnitude. Another mechanism presented is a so called antikicker, that is no longer discussed in [M$^+$01]. The prefire of a single module is compensated by an opposite module charged with an opposite voltage. The antikicker should be fired with a delay less than 1μs after the kicker prefire to eliminate losses in IP5. After this, the beam can be safely aborted using the abort gap.

Nevertheless, at the start of the beam loss studies in Karlsruhe and CERN in 2002, the advance in the development of the two presented protection mechanisms hasn't exceeded the state of a proposal. Thus, all studies of the impact of an *unsynchronized abort* on the CMS strip tracker are dimensioned and calculated for the unprotected case.

2.2 Physics at the LHC

The center of mass energies reached in the LHC allow the probe of the Standard Model (SM) of Particle Physics as well as the search for new physics beyond it. The main objective is the search for the Higgs Bosons postulated by Standard Model and Minimal Supersymmetric Standard Model (MSSM) and for other supersymmetric particles. Measurements of $\mathcal{CP}$-violation in the B system and the exploration of B_S oscillations are foreseen. In heavy ion collisions, the hadronic form factors are studied as well as existance and properties of Quark-Gluon-Plasma. New physics aspects cover advanced theoretical approaches like extra dimensions and new particles beyond the MSSM [Roy03].

2.2.1 Higgs Search

The SM describes the elementary constituents of the known matter (quarks and leptons), as well as their interaction via three fundamental fields by means of the exchange of gauge bosons (photon, W and Z boson, gluon). All quarks, leptons and gauge bosons have been observed in experiments so far. But the SM is not able to explain the masses of the elementary fermions and the weak gauge bosons. If mass terms for them are introduced by hand, they destroy the gauge invariance of the theory. This problem has been solved by means of the Higgs mechanism in which masses are introduced into gauge theories in a consistent way. The solution of the problem is achieved at the expense of a new fundamental degree of freedom, the scalar Higgs field. The interaction energies of massless gauge bosons and fermions with the Higgs field in the ground state can be re-interpreted as the gauge boson and fermion masses. This mechanism claims for the existance of a spin-less, neutral particle, the Higgs boson. Its discovery and the measurement of its mass would complete the Standard Model of particle physics.

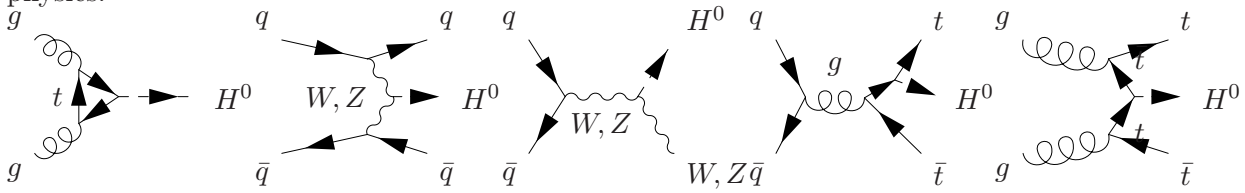

a. gluon fusion | b. vector boson fusion | c. higgs strahlung off vector bosons | d. higgs strahlung off top | e. higgs strahlung off top

Figure 2.4: Standard Model Higgs production [KM04] *by either gluon fusion via a top loop, which is the dominant process (Fig. a), vector boson fusion (Fig. b) or "Higgs strahlung" off vector bosons (Fig. c) and heavy quarks (Figs. d and e).*

Typical processes that can be exploited to produce Higgs bosons are gluon fusion, vector boson fusion and Higgs strahlung (see Fig. 2.4). The gluon fusion dominantes the Higgs production cross section throughout the entire Higgs boson mass range of up to 1TeV [KM04] (see Fig. 2.5). The gluon coupling of the Higgs boson in the SM is mediated by triangular loops of top and bottom quarks. Since the Yukawa coupling of the Higgs particle to heavy quarks grows with their mass, the top quark dominates this process. The other interesting production process is the vector boson fusion $q\bar{q} \rightarrow W^+W^-(ZZ)q\bar{q} \rightarrow q\bar{q}H$. It becomes competitive to the gluon fusion for large Higgs masses. A very important mechanism for the Higgs search at hadron colliders is the Higgs strahlung off vector bosons $q\bar{q} \rightarrow W(Z)^* \rightarrow W(Z)H$. Although the cross section is smaller than for gluon fusion, leptonic decays of the electroweak vector bosons are extremly useful to filter Higgs signal events out of the huge background. The Higgs strahlung off top quarks $q\bar{q} \rightarrow t\bar{t}H$ is relevant only for small Higgs masses. But it is an

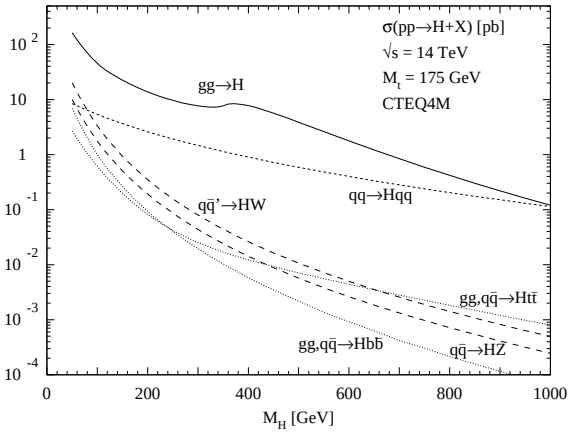

Figure 2.5: Higgs production cross sections [SSZ00]. *Various production mechanisms are shown as a function of the Higgs mass. The gluon fusion is dominating all over the total energy range.*

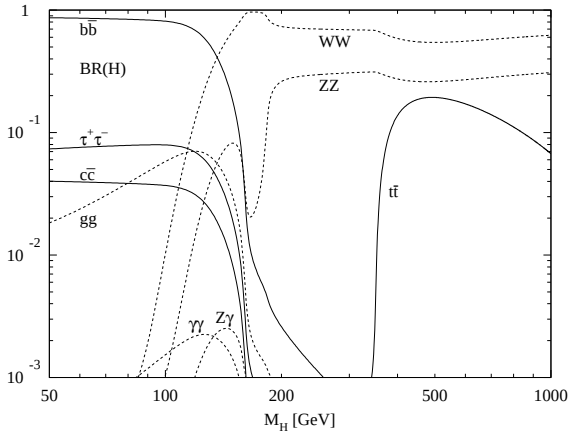

Figure 2.6: Higgs decay branching ratios [Roy03]. *Various decay mechanisms are shown as a function of the Higgs mass. Vector bosonic decays dominate at energies beyond the weak scale.*

interesting process to measure the Htt̄ Yukawa coupling.

The mass dependent Higgs decay branching ratios are displayed in Fig. 2.6. The dominating channel in the low mass region between 100GeV and 150GeV region is $H \to b\bar{b}$ unfortunately having a large QCD background, which is about 1000 times larger than the signal. Thus, one of the most promising decay channels in this region is $H \to \gamma\gamma$ [KM04], that unfortunately has a branching ration of only 10^{-3}. The background is small and due to $q\bar{q}$ annihilation, gluon fusion and bremsstrahlung. This requires an electromagnetic calorimeter with good energy resolution and high granularity. The signature $H \to WW^* \to l^-\bar{\nu}l^+\nu$ provides the Higgs discovery for the mass region between 155GeV and 180GeV at the opening of the W-channel. But it suffers from a much larger background for two reasons [Roy03]. It is not possible to reconstruct the two W masses due to missing energy from the two neutrinos, and there is a large WW background from $t\bar{t}$ decay. The most promising channel on the very large mass scale starting at the ZZ region and ending up to 600GeV is $H \to ZZ \to l^+l^-l^+l^-$. The reconstruction of the lepton masses is practically background free. For higher energies, the channels $H \to WW \to l\nu q\bar{q}$ and $H \to ZZ \to l^+l^-\nu\bar{\nu}$ have to be used.

2.2.2 B Physics

B physics allows the test of the SM description of $\mathcal{CP}$-violation. The cross section of $b\bar{b}$ production increases with energy and gives the LHC an advantage to the Tevatron. Together with the large luminosity, a high production rate of B mesons is expected opening up entirely new areas of B physics where the present data samples are very limited [Ege03]. LHCb is optimized for B-tagging and the detection of B-vertices. Although this is not the major design criterion for CMS and ATLAS, there will also be a B physics program demanding for an excellent vertex detector.

In the SM a complex unitary mass mixing matrix, the CKM matrix, parametrises the weak charged current and flavour changing interactions of quarks. When determined precisely, one is sensitive on $\mathcal{CP}$ violating and rare decay processes as well as on new physics [B+03]. The CKM matrix can be represented in various ways. The most common one is the *Wolfenstein Parametrisation* with four independent parameters A, λ, ρ and η [B+03]. One of them (λ) is responsible for the matrix being complex and is a measure for $\mathcal{CP}$ violation. The other ones can be geometrically illustrated in the so called unitarity triangle (Fig. 2.7 on the next page).

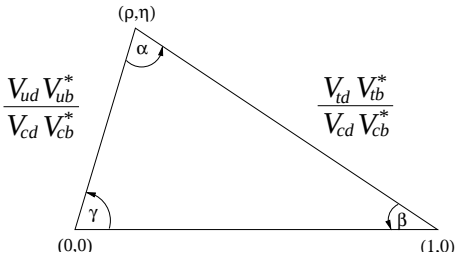

Figure 2.7: Unitarity triangle of the CKM matrix. *The rescaled parameters $\bar{\rho}$ and $\bar{\eta}$ are used.*

The measurement of the angle γ is one of the main purposes of B-experiments. The decay of the B_s into a D-meson and a Kaon is sensitive to this angle. The $\mathcal{CP}$-violating phase $\delta\gamma$ can be determined by means of B_s mixing measurements.

2.2.3 Supersymmetry

Supersymmetry (SUSY) is a symmetry between fermions and bosons. It predicts the quarks and leptons to have scalar superpartners called squarks and sleptons ($\tilde{q}$, $\tilde{l}$) and the gauge bosons to have fermionic superpartners called gauginos ($\tilde{\gamma}$, $\tilde{W}$, $\tilde{Z}$, $\tilde{g}$). In the minimal supersymmetric extension of the SM (MSSM), one needs two Higgs doublets $H_{1,2}$ with opposite hypercharge to give masses to the up and down type quarks [Roy03]. The corresponding fermionic superpartners are called Higgsinos ($\tilde{H}_{1,2}$). SUSY ensures that the quadratically divergent quantum corrections from quark, lepton and Higgs boson loops are cancelled by the contributions from the corresponding squark, slepton and Higgsino loops. Thus, the Higgs masses can be kept in a range of several hundret GeV. SUSY is a broken symmetry in masses. Its mass scale should be not too far above the SM mass scale of 100GeV. Therefore, if SUSY is realised by nature, hints on its existance should be found at the LHC.

2.3 The CMS Detector

The following sections briefly describe the Compact Muon Solenoid (CMS) detector, in particular the realisation of the physical intentions within the technical design and the various subdetectors, especially the silicon strip tracker to whose development this thesis is a contribution.

2.3.1 Design Objectives

For the design objectives of the CMS detector both parameters given by the LHC and constraints from the physical program have to be taken into account. The low production cross sections for the physics such as Higgs and supersymmetric particles at a center of mass energy of 14TeV requires a high collision rate resulting in a large hadronic background, out of which the interesting events have to be extracted. The bunch crossing frequency of 40MHz and the high luminosity resulting in an occupancy of 20 collisions per bunch crossing (corresponding to an event rate of 800MHz) put great demands on the detector and its readout electronics [CMS94, Wei04].

From these considerations and the demands of the reaction of interest follow, that an optimized and redundant muon system is needed to separate interesting events from background. In addition, a compact design and good momentum resolution ask for a strong magnetic field realized by a superconducting solenoid and an efficient all-silicon tracking system with high spatial resolution. A precise electromagnetic calorimeter for efficient detection of an

intermediate mass Higgs boson decaying via two photons fits naturally in the CMS design. The electromagnetic calorimeter and a hadronic calorimeter with good energy resolution are essential to trigger on missing energy events. And a high quality central tracking system of large granularity is needed not only to achieve the above mentioned points but also to be able to track B-vertices in an environment of large track density.

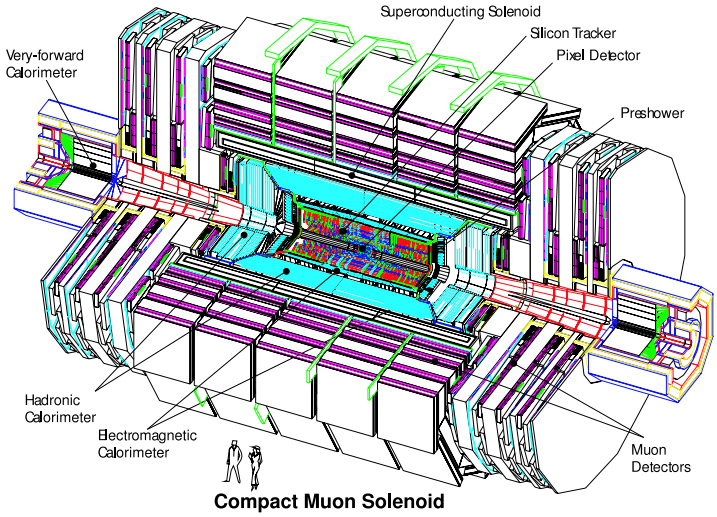

Figure 2.8: Schematic view on the CMS Detector [CMS06].

Figure 2.8 shows a schematic of the CMS detector. The silicon pixel detector is located closest to the beam pipe and is surrounded by the silicon strip tracker. The next shell is the electromagnetic calorimeter followed by the hadronic calorimeter. All components mentioned so far are located within a superconducting solenoid of 4T. As a speciality of the CMS detector design, the muon system surrounds the complete detector and uses the return yoke of the solenoid as absorber that provides, in addition, a finite magnetic field to the muon system. Two very forward calorimeters absorbing particles with large rapidity surround the beam pipe outside the solenoid on both sides of the detector.

The rapidity is a Lorentz-invariant measure of the longitudinal momentum of a particle and is defined as follows:

$$y = \frac{1}{2} \ln \left(\frac{E + p_l}{E - p_l} \right) = \tanh^{-1} \left(\frac{p_l}{E} \right). \tag{2.4}$$

The large momentum approximation of the rapidity (E $\gg$ m) is called pseudo-rapidity η.

$$y \approx -\ln \tan \left(\frac{\Theta}{2} \right) \stackrel{\text{def}}{=} \eta \tag{2.5}$$

Thus, η is a measure for the longitudinal angular deviation of a relativistic particle from the beam-axis.

2.3.2 Magnet System

The superconducting 4T solenoid is the main structure of CMS and defines dimensions and weight of the whole detector. The free magnetic field space within the solenoid where all subdetectors are placed (except for the muon detector and very forward calorimeter) has a length of 13m and a diameter of 6m. The return yoke of the solenoid, wherein the muon system is placed, provides a finit field enabling precise muon tracking without the need of additional toroidal solenoids [CMS94, CMS97c].

2.3.3 Muon Detector

The task of the muon detector system is the efficient identification of muons and the measurement of their momenta from a few GeV to a few TeV over a large rapidity interval and at largest luminosities. It is geometrically made out of a cylindrical barrel closed at both ends by two endcaps and is integrated in the return yoke of the magnet. Three different detector technologies are in use: Trift tubes in the barrel region ($0.0 < |\eta| < 1.3$), cathode strip chambers in the endcap region ($0.9 < |\eta| < 2.4$) and resistive plate chambers in both barrel and endcap regions ($0.0 < |\eta| < 2.1$) for trigger purposes. The spatial resolution ranges between 50 and 200μm across the covered pseudo-rapidity and ensures a standalone transverse momentum resolution of about 10% [Gia02, CMS97d].

2.3.4 Hadronic Calorimeter

The combined CMS calorimeter system will measure quark, gluon and neutrino directions and energies by measuring the energy and direction of particle jets and of the missing transverse energy flow. This determination of missing energy will also form a crucial signature for new particles and phenomena, such as will be encountered in the searches for the supersymmetric partners of quarks and gluons. The hadron calorimeter will also help in the identification of electrons, photons and muons in conjunction with the electromagnetic calorimeter and the muon system [CMS97b]. The hadronic calorimeter consists of three parts, the barrel, two end-caps and the two very forward calorimeters [Mer98]. The central pseudorapidity range is covered by the barrel and endcap both experiencing the 4 Tesla field and hence necessarily must consist of non-magnetic material (copper alloy and stainless steel). It is a sampling calorimeter and consists of active material (4mm thick plastic scintillator) inserted between copper absorber plates, 5cm thick in the barrel and 8cm thick in the endcap. The barrel covers an $\eta < 1.3$, the endcap a range of $1.3 < \eta < 3.0$ and the very forward calorimeter covers $2.75 < \eta < 5.25$ allowing the measurement of missing transverse energy and forward jet tagging. It uses quartz fibers as the active medium, embedded in a copper absorber matrix. Therefore it is only sensitive to relativistic charged particles. Hence, it does not see low-energy neutrons, which will traverse in large numbers.

2.3.5 Electromagnetic Calorimeter

The electromagnetic calorimeter (ECAL) will play an essential role in the study of the physics of electroweak symmetry breaking, particularly through the exploration of the Higgs sector. The search for the Higgs at the LHC will rely on information from the ECAL by measuring the decay mode $H \rightarrow \gamma\gamma$ for $m_H < 150GeV$ and by measuring the electrons and positrons from the decay of Ws and Zs originating from the Higgs decay for $140GeV < m_H < 700GeV$. A scintillating crystal calorimeter offers the best performance for energy resolution since most of the energy from electrons or photons is deposited within the homogeneous crystal volume of the calorimeter. Lead tungstate ($PbWO_4$) crystals were chosen because they offer the best prospects of meeting the demanding requirements of high density fast scintillating crystals with a small Molière radius and a short radiation length for a very compact electromagnetic calorimeter system.

The ECAL consists of a barrel part ($|\eta| < 1.49$), two endcaps ($1.48 < |\eta| < 2.6$) and a preshower detector. The crystals in the barrel are read out by avalanche photodiodes and in the endcaps by vacuum photo-triodes as they are more radiation tolerant [CMS97a].

2.3.6 Central Tracker

The central tracker consists of a silicon pixel detector close to the beam-pipe and is surrounded by a full silicon strip detector.

The task of the pixel detector is to provide high-resolution 3D space points required for the track pattern recognition and for b-tagging. There will be three 53cm long barrel layers supplemented by two end disks on each side. In order to achieve the optimal vertex position resolution in both the (r,ϕ) and the z coordinates a design with a square pixel shape $150 \times 150\text{mm}^2$ was adopted. The whole pixel system consists of about 1500 detector modules arranged into half-ladders of 4 identical modules each in the barrel and blades with 7 different modules each in the disks. To read out the detector, about 16 000 readout chips are bump-bonded to the detector modules. The total number of readout channels (pixels) is about 45×10^6 [Kot01].

The overall dimensions of the silicon strip tracker will be a cylindrical volume with 6m length, an inner diameter of 40cm and outer diameter of 2.4m. In the central rapidty region, detectors are arranged in 7 inner (TIB) and 6 outer barrels (TOB) with strips parallel to the beam-axis, while in the forward regions, for each of the two end caps, they are arranged in 3 inner (TID) and 9 outer disks with up to 7 rings (TEC) with strips radial to the beam-axis (Fig. 2.9). This layout performs best momentum resolution for the total covered rapidity range.

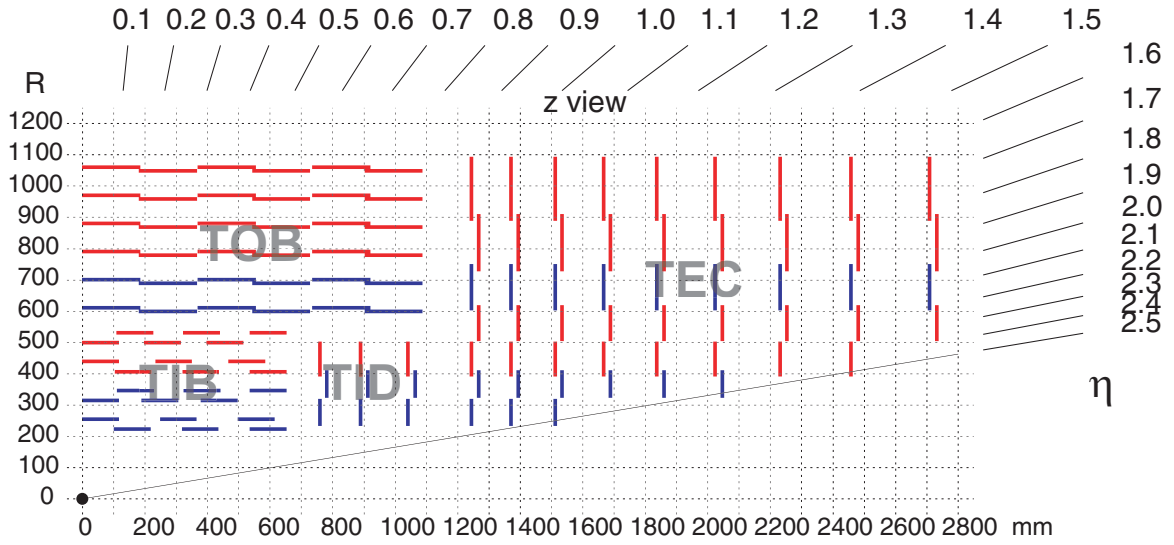

Figure 2.9: Layout of the Strip Tracker. *The longitudinal section of one quadrant is shown [Die03]. There are single sided (red) and double sided modules (blue). The meanings of the abbreviations are: Tracker Inner Barrel (TIB), Tracker Outer Barrel (TOB), Tracker Inner Disk (TID) and Tracker Endcap (TEC).*

For 100GeV muons, the transverse momentum resolution starts at 1.5% for low rapidities and worsens with rapidity due to a larger arm of lever (Fig. 2.10a on the next page). The impact parameter resolution is between 20 and 30 μm (Fig. 2.10b on the next page). The single track reconstruction efficieny is 100% over most of the rapidity coverage for muons [Len01] and drops to 90 to 95% for pions, mostly due to nuclear interactions [Tri04]. The track finding efficiency within jets allway is better than 87% for $E_T = 200$GeV in the full rapidity range and the fake rate is lower than 1.5%. The b-jet tagging probability is best for $E_T = 100$GeV and ranges between 65% in the barrel region and drops to 43% in the endcap region. The misstagging rate is smaller than 1% [Len01].

The tracker's smallest substructure, the silicon strip module, consists of one or two single

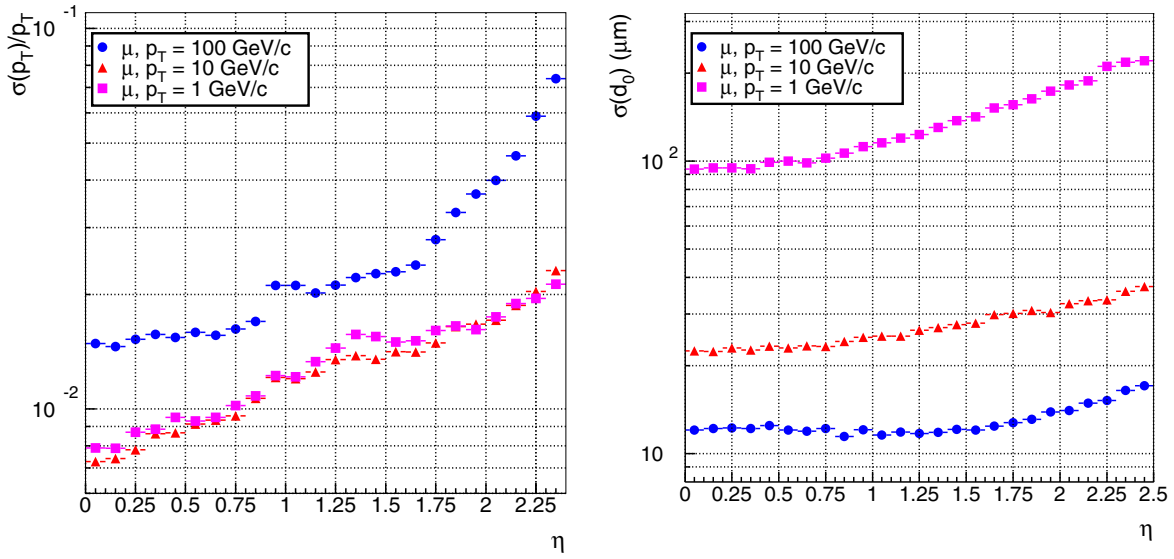

a. transverse momentum resolution

b. transverse impact parameter resolution

Figure 2.10: *Tracker transverse momentum (Fig. a) and impact parameter resolution (Fig. b) vs. rapidity η for muons at three different transverse momenta* p_T *[Tri04].*

sided silicon strip sensors of different thicknesses, strip pitches and strip lengths. To get a three-dimensional information, some modules are arranged back-to-back at a small relative angle (*double sided* modules, Fig. 2.9 on the previous page). For the inner barrel, the strip length is about 10cm and the thickness of the sensitive silicon volume is 320μm to reduce leakage current and noise caused by the larger radiation dose. For modules in the outer reagions, strip lengths of 20cm (two sensors in series) are sufficient. This reduces the number of electronical channels. The larger noise is compensated by using silicon of 500μm thickness [CMS98, CMS00a]. Another criterion is the operational voltage before and after radiation impact to the silicon. This forces the use of low resisitive silicon in the inner part of the strip tracker to start at a relatively high depletion voltage and high resistive silicon in the outer part. Both configurations end in a voltage of about 400V after ten years of LHC operation.

2.4 Silicon Sensors

A brief introduction on the physical basis of radiation sensitive silicon devices needed in this thesis is given. For deeper examinations of this topic, the reader is referred to textbooks [Sze81, Sze94, Sze02, Lut99].

The existance of allowed and not allowed continua of energetic states in solids, so called *bands*, is a quantum mechanical effect and is due to the overlap of wavefunctions of electrons in the periodic potential of the remaining atoms. This fact concludes to space periodic solutions of the Schroedinger Equation of this problem. Thus, the energies corresponding to this solutions are plotted in the momentum domain between the according points of crystal symmetry. On the one hand, there are energy bands, that are fully populated at any time and such ones, that are populated only by means of excitation. The highest energetic band of the permanently filled type is called *valence band* and the band with lowest energy of the other type is called *conduction band*. The energetic gap between them is characteristic and is called *bandgap* (E_g). Depending on the bandgap, the population density in the conduction band at

room temperature due to thermal excitation is large for a *conductor*, by orders of magnitude smaller (but not zero) for a *semiconductor* and practically zero for an *insulator*. In an indirect semiconductor, like silicon, excitation to the lowest energy of the conduction band is possible only by means of an additional momentum transfer (see Fig. 2.11). The indirect bandgap in silicon is 1.12eV and is from crucial importance for the comprehension of near infrared (NIR) light induced excitation (see Section 2.4.3 on Page 27).

2.4.1 pn-Junction

Pure and undisturbed semiconductors (e.g. without lattice defects and impurities and not under mechanical stress) are called *intrinsic*. The insertion of impurities into the crystal lattice is called *doping*, and those semiconductors are called *extrinsic*. Silicon is formed in a diamond type lattice with four valence electrons. Atoms with five valence electrons, included into the lattice, are called *donors* (n-type doping e.g. with phosphor), as one of the electrons is weakly bound and causes an excess of electrons. In the opposite case, the p-type doping, atoms with three valence electrons (*acceptors*, e.g. boron) are put into the lattice and cause an excess of holes. In terms of the band-model, a doped semiconductor has additional energy levels in the band gap. In a common n-type semiconductor, donor levels are closely (some 10meV) below the conduction band and are therefore completely ionized thermically and thus significantly increasing the electron conduction of the material. In a p-type semiconductor, acceptor levels are closely above the valence band increasing significantly the hole conduction.

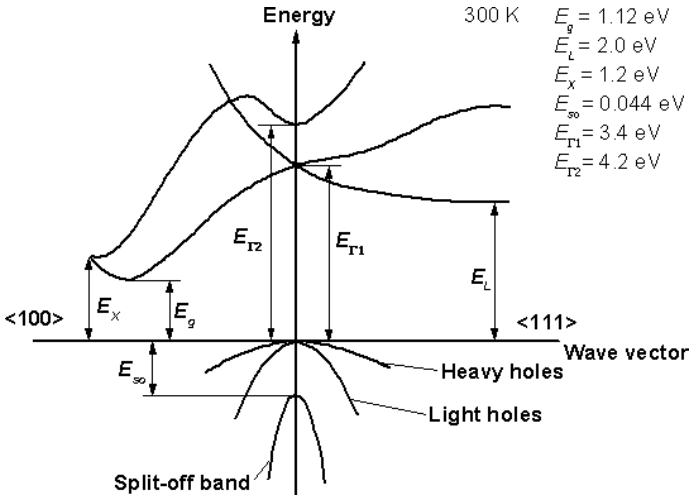

Figure 2.11: Energy band structure of silicon [Tol03]. *Silicon of <100> lattice orientation is used for CMS strip sensors. A detaild explanation is seen in Section 3.1 on Page 30.*

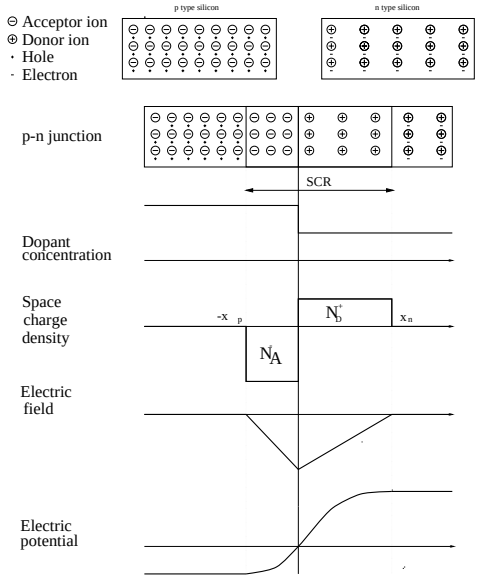

Figure 2.12: *Schematic of pn-junction in thermal equilibrium [Kra01].*

In a purely doped material, electrons and holes respectively, are homogeneously distributed over the whole volume. Joining two semiconductor materials of opposite doping gives a *pn-junction* (Fig. 2.12). As the electons in the n-region are on a higher energy level than the holes in the p-region, they start to drift into the p-region filling some of the excess holes. This results in a space charge region near the junction causing the development of a contact voltage. The space charge region can be expanded over the whole doped volume by applying an external voltage to the device in reverse direction with respect to the energy barrier at

the pn-junction. Dependent on the voltage, this will *deplete* a part of the volume from charge carriers. An electrical field gradient developes in the depleted zone. The dependence of the field on the location can be simply obtained from the Gaussian Theorem. The electrical flux flowing through a plane perpendicular to the direction of depletion growth is

$$\int E\ dA = Q/\epsilon \Rightarrow E\ A = \frac{A\ x\ e\ N_{\text{eff}}}{\epsilon_r \epsilon_0} \tag{2.6}$$

where A is the area of the device, x is the distance of the plane from the edge, N_{eff} is the effective charge carrier concentration, that is the difference of donor and acceptor concentrations in a general case ($N_{\text{eff}} = |N_a - N_d|$). In an highly n-type doped semiconductor for example, one has $N_d \gg N_a$ and $N_d \gg N_i$ (intrinsic charge carrier concentration) and thus $N_{\text{eff}} \approx N_d$. The voltage drop over the space charge region with a thickness of d is then

$$V = \int_0^d E\ dx = \frac{e\ N_{\text{eff}}\ d^2}{2\ \epsilon_r \epsilon_0} \Rightarrow d = \sqrt{\frac{2\ \epsilon_r \epsilon_0\ V}{N_{\text{eff}}\ e}} \tag{2.7}$$

Full depletion is reached when the thickness of the depletion zone d reaches the total thickness D of the doped layer. This occurs at the so called *depletion voltage* V_{dep}.

$$V_{\text{dep}} = \frac{e\ N_{\text{eff}}\ D^2}{2\ \epsilon_r \epsilon_0} \tag{2.8}$$

The concentration of any type of charge carriers N_x can be expressed in terms of charge carrier mobility μ and electrical resistivity ρ : $N_x = 1/(e\rho\mu_x)$. Mobilities are different for electrons and holes, thus

$$N_{\text{eff}} = |N_a - N_d| = \frac{1}{e\rho} \left| \frac{1}{\mu_e} - \frac{1}{\mu_h} \right|. \tag{2.9}$$

In a n-doped semiconductor, n-type charge carriers dominate: $N_{\text{eff}} \approx N_d$. With Eq. 2.8, this gives

$$V_{\text{dep}} = \frac{D^2}{2\ \epsilon_r\ \epsilon_0\ \rho\ \mu_e} \tag{2.10}$$

With Eq. 2.7, the voltage dependent capacitance per area unit of the device is

$$C/A = \epsilon_r \epsilon_0\ /d = \sqrt{\frac{\epsilon_r \epsilon_0\ e\ N_{\text{eff}}}{2\ V}} \tag{2.11}$$

Plotting $1/C^2$ will result in a straight line with positive gradient until V_{dep} for a constant doping profile and effective charge carrier concentration respectively over the whole width of the probe. From then on, total depletion is reached and no change in capacitance should be observed.

Electron-hole pairs that are not separated by an electrical field recombine with a certain decaytime. Therefore, an electrical field must be established in the sensitive volume. As seen previously, this can be done by means of reverse-biasing a pn-junction giving a depleted detector. Excited electrons and holes are separated then and drift along the electrical field to the edges of the sensor where they can be readout capacitively from a metal oxide semiconductor (`MOS`) structure or directly by their induced current pulse. The mobility of electrons and holes directly gives the drift time of the charge carriers at a given bias voltage and thickness. The drift time defines the response time respectively clearing time of the whole device being from crucial importance in fast bunch crossing experiments like CMS.

2.4.2 Interaction of charged Particles with Silicon

The energy loss of moderately relativistic charged particles in matter due to ionization and atomic excitation is described best by the Bethe-Bloch equation. The energy loss mainly depends on atomic weight and number (Z) of the material, its ionization potential and the relativistic factor $\beta\gamma$ of the particle. A minimum is reached at values of arround $\beta\gamma = 3.2$ for almost all elements. From then on, ionizing energy loss starts a moderate logarithmic increase with $\beta\gamma$. Therefore, in practical cases, almost all relativistic particles can be assumed and therefore are said to be *minimum ionizing*. But for *ultra* relativistic charged particles, like electrons in the momentum order of 1GeV/c, the energy loss by *bremsstrahlung* starts to dominate. It is emitted, when particles are decelerated in the atomic potential of the traversed matter. The energy loss due to bremsstrahlung simply is proportional to the particle energy with a characteristic attenuation length X_0, the so called *radiation length*, that is characteristic for materials.

The Bethe-Block equation gives the *mean* energy loss per unit length. But this value is useless in describing the behaviour of a single particle because of stochastic fluctuations of the energy loss. The probability density of the energy loss in a thin absorber is Landau-distributed arround a *most probable* value. This value is more relevant for detector calibration since the tail of the Landau-function is often lost in background and in any case is difficult to define because of the weight of a few high-loss events [E$^+$04].

The evaluation of the Bethe-Block equation for silicon results in a mean energy loss of a mimimum ionizing particle of 388eV/μm. The calculation of the Landau-distribution depends on the absorber thickness and gives a most probable energy loss of 275eV/μm in a 640μm thick silicon absorber [E$^+$04].

Ionization in a semiconductor is equivalent to the creation of electron-hole pairs (EHPs). For this, an energy of 3.63eV is needed in average [Lut99, ABS80] being slightly larger than the direct bandgap of 3.4eV (see Fig. 2.11 on Page 25) because of phonon emission [ABS80].

2.4.3 NIR Light Absorption in Silicon

High energetic photons are absorbed in matter mainly by means of e^+e^- pair production having a characteristic mean free path of $\frac{9}{7}X_0$ [E$^+$04]. But this process is unwanted in a silicon sensor used in a detector dedicated to the tracking of charged particles, as it would cause electromagnetic showers impurifying the relevant tracks. Therefore, the radiation length X_0 of a tracking detector must be minimized.

Although CMS silicon strip detectors (Section 3 on Page 30) are not intended to use as photo detectors (photo diodes), within the scope of this thesis, high intensive near infrared (NIR) light has been used to simulate the passage of a large amount of particles through the detector. Thus, this section describes the absorption mechanism of NIR photons in silicon and gives a quantitative comprehension. This knowledge is needed later to be able to estimate charges and currents flowed through the silicon sensor, that are a measure of the electrical stress the sensor suffers from due to illumination.

The penetration depth δ is the reciprocal of the absorption coefficient α and specifies the length in a material, on which the light intensity is reduced to 1/e of the initial value (law of Lambert-Beer).

$$I(x) = I_0 \; e^{-x/\delta} \tag{2.12}$$

So, the probability of absorption p(x) after the penetration way x increases by the following equation:

$$p(x) = 1 - e^{-x/\delta}. \tag{2.13}$$

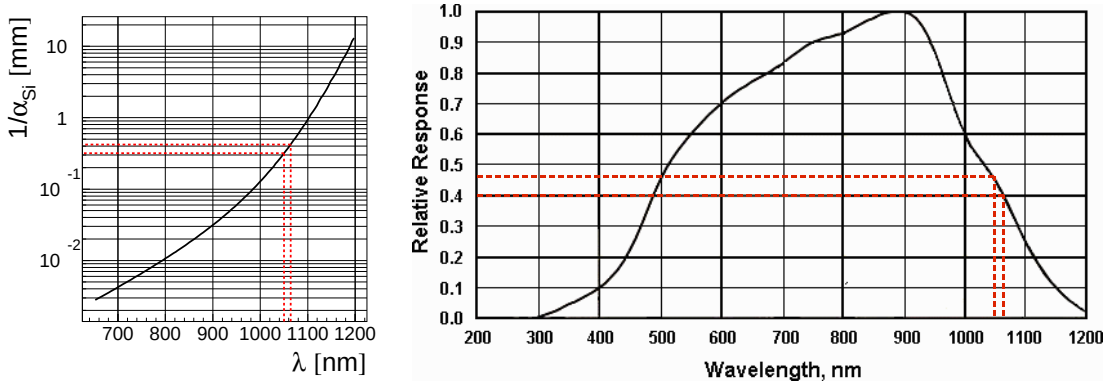

a. $1/\alpha$ vs. λ b. spectral response vs. λ

Figure 2.13: Light absorption in silicon. *Fig. a: penetration depth of light $1/\alpha$ vs. wavelength at room temperature calculated from [H^+98, Kvi04] and approximately agreeing with [Sze81, Sze02] in the interesting* NIR *wavelength range. Fig. b: Relative spectral response (quantum efficiency) vs. wavelength of standard silicon corresponding well to [RS 02]. The dashed lines denote the values at the relevant wavelengths of 1050nm and 1064nm respectively.*

δ is strongly dependent on the wavelength and varies in silicon from some μm for red light to 10mm for NIR light (see Fig. 2.13a). NIR photons with a wavelength of 1064nm, that is typical for IR lasers and has been used within this thesis, have an energy of 1.17eV. This is by far not enough for direct excitations into the conduction band as 3.63eV is needed for this. But the indirect bandgap of 1.12eV allows the excitation of electrons into the conduction band by means of additional momentum transfer from lattice phonons.

Not each photon creates an electron-hole pair. The efficiency of this process is called *quantum efficiency* η or *spectral response* (Fig. 2.13b) and depends amongst others on the wavelength and is defined as the fraction of electron-hole pairs created for each incident photon:

$$\eta = \left(\frac{Q}{e}\right) \cdot \left(\frac{E_{opt}}{h\nu}\right)^{-1} \tag{2.14}$$

E_{opt} is the incident light energy, and Q is the amount of created electron-hole pairs. The quantum efficiency shows a steep decrease at larger wavelengths, as the remaining photon energy available for phonon interaction decreases. The decrease down to shorter wavelengths is due to the very small penetration depth. Most of the light is absorbed near the surface. The lifetime of the created charge carriers is very small due to surface recombination (see the following section and [Sze94]).

2.4.4 Recombination

Recombination (dissapearance/annihilation of an electron and a hole) is mentioned here as it explains the loss of incident light energy within the scope of the high power pulsed laser test (see Chapter 7 on Page 95).

Recombination occurs in pure semiconductors, but it is eased by any defect in the lattice like doping and other impurities or deformations (*defect recombination*) or near the surface, that also can be considered as a "lattice defect" (*surface recombination*). There are several recombination processes.

Direct Recombination

It occurs only in direct semiconductors, like Gallium Arsenide, where no momentum transfer is needed to excite an electron into the conduction band. When an electron-hole pair is created, its annihilation is very likely, as no additional phonons are required [Sze02]. The recombination rate is proportional to the concentration of electrons in the conduction band (n) and of holes in the valence band (p). In thermal equilibrium (n_0 and p_0), recombination (R) and thermal generation G_{th} rates are equal. But when excess carriers are introduced for example by illumination, and steady state is reached, net recombination rate $U = R - G_{th}$ and light induced creation rate G_L are equal. After some calculation and for low injection rates, this yields to

$$U = \frac{p - p_0}{\tau_p} \tag{2.15}$$

with $\tau_p = \frac{1}{\beta n_0}$ is the charge carrier lifetime.

Indirect Recombination

For indirect semiconductors like silicon, a direct recombination process is impossible, as momentum transfer from the lattice is required (Fig. 2.11 on Page 25). Therefore, the dominant recombination process is indirect transition via lokalized energy states in the forbidden energy gap. These states act as stepping stones between conduction and valence band. It is obvious, that the recombination rate depends on the concentration of recombination centers in the lattice. Under low external injection, the rate is from the same type as seen in Eq. 2.15, but the lifetime additionally depends on the location of the additional states in the energy domain.

Surface Recombination

Due to the abrupt discontinuity of the lattice structure at the surface, it can be considered as a large number of localized energy states or recombination centers. These additional states will greatly enhance the recombination rate near the surface. It is no longer measured as a volume rate but as a rate per area unit and is at low injection condition again proportional to the excess hole concentration at the surface.

Auger Recombination

This process occurs by the transfer of the energy and momentum released by the recombination of an electron-hole pair to a third particle that can be either an electron or a hole. After the Auger process, the third particle may loose its energy by lattice scattering events. Auger recombination becomes important when the charge carrier concentration is very high as a result of either high doping or high injection.

The electron energy released due to any type of recombination can be emitted as photon (*radiative recombination*) or by multiple phonon scatterings (*non radiative recombination*).

3 The CMS Silicon Strip Tracker Modules

CMS strip tracker modules consist mainly of one or two silicon sensors, the front end hybrid (FEH) for amplification and pipelining of the analogue data and the T-filter in the HV-line for filtering and buffering the bias voltage. The technical and physical intentions of the CMS silicon sensor design are presented as well as the module design and an overview on the analogue readout chain. With the gained knowledge, the signal performance of the whole device is briefly introduced.

3.1 The CMS Silicon Strip Sensors

Strip detectors are intended for precise position measurements of particle tracks. Created electron-hole pairs are separated and drift along the field to any readout structure that is usually of MOS type. The position is then calculated as center of gravity of the charge collected by the affected strips.

The choosen design of the sensors is motivated in the first section. Then, its technical implementation is briefly described. Afterwards, the sensor qualification procedure, that has been established for mass production, is introduced since it is used within the scope of this thesis several times.

3.1.1 Design Objectives

The large rate of hadron collisions inside the LHC detectors will create an enormous radiation background which will damage every detector material. The innermost layers of the strip tracker will receive an estimated equivalent fluence of $1.6 \times 10^{14} \mathrm{n_{1MeV}/cm^2}$ during 10 years of LHC operation. See [Die03, Wei04] for details on the radiation quality studies of CMS strip sensors and modules. The load, the outer layers are exposed to, decreases with the distance from the interaction point.

Thus, the main objective in sensor design has been the correct choice of parameters that are strongly coupled to irradiation effects in the silicon.

Silicon Resistivity

One effect of radiation induced damage to the silicon is type inversion of the effective charge carriers. During irradiation, p-type deffects mainly due to displacement of lattice atoms are introduced into the silicon. Starting at n-type silicon, this will result in a reduction of the effective doping concentration $\mathrm{N_{eff}} = |\mathrm{N_n} - \mathrm{N_p}|$ and then to an excess of p-type defects: $\mathrm{N_p} > \mathrm{N_n}$. Accordingly, the depletion voltage firstly decreases and then increases again reaching any value depending on the radiation dose. Since sensors must be fully depleted in any case to enable a free drift of the charge carriers, the depletion voltage reached at the end of LHC operation should be not too large to minimize the risk of breakdown. By choosing the initial concentration of n-type defects, one can adjust the starting value of the depletion to reach a reasonable value at the end of LHC operation. Low resistivity silicon (1.25-3.25kΩcm) having a large doping concentration (Eq. 2.8 on Page 26) is used for the innermost layers suffering from the highest radiation rate, thus starting at a large depletion voltage (Eq. 2.10 on Page 26) of 330V. High resistivity silicon (3.5-7.5kΩcm) with smaller doping concentration is used for the

outermost layers starting at a smaller depletion voltage [Kra04]. Both configurations result in depletion voltages of 400V to 500V in the end.

The second effect of radiation to silicon is the increase of the *leakage current* of the sensor linearily with the increase of impurity concentration or radiation fluence respectively. Starting at relatively small leakage currents with room temperature of about 10nA/cm^2 sensor surface, after irradiation, it is impossible to bias the sensor at room temperature due to the increase of the defect concentration by orders of magnitude. As the leakage current decreases for lower temperatures, the sensor can be operated at $-10°C$ with a reasonable current density in the order of 5μA/cm^2 at 500V.

Lattice Orientation

A further design criterion related to radiation hardness is the choose of the $<100>$ lattice orientation for CMS strip sensors. This leads to a suppression of surface damage resulting in reduced increase of interstrip capacitance, i.e. capacitive noise after irradiation, which is the main noise contribution at the working temperature of $-10°C$ [A$^+$04].

Sensor Thickness

The sensor thickness is another design criterion that influences the sensor's performance. A compromise has to be found between a gain in signal when using thick sensors but an increase of radiation damage and thus depletion voltage after radiation. This problem has been solved for the CMS strip tracker by choosing 320μm for the innermost (low resistivity) sensors to have a comfortable depletion voltage after irradiation [Sgu04]. 500μm can be safely choosen for the outer sensors giving an increased gain, that compensates the increased noise of double-length strips in modules with two sensors.

Production related Constraints

The CMS tracking detector will consist of about 24000 silicon strip sensors [Kra04]. Thus, one of the constraints in setting up the design of the sensors has been mass production capabilities. The result was a simple design compared to previous projects in high energy physics. Single sided sensors are used easing much the production and handling of such devices. The second constraint is the use of the availabe 6" wafer area. All 15 sensor geometries have been optimized to make maximum use of it. Test structures for R&D and quality assurance purposes cover the remaining half-moons.

3.1.2 Sensor Layout

A layout of the sensor in cuts through all three space planes is shown in Fig. 3.1 on the next page. The sensitive volume of the detector is of n-type silicon. Together with p$^+$-strips implanted into the n-bulk on top of the sensor, the pn-junction is formed. The diode is depleted by applying a positive voltage to the aluminium backplane that is connected to the sensor via a highly n-doped zone (n^{++}). On the other side, the potential of the p$^+$-strips is defined by a bias resistor (R_{bias}) connecting them over the common bias ring with ground. Incident particles create a track of electron-hole pairs in the sensitive volume along their path of flight. They are separated by the electrical field and drift along the field lines to the p$^+$-strips where they are acquired capacitively coupled (C_c) via aluminium strips. An overhang of the Al strips moves the high electrical field from the p$^+$-implants into the oxide layer (Fig. 3.1a on the next page) allowing to operate the detectors at higher bias voltages

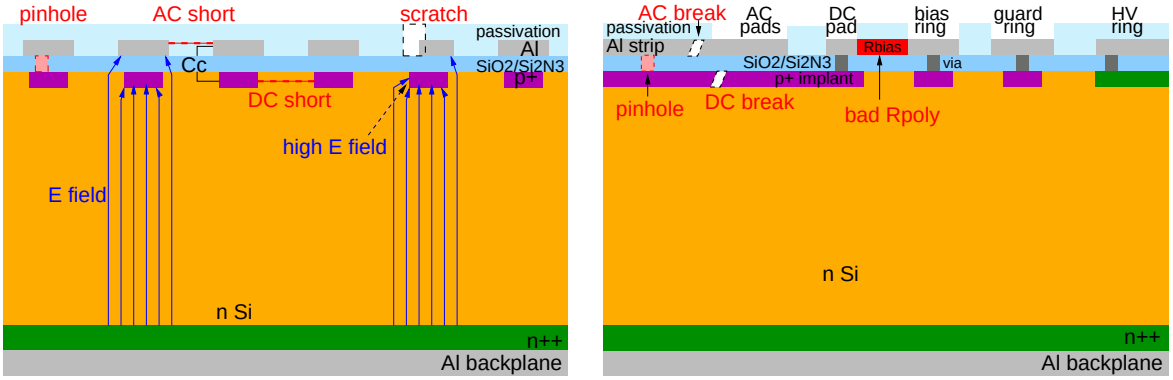

a. cross section

b. longitudinal section

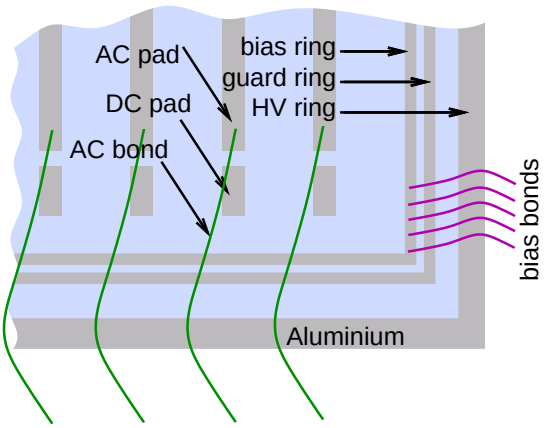

c. top view on an edge

Figure 3.1: Different views on a sensor with sensor faults. *The sensitive volume is of n-type silicon. It is connected to the highvolage via a highly n-doped zone (n^{++}) and an aluminium backplane. n-bulk and p^+-strips implanted into it on top of the sensor form the pn-junction. Their potential is defined by a bias resistor (R_{bias}) connecting them over the common bias ring with ground. Signals are acquired capacitively coupled (C_c) via aluminium strips. An overhang of the Al strips reduces the electrical field in the silicon (Fig. a). The p^+-strips are connected to ground via bias resistors and the common bias ring. The guard ring (Fig. b) smoothes the electrical field. Bond wires connect the bias ring with ground and the aluminium strips with the readout (Fig. c).*

[Wei04]. The p^+-strips are connected to ground via bias resistors and the common bias ring. The guard ring located between bias and high voltage ring at the edge (Fig. 3.1b) attenuates the electrical field between them. Bond wires connect the bias ring with ground and the aluminium strips with the readout (Fig. 3.1c).

3.1.3 Sensor Quality Control

The quality of the sensors has to be verified throughout the whole mass production process. Therefore, quality control procedures have been specified including standardized test measurements performed by the collaborating institutes for a fraction of all sensors [Har02]. These measurements also have been performed for almost all sensors used within the scope of this thesis.

The standard test contains the measurement of leakage current and total sensor capacitance over bias voltage. The first one mainly is sensitive to mechanical and structural integrity of the sensor. The second one gives the depletion voltage, that is a measure of the effective doping concentration (Section 2.4.1 on Page 25). In addition, four quantities are measured for each strip to detect individual strip failures (see Fig. 3.1). The standard test is sensitive to pinholes (an ohmic-like connection of aluminium strip and p^+-implant destroying the capacitive signal coupling and endangering the signal preamplifier), shorted strips, some local defects like scratches or breaks and bad bias resistors. The measurements done are as follows.

parameter	symbol (and formula)	expectation	condition
	global parameters		
leakage current	I_{leak}/A	$< 100nA/cm^2$	$V_{bias} = 450V$
depletion capacitance	$C_{dep}/A = \epsilon_0\epsilon_{Si}/d_{bulk}$	$\approx 21pF/cm^2$	$f = 1kHz$
depletion voltage	V_{dep}	$> 100V, < 300V$	-
	local parameters		
strip leakage current	I_{strip}	$< 100nA$	$V_{bias} = 450V$
pinhole measurement	$I_{diel} = V_{diel}/R_{pinhole}$	$< 1nA$	$V_{diel} = 120V$
coupling capacitance	$C_c/(l \cdot p) = \epsilon_0\epsilon_{SiO_2}/d_{diel}$	$\approx 1.2pF/cm/\mu m$	$f = 100Hz$
poly silicon resistance	R_{poly}	$> 1M\Omega, < 2M\Omega$	$V_{bias} = 450V$

Table 3.1: Sensor qualification procedure. *The expected values are quoted from [CMS00b] or calculated for 500μm thick sensors from simple geometrical considerations. The listed measurement conditions refer to the standard sensor test during quality control. Some symbols and their meanings: area (A), thickness (d), strip length (l), (average) strip width (p)*

The strip leakage current I_{leak} indicates local mechanical or structural defects. The coupling capacitance C_c probes for pinholes, shorts and breaks. The bias resistor R_{poly} is measured directly and gives evidence on defect resistors. The pinhole measurement also is directly sensitive to the appropriate defect. All measured quantities, the expected values, the formula, if available, and the measurement condition are summarized in Table 3.1.

3.2 Module Layout

a. Ring6 b. OB2

Figure 3.2: Modules of two different types. *A wedge shape detector module for the Tracker Endcap of Ring6 geometry is shown in Fig. a and a module for the Outer Barrel in Fig. b.*

The silicon strip tracker will consist of about 15000 modules [Dir03] each forming the smallest detector unit that is operable individually. Modules with wedge shaped sensors will be used in the tracker endcaps (see Fig 3.2a) to obatin a radial symmetry of the strips with respect to the beam axis. There are 10 different geometries, 7 with strips at a radial angle orientation and 3 ones with a slight stereo orientation. To each stereo module, a normal module is mounted back-to-back. This improves the spatial resolution of the whole detector by minimizing hit ambiguities. Rectangular shaped sensors are used in the barrel regions of the tracker (see Fig 3.2b). The larger demanded granularity of the tracker near by the beam

pipe is allowed for by means of single sensor modules with 768 strips. In the outer tracker regions, two-sensor modules with 512 strips are used.

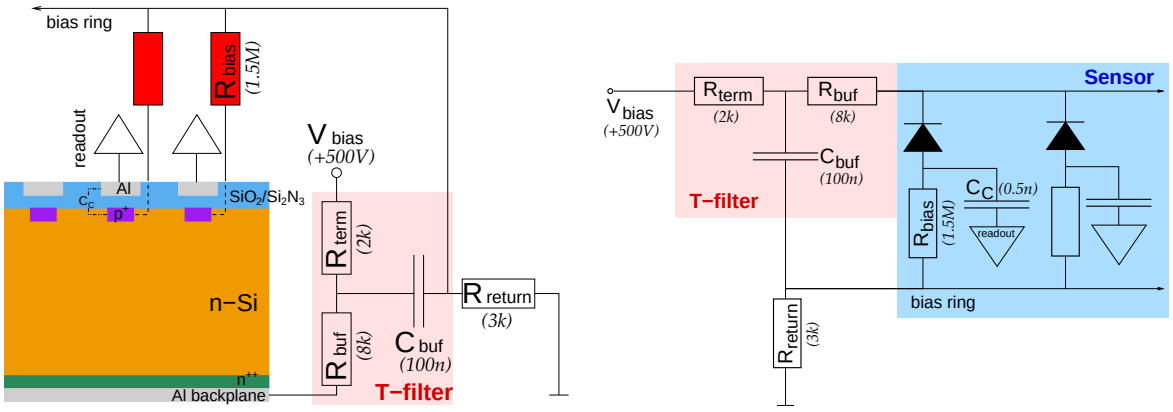

Figure 3.3: Schematics of a silicon sensor and its electrical components. *The sensor schematic on the left gives the equivalent circuit on the right: Each of the 512 or 768 channels of a module is represented as a diode with a series resistor (bias resistor), a shunted capacitor (couping capacitance) and an operational amplifier symbolizing the first stage of the analogue readout. The bias voltage (V_{bias}) is applied to the backplane via a T-filter (R_{term}, R_{buf}, C_{buf}). The total return current flows to ground via a resistor R_{return} placed on the front end hybrid.*

A module is supported by a carbon fiber frame onto which one or two sensors, the front end hybrid (FEH), the pitch-adapter (from sensor to FEH) and the kapton cable with high voltage line and appropriate filter circuit are glued. Bond wires connect the bias ring with the bias current return line on the FEH, the strips with the pitch-adapter and the strips of eventual two sensors.

Figure 3.3 shows the schematic of a silicon sensor and its circuit on a detector module. The bias voltage is applied via an externally mounted T-filter to the backplane of the sensor. It buffers the high voltage and is dimensioned to filter small ripple captured along the high voltage line. The T-filter is dimensioned as follows: $R_{buf} = 2.2k\Omega$, $R_{term} = 8.2k\Omega$, $C_{buf} = 100nF$.

3.3 Readout and Control Chain

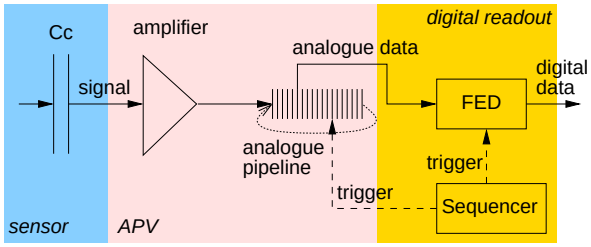

Figure 3.4: *Rough scheme of the analogue and digital data path of the readout.*

Giving an elaborate explanation of all details of the CMS module readout system would exceed the topic of this thesis. The reader is referred to various thesises covering this topic

in detail [Fri01, Dir03]. Thus, only a rough description is given. The charge signal coupled into the aluminium strip of the sensor is amplified with the LHC bunch crossing frequency of 40MHz and stored circular in an analogue pipeline with 192 cells. Thus, an APV can hold data from 192 bunch crossings or 4.8μs. The sequencer sends a trigger to the APV in case of an interesting event. The pipeline cell located an adjustable delay before the current write position is marked and readout when reaching the end of the pipeline. The sequencer also triggers the front end driver (`FED`) and thus perpairs it for incoming data.

3.4 Module Performace

The noise of each strip of a module is an important parameter when describing its performance. There are several sources contributing to the overall noise of a silicon strip detector arising from leakage current, resistors and capacitances in the sensor and the front-end electronic [Dir03]. Before irradiation, the front-end contribution dominates the noise. After irradiation, the contribution from the leakage current becomes dominant. Studies on the overall module's behaviour after irradiation have been done [Wei04]. The expected irradiation fluence dependent strong decrease in the signal over noise ratio due to the increased noise has been observerd.

Another aspect concerning the module's performance is its clearing time. Since the LHC has a bunch crossing frequency of 40MHz, any detector volume in CMS must be cleared fast enough. In case of the silicon sensors, the clearing time is given by the maximum drift length (width of the bulk) of charge carriers and the drift velocity of holes, that are slower than electrons. For small electrical fields, drift velocity and field are proprtional.

$$v = \mu E \tag{3.1}$$

For larger fields in the order of the thermal velocity, the drift velocity starts to saturate and can be approximated as follows (for holes)

$$v_p = \frac{10^7 cm/s}{1 + \frac{2\times10^4 V/cm}{E}} \tag{3.2}$$

For typical electrical fields in CMS silicon sensors of 10kV/cm, the latter equation must be applied and results in a hole drift velocity of $\mathrm{v_p} = 3.3 \times 10^6$cm/s. With a sensor thickness of 500μm this gives a clearing time of 15ns that is sufficient at the given bunch crossing time of 25ns.

4 Motivation on Beam Loss Studies

4.1 Introduction

CMS is set up at interaction point (IP5) adjacent to the beam dump at IP6. A failure in dumping the counter clockwise beam can cause severe radiation problems in the neighboured interaction point where CMS is placed (Fig. 4.1).

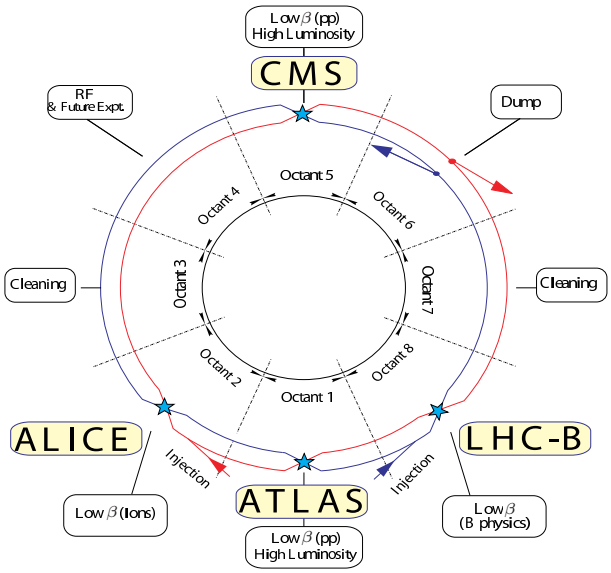

Figure 4.1: Layout of the LHC. CMS *is affected most by beam losses as it is placed in the octant that is counter clockwise neighboured to the beam dump [LHC05].*

The impact on the CMS silicon tracker modules has been investigated in this thesis. The planning of the tests with protons and light are based on simulations for the LHC beam abort kicker [M$^+$99]. The most likely failure is asumed to be an *unsynchronized abort* predicted to occur about once per year. This scenario can have two reasons. Firstly, the dump kicker, that has a rise time of 3μs, does not hit the abort gap of 3.17μs in the beam structure [H$^+$99]. An other reason can be a *single module prefire*, that is cured by an immediate re-trigger of all remaining 14 modules. In both cases, some deviated bunches continue in the beam line and are lost at the next limiting aperture. Oszillating bunches may scratch the beam pipe, so that the major stress to CMS will be caused by secondary particles. The accident duration is predicted to be 260ns with a total of 10^{12} protons deposed in IP5, corresponding to about 10^9 protons per cm^2 in the CMS Tracker and 10^{11} protons per detector module. That is about 10^8 times the nominal fluence. This numbers refer to a setup *without* any dedicated protection mechanisms.

At the worst case beam loss scenario, the so called *single module prefire*, only one of the 15 abort kicker magnets fires prematurely *without* any re-trigger of the rest of the modules. The beam is deviated and continues in the machine. About 10% of the beam is lost at the next limiting aperture. 4×10^{13} protons are deposed in IP5 within 86μs. This scenario is very unlikely as the beam abort system is designed such that all remaining 14 kicker modules will be re-triggered within 1.3μs to establish the nominal dump kick within the abort gap [A$^+$02]. The following calculations and most of the considerations in this thesis refer to the most likely scenario, the *unsynchronized beam abort*, without dedicated protection dumping 10^9p/cm^2.

The protons deposited in IP5 have MIP-like energies, so that the most probable energy loss is 275eV/μm per proton. With an excitation energy for one electron-hole pair (EHP) of 3.63eV in silicon (Section 2.4.2 on Page 27) and a bulk width of 500μm, this complies with 38000 EHPs generated per proton. Assuming perpendicular penetration (for a conservative calculation), one obtains during a beam loss in sensors with an area of 100cm^2 an energy deposition of 2.2mJ according to 3.8×10^{15} EHP or a ionisation charge of 611μC, respectively.

One assumes a beam loss at the LHC at least about once per year. At the Tevatron at Fermilab beam losses occur several times a year [Mac05]. This experience gives a strong

motivation to investigate beam loss induced damages to the Tracker.

4.2 Expectations

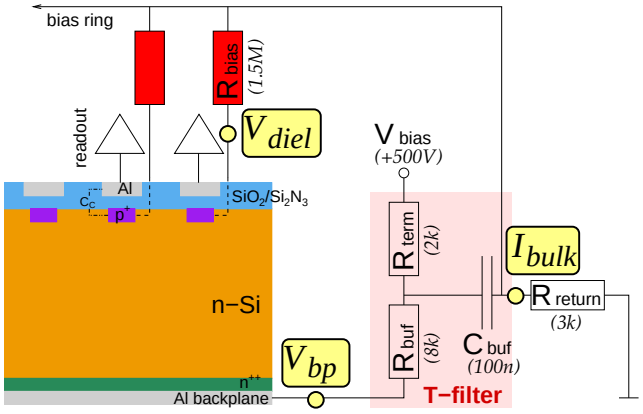

Figure 4.2: Schematic of a silicon sensor and its electrical components. *The sensor, its externally mounted T-filter on the module and the bias current return line resistor placed on the* FEH *is shown. The voltage at the sensor's backplane (V_{bp}), the voltage over the dielectric layer (V_{diel}) and the total current flowing through the sensor (I_{sensor}) are the most important parameters to measure in order to obtain a comprehension of damages to the sensor possibly occuring during a beam loss.*

The accumulated irradiation dose of the CMS Inner Tracker is in the order of 10^{14} n_{1MeV}/cm^2 within 10 years. No integral radiation damage is expected from a beam loss, as a dose of 10^9 protons ($\approx 10^9 n_{1MeV}$) per cm^2 corresponds to some days of normal LHC operation.

However, the huge particle flux will ionise the sensor material instantaneously. At a first glance, it is imaginable, that such an electrical shock can cause voltage peaks and large currents through some module components. It has to be insured that this will not create irreversible damages. Figure 4.2 shows a schematic of a silicon sensor and its circuit on a detector module. The bias voltage, that is set to values of up to 500V at the end of LHC operation [Fur06], is applied via an externally mounted T-filter to the backplane of the sensor. It buffers the high voltage in case of multiple highly ionizing particle (HIP) events and is dimensioned to filter small ripples captured along the high voltage line. The T-filter is dimensioned as follows: $R_{buf} = 2.2k\Omega$, $R_{term} = 8.2k\Omega$, $C_{buf} = 100nF$. Poly silicon resistors, also called *bias resistors* or *poly resistors*, implanted on the front side of the sensor, contact the p^+-implants to the bias ring. Their resistance is in the order of $R_{poly} = 1.5M\Omega$. The Aluminium readout strips placed on top of the sensor's surface are capacitively coupled (C_C) via the dielectric to the p^+-implants. C_C is in the order of 500pF.

The module's components displayed in Fig. 4.2 and the sensor's components shown in detail in Fig. 3.1 on Page 32 eventually have to stand an enormous electrical stress in case of a beam loss: The sensor's bulk will be highly ionised, that can be basically considered as a short-circuit. This will cause a partial breakdown of the bias voltage. The remaining field separates the created EHPs. A large current starts to flow through sensor and bias resistors raising the potential of the p^+-implants. This potential drops across the dielectric layer as the readout strips are connected to the preamplifier's input lying on a potential of 0.85V and therefore can be factually considered as grounded within this scope. Thus, dielectric voltage and current through one poly silicon resistor are related by the simple Ohmic Relation $V_{diel} = R_{poly} \cdot I_{R_{poly}} + R_{return} \cdot I_{sensor}$. This voltage V_{diel} (see Fig. 4.2) would be destructive to the dielectric layer causing pinholes if staying too long above the maximum rated DC voltage of 120V [CMS00b]. Thus, it is important to clarify, that the backplane voltage V_{bp} will decrease below this threshold. Furthermore, it has to be checked, that the appropriate current flowing

through the poly silicon resistors[1] will not destroy them.

The (not recombining) charge carriers created by the traversing particle beam have to be drained off. This causes a large current through the whole device, namely the T-filter-resistors and the silicon bulk. The latter one will not be critical as the surface of a sensor is large enough to drain off the dissipated ohmic heat. But the T-filter-resistors are endangered.

Another critical issue is the behaviour of the high voltage supply in case of a short-circuited output. It is influenced by the capacitive load on the output and its maximum rated constant current. The maximum rated current of the CMS Tracker power supplies will not be far above 1mA per sensor. This is approximately two times the current needed to bias a sensor after ten years of LHC operation. Tests with two different power supplies have been done to investigate the impact of the maximum current to the module during a beam loss. Official CMS high voltage supplies have not been avaliable yet for the accelerator and lab tests.

4.3 Questions and Aims

In order to scrutinise those expectations, experimental beam loss tests were done both with particles and light. To evaluate an eventual damage in detail, important operation parameters have been recorded with a time resolution on the μs scale during and shortly after the beam loss test. The following experiments have been done to answer open questions.

- **Testbeam with intensive proton bunches at the PS/CERN**
  What is the *survival status* of modules and its components (sensor and electronics)? In case of a damage, what is the electrical and physical reason?

- **Lab test with fast IR LEDs**
  Results from the testbeam can be reproduced, and in addition, deep studies on the short term sensor behaviour after a pulsed excitation can be done by varying design and operational parameters.

- **Lab test with an IR laser**
  Reproduction of testbeam and LED test results was an issue also in this test. A further question has been the damage threshold: Which configuration (T-filter and power supply) will destroy the sensor? What is then the safety margin for the configuration used in CMS?

[1] A synonym for *poly silicon resistor* is *bias resistor*. Both expressions will occur in this thesis.

5 Testbeam at CERN PS

5.1 Abstract

The impact of an *unsynchronized beam abort* to the CMS Tracker is investigated most realisticly with single, high intensive particle bunches. In October 2002, fully and over depleted sensors and modules were exposed to 42ns long bunches with up to $\approx 10^{11}$ protons of 24GeV. An extraction scenario with two consecutive pulses with a spacing of $\approx$ 500ns was optional. The test was done at the Proton Synchrotron (PS) at CERN in T7, East Hall.

The following important operational parameters of a module were recorded online in several time resolutions from ms down to 100ns:

- bias voltage,
- voltage over the dielectric layer,
- current through the poly silicon resistors,
- sensor current and
- front end hybrid (FEH) supply voltages.

This data together with the before and after beam qualification data is helpful to disentangle possible failures caused by the impact of the protons. The question of individual component survival can be answered as well.

5.2 Setup

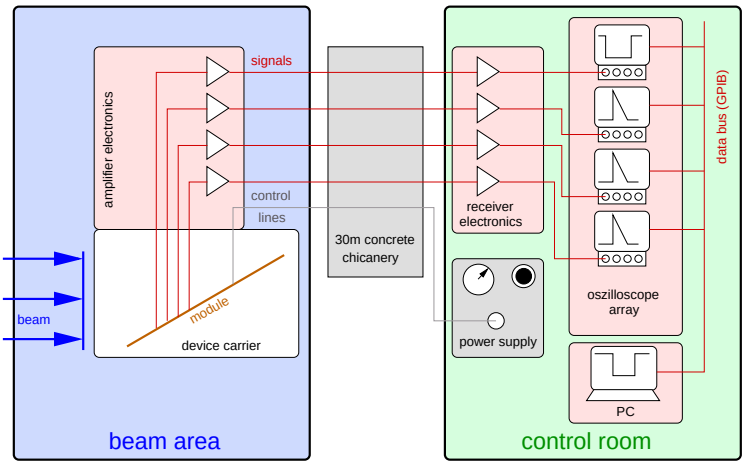

Figure 5.1: Schematic of testbeam setup. *The fast signal responses coming from sensor and electronics are amplified directly above the device carriers. They are passed through the concrete chicanery via 30m long network cables to the receiver electronics in the control room where they are digitised, monitored and stored.*

Figure 5.1 shows an overview of the complete setup. The beam hits the sensor and module resp. hybrid in the device carrier. The signals are amplified and converted to be transfered via twisted pair lines[1] over 30m into the control room. Receiver electronics prepare the signals for the acquisition by an array of oscilloscopes triggered by the increasing sensor's leakage current. A detailed description of the setup components is given in the following sections.

[1] Cat. 6 network

5.2.1 Beam

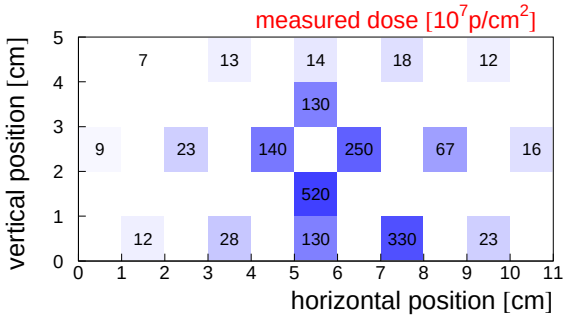

a. measured dose

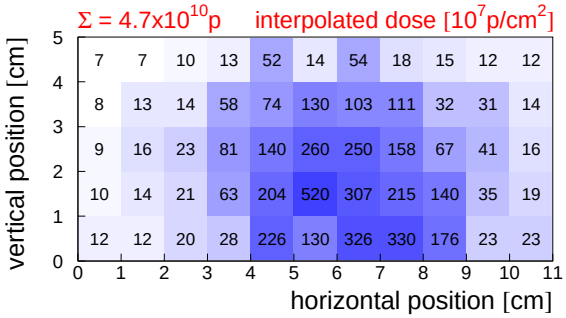

b. interpolated dose

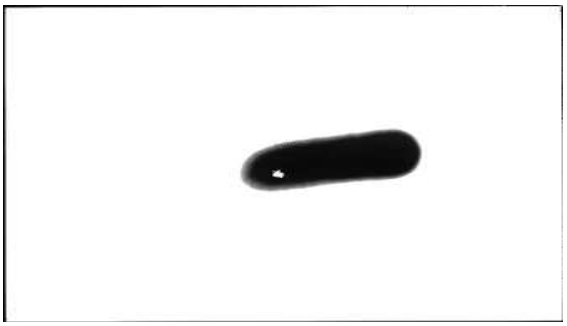

c. polaroid photo of beam spot (b/w inverted)

Figure 5.2: Beam profile. *The beam has been measured with ^{11}C dosimetry. 18 blocks with dimensions of* $10\text{mm}^2 \times 1\text{mm}$ *were used (Fig. a). Figure b shows the interpolated dose and Fig. c one of the reference polaroids. A total fluence of about* 5×10^{10} *protons has been reached in this shot corresponding to an average of* $1.5 \times 10^9/\text{cm}^2$. *In a double shot event, up to* 10^{11} *protons were possible. The beam profile is cigar shaped. Therefore, some devices had to be mounted in an almost horizontal position (Fig. 5.3).*

The PS crew was able to provide a fast beam extraction of 42ns long bunches with about 10^{11} 24GeV protons in a double Gaussian cigar shape pulse of 10×5 cm^2 with approximately 10^9 to 10^{10} protons per cm^2. To reproduce the length of a beam loss, a single bunch extraction and a double bunch extraction with a spacing of 527ns, were used. The alignment of the sensors against the beam was done with polaroid pictures of the beam profile before each installation. This enabled a mounting of the devices under test with respect to a common reference frame. Exact beam profiles were measured with ^{11}C and Al dosimetry (see Fig. 5.2).

5.2.2 Device Carrier

Device carriers were built in Karlsruhe using an AutoCAD template provided by the crew of the ATLAS SCT irradiation facility in T7/East Hall [Gri00]. They fit into the stationary installed cold-boxes. As the beam position is well known, the alignment of the devices in the carrier with respect to the beam is feasible and can be done during preparation in the home institute. Two devices are mounted into one carrier and can be tested simultaneously. Exchanging them is very easy. No glue or screws are necessary. This provides an efficient use of the testbeam time. Figure 5.3 shows two of the three used and fully equipped carriers. All modules have been mounted at a small horizontal angle to cover all channels by the cigar shaped beam. This caused an increase of the effective thickness and the energy deposition of the sensitive area by an estimated factor of 3 comparing with plain sensors, that have been oriented vertically.

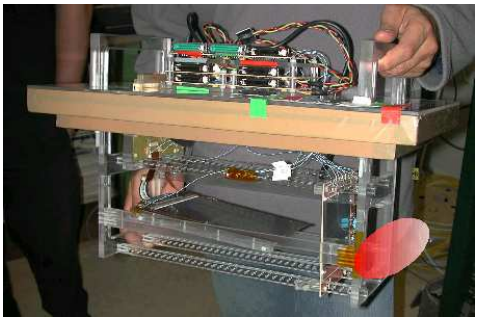

a. Carrier with TOB module and OB2 sensor

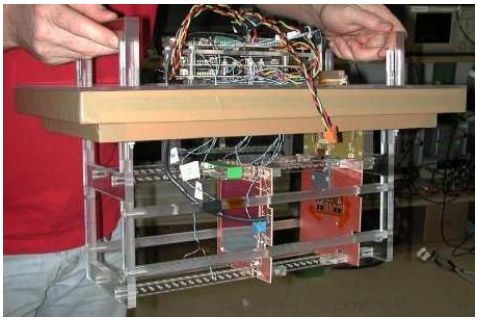

b. Carrier with W6A sensor and hybrid

Figure 5.3: Device carriers *were equipped with two devices. Figure a shows a carrier with a* TOB *module at a small horizontal angle to get a homogenous beam across its thickness to cover all channels by the cigar shaped beam spot (drawn in photo a, schematic in Fig. 5.2). Sensors are oriented vertically due to lack of space leading to an inhomogeneous irradiation by the beam spot. The hybrid in Fig. b is small enough for vertical placement.*

5.2.3 Supply and Signal Path

Fast signals coming from sensor and module are amplified and converted near the location of their creation into differential signals. They are transported via twisted pair lines within a Cat. 6 network cable over a distance of 30m into the control room. Receiver electronics converts them into unipolar signals that can be acquired and digitized by oscilloscopes. Remaining lines in the cable transport two control signals to the FEH. High and low voltage supply lines are needed to bias the sensor(s)/module and to power the FEH.

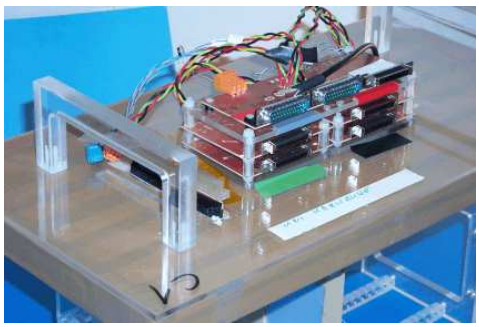

Figure 5.4: Amplifier electronics with patch panel [Hei02]. *Mounted directly on top of the device carrier, the amount of injected disturbances during unprotected signal propagation is minimized. To speed up the exchange of carriers, few plugs with multiple pins were used to connect the carrier with all the cables.*

A schematic of the amplification and impedance changing circuit for one signal channel is given in Fig. D.2 in the Appendix on Page 130. Unipolar and bipolar signals may be processed by this circuit. In the first case, the negative input must be connected with the local ground. The (differential) voltage is amplified and converted into a differential signal fed into a twisted pair of wires within the network cable. A schematic of the receiver circuit is shown in Fig. D.3 in the Appendix on Page 130. It converts the differential signal into an unipolar signal, referenced to the local ground. Figure 5.4 gives an impression of the narrowness one had to deal with when planning and building the sender electronics. Stacks of circuits were necessary to place all the amplifier and conversion electronics for up to 14 physical signal channels, three supply lines and two control lines on top of one device carrier. An optical link was used for the readout of the FEH.

Table 5.1 on the next page gives an overview on all types of lines in use. The meaning of the different signal channels is described in Section 5.3.1 on Page 45.

line	sensor	module	hybrid	sensor and module	sensor and hybrid
signal lines					
V_{bias}	1	1	-	2	1
I_{sensor}	1	1	-	2	1
$V_{diel\ 1-6}$	6	-	-	6	6
$V/I_{250/125}$	-	4	4	4	4
Σ signal lines	**8**	**6**	**4**	**14**	**12**
control lines					
APV clock&trigger	-	1	1	1	1
I^2C	-	1	1	1	1
Σ control lines	**-**	**2**	**2**	**2**	**2**
Σ fast lines	**8**	**8**	**6**	**16**	**14**
supply lines					
high voltage	1	1	-	2	1
low voltage	-	1	1	1	1
Σ supply lines	**1**	**2**	**1**	**3**	**2**

Table 5.1: Overview of signal and supply lines. *Signal and control signals are most critical with respect to their time behavior. Therefore, great care had to be put on the quality of signal propagation. Summaries of all lines used to supply a total carrier (Section 5.3.2 on Page 45) with two devices are also given in this table.*

5.2.4 Data Acquisition

During preparation of this test, one recognised quickly that an array of many oscilloscopes would be the best solution for a data acquisition (DAQ) of those fast signals. Table 5.2 gives an overview of advantages and disadvantages of an oscilloscope array in comparison to a multichannel analogue to digital converter (ADC), that would have been the alternative.

Argument	**Oscilloscope Array**	**Multichannel ADC**
flexibility	fully flexible and fast adjustable horizontal and vertical setup of each channel individually	setup of sampling depth / rate and vertical resolution only for groups of channels
programming	easy with labview: libraries available, online data visualisation is costless	for rented, old devices: libraries often hard to find, readout "by hand", online visualisation probably impossible.
installation	large amount of big devices, much cabling (power supply and trigger chain)	one device: trigger setup easier (only one trigger input for many channels)
rental fee	CHF 600 (estimation)	less (fewer devices)
transportation	laborious	easy

Table 5.2: (Dis-)Advantages of oscilloscopes and multichannel ADCs. *The arguments are ordered by their importance. Emphasis has been put on fast and flexible handling during operation. This results in an overhang of advantages for the oscilloscope array. The disadvantage of this solution is a laborious installation.*

15 scopes with 38 channels with different horizontal and vertical configurations were set up to get information about signals in different time resolutions. All channels are configured and read out by one computer. One scope has been triggered on the increasing leakage current of one sensor available in each test run. The trigger output of this reference scope has been daisy chained to all other scopes and used there as external trigger source. 20% pretrigger information has been recorded, so that no dedicated study of trigger and signal delays was necessary. Figure 5.5 shows the main part of the oscilloscope setup.

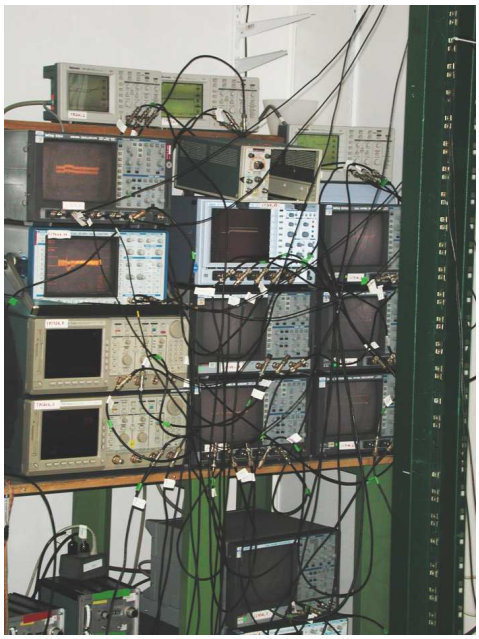

Figure 5.5: Data acquisition with oscilloscopes. *For this study, a very flexible and easy to build and use data taking facility is needed. One wanted to adjust time and voltage resolution on a large scale within seconds as time slots in testbeams always are very narrow.*

DAQ and final data analysis has been done with a LabView [Nat03] and C++-based software package. It is described in detail in Chapter 6.2.5 on Page 60.

5.2.5 Sensor Circuit

All sensors were mounted on a printed circuit board (PCB). The schematic is shown in Fig. 5.6 on the next page. The sensor's backplane was supplied with high voltage by direct contact with a large area on the PCB, that is connected with the high voltage supply. Microbonds between bias ring on the front side and circuit ground closed the basic circuit. In order to measure the voltage over the dielectric layer, additional bonds connected six groups of five DC-pads each with pads on the PCB. For some strip groups the corresponding AC-pads are bonded to the circuit's ground. The measurement is done with a voltage divider between the circuit's pad and ground. The bonding scheme is seen in Fig. 5.7 on the next page.

In normal operation, the DC-pads are unbonded and connected only via its bias resistors with ground, so that their potential is defined by the individual strip leakage current. The AC-pads are connected with the input of the charge preamplifier, that is almost on ground potential (0.85V).

The bias return line resistor of 10kΩ on the formerly used hybrids is not considered in this tests. With such a resistor, the sensor current causes a significant rise of the bias ring potential. But this would not endanger the coupling capacitors as the p^+-implants are protected by the bias resistors. Moreover, the observed survival of a module, containing such a bias current return resistor, in the testbeam and LED test justifies with hindsight its disregard in the beam loss studies!

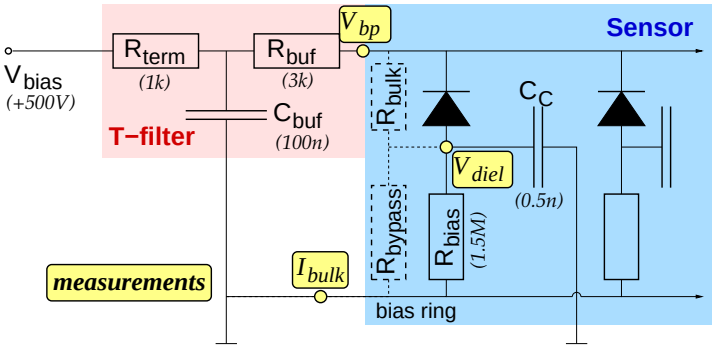

Figure 5.6: Schematic of the sensor and measurement circuit. *All voltage measurements (V_{bp}, V_{diel}) were done against ground using voltage dividers. The coupling capacitors, that are not used for the measurement of the dielectric voltage, are floating in this test setup.* $R_{sensor} = R_{bulk} + R_{bypass}$, *drawn in parallel to the strips, represents a simple model of the sensor during backplane voltage breakdown.*

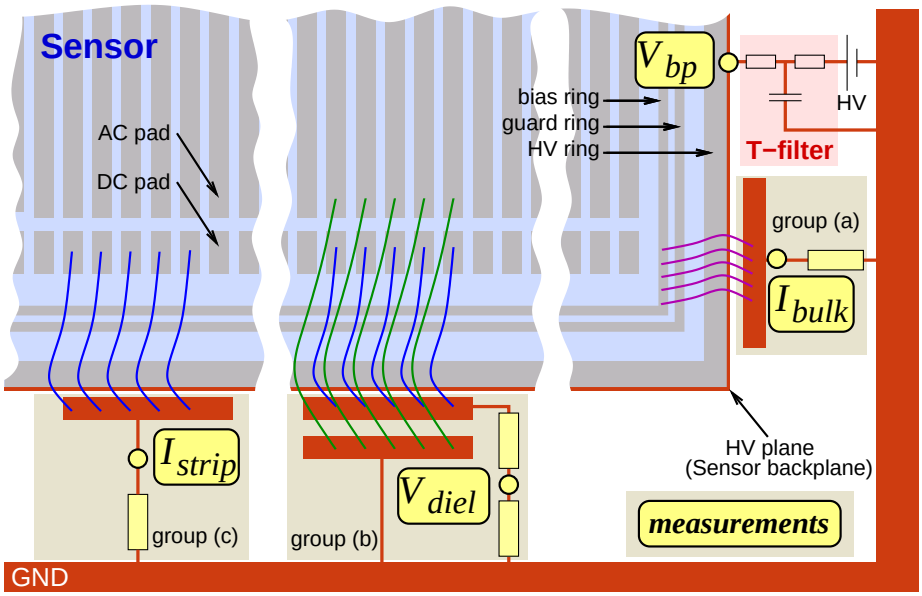

Figure 5.7: Bonding schematic of sensor support PCB (top view). *Three types of bond groups are used (a,b and c). Group (a) connects the bias ring via the* I_{sensor} *measurement resistor with ground. Groups (b) and (c) measure the voltage over the dielectric layer* (p^+ *potential) by probing the DC-voltage. They are equivalent with respect to the measurement principle. Difference comes up with the behaviour, when applying voltage peaks to the* p^+*-implants. In case of group (b), that has its AC-pads bonded to ground, those peaks will fall directly over the dielectric layer and endanger it, so that this one reflects best the real situation regarding the risk of pinhole creation. Thus, group (c) is not used in lab tests any more.*

All voltages were measured via voltage dividers due to different reasons. In case of the backplane voltage V_{bp}, the constant voltage is too large (up to 550V) to be measured directly due to the limited maximum amplifier range. And the voltage over the dielectric layer may reach large peak values theoretically up to the value of the backplane voltage. Voltage dividers reduce the measured value in this worst case to an uncritical level to exclude damages to the data acquisition electronics and to fit the voltage values into the amplifier's dynamic range. The sensor current can be obtained from the voltage drop over a small resistor between bias bond and ground.

5.3 Measurement Program

To disentangle eventual failure types, three sensors, one hybrid and two modules were installed in three device carriers. Sensors from two manufacturers with low and high resistivity (ρ) were

used, corresponding to the sensors of the two modules of different geometry. In case of a failure of the frontend electronics induced by over-current or over-voltage from the sensors, it had to be tested, wether the hybrid survives an impact on its own. On the sensors, the bias voltage behavior, its total current, the individual strip current and the voltage over the dielectric layer was monitored vs. time.

5.3.1 Measured Parameters

An overview of all parameters measured is given in Table 5.1 on Page 42. For each sensor, 8 signals have been acquired: the bias voltage resp. backplane voltage V_{bias}, the sensor current I_{sensor} and the voltage over the dielectric layer V_{diel} for six groups of five strips each. The groups are well distributed over the full width of the sensor. Within one group, the potential of five DC-pads is averaged to have a small statistics of the electrical conditions near the p^+-implants during a beam loss.

All AC-pads of a module are connected with the appropriate position on the pitch adapter. Thus, dielectric layer measurements are not possible on module basis. Only bias voltage and sensor current can be monitored during the impact.

`FEH`s are supplied with the two low voltages $V_{250} = 2.5V$ and $V_{125} = 1.25V$. Their behaviour as well as their corresponding currents (I_{250} and I_{125}) are measured.

The knowledge of the short-circuit behaviour of the bias voltage and the total current is essential for the comprehension of the whole situation. In case of new appearing pinholes or problems with the poly silicon resistors [2] after the testbeam, the voltage over the dielectric layer would have given a strong hint on the reason. Table 5.3 summarises all parameters and the motivation of measuring them.

parameter	**description**	**motivation**
V_{bias} resp. V_{bp}	bias (backplane) voltage	global comprehension
I_{sensor}	global (sensor) current	global comprehension
V_{diel}	voltage over the dielectric layer	indicator of pinholes and problems with polysilicon resistors
$V/I_{250/125}$	hybrid's supply voltages and currents	indicates the reason of a possible malfunction after testbeam

Table 5.3: Summary of parameters and the motivation of their measurement. *A main focus was on the investigation of possible pinhole creation and poly silicon resistor destruction*

5.3.2 Test Scenarios

The first installation in the testbeam with one sensor and one hybrid served mainly for trigger commissioning and to establish reasonable amplification factors for the second and third test. The second installation with one module and one sensor of corresponding geometry received only one double shot to have a certain binary *yes/no* answer of the robustness, to be post-qualified in the laboratory. This motivated the extension of the third test with one module plus one sensor for many shots at high voltage. The available margin could be exploited to get as much data as possible, while taking the risk of breakdown. This last module had to endure nine shots with voltages at 500V. For the first and third carrier, the bias voltage has

[2] One has to keep in mind that the dielectric voltage defines the potential of the p^+-implant and therefore, in case of a grounded bias ring, the current through the poly silicon resistor by $I_{Rpoly} = V_{diel}/R_{poly}$.

been scanned from 100V to 400V and 500V respectively. An overview of all three scenarios is given in Table 5.5. The devices under test are listed in Table 5.4

thesis ID	database ID	type	geometry	V_{dep} [V] before	V_{dep} [V] after	resistivity (ρ)	in carrier
A	30221116054840	sensor	W6A	176	187	low	1
B	30210414739617	sensor	OB2	197	204	low	2
C	30221216053316	sensor	W6B	33	50	high	3
M	30216630200027	module	R6	-		-	3
-	?	module	TOB	-		-	2
-	?	hybrid	-	-		-	1

Table 5.4: Devices under Test. *Six devices have been installed on three device carriers (see Table 5.5). Geometric data can be looked up in Table E.2 in the Appendix on Page 132. The thesis identifier (ID) is used in plot legends and descriptions.*

#	devices in carrier	action	# shots
1	sensor A, `FEH`	V_{bias}-scan at 10, 100, 150, 200, 400 V. One shot per scanpoint.	5
2	sensor B, `TOB`-module	one double shot at 400 V	2
3	sensor C, module M	V_{bias}-scan at 100, 200, 300, 400, 500 V. One double shot per scanpoint. robustness test: 4 double shots at 500 V	18

Table 5.5: Summary of test scenarios. *Three device carriers have been built in Karlsruhe, one for each scenario.*

Results and Interpretation

All sensors were tested in the lab, according to the standard quality assurance procedures [Har02] including the global and the strip-by-strip (local) characterisation of the sensor. Measurements of the global characteristics provide the leakage current and the capacitance vs. bias voltage curve, which reveals the depletion voltage. Measurements of the local characteristics are done for each strip, concerning the coupling capacitance, the poly silicon resistor, the strip leakage current and the pinhole detection. Postqualification has been done globally and locally only arround the bonded groups of strips. Qualification data and its evaluation is shown in Section 5.5 on Page 50.

In the following section, the dynamic behaviour of V_{bias}, V_{diel} and I_{sensor} is presented as well as its interpretation.

As the maximal V_{diel} also disturbs and endangers the pre-amplifier, in particular in case of pinhole creation, the robustness of the front-end electronics in case of indirect stress from voltage peaks at the inputs and stress from direct pulsed irradiation is investigated in Section 5.6 on Page 51.

5.4 Dynamic Sensor Behaviour

5.4.1 Bias Voltage Breakdown

When the beam of 10^{11} protons traverses the sensor, the silicon bulk material is highly ionized, producing at least 10^{15} electron-hole pairs (EHPs). Free charges move to the backplane and p^+-implants and (partially) discharge the sensor and T-filter buffer capacitance. A detailed calculation of the available charges to separate the created EHPs follows.

The number of space charges N_{dep} in the depleted sensor is three orders of magnitude below the created number of EHPs and therefore neglectible for further considerations:

$$N_{eff} = \frac{2\epsilon\epsilon_0 \, V_{dep}}{e \, d^2} \tag{5.1}$$

$$N_{dep} = N_{eff} \, A \, d \approx 2 \times 10^{12} \tag{5.2}$$

$$\text{with } d = 500\mu m, A = 100 \; cm^2, \epsilon = 12, V_{dep} = 100 \; V$$

Measurements within the scope of LED and laser test prove, that the voltage at the buffer capacitor $C_{buf} = 100nF$ does not decrease by more than 100V during the event at a bias voltage of 500V (see Fig. B.3 in the Appendix on Page 122). This voltage drop corresponds to about 6×10^{13} electrons and is only 6% of the created EHPs. From this considerations, one can conclude, that the total electrical field energy in the sensor capacitance $C_{sensor} = 2nF$ but only a part of the charges in the high voltage buffer capacitance $C_{buf} \gg C_{senosr}$ is consumed to separate a fraction of the EHPs. More of the created EHPs are separated by the power supply!

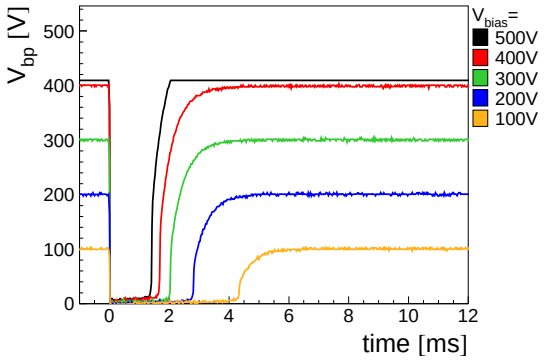

Figure 5.8: Backplane voltage breakdown and its recovery [F+04]. *The almost complete breakdown protects the sensitive parts of the sensor from damages, espcecially the dielectric layer. Unfortunately, the measured voltage at* $V_{bias} = 500V$ *ran into digital saturation.*

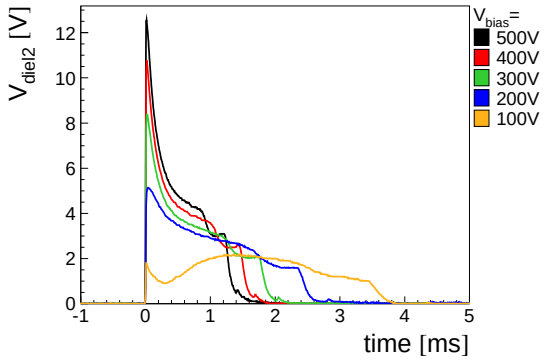

Figure 5.9: Voltage over the dielelectric layer. *Six groups of strips, distributed over the whole sensor, have been measured. One of those is shown. The data is smoothed, so peaks are cut. A summary of the peak values is shown in Fig. 5.12 on Page 49.*

The factual short-circuit of the bulk material leads to an almost complete breakdown of the sensor bias voltage (Fig. 5.8) preventing it from reaching the p^+-implants! The residual voltage is seen as a voltage over the coupling capacitance resp. the dielectric layer (Fig. 5.9). A variance in the shape is observed between $V_{bias} = 100V$ and the higher voltages. This effect could be due to the transition from partial to full depletion. The highest peak of about 23V is far below the specified limit of 120V, which would destroy the complete sensor by breaking the dielectric layer between p^+-implants and readout strips causing pinholes. Monitoring this voltage in a much shorter time scale of about $1\mu s$ gave the evidence, that no additional spikes happened.

The corresponding single strip leakage current (Fig. 5.10a) derivable from the dielectric voltage does not exceed some μA and therefore does not damage the poly silicon resistors.

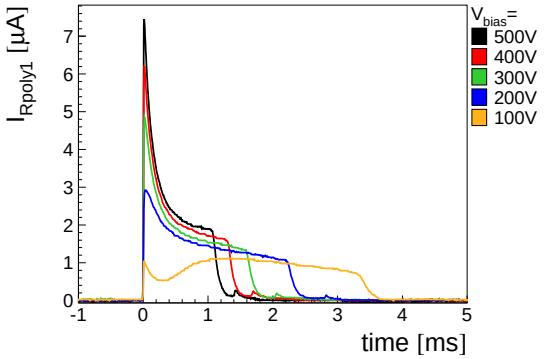

a. current through one R_{poly}

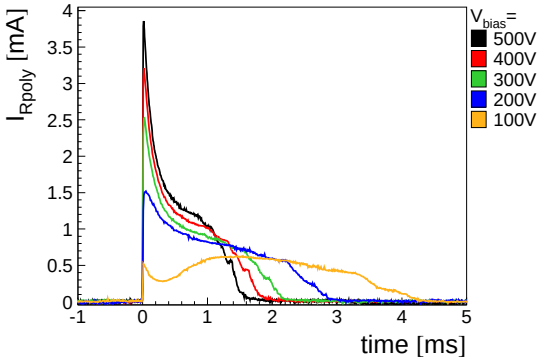

b. current through all R_{poly}

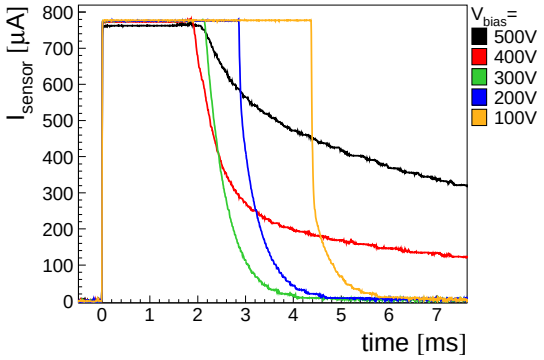

c. total sensor current

Figure 5.10: Derived and measured currents. *Figure a shows the current through one poly resistor of group 1 derived from its dielectric voltage. Taking the average of all groups and extrapolating to 512 strips, one gets plot (b). (c) shows the measured total sensor current. Unfortunately, the sender's* `OPA`*s were in saturation very early. So, one only can estimate that the total current has been far above 10mA.*

Further lab tests prove that the bias voltage breakdown is in this case not caused by a terminal voltage breakdown of the power supply but by a voltage drop over the T-filter-resistors (Section 6.5.1 on Page 70). The power supply used in the testbeam and the lab test is capable to deliver a constant current of up to 300mA at maximum voltage [Olt04]! It came out in the lab studies that this device represents the worst case with respect to the high voltage supply.

5.4.2 Bias Voltage Recovery

The bias voltage recovers after a few ms when all redundant free charges have recombined or been drained off. After that, the voltage recovers re-establishing the space charge region. Such recovery occurs faster at higher bias voltages, as the current supplied by the power supply is larger, so permitting the excess free charges to be removed faster. The reinstating of the depletion layer displays the shape of an RC charging curve and returns to the initial bias voltage. The recovery time constant (Fig. 5.11) corresponds approximately to the values of the T-filter-components ($R_{buf} = 3.3k\Omega$, $R_{term} = 1k\Omega$ and $C_{buf} = 100nF$) and the estimated internal resistance of power supply and leakage current measurement device ($R_{int} \approx 2k\Omega$).

$$\tau_{recover} = C_{buf} \times (R_{int} + R_{buf}||R_{term}) \approx 300\mu s \tag{5.3}$$

A detailed and more precise study of the bias voltage recovery has been done in the lab tests. The correlation between breakdown time and duration of the signal at the dielectric layer

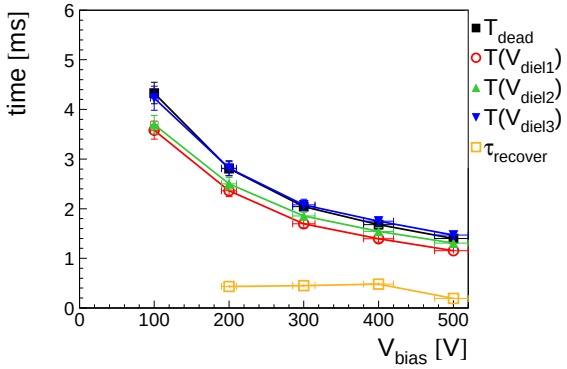

Figure 5.11: Summary of time constants. *The backplane voltage dead time fits well with the length of the signal at the dielectric layer. The recovery time constant is independed on the inital bias voltage, as expected. The last value at 500V deviates from the others due to the digital saturation of the raw data (Fig. 5.8 on Page 47).*

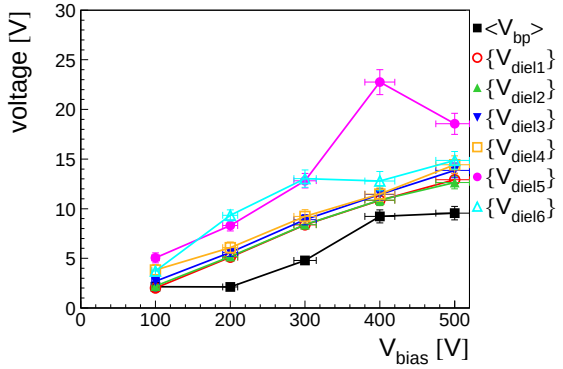

Figure 5.12: Summary of voltages. *Although the sensor has not been illuminated homogeneously by the beam (Fig. 5.3a on Page 41),* V_{diel} *is homogeneous along the sensor. This leads to the conclusion that the beam halo, that is orders of magnitude less intensive than the beam centre, nevertheless has been sufficient to completely short-circuit the hit regions.*

(Fig. 5.11) is obvious and prove the electrical coherence of both signals. A further evidence for this fact is the correlation (Fig. 5.12) between the peak voltage over the dielectric layer (V_{diel}) and the mean breakdown voltage (V_{bp}). This fact also proves the hypothesis of a short-circuit of the silicon bulk.

The remaining voltage charges the coupling capacitance fast, in about 1μs. The consecutive discharge of the coupling capacitance over the bias resistor is expressed in the exponential decay of the remaining voltage V_{diel}. A detailed study of the RC-like decay of the voltage over the dielectric layer is described in Section 6.5.3 on Page 74.

The variation in time of the bias voltage (Fig. 5.8 on Page 47) and the voltage over the dielectric layer (Fig. 5.9 on the same page) show a nice correlation: the instant bias voltage breakdown is seen as an instant increase of the dielectric voltage. The kink after a few ms marks the start of recovery.

5.4.3 Total Sensor Current

Figure 5.10a shows the current dynamics for one group of five strips and the increase with bias voltage. Using the measurements of the dielectric voltage $V_{diel,i}$ for six groups of strips ($i = 1 \ldots 6$), the total current flowing through all polysilicon (bias) resistors ($I_{R_{poly}}$) can be estimated as follows.

$$I_{R_{poly}} = \sum_{i=1}^{512} I_{R_{poly},i} \approx \frac{512}{< R_{poly} >} \cdot \frac{1}{6} \sum_{i=1}^{6} V_{diel,i} \tag{5.4}$$

The bias current return line resistor has not been considered in the testbeam setup. Thus, the bias ring is directly connected to ground, and the current through one bias resistor is given by its resistance and the voltage drop. The projection to all 512 strips concludes to formula 5.4. Figure 5.10b shows the result of this calculation. But from the attempt to measure directly the total sensor current (Fig. 5.10c), there is a strong evidence, that it must be much larger than the calculated poly resistor current. Final assurance on the question of missing current has been obtained with the lab tests (Section 6.6.4 on Page 83).

5.5 Sensor Qualification

All sensors were qualified according the standard quality assurance procedure before the test [Har02, Har05]. See Section 3.1.3 on Page 32 for details. Only the pinhole measurement is missing for most of the strips. The qualification after the beam loss study (post-qualification) included the two global measurements and the four local ones covering *only* the regions arround the AC-bonded strips. The data is placed in Section C.1.3 in the Appendix on Page 126. Limits included into the figures are extracted and calculated from Table 3.1 on Page 33.

In summary all checked parameters did not change during the beam loss study as expected after evaluating the dynamical behaviour of currents and voltages.

Total Leakage Current

The IV characteristics (Fig. C.3 in the Appendix on Page 126) indicate some increases. But the total leakage current at 450V is still below the specified limit of 10μA. The sensors behave quite nicely considering the (mechanical) stress they were exposed to: gluing on top of support PCBs, a lot of transportation and some knocks during the testbeam, removal from the PCB for post-qualification.

Total Capacitance / Depletion Voltage

Extracted depletion voltages from global CV characteristics (Fig. C.5 in the Appendix on Page 126) exhibit no significant deviation from their pre-beam values. This proves the assumption that no integral radiation damage was introduced. Sensor C shows a depletion voltage below specification *before* and after the testbeam due to its different silicon resistivity respectively effective charge carrier concentration. They are taken from a pre-series and are accepted for special purposes anyhow.

The total capacitance at full depletion shows no significant variance for all sensors and is perfect before and after the beam (see Table E.1 in the Appendix on Page 131).

Strip Leakage Current

Sensor B showed problems before and afterwards (Fig. C.4 in the Appendix on Page 126). It comes from an old production batch, that showed some problems, e.g. a susceptibility to pinhole creation. The other two sensors behaved very well as the leakage current of all their strips stayed far below the acceptance limit. Leaky strips on sensor C detected before were not taken into account during testbeam and were not qualified again after.

Coupling Capacitance

The coupling capacitors are the main critical objects with respect to module performance as well as stability against a beam loss. Their measurement (Fig. C.6 in the Appendix on Page 126) was done as specified in the standardised sensor quality assurance procedure [Har02, Har05, Pia01]. The 1nF value show a strip-to-strip short ($2 \times C_{normal}$) whereas infinity, representing a pinhole, is artificially set to 2nF. Values below the expectation could result from a bad contact during measurement.

The pinholes at strips 8, 121 and 253 already existed before the test and do not appear in post-qualification as they did not belong to the measured groups. Thus, the pre- and post-qualification on sensor basis indicates not only no additional pinholes but also a homogeneous value of 500nF before and after the testbeam.

Pinhole Measurement (Current through Dielectric Layer)

The pinhole measurement (Fig. C.7 in the Appendix on Page 126) gives further evidence that no additional pinholes appeared after the testbeam.

Bias (Poly Silicon) Resistors

Also bias resistors are not affected by the beam impact. Different levels of resistances outline different sensors, whereas values before and after match quite well (Fig. C.8 in the Appendix on Page 126). The apprehension, that a too high current during the shock will damage the resistors, is ruled out. But nevertheless, there are single resistors deviating slightly after the beam, especially for sensor A. This can be explained once more with bad handling, a point to be scrutinised in the lab tests.

5.6 APV Response

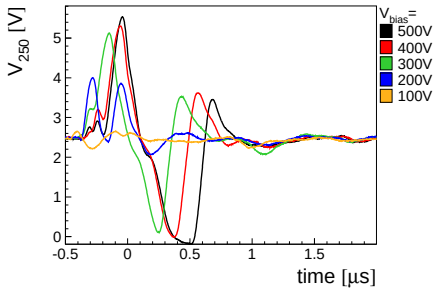

Figure 5.13: V_{250} vs. time. *The* APV*'s supply voltage, that consumes most current, shows oscillations independent on the sensor's bias voltage. The pretrigger signal comes from the time delay.*

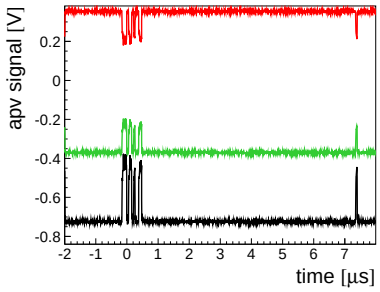

Figure 5.14: APV header and tickmark. *Some minutes after the shot, an* APV *header and the subsequent tickmark could be observed. The two upper lines show the two raw differential signals. The bottom curve is the resulting calculated difference.*

A FEH has been hit directly by the beam under normal operational conditions, that is the supply with the two low voltages and with clock and (random) trigger. While the FEH low voltage shows some uncritical oscillations on the μs-scale (Fig. 5.13), the readout could be operated after a short period of time: Soft resets were necessary to bring back the APVs to normal operation. Then after some minutes, tickmarks, which are produced continuously, and frame headers, which are generated for each event, could be observed (Fig. 5.14).

5.7 Module Qualification

Module M was subjected to several beam shots at different bias voltages from 100V up to 500V. It was taken from the 1st pre-series of tracker end-cap (TEC) Modules all of Ring 6 type in the final design.

The module has been qualified in the lab before and after the testbeam with a now fully automated, multi-purpose and programmable test station thus capable of processing a large amount of modules during R&D and mass-production. A complex modular software for user interaction, data analysis and visualisation, automated and programmable testing and module qualification has been developped and is introduced in Chapter A in the Appendix on Page 108.

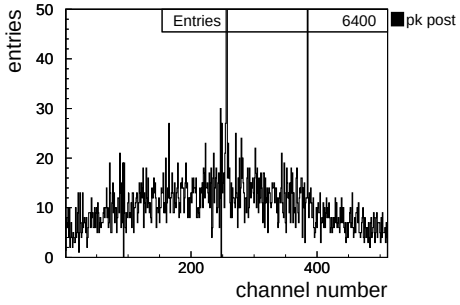

a. number of hits vs. strips

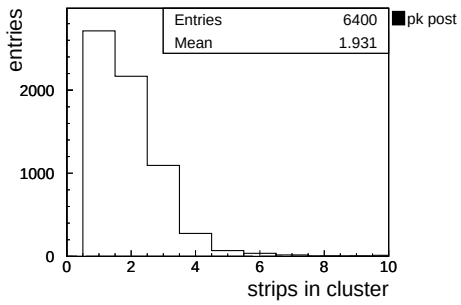

b. cluster size distribution

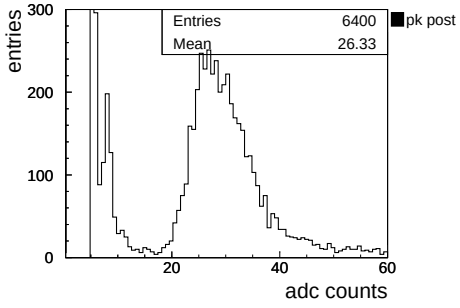

c. SNR distribution

Figure 5.15: Test with cosmic rays after testbeam. *Module M was tested for several days with cosmic rays under slight over-depletion and at -10°C in* `APV`*'s peak mode.*

An important parameter of the module's quality is its noise. It does not only depend on strip length and preamplifier electronics but also on the test facility and electrical shielding. The noise performance of our test station has been improved between pre- and post-qualification. That explains the improved noise behaviour (Fig. C.2b in the Appendix on Page 125). But nevertheless, two failures are visible in both pre- and post-qualification. Together with the calibration signal amplitude (Fig. C.2c) it turns out that strip 93 had a pinhole already before the test run. Strip 248 shows deviances from the normal behaviour in the noise and LED-tests[3] before and after (Figs. C.2e and C.2f). This leads to the conclusion that the bond between hybrid and pitch adapter or pitch adapter and first sensor already has been missing before the testbeam.

A very long lasting and successful lab test with cosmic myons is shown in Fig. 5.15.

Analysis of Particle Data

A strip is considered *hit*, when the signal S_i is a multiple of its noise N_i: $S_i/N_i \geq 3$. A sequence of coherent strips fulfilling the hit criterion is called *cluster*, when the largest strip meets a more strict condition: $S_i/N_i \geq 5$. The *cluster size* n is the number of strips beloning to a cluster. The *cluster signal* S_{clu} is the arithmetic sum of the strip signals S_i in a cluster: $S_{clu} = \sum_{i=1}^{n} S_i$. The *cluster noise* N_{clu} is the squared mean of the noise N_i of all strips in a cluster: $N_{clu} = \sqrt{\frac{1}{n}\sum_{i=1}^{n} N_i^2}$. The *cluster* signal to noise ratio (`SNR`) is defined as ratio of cluster signal and cluster noise: $SNR = \frac{S_{clu}}{N_{clu}}$. This test demonstrates that this module, which underwent an enormous stress by the beam test, is still efficiently operational.

[3] CMS method to detect errors, by illuminating the modules with IR light - in pulsed operation to generate a signal or continuously to artificially increase the leakage current [Dir03]

5.8 Hybrid Behaviour

Front end electronics, whose main part is the preamplifying, shaping and analog buffering chip (analogue pipeline voltage type (APV)), has been exposed to the beam. The front end hybrids (FEHs) were always clocked and powered. One hybrid was hit directly and two others, AC-connected with sensors, were within the beam halo. Furthermore, the two latter ones got some electrical stresses from large charge pulses due to the fast development of the signal at the dielectric layer of their sensors.

The short-circuiting of all passive components like capacitors and resistors is expected.

The survival and an upper value of the electronics deadtime was determined. The electronics showed no damage after the test with and without the extra load of the two silicon sensors rising the input stages to voltages up to 22V *only* in case of a pinhole. A *soft* reset was sufficient to revive the electronics during the test after some minutes. Figure C.1 in the Appendix on Page 124 shows the post-qualification of the direct hit hybrid.

5.9 Conclusion and Outlook

Six devices were tested within a total time slice of only five hours. During this period of time, 13 shots were applied to three device carriers. One of them had to be repaired. The data acquisition had to be adjusted for each shot. Two modules and three silicon sensors were biases with up to $V_{bias} = 500V$. All three hybrids, the bare one and the two on modules, were powered and clocked. Two devices received 18 bunches with about 10^{11} protons each. The two modules even suffered from a much larger energy deposition due to their almost horizontal orientation with respect to the beam. None of the devices under test showed any sign of crucial breakdown. Thus, there is strong evidence that CMS silicon strip modules will survive a beam loss. In particular, the fast breakdown of bias voltage protects electronics and sensors, and most notably the dielectric layer and the poly silicon resistors. Only a negligible, non-destructive voltage is remaining on the coupling capacitor. This voltage decays correlated with the bias voltage recovery of the sensors after some ms. The readout recovery takes some soft resets. First data has been observed after some minutes, but the readout probably could have been restored earlier. Oscillations on the low voltage lines are short-lived and therefore uncritical. Post-qualification of all silicon sensors and hybrid showed no additional defects. The leakage current increased slightly, CV curves showed no critical devolution. Strip parameters still fulfilled the specifications. One module survived perfectly proved in a very long run with cosmic rays, and another one, an early prototype, developped only some pinholes. Its sensors were from a pre-series, where an additional layer in the coupling capacitors dielectric was still missing. So, at this prototype stage, pinhole development was not unexpected.

This test covered the worst impacts in case of a beam loss with respect to beam fluence and high voltage supply. Protection with collimators is in discussion, which could reduce the fluence of a beam loss by 10^{-3} (see Section 2.1.3 on Page 17).

Some still open questions will be answered in the following chapters. What is the behaviour of irradiated sensors? What is the influence of HV-filter capacitor and resistor? Can the sensor current be measured correctly? New measurement parameters conserning the HV-filter will give a deep understanding of the bias voltage behaviour.

The results are in agreement with another study of beam loss effects on silicon detectors [D+00]. There, a strong laser signal was sufficient to short-circuit the bulk material even though the number of produced electron-hole pairs (EHPs) was much less than in our experiment.

6 Lab Test with IR LEDs

6.1 Motivation

For deepter and extended studies of the beam loss impact, an irradiation with LEDs has been used. The energy deposition in a sensor during a beam loss is 2.2mJ (see Chapter 4.1 on Page 36) within 260ns. A light beam reflecting this conditions must therefore provide a pulsed illumination power density of 8.5kW per 100cm^2! This is obviously not achievable with LEDs. But during the first tryouts, it became obvious, that the electrical stress for a sensor and its circuit is *larger* when applying energy during *longer time scales*! So, with hindsight, much too *small* illumination power reached with the LED array presented in the following sections is justified.

The aim of this test has been the comparison of the results with those obtained in the beam loss study at PS and its verification. In addition, bias voltage breakdown, sensor current and the electrical conditions leading to this behaviour have been understood. An electrical and physical model has been obtained.

Some points concerning setup, analysis techniques and the interpretation of the results will rise again in the laser test (Chapter 7 on Page 95) but are described here only once.

6.2 Setup

6.2.1 Overview

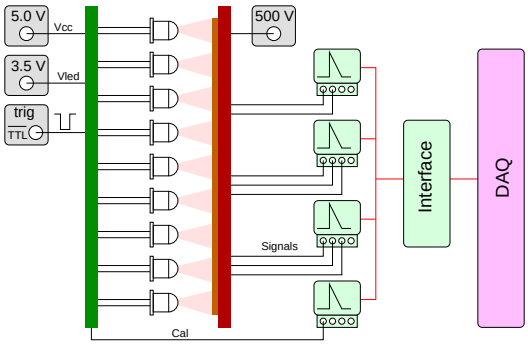

Figure 6.1: *Schematic of LED test setup*

Figure 6.1 gives a schematic overview of the whole test setup. Sensor and LED array have been mounted perpendicular due to practical reasons. The sensor is glued on its support PCB. The distance between sensor and array has been choosen very small (about 5mm) to minimize energy losses at the edges of the sensor. The LEDs on the array are powered indirectly by large buffer capacitors. The length of the pulses are choosen by closing switches between buffer and LED. This is done by an external pulser providing an inverse transistor-transistor logic (TTL) signal. In almost all tests, the pulse height is set to the LED's maximum rated current allowed in pulsed operation. The signal responses on sensor side are acquired simultaniously for each shot. Analogue signals from the sensor and the current monitor signal needed for energy calibration coming from the LED array are acquired by oscilloscopes.

6.2.2 IR Light Absorption in CMS Sensors

Absorption of light in Silicon comes about by the photo effect. It is described in Section 2.4.3 on Page 27. The penetration depth $\delta = 1/\alpha$ is the relevant parameter to choose a proper wavelength of the light used in the lab tests. But not any wavelength could be selected for the LED test. In the near infrared (NIR), the interesting part of the spectrum, only few wavelengths with reasonable power and cost are available. Thus, 1050nm-LEDs corresponding

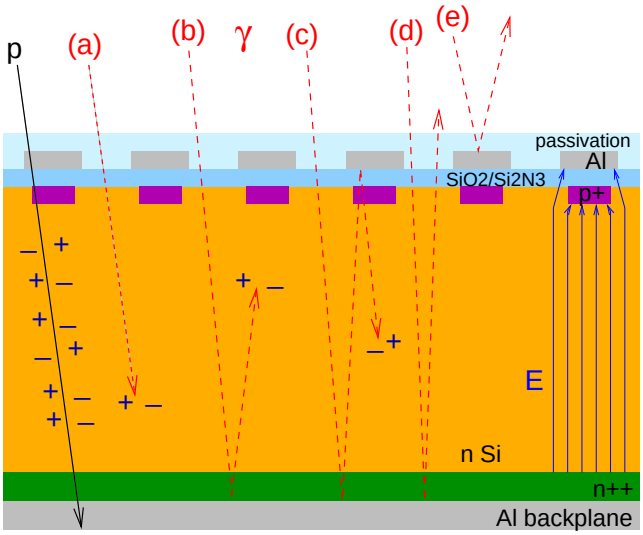

Figure 6.2: Interaction of IR Photons with a Strip Sensor. *Charged high energetic particles penetrate the whole detector leaving a trace of ionisation (solid line) but not so do photons (dashed lines). 25% of the photons are reflected by the strips (e). The other 75% enter the bulk (a-d). Most of them (96%) are aborbed (a,b), The remainder of 4% reaches the upper border of the bulk (c,d). Three quarters of them (3%) leave the bulk (d) and 1% are reflected back to the bulk (c).*

to a penetration depth of $\delta = 312\mu$m have been choosen.

Figure 6.2 shows different absorption scenarios of single photons in a silicon strip sensor. 25% of the sensor's surface is covered with Aliminum strips. So this share of the photons is reflected and lost. The remaining 75% enter the bulk. The inner side of the backplane reflects photons back to the bulk, so that the effective bulk thickness is

$$d_{bulk,eff} = 2 \times d_{bulk} = 1000\mu m \approx 3.2\delta \tag{6.1}$$

So, almost all photons are absorbed.

$$p_{abs}(d_{bulk,eff}) = 1 - e^{-d_{bulk,eff}/\delta} \approx 1 - e^{-3.2} \approx 96\% \tag{6.2}$$

Three quarters of the photons traversing the bulk twice are lost. Most of the remaining fraction (1%) will be absorbed. A very good estimation of the photon's balance may be calculated from Fig. 6.2: $75\% \times (96\% + 1\%) \approx 73\%$ of the photons are absorbed in the bulk[1].

The above mentioned exponential dependence of the intensity on the penetration depth leads to the conclusion that light absorption is inhomogeneous. Half of the light is absorbed within the first 200μm of the sensor. This is an important physical difference between light tests and testbeam, where energy deposition is perfectly homogeneous.

6.2.3 LED Array

6.2.3.1 Construction

81 GaAs (Gallium Arsenide) LEDs with a wavelength of 1050nm arranged in a matrix of 9×9 were used to cover an area of about 100cm^2. The intensity profile of one LED is a rotational symmetric gaussian with a half angle[2] of ±15°. This leads to an overlap of neighboured LEDs and therefore to a homogeneus illumination of the sensor.

With a nominal rise and fall time of 10ns each, the light pulse is very fast [Roi04]. This would have been a nice value, if an exact beam loss test worked with this setup especially concerning the time behaviour. But it turned out, that LED pulses must be some orders of magnitude longer than the length of an *unsynchronised abort* (260ns) to depose the desired energy. So, the feature of speed is only used in the module study presented in Section 6.9 on Page 92.

[1] Reflections at the transition between the bulk and the Silicon Oxide layer were not considered.
[2] angle of half of the central intensity

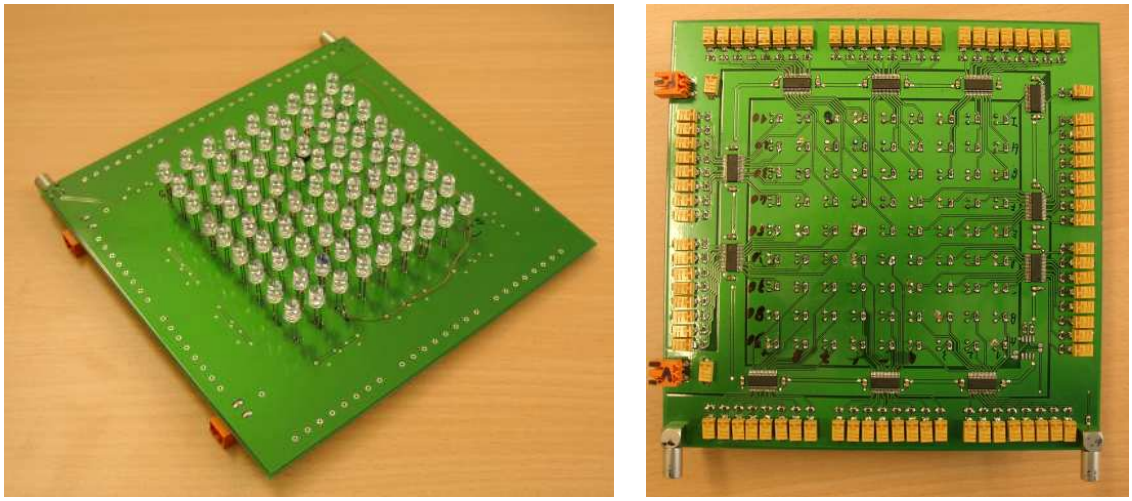

a. top view b. back view

Figure 6.3: Photos of LED-array. *Two low voltage inputs are needed (*Weidmüller *plugs): one as* V_{CC} *for the Quickswitches and the other to supply the LED circuits. One Lemo female is for the switches' trigger, the other provides a signal proportional to the current flowing through one selected LED. This is of great importance to be able to reconstruct the energy of the current shot.*

The maximum rated pulsed forward current is 500mA. From a radiation power of 2.5mW at a constant current of 50mA, the pulsed power is estimated to be 25mW. This has been reproduced within the calibration process.

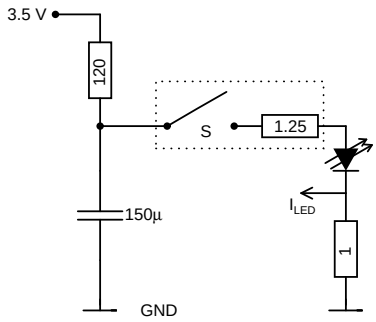

Figure 6.4: *Schematic of LED driving circuit.*

A schematic of the circuit driving one LED is given in Fig. 6.4. This circuit has been realised for each of the 81 LEDs independently to avoid electrical cross-talk between LEDs with different I(V)-characteristics. The main purpose of this circuit is to provide a current of about 500mA per LED as long as possible. In addition, the option of a variation of the pulse length resp. energy also was desired. This is best realised with a fast and low ohmic semiconductor switch. Two of 16 inputs of a high speed CMOS bus switch [Int99] have been shunted to reach an on-resistance of only 1.25Ω. A further resistance of 1Ω in series to LED and switch allowed the direct measurement of the current through each single LED for debugging and calibration purposes. This two resistors and the constant supply voltage of 3.5V select the working point in the I(V)-characteristic of the LED at the start of the buffer capacitor's dischargement. By varying the supply voltage, the maximum current could be fine-tuned and has been adjusted to the very limit of 600mA to provide maximum power. This results in a peak current of 49A flowing through the whole device. The buffer capacitance has been selected to the maximum available value realised as surface mounted device (SMD) with a reasoable package size. 150μF were sufficient to keep the LED current above 400mA during the standard pulse length of 300μs. The power supply series resistor of 120Ω has been chosen to maximize the speed of recharging of all buffer capacitors without rising above the maximum rated current for the power supply of 2A. With a buffer capacitor recharging time constant of $\tau = 120\Omega \cdot 150\mu\text{F} = 18\text{ms}$, a maximal pulse frequency of $f = 1/(3 \cdot \tau) \approx 18\text{Hz}$ has been reached. But 10Hz was enough to obtain sufficient statistics for data averaging during

a reasonable measurement time. The LED-array is pictured in Fig. 6.3.

6.2.3.2 Setup for Array Calibration

In principle, a CMS Silicon Strip Sensor is a good device to calibrate any light source emitting in the NIR. The charge Q_{sensor} flowing through the sensor during illumination gives a direct measure for the absorbed (detected) energy E_{sensor}. Considering the spectral response of 0.3 at 1050nm [RS 02], the photon energy of 1.18eV and the absorption efficiency of $1/75\% \cdot 1/97\%$ specific for CMS Silicon Strip Sensors at a wavelength of 1050nm (Section 6.2.2 on Page 54), this gives

$$E_{sensor} = \frac{1.18V}{0.3} \cdot 1/75\% \cdot 1/97\% \cdot Q_{sensor} = 5.4V \cdot Q_{sensor} \tag{6.3}$$

As the luminosity of the LEDs have a certain spread, one has to measure it and arrange the LEDs accordingly to achieve a homogeneous illumination profile. For this reason, a dedicated photoreceiver was built.

A large-area Silicon photo diode is reverse-biased (fully depleted). The diode's output current is converted into a voltage signal and amplified by an operational amplifier (OPA) with variable gain resistor. The OPA's output can be monitored directly with an oscilloscope. The sensivity of the diode is specified to be 2W/A = 2J/C [Int04] at a wavelength of 900nm. The relative spectral response is 0.3 at 1050nm [RS 02]. This gives the following calibration relation between the energy absorbed (detected) by the photo-diode ($E_{photo-diode}$) and the charge flowed through it ($Q_{photo-diode}$).

$$E_{photo-diode} = 2J/C \cdot 1/0.3 \cdot Q_{photo-diode} = 6.7V \cdot Q_{photo-diode} \tag{6.4}$$

Both equations 6.3 and 6.4, whose calibration factors have been obtained from completely different sources, have been tested with an arbitrary LED from the array (number 52). Current pulses of different lengths and charges Q_{led52} have been sent through this LED, and the response of both photo detecting devices has been measured and put into the equations derived above. Figure 6.5 on the next page shows the result. Both curves are straight lines showing that the response signals of the photo diodes are proportional to the charge flowed through the LED. And the factors of proportionality are equal as well proving the consistency of both calibration methods.

$$E_{sensor} = E_{photo-diode} = Q_{led52} \cdot 0.13\mu J/\mu C$$

6.2.3.3 Before and after Test Calibration

The array has been calibrated before and after all tests. This has been done by applying pulses of 400μs length and the maximum current of about 600mA per LED to all LEDs in the array. The energy and power response of each LED has been measured and added up. The result of the calibration before the tests is shown in Fig. 6.6 on the next page.

The array's total pulse energy of $E_{array} = 820\mu J$ together with a charge of $Q_{LED} = 185\mu C$ flowed through the reference LED (17) results into a calibration factor of

$$E_{array}/Q_{LED} = 4.4V \tag{6.5}$$

This number is used to reconstruct the currently used pulse energy in all physical test runs. As seen in Section 6.2.2 on Page 54, the portion of absorbed intensity at a wavelength of 1050nm

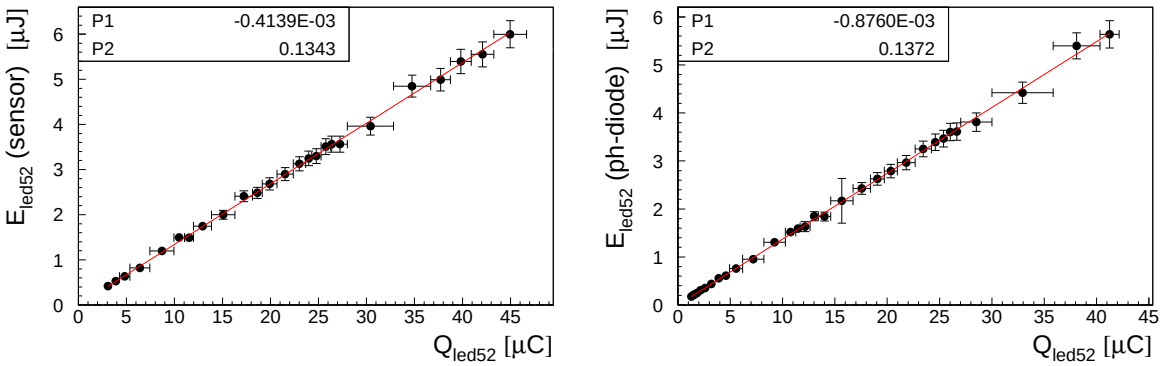

a. E_{sensor} vs. Q_{LED} b. $E_{photodiode}$ vs. Q_{LED}

Figure 6.5: Preparation of calibration. *The consistency of both calibration methodes has been proven: The gradients of energy vs. LED charge are equal (fit parameter P2). So, the energy responses of both photo detecting devices are equal and the energy emitted by a LED is proportional to the pulse charge flowing through the LED.*

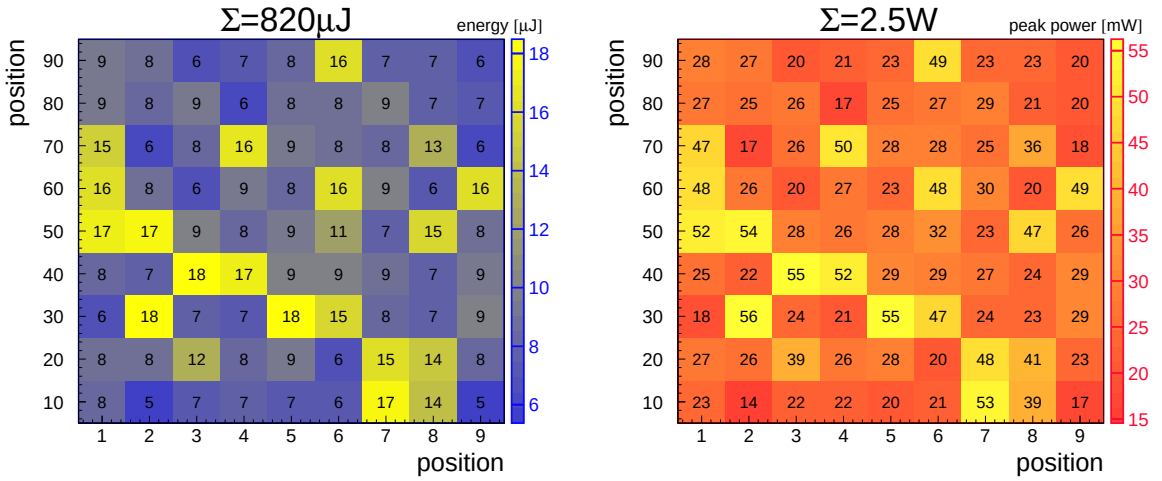

a. pulse energy b. pulse peak power

Figure 6.6: LED array calibration before tests. *A homogeneous distribution of bright LEDs has been tried but was not successful in all cases as too much of them would have been to be unsoldered and re-mounted.*
The total peak power of 2.5W is much too low for a realistic *beam loss experiment. See the discussion in Section 6.1 on Page 54 for more details.*

in a 500μm-sensor with reflecting backplane and a strip covering of 25% is $\epsilon = 73\%$. This gives an energy deposition in the Silicon bulk in dependence on the charge flowing through the reference LED of

$$E_{Si} = \epsilon \cdot E_{array} \overset{Eq.\ 6.5}{=} 73\% \cdot 4.4V \cdot Q_{LED} = 3.2V \cdot Q_{LED} \tag{6.6}$$

A slight decrease of the peak power to 2.4W after 30000 shots has been observed. Thus, the standard pulse energy decreased to 800μJ. This minor deviation has not been considered in the data analysis as much larger imprecisions coming from illumination losses at the edges of

the sensor and from reflections at the dielectric layer dominate this effect.

6.2.3.4 Error of Calibration

The systematic error of the energy calibration is estimated as follows. The calculation of the absorption efficieny of 73% has a relative inaccuracy of about 5% due to geometrical uncertainities concerning the cover with strips and due to reflections at the surface. Any eventual systematic error in measuring the charge flowed throuh the reference LED, e.g. due to a deviation of the measurement resistor from its nominal value, will cancel as this error already is considered within the calibration factor. The metering of the quantum efficiency out of [RS 02] was done with an error of 10% as this curve has a steep gradient in the interesting region and since some other plots found in literature (see Fig. 2.13b on Page 28) show a deviation of appropriate size. The relative systematic errors of all quantities add up following the linear error propagation law. The detailed derivation follows. A quantity y shall depend on its variables x_i only by the product of their powers with an exponent p_i.

$$y = A \prod_i x_i^{p_i} \tag{6.7}$$

The partial derivative of y by one of its variables x_k is then

$$\frac{\partial y}{\partial x_k} = A p_k x_k^{p_k - 1} \prod_{i \neq k} x_i^{p_i} = \frac{A p_k}{x_k} \prod_i x_i^{p_i} = \frac{p_k}{x_k} y \tag{6.8}$$

This gives the total *absolute* systematic error.

$$\Delta y = \sum_i \left| \frac{\partial y}{\partial x_k} \right| \Delta x_i = \sum_i \left| \frac{p_i}{x_i} y \right| \Delta x_i \tag{6.9}$$

And this results in the total *relative* systematic error.

$$\left| \frac{\Delta y}{y} \right| = \sum_i \left| p_i \frac{\Delta x_i}{x_i} \right| \tag{6.10}$$

In the present case, the energy calibration factor is a pure product of its dependent variables in simple power. Thus, the relative systematic errors add up to the total relative systematic error, giving 15%.

6.2.3.5 Setup of Energy Scans

As mentioned above, this array is capable to vary the pulse energy in either by modifying pulse length or pulse height. The first one is interesting from physics point of view, as the maximum power is applied at different pulse lengths. This allows the study of saturation effects much better than committing oneself to a fixed pulse duration and increase the pulse height. Therefore, a large energy resp. time scale has been covered. A standard scan consists of 10 pulse lengths: 100ns, 300ns, 1μs, 3μs, 10μs, 30μs, 100μs, 300μs, 1ms and 3ms. This is an increase in time and energy by a factor of approximately 3 per step, so that a logarithmic energy scale is covered homogeneously, and time adjustment is as easy as possible. Figure 6.7b on the next page demonstrates the relation between pulse length and energy being quite linear. But for long pulses, the energy drops as the pulse height decreases when the buffer capacitors almost are discharged. This fact can be seen in Fig. 6.7a. It shows the time behaviour of all 10 pulses (pulse shapes) of different lengths on a logarithmic time scale. The legend already contains the energy calibration.

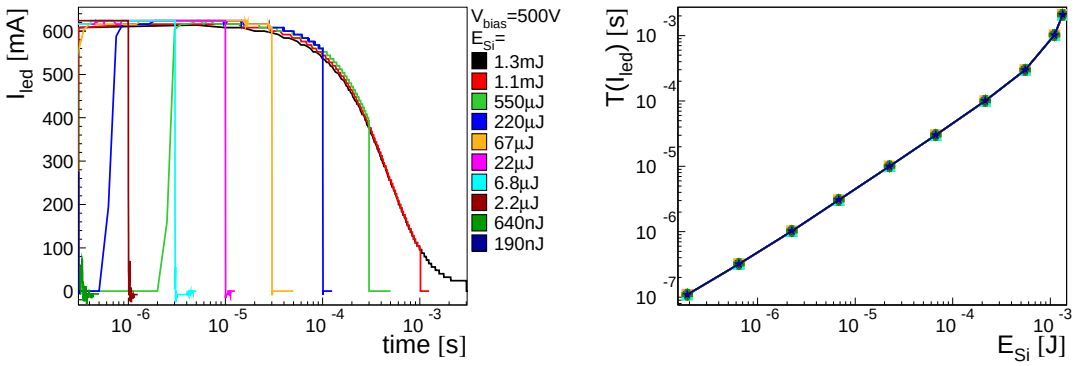

a. pulse shapes

b. pulse lengths vs. energy

Figure 6.7: Pulse shapes and lengths vs. energy. *The shapes of all 10 pulses of different lengths are shown on a logarithmic time scale. The legend already contains the energy calibration. The current is almost constant for pulses of a length up to 100µs (Fig. a). Therefore, pulse energies are quite linear versus pulse lengths (Fig. b).*

6.2.4 Sensor Setup

Each sensor has been glued on a seperate measurement and support printed circuit board (PCB). Conductive glue was used to make a connection between the sensors's backplane and the PCB's high voltage plane. The circuit of the support PCB is comparable to those used during the testbeam (Fig. 5.6 on Page 44) except for minor extensions and modifications.

- No signal pre-amplification is needed any more as the signal path in the lab is very short.
- The sensor current is measured with a much smaller resistor of 10Ω as the expected current is in the order of several 10mA.
- The measurements of the voltages over the dielectric layer are now done with a voltage divider whose total size of 2MΩ is comparable to the poly resistors.
- Three new parameters are acquired to study the behaviour of the T-filter during a beam loss.

A schematic of the new circuit is pictured in Fig. 6.8. A photo of a sensor setup with its circuit and a detailed description of its components can be seen in Fig. 7.2 on Page 95. A summary of all measured parameters is given in Table 6.1 on Page 64.

Two different high voltage supplies have been used. One low power device from CAEN with a maximum current of 1mA at 500V and a power supply from Oltronix with a maximum current of 300mA at 500V [Olt04]. The latter one has also been used at the testbeam. It is obvious, that this device is by far not the advantageous device to provide the sensor voltage. A discussion of the impact on sensor and circuit for both power supplies is given in Section 6.5.4 on Page 76.

6.2.5 Data Analysis

Figure 6.9 shows the data flow diagram for the whole test process. Analogue signals produced by the sensor circuit are digitised with oscilloscopes. Communication with them is

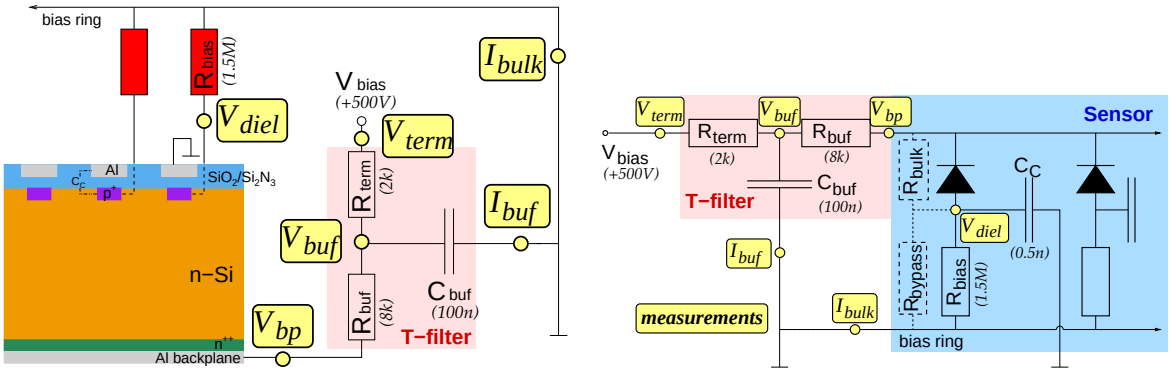

a. sensor schematic b. equivalent circuit

Figure 6.8: Schematic of the sensor and measurement circuit for light tests. *The circuit is the same for LED and laser test. The convention of highlighting the module's parts has been adapted from the testbeam schematic (Fig. 5.6 on Page 44). Each of the 512 or 768 strips of a sensor can be considered as equivalent to a diode, a coupling capacitor and a bias resistor (Fig. 6.8b). All voltages* (V_{term}, V_{buf}, V_{bp}, V_{diel}) *are measured against ground using voltage dividers* (2MΩ/66.5kΩ *for* V_{diel} *and* 10MΩ/12kΩ *for the others). All currents* (I_{sensor}, I_{buf}) *are measured as voltage drop over small resistors* (10Ω). *The dashed resistors* R_{bulk} *and* R_{bypass} *represent a very simple model of the short-circuited sensor. The proof of the latter one is given in Section 6.6.4 on Page 83.*

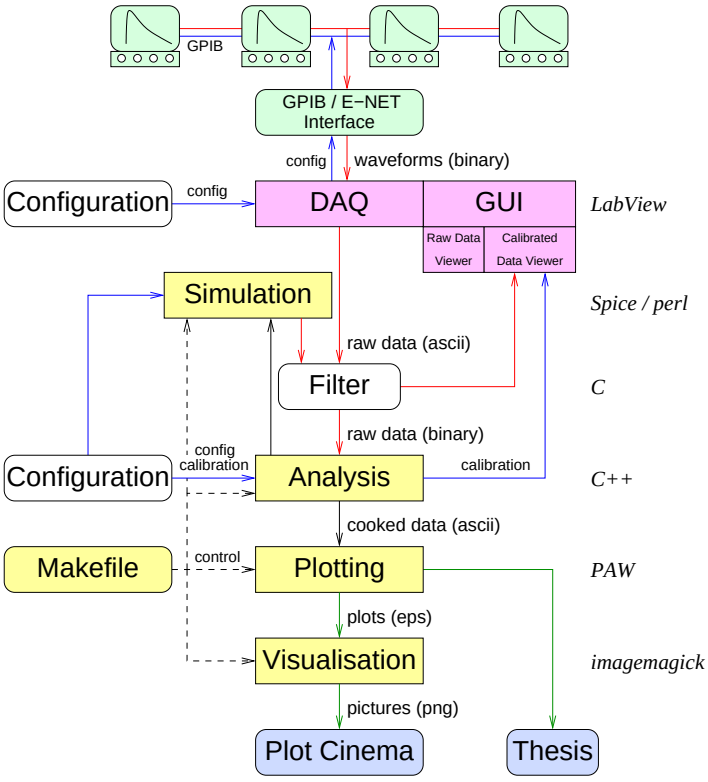

Figure 6.9: Schematic of data flow. *Four layers exist: Hardware, data acquisition and graphical user interface, data analysis, consumer. The left column shows the user controls, the right one the development tools.*

done via General Purpose Interface Bus (`GPIB`) and `GPIB` to Ethernet-Interface. The data acquisition (`DAQ`) software controls the behaviour of the oscilloscopes. Their time base, sampling depth and vertical resolution can be adjusted automatically according to channel and scope definitions in configuration files. Channels are named by the user to simplify the identification of the data during the following analysis. Filtering the raw data from a text format

to binary representation speeds up the data access for the analysis program. The automatic extensive analysis of a large amount of data has been the most challenging task. About 3000 measurement points were taken in approximately 40 runs during LED and laser tests. This resulted into 1 GByte of binary data. The best way to keep track over all the analysis results was the implementation of a relatively free configurable analysis software package, which had to take care of data and plot administration. It automatically analyses peaks, integrals, edges, rise- and fall-times, exponential time constants and values calculated from this items as well as statistical errors derived from the noise of the raw data. The error bars in all plots in this thesis denote those statistical errors.

The user configures the output of the software defining the runs to be evaluated and the set and type of plots to write to disk. The plot data is represented in a text format that is easy readable by `PAW`[3] [paw01]. A lot of complex `PAW`-macros have been written to automatically create postscript plots. The rendering of all plots is done in a last step by converting them into a pixel format like `PNG`. This enabled the user to fast inspect the large amount ($\approx$ 20000) of plots. The complete analysis is controlled by one makefile calling the three mentioned modules: data analysis, plot creation and conversion into pictures. Each module also may be started separately by invoking a specific rule. Partial data analysis also is possible. By disentangling data analysis from plot creation, it is possible to reprocess a subset of plots, e.g. to change their appearance.
A spice [spi02] simulation also has been done. It is described in Section 6.2.6 in detail. The simulation needs one physical value provided by the analysis of real data resulting in a data loop: The simulation cannot start unless all physics data has been analysed. The simulated data is in the same format as physics data and has therefore been integrated into the whole analysis and visualization process.
The development of the whole package has been complex and the operation respectively configuration is not easy at all. But the effort is justified in order to obtain a systematic overview on the large amout of data.

6.2.6 Spice Model

A simulation of the electrical conditions during a beam loss has been performed. The aim was to cross-check the physics data with a simple electrical model. Solving many differential equations and fitting the solutions to the data hence could be avoided. The main focus lay on the sensor circuit as its implementation in spice is straight forward. The sensor itself has been realised as switch with a finite resistance R_{sensor}. It represents the resistance of the sensor during short-circuit and is assumed to be $R_{sensor} = 300\ \Omega$. A shunted capacitor of C_{sensor} = 5nF simulates the sensor's capacitance averaged over the whole depletion process. (See Fig. 6.10 for an equivalent circuit.)

Both values are only estimations and develope vs. time in reality as charge carriers are drained off and resistivity increases dramatically. Trying to find a model for the dependency of the sensor's capacitance on the field C(E) also is useless under such conditions of large charge concentrations. So, the introduction of finite and constant sensor resistance and capacitance has only a symbolic character. It makes the shape of the simulated data fitting better to the reality. Another fact has to be mentioned here. The electrical behaviour of the simulated external parameters is dominated by the T-filter, not by resistance and capacitance of the sensor, as the T-filter consists of resistances in the range of kΩ and a capacitance in the order of 100nF.

[3]Physics Analysis Workstation is a software package to analyse data, mostly used in High Energy Physics

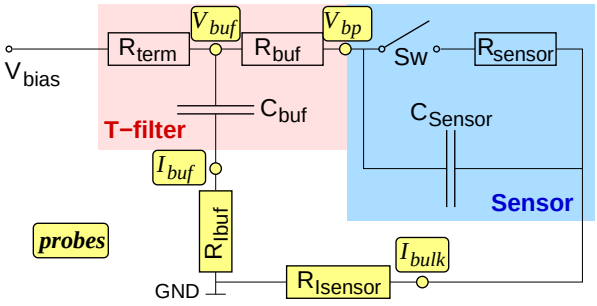

Figure 6.10: Schematic of circuit in spice model. *The convention of highlighting the different parts is the same as in Fig. 6.8 on Page 61. The sensor is modelled as switch with a series resistor and a shunted capacitor. The resistor* ($R_{sensor} = 300\Omega$) *simulates the short-circuited sensor and the capacitor* ($C_{sensor} = 5nF$) *the average (undepleted) sensor's capacitance.*

Unfortunately, it has not been possible to model the sensor as capacitor-coupled photo-diode. Thus, the voltage drop over the coupling capacitance is missing in simulated data. The raw time behaviour of the 5 external circuit parameters is provided by the spice runs. They are listed in Table 6.1 on the next page.
Only *one* input value from the analysed physics data had to be put into the spice model! The total charge flowing through the sensor during a shot

$$Q_{shot} = \int I_{sensor}\ dt \tag{6.11}$$

could not be calculated exactly from physical considerations. A model for a *qualitative* understanding of this value is described in Section 6.6 on Page 79. The sensor current (I_{sensor}) during a shot can be easily calculated from the bias voltage (V_{bias}) and both T-filter-resistors (R_{term} and R_{buf}). This current together with the flowed charge (Q_{shot}) gives a quite exact value for the breakdown time (T_{break}) of the bias voltage. This fact is extensively discussed and proven in Sections 6.5.1 on Page 70 and 6.5.2 on Page 73.

$$T_{break} = \frac{Q_{shot}}{I_{sensor}} = \frac{Q_{shot} \cdot (R_{term} + R_{buf})}{V_{bias}} \tag{6.12}$$

This relation only is true, when the terminal voltage stays constant. This is the case, for the Oltronix power supply. For each shot, a perl script calculates T_{break} and inserts it into the spice template file to specify the individual closing time of the switch. Other parameters the template had to be filled with are the applied high voltage V_{bias} and the T-filter components R_{term}, R_{buf} and C_{buf}. The spice output is converted into run data processable by the analysis and visualization package.

6.3 Measurement Program

6.3.1 Measured Parameters

The sensor circuit with the measurement principle of all parameters is shown in Fig. 6.8 on Page 61. Table 6.1 on the next page summarizes the measured parameters. Six quantities are measured: currents as voltage drop over small resistors and voltages with the help of voltage dividers. The dielectric voltage is taken from three groups of channels. This results in nine measured values, but only eight were used. The voltage over the dielectric layer of strip group three sometimes has not been available. So, in all analysis steps, only the first and second group are considered.

Symbol	Description	plot	spice
E_{Si}	Energy deposition in silicon bulk	-	-
V_{bias}	Applied bias voltage	-	-
R_{term}	Terminal resistor in T-filter	-	-
R_{buf}	Buffer resistor in T-filter	-	-
C_{buf}	Buffer capacitor in T-filter	-	-
I_{LED}	Calibrating LED current	6.7a	-
V_{bp}	Backplane voltage	6.11a	yes
I_{sensor}	Sensor current	B.6	yes
$V_{diel,n}$	Voltage over dielectric (3)	6.12a	no
I_{buf}	Charging current of buffer capacitor	B.8	yes
V_{buf}	Voltage over buffer capacitor	B.3	yes
V_{term}	Terminal voltage	B.1	(yes)

Table 6.1: Summary of defined and measured parameters. *The six ones in the second part are measured values, and the others are derived out from the measurement. The three last-mentioned parameters are new in light tests. References to figures with example plots are listed in the appropriate column. The column* spice *gives information wether the measured value also is simulated.*

6.3.2 Derived Parameters

The measured parameters V_{bp}, V_{diel}, V_{term}, V_{buf}, I_{buf} and I_{sensor} described in the previous section have been recorded by oscilloscopes. The data has then been processed by the analysis software. Many calculations have been done on the raw data automatically. The aim was to get a fast overview of peaking times, peaking positions, integrals and edge positions versus the scanned values like bias voltage or energy. All values provided are listed in Table 6.2. An other important issue has been the calculation of dynamic data using raw data and analysed items to illustrate the behaviour of special components in the circuit. Those calculated data plots are explained in the same Table 6.2. The complete terminal voltage V_{term} divides into three parts: The voltage over the T-filter-resistors $V_{Tfilter}$, the voltage over the silicon bulk V_{bulk} and the DC/p^+ potential resp. voltage over the dielectric layer $V_{diel,i}$.

$I_{R_{poly}}$ is the current through the poly silicon resistors. This current determines the voltage at the dieletric layer. V_{diel} is measured and $I_{R_{poly}}$ can be derived from it with usage of R_{poly}.

$< V_{dead} >$ is partially interessting only to verify the order of magnitude of the voltage over the dielectric. The backplane voltage itself, from which this value is derived, strongly varies during its dead time.

$\frac{1}{T_{mid}} \int_{mid}$ denotes the averaging over a mid area of 40% to 60% of the dead time T_{dead}. The raw data shows, that during this time interval, all parameters vary fewest.

6.3.3 Sensors under Test

Five sensors have been tested (see Table 6.3 on Page 66). Diversification with respect to geometry, manufacturer and bulk resistivity has been aimed at, considering the limitation of availability. The sensors were not planned to be built into detector modules, as they come either from a pre-series or were used in special lab tests.

6.3.4 Test Runs

Test runs consist of several measurements at different conditions. Deposed energy (E_{Si}), bias voltage (V_{bias}) and T-filter parameters (R_{buf}, R_{term}, C_{buf}) can be adjusted independently. The combined variation of two or three of those values in one test run results in a multidimensional parameter space with an appropriate number of measurement points. More than one LED shot is normally necessary to obtain well averaged raw data for one measurement point. All test runs, the varied parameters, the multiplicities of measurement points and the sensors, they were performed with, are listed in Table 6.4 on Page 66. Some of the test runs are redundant but evaluated anyway due to statistics of different sensor manufacturers, geometries and bulk

Symbol	Formula	fig	Description
$V_{Tfilter}$	$V_{term} - V_{bp}$	B.4	voltage drop over t-filter resistors
V_{bulk}	$V_{bp} - < V_{diel} >$	6.28	estimated voltage drop over bulk
$I_{R_{poly}}$	$\frac{<V_{diel}>}{<R_{poly}>/512}$	6.32	estimated current through all poly resistors
P_{tot}	$V_{term} \cdot I_{sensor}$	na	totally dissipated power
$P_{Tfilter}$	$V_{Tfilter} \cdot I_{sensor}$	na	power dissipated by T-filter resistors
P_{bulk}	$V_{bulk} \cdot I_{sensor}$	na	power absorbed from silicon bulk
P_{poly}	$< V_{diel} > \cdot I_{R_{poly}}$	na	power dissipated by poly silicon resistors
T_{dead}	-	6.34b	backplane voltage breakdown time
$< V_{bp} >$	$\approx \frac{1}{T_{mid}} \int_{mid} V_{bp}\ dt$	6.13a	mean backplane voltage during breakdown
$\tau_{recover}$	-	6.23	time constant of backplane voltage recovery
$\tau_{discharge}$	-	6.23	time constant of buffer capacitor current decay
$\{I_{dischar.}\}$	-	6.36b	maximum buffer capacitor discharging current
$\{I_{recharge}\}$	-	6.36b	maximum buffer capacitor recharging current
$Q_{discharge}$	$\int_{discharge} I_{buf}\ dt$	na	discharge of buffer capacitor
ΔT_{buf}	$\approx T_{dead}$	6.18	distance of buf. cap. dis- and recharge peaks
Q_{sensor}	$\int_0^{T_{dead}} I_{sensor}\ dt$	6.29	charge flowing through the bulk during a shot
ϵ_{charge}	$\frac{Q_{sensor} \cdot 3.9V}{E_{Si}}$	6.30c	fraction of drained off charge
$\{I_{sensor}\}$	-	6.25f	maximum sensor current
$< I_{sensor} >$	$\approx I_{sensor}\vert_{t=T_{dead}/2}$	7.5a	mid value of sensor current
$T(I_{sensor})$	$\approx T_{dead}$	6.18	duration of sensor current signal
Q_{LED}	$\int_0^{T_{pulse}} I_{LED}\ dt$	6.5	charge through reference LED
$T(I_{LED})$	$\approx T_{pulse}$	6.7b	duration of LED pulse
C_{buf}	$\frac{\int I_{discharge}\ dt}{(V_{bias} - <V_{buf}>)}$	6.22	reproduction of buffer capacitance
R_{buf}	$\frac{1}{T_{mid}} \int_{mid} \frac{V_{buf} - V_{bp}}{I_{sensor}}\ dt$	6.21	reproduction of buffer resistance
R_{term}	$\frac{1}{T_{mid}} \int_{mid} \frac{V_{term} - V_{buf}}{I_{sensor}}\ dt$	6.21	reproduction of terminal resistance
$< V_{Tfilter} >$	$\frac{1}{T_{mid}} \int_{mid} V_{term} - V_{bp}\ dt$	6.36a	mean voltage drop over T-filter resistors
$\{V_{diel,i}\}$	-	6.35	maximum voltage over the dielectric layer
$[V_{bulk}]$	-	6.36a	minimum bulk voltage
$T(V_{diel,i})$	$\approx T_{dead}$	6.18	duration of dielectric voltage signal
$\tau(I_{sensor})$	-	6.23	time constant of sensor current decay
$\tau(V_{diel,i})$	-	6.23	time constant of dielectric voltage decay
$< P_{part} >$	$\frac{1}{T_{length}} \int_{length} P_{part}\ dt$	6.37a	mean dissipated power by *part*
E_{part}	$\int P_{part}\ dt$	6.37b	dissipated energy by *part*
E_{buf}	$\frac{1}{2} C_{buf} (V_{bias}{}^2 - [V_{buf}]^2)$	6.37b	energy loss of buffer capacitor

Table 6.2: Calculations in data analysis. *Symbols or formulas occur in the axis labels of the plots in the results Sections 6.4 to 6.8 and 7.4 to 7.6. References to figures with example plots are listed in the appropriate column. Three pairs of brackets with different meanings are used: <> denote a mean, {} a maximum and [] a minimum value. All values described here refer to the time period of voltage breakdown. Figure 6.8 on Page 61 displays the sensor and its circuit together with the defined voltages, resistances and capacitances and the measured values (summarised in Table 6.1), that are the basis of the above calculations.*

resistivities.

Bias Voltage and Energy Scans

The standard test for all sensors was a combined energy and bias voltage scan (two-dimensional parameter space). 10 pulse lengths from 100ns up to 3ms (see Section 6.2.3.5 on Page 59) were used to scan over a large energy scale from 190nJ to 1.3mJ. The standard scan contained 10 voltages up to 500V. The values have been compressed arround the most interesting region, namely the sensor depletion: 25V, 50V, 75V, 100V, 130V, 160V, 200V, 300V, 400V, 500V. Scans with more than 10 values contain 550V or 0V and 1V. The conditions, under which the

thesis ID	database ID	geometry	V_{dep} [V] before	after	resistivity (ρ)
D	30221116053219	W6A	40	44	high
E	30221116053220	W6A	37	42	high
F	30210431112924	OB2	148	165	low
G	30210433608620	OB2	148	200	low
H	30211434603447	W7B	?		[irradiated]

Table 6.3: Sensors under Test. *Geometric data can be looked up in Table E.2 in the Appendix on Page 132. The thesis identifier (ID) is used in plot legends and descriptions.*

test run	measurement points	**sensor's thesis ID** **D**	**E**	**F**	**G**	**H**
$V_{bias} \otimes E_{Si}$	$10 \otimes 10$	1	2	1	1	
	$11 \otimes 10$		1	1		
	$12 \otimes 10$	1	1		1	
	$20 \otimes 10$					1
E_{Si}	28	1				
	24		1			
V_{bias}	60	2				
Temperature Θ	38					1
$V_{bias} \otimes C_{buf}$	$10 \otimes 40$			1		
$R_{buf} \otimes V_{bias} \otimes E_{Si}$	$9 \otimes 5 \otimes 4$	1			1	
$\Sigma_{LEDshots}$ (estimated)		**8220**	**6810**	**9150**	**6000**	**3570**

Table 6.4: Summary of LED test runs. *Several tests with one, two or even three-dimensional parameter space were performed. All sensors are listed together with the multiplicity of test run(s) they suffered from. For each measurement point, about 15 LED shots were needed to aqcuire nicely fitting and well averaged data.*

tests were done, changed during the whole study. Early runs with all available sensors were done with a preliminary T-filter and a CAEN high voltage supply and the Oltronix power supply. They were not rejected as this has been the only data set enabling the comparison of different sensors under same conditions with good statistics. Furthermore, a current meter in the high voltage line has been used to monitor the equilibrium current before and after the shots. The finite internal resistance of this device caused the terminal voltage at the sensor circuit partially breaking down and hence weighting the results. The last standard test has been done with sensor E under optimal conditions using the correct T-filter, the Oltronix power supply, representing the worst case, and no current meter. Therefore, this run mostly is referred to in the results sections (see Figs. 6.29 on Page 81 and 6.30c on Page 82 for example plots). Raw data of this run is displayed in Chapter B in the Appendix on Page 122. Other combined energy and bias voltage scans have been done for example with sensor D (Fig. 6.30b on Page 82) and sensor H (Fig. 6.39b on Page 90).

For deeper studies, pure bias voltage and energy scans were done using an increased density of measurement points with and without T-filter resistors (for an example, see Fig. 6.30a on Page 82).

T-filter Resistance Scans

A very informative and fruitful study has been the scans over the T-filter resistances and capacitance. The resistor scans covered a three-dimensional parameter space: For each of the 9 resistor-configurations, a small energy and bias voltage scan has been done: 25V, 50V, 100V, 200V, 500V and 300ns, 3μs, 30μs, 300μs, 3ms. Both resistances R_{term} and R_{buf} were changed in parallel by fulfilling the relation

$$R_{buf} \approx 4 \cdot R_{term} \tag{6.13}$$

A large scale from R_{buf} of 1Ω up to 100kΩ has been covered logarithmicly. The exchange of the resistors had to be done by unmounting the sensor circuit from the setup, unsoldering the old ones, soldering the new ones and remounting the circuit into the setup. Thus, only two such tests were done. The following pairs of T-filter resistances were used. The configuration

R_{buf}	100 kΩ	33 kΩ	10 kΩ	3.3 kΩ	1 kΩ	330 Ω	110 Ω	33 Ω	1 Ω
R_{term}	27 kΩ	8.2 kΩ	2.7 kΩ	820 Ω	270 Ω	82 Ω	27 Ω	10 Ω	1 Ω

in the box is nearest to the officially used T-filter of

$$R_{buf} = 9\ k\Omega \text{ and } R_{term} = 2.2\ k\Omega \tag{6.14}$$

The results of both T-filter scans are distributed over several sections: see Figs. 6.21, 6.23 on Page 75, 6.31a, 6.35c, 6.35d on Page 86, 6.36a, 6.36b, 6.36c on Page 88 and 6.37a, 6.37b on Page 88.

T-filter Capacitance Scan

The scan over the T-filter capacitance covered the 10 standard voltages and 40 capacitances from 10nF to 1μF (two-dimensional parameter space). Such a large amount of values can not be obtained by soldering each component! The capacitor on the sensor circuit has been unmounted and connected to an external circuit with 8 different shunted capacitors. With an 8 bit switch, one could (de-)select capacitances adding up to the wished value. The values were again selected to increase exponentially.

The results of this test are needed for various argumentations and therefore are distributed over several sections: see Figs. 6.22 on Page 75, 6.24 on Page 76, 6.26b on Page 79, 6.31b on Page 83 and 6.35b on Page 86.

Temperature Scan

Sensor H has been irradiated with an equivalent dose of 15 years of `LHC` operation. It received the standard scan at temperatures between −20°C and −30°C. Keeping the temperature constant was not easy with the available setup. It consisted of a bottle with liquid nitrogen, an insulated lid and steel pipes with a valve. The pipes lead dry air through the nitrogen and onward to the case with the sensor circuit. The valve controls the air flux. But condensed water from remaining humidity in the air regularly narrowed the pipe avoiding the system to come to a stable equilibrium and making it necessary to adjust the flux manually.

After the standard test, a temperature scan has been done to take advantage of the warm up phase starting at −30°C. The scan was finished when a temperature of 0°C has been reached. The results of this test are presented in Section 6.8 on Page 89.

Results and Interpretation

The following sections summarise the most important results obtained from the above presented measurement program. An interpretation resp. model is given.

6.4 Verification of Testbeam

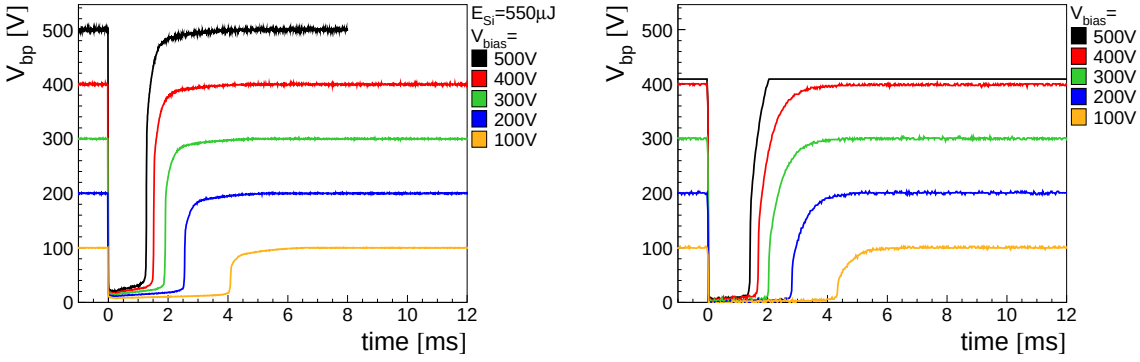

a. LED test

b. testbeam

Figure 6.11: Verification of backplane voltage. *The shape of voltage breakdown and its recovery is perfectly reproduced. The exact comparison of time constants and voltage peaks during breakdown is seen in Figs. 6.13 and 6.14 on Page 70.*

The behaviour of a high resistivity sensor during the testbeam has been reproduced illuminating a sensor of the same type with light of LEDs. All plots shown in this section refer to sensor E (high ρ) biased with the Oltronix power supply and equipped with a *preliminary* T-filter ($R_{buf} = 3.3k\Omega$, $R_{term} = 1k\Omega$). Both, the power supply and the preliminary T-filter, have been used during the testbeam. There is only one minor difference. During the LED test, a current measurement device has been placed in the HV line. The voltage drop over its internal resistance is leading to a slight breakdown of the circuit's terminal voltage and hence to an effective reduction of the bias voltage by 20%. This fact together with a difference in the deposed energy explains the slightly different results. Furthermore, only those five of the ten bias voltages points measured during the LED test, representing the voltages set during the testbeam (100V, 200V, 300V, 400V and 500V), are displayed in the plots.

The deposed light energy of $E_{Si} = 550\mu J$ complies with a number of minimum ionizing particles (`MIP`s) of

$$N_{MIP} = \frac{N_{EHP}}{38000\ EHPs/MIPs} = \frac{E_{Si}}{3.6eV/EHP \cdot 38000\ EHPs/MIPs} = 2.5 \times 10^{10}\ MIPs \tag{6.15}$$

This compares approximately to the intensity reached in some shots during the testbeam of 4.7×10^{10} `MIP`s. See Fig. 5.2 on Page 40 for the beam profile providing this number.

The shape of the backplane voltage breakdown and its recovery has been well reproduced (Fig. 6.11). During dead time, in both cases there is a slight increase in the remaining voltage. The recovery shows an exponential behaviour reaching the original voltage asymptotically.

The shape of the voltage over the coupling capacitors (Fig. 6.12) is verified qualitatively. At the LED test, the voltage stays near its peak value for a longer period of time due to the finite duration of the shot. The shape strongly depends not only on the length of the shot and

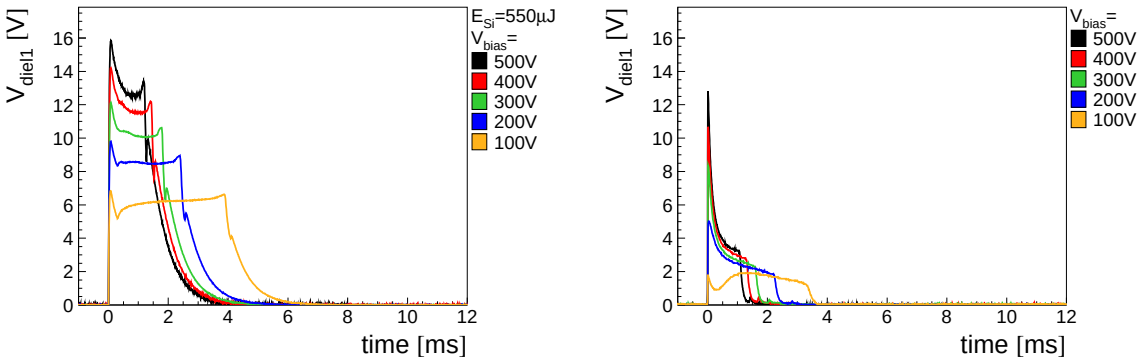

a. LED test b. testbeam

Figure 6.12: Verification of voltage over the dielectric layer. *Its shape is qualitatively reproduced: A steep increase at zero time in both cases is followed by a constant period in the LED test due to the finite duration of the shot and by the immediate decay in the testbeam. Differences are due to inhomogeneous absorption of light in the silicon bulk. See Section 6.2.2 on Page 54.*

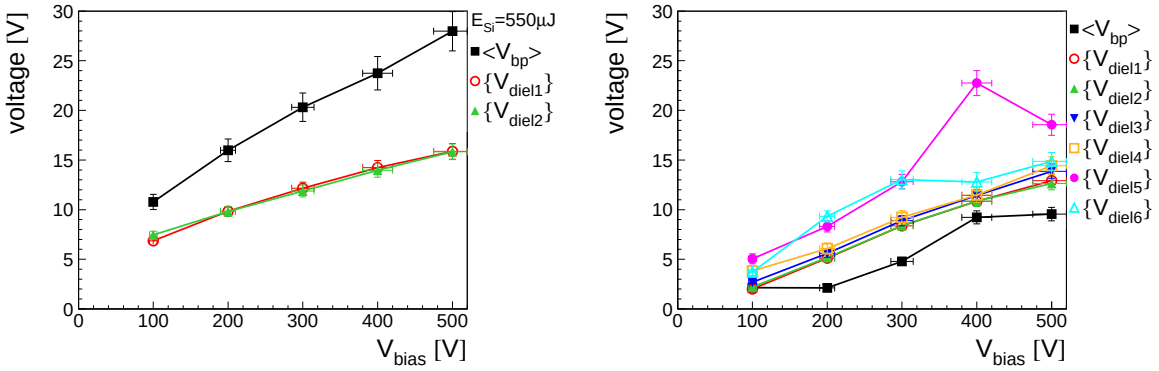

a. LED test b. testbeam

Figure 6.13: Verification of voltage peaks. *The peaks of the voltage over the dielectric fit well, but the breakdown voltage only is verified by its order of magnitude. The relation of breakdown to dielectric voltage is not verified. This can be due to an effect of different grounding in both cases.*

on the used power supply[4] but also on the kind of absorption. In case of minimum ionizing particles (MIPs), energy deposition is homogeneous along a thin sensor, but in case of NIR light, absorption mainly occurs near the p^+-implants (Section 6.2.2 on Page 54).

Even if the shape could not be reconstructed very well, the peak values of voltages over the dielectric layer match quite well (Fig. 6.13). But the mean values of the backplane voltage during breakdown are verified only by their order of magnitude. And the relation of breakdown to dielectric voltage is not verified. Both discrepancies could be due to different grounding during LED test and testbeam.

Time constants (Fig. 6.14 on the next page) match perfectly as those only depend on the speed of draining off the generated charge carriers. This drain-off-current (*sensor current*) on his part depends on the electrical setup only, which is the same in both cases.

The good accordance of the testbeam with the LED test results is astonishing at first

[4]Refer to Section 6.5.4 on Page 76 for a detailed discussion.

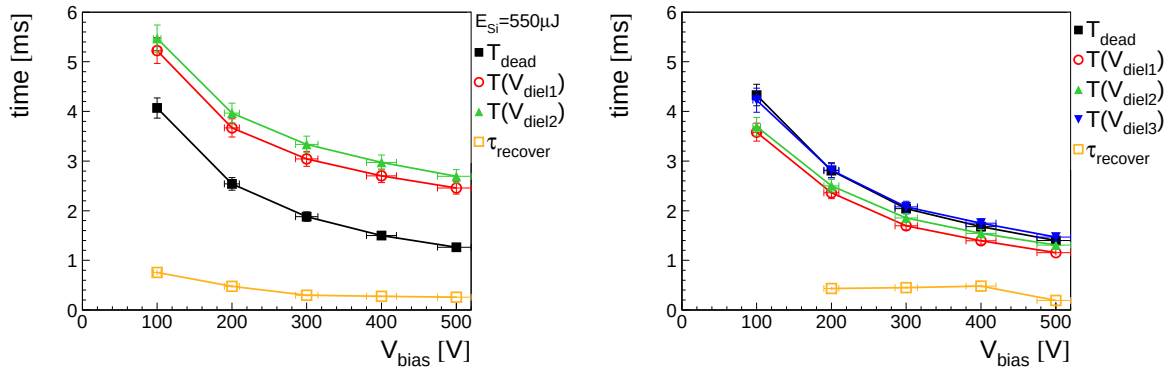

a. LED test b. testbeam

Figure 6.14: Verification of time constants. *Backplane voltage deadtime, length of the dielectric voltage signal and backplane voltage recovery time constant are compared to each other. The time behaviour matches quite well in both cases.*

glance as durations of both events differ by three orders of magnitude. But the electrical and physical model developed in the following sections explains this seeming discrepance.

6.5 Electrical Model and SPICE Simulation

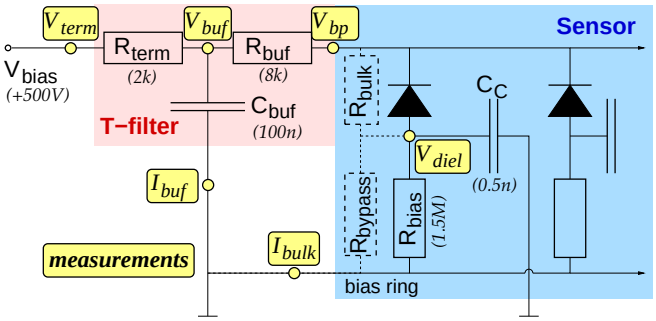

Figure 6.15: Equivalent circuit of a silicon sensor and its electical components. *The equivalent bulk resistor and the resistor bypassing the* R_{bias} *(dashed) represent a simple model for the whole sensor during voltage breakdown:* $R_{sensor} = R_{bulk} + R_{bypass}$. *The proof of the latter one is given in Section 6.6.4 on Page 83.*

The sensor circuit and its dimensioning dominates the behaviour of most of the sensor parameters during a beam loss. Many observed effects can be derived from a simple electrical model. It allows the simulation of almost all observed and calculated parameters (see Tables 6.1 on Page 64 and 6.2 on Page 65). A schematic of the sensor and its electrical circuit is repeated in Fig. 6.15.

6.5.1 Circuit Voltages and Currents

All data shown in this section has been extracted from the standard test of sensor E (high ρ) with a final T-filter ($R_{term} = 2.2k\Omega$, $R_{buf} = 8k\Omega$ and $C_{buf} = 100nF$) and biased by the Oltronix power supply. Each presented figure contains test data and the appropriate SPICE simulation. The raw data in this section has been taken under standard conditions biasing the sensor circuit with $V_{bias} = 500$ V and applying to the Silicon bulk a defined energy per shot of $E_{Si} \approx 550$ μJ. A more detailed look on the raw data can be taken in Chapter B in the Appendix on Page 122 starting presenting scans over bias voltage and shot energy.

Measurements of the sensor circuit's terminal voltage (Figs. 6.16 and B.1 in the Appendix on Page 122) prove its stability during all tests when using the Oltronix high voltage supply, so that the total bias voltage drops over the T-filter resistors and the sensor. Figures 6.16 and B.4 demonstrate that the T-filter resistors catch the very most of the bias voltage. The small remainder at the sensor's backplane (Figs. 6.16, 6.28 on Page 80 and B.5) causes the voltage drop over the dielectric layer (Figs. 6.28 on Page 80 and B.2), that cannot be simulated with the used simple SPICE model. As the measured value of the backplane voltage during breakdown cannot be reproduced with SPICE, it can be used to develop a very simple model of the sensor during breakdown. At $V_{bias} = 500V$, the average breakdown voltage V_{bp} is about 15V (Fig. 6.28 on Page 80) at a flowing current of $I_{sensor} \approx 50mA$ (Fig. 6.17 on the next page). This concludes to an estimated total *sensor resistance* during short-circuit phase (see the circuit schematic in Fig. 6.15) of

$$R_{sensor} \approx V_{bp}/I_{sensor} = 300\Omega = 3\%\ R_{Tfilter}. \tag{6.16}$$

This value together with the estimated average sensor capacitance of 5nF during breakdown flowed into the SPICE model described in Section 6.2.6 on Page 62.

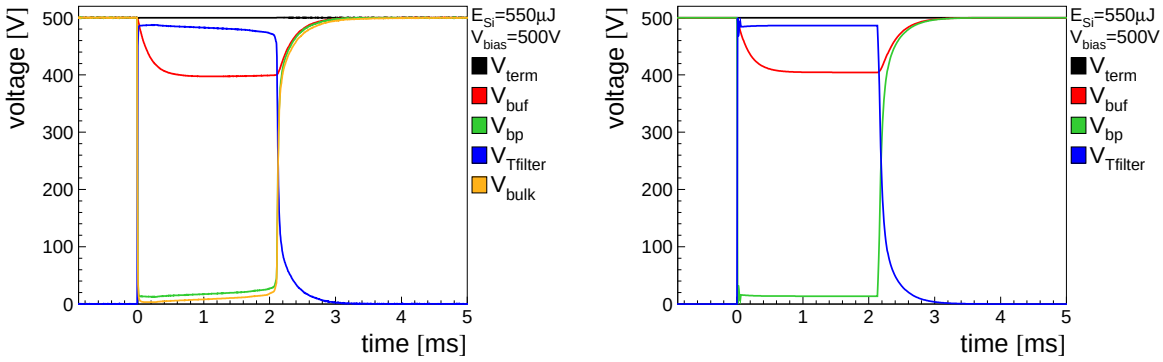

a. measurement b. SPICE simulation

Figure 6.16: Raw data sample of measured and derived voltages vs. time. *The bulk voltage ($V_{bulk} = V_{bp} - V_{diel}$) is missing in the simulation as the dielectric voltage is needed for its calculation. And the latter one could not be simulated. The breakdown of the backplane voltage V_{bp} has not been simulated exactly as it depends on the sensor and charge carrier dynamics during ionisation. Therefore, simulated and measured T-filter voltage drop ($V_{Tfilter} = V_{term} - V_{bp}$) also differ slightly during breakdown.*

One can conclude, that the T-filter resistors protect the sensor by absorbing almost the total bias voltage:

$$R_{Tfilter} \overset{Eq.\ 6.16}{\approx} 33 \times R_{sensor} \tag{6.17}$$

They dominate the sensor current through the whole device, and the bulk itself can be considered as short-circuited. So the sensor current is limited at high energies (Fig. B.7 in the Appendix on Page 123), approximately constant vs. time (see Figs. 6.17 on the next page and B.6) and can be expressed as follows.

$$I_{sensor} = \frac{V_{bias}}{R_{Tfilter}} \tag{6.18}$$

$$with \quad R_{Tfilter} \overset{def}{=} R_{buf} + R_{term} \tag{6.19}$$

The deviation from this simple constant sensor current model, namely the peak at t=0 and the finite decay constant, is caused by the discharge respectively recharge of the buffer capacitor

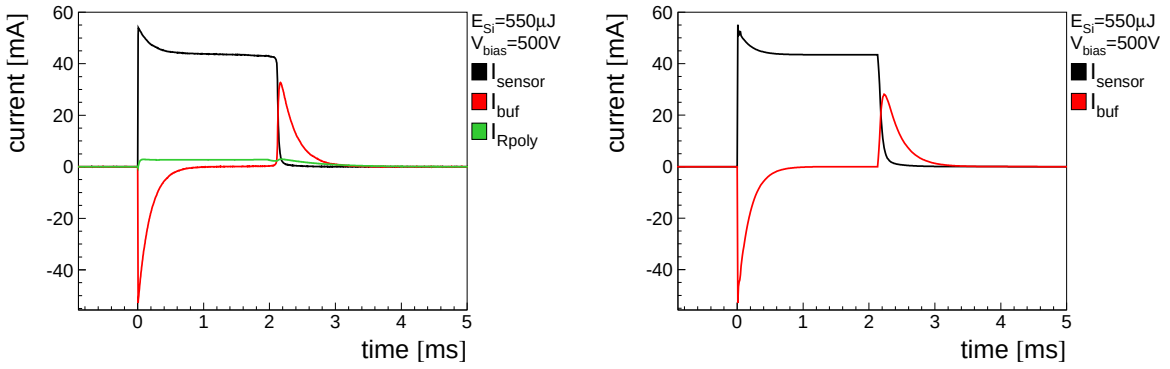

a. measurement b. SPICE simulation

Figure 6.17: Raw data sample of measured and derived currents vs. time. *The poly silicon resistor current* ($I_{Rpoly} \approx 512 \cdot V_{diel}/R_{poly}$) *is missing in the simulation for the same reason as explained in Fig. 6.16 on the previous page: The not simulated dielectric voltage is needed for its calculation. Both simulated currents* (I_{sensor} *and* I_{buf}) *fit exactly as they are dominated from circuit properties.*

(Figs. 6.17 and B.8). The slight negative slope in the sensor current not seen in the simulation comes from the increase of the bulk resistance during charge carrier drain-off.

Calculations of the areas of the discharging and recharging current peaks in Figs. 6.17 and B.8 result in almost equal charges as expected. Figures 6.16 on the previous page and B.3 prove that the buffer capacitor is not discharged completely during dead time. The appropriate voltage V_{buf} between both T-filter resistors is rather devided by them and therefore defined by their ratio. So, the available buffer charge is

$$Q_{buf} = C_{buf} \cdot V_{buf} = C_{buf} \cdot V_{bias} \cdot \frac{R_{buf}}{R_{buf} + R_{term}} \tag{6.20}$$

Some time constants have been evaluated from the above mentioned and explained raw data plots. The voltage dependence is summarised in Fig. 6.18 and the energy dependence in Fig. 6.19. Dead time, length of the sensor current signal and the distance of the discharging from the recharging current peak correspond to each other. This fact is not surprising as the backplane voltage starts to recover when all excess charge carriers are drained off and therefore the sensor current signal is about to decay. Furthermore, all simulated time constants (listed in Table 6.1 on Page 64) again are dominated from the circuit parameters. So, measurement and simulation match perfectly. In particular, bias voltage dead time T_{dead}, length of sensor current signal $T(I_{sensor})$ and distance of discharging from recharging peak in buffer capacitor current signal ΔT_{buf} (compare to Fig. B.8 in the Appendix on Page 123) are exactly equal. The voltage over dielectric signal $T(V_{diel\,n})$ always is a bit longer as it decays with a much larger time constant (see Fig. 6.23 on Page 75) than the sensor current decays or the backplane voltage recovers.

The time behaviour of the measured sensor current vs. energy is shown in Fig. B.7 in the Appendix on Page 123 and its evaluation in Fig. 6.19. Less incident energy produces less charge carriers that have to be drained off. So, the current signal, whose height is always given by bias voltage and T-filter (Eq. 6.18 on the previous page), gets shorter. Furthermore, the LED pulse $T(I_{les})$ is much faster than all other signals due to the charge carrier lifetime (Section 6.6.1 on Page 80) and the electrical limitation of the bulk current. A detailed study of the dependence of the charge flowed through the bulk on the energy is given in the physics model Chapter 6.6 on Page 79.

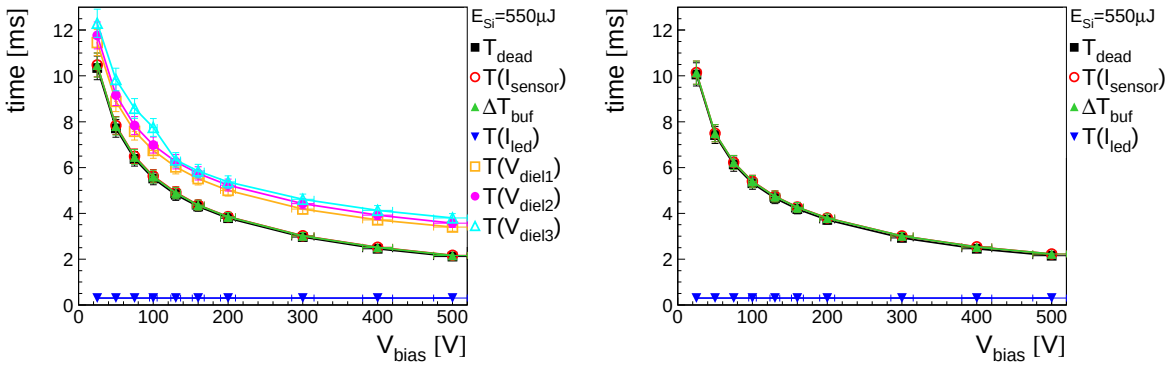

a. measurement b. SPICE simulation

Figure 6.18: Time constants vs V_{bias}. *The length of the dielectric voltage signal is missing in the simulation. All simulated time constants (listed in Table 6.1 on Page 64) again are dominated from the circuit parameters. So, measurement and simulation match perfectly. In particular, bias voltage dead time* T_{dead}*, length of sensor current signal* $T(I_{sensor})$ *and distance of discharging from recharging peak in buffer capacitor current signal* ΔT_{buf} *(compare to Fig. B.8 in the Appendix on Page 123) are exactly equal. The slight deviance to the dielectric voltage signal duration* $T(V_{diel_n})$ *are due to different peak analysis. The LED pulse duration* $T(I_{led})$ *is included for comparison.*

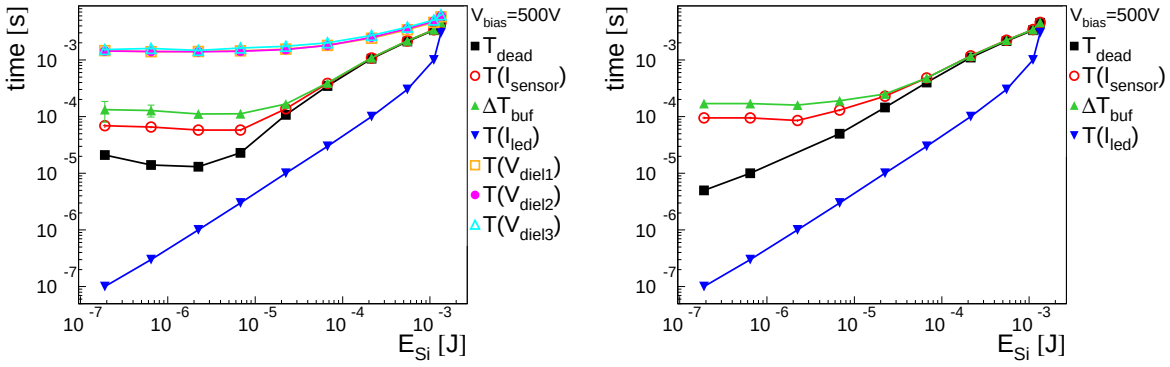

a. measurement b. SPICE simulation

Figure 6.19: Time constants vs. E_{Si}. *For detailed explanations, see the previous Fig. 6.18. There is a strong dependence of all sensor circuit related time constants* T_{dead}, $T(I_{sensor})$ *and* ΔT_{buf} *on the incident light energy. The expected linear dependence is lost at low energies due to analysis reasons. The dielectric voltage signal duration* $T(V_{diel_n})$ *is less dependent on the energy as the time constant of decay is much larger than in the previously mentioned cases (see Fig. 6.23 on Page 75) therefore dominating the signal duration.*

All simulation data presented in this section fits very well to the measurements. The reader has to remember that the SPICE model is supplied with only *two* parameters gained from measurements, namely the integrated sensor current ($\int I_{sensor}\ dt$) and the fact of permanence of the terminal voltage ($V_{term} \equiv$ const).

6.5.2 Backplane Voltage Dead Time

It has been proven in the previous chapter, that the sensor current I_{sensor} is limited by the dimensioning of the T-filter resistors. Thus, the time necessary to drain the sensor from the excess charge carriers Q can be easily derived. As seen in Fig. 6.18 and discussed there, the

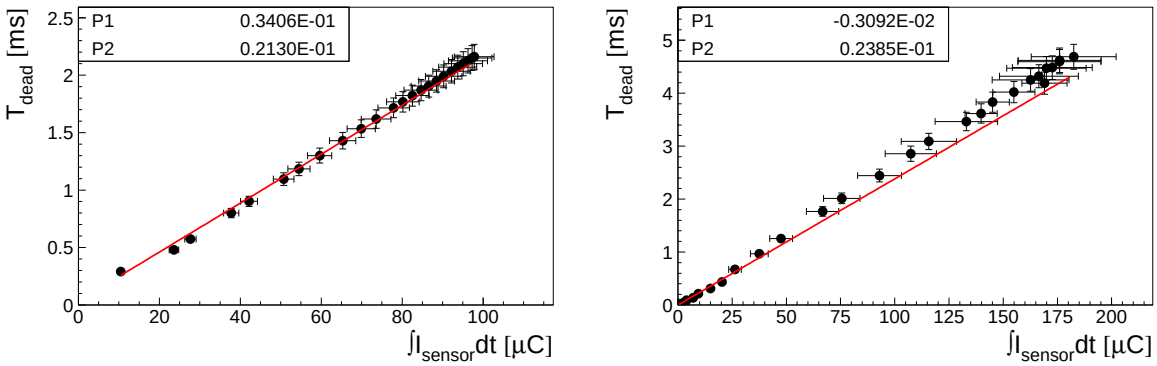

a. sensor E (LED test)

b. sensor L (laser test)

Figure 6.20: Dead time vs. total flowed charge. *Both plots show shots of different energies at a constant bias of 500V. Exceptionally, results from the laser test have been anticipated here. Their gradients (fit parameter P2) are almost equal although the pulse durations differ by orders of magnitude. This demonstrates the far independency of the system's response time of the duration of the incident light pulse.*

backplane voltage dead time T_{dead} is exactly equal to the length of the sensor current signal. This results in

$$T_{dead} = \frac{Q}{I_{sensor}} \overset{Eq.\ 6.18}{=} Q \cdot \frac{R_{Tfilter}}{V_{bias}} \overset{Eq.\ 6.19}{=} Q \cdot \frac{R_{buf} + R_{term}}{V_{bias}} \tag{6.21}$$

With $R_{Tfilter} \approx 10$ kΩ and $V_{bias} = 500$ V one obtains

$$T_{dead} = \frac{0.02ms}{\mu C} \cdot Q \tag{6.22}$$

This gradient is approximately reached in both plots in Fig. 6.20 (fit parameter P2). Equation 6.21 says that the dead time should be inverse proportional to the bias voltage at constant total charge. Unfortunately, this condition has not been reached exactly in any test even at low energies. So, an exact evaluation of this fact cannot be presented. At high energies, the total charge strongly depends on the bias voltage. Refer to Section 6.6.1 on Page 80 for more details.

6.5.3 Circuit Parameter Verification

A consistency check of the electrical model with the circuit parameters is given in this section. All T-filter components can be easily reconstructed from measurement data. The dependence of the T-filter resistors on the raw data is as follows.

$$R_{buf} = \frac{1}{T_{mid}} \int_{mid} \frac{V_{buf} - V_{bp}}{I_{sensor}}\, dt \tag{6.23}$$

$$R_{term} = \frac{1}{T_{mid}} \int_{mid} \frac{V_{term} - V_{buf}}{I_{sensor}}\, dt \tag{6.24}$$

Herewith, the resistors' values are gained from the average of their voltage drop divided by the current flowing through them. The integration is done over an interval in the middle of the sensor current signal where it is supposed to be approximately constant. Figure 6.21 shows an almost perfect reproduction of both resistor values. One has to remind, that in T-filter scans, R_{buf} always has been choosen to be four times R_{term}.

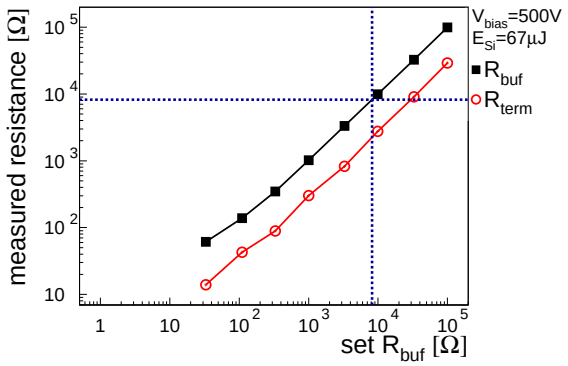

Figure 6.21: Extraction of T-filter resistances from data. *The plot shows data from a T-filter resistor scan using sensor D (high ρ). The x-axis displayes the set buffer resistance. The terminal resistance* R_{term} *always is set to a fourth of this value. The data (y-direction) shows both reconstructed resistances. The dashed line marks the CMS design value for the buffer resistor.*

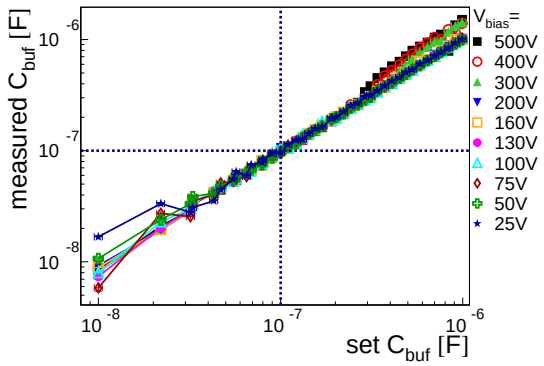

Figure 6.22: Extraction of T-filter capacitance from data. *The plot shows the results from a T-filter capacitor scan using sensor F. The x-axis displays the set buffer capacitance. The data (y-direction) shows the reconstructed values staying almost equal for various bias voltages. The dashed line marks the CMS design value for the buffer capacitor.*

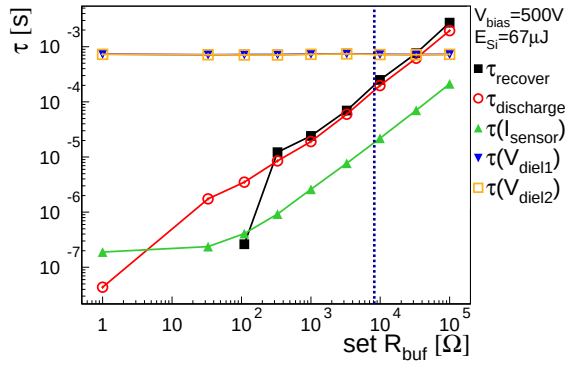

Figure 6.23: T-filter dependence of time constants. *The circuit related constants* τ_{recover}, $\tau_{\text{discharge}}$ *and* $\tau_{\text{decay,I}_{\text{sensor}}}$ *are dominated by the T-filter resistors. But the decay constant of the dielectric voltage is independent of them.*
The data has been obtained from the T-filter scan of sensor D (Fig. 6.21). The dashed line marks the CMS design value for the buffer resistor.

The buffer capacitance is calculated from its (partial) discharge ($Q_{\text{discharge}}$) at the beginning of backplane voltage breakdown and the voltage loss ($V_{\text{bias}} - V_{\text{buf}}$) due to its discharge. The capacitance then results from its defining relation C = Q/U.

$$C_{buf} = \frac{Q_{discharge}}{V_{bias} - V_{buf}} \tag{6.25}$$

The result is displayed in Fig. 6.22 and proves a nice reproduction of this value even at different bias voltages.

A sample of time constants and their dependency on the T-filter resistors is presented in Fig. 6.23. The time constants of the backplane voltage recovery (τ_{recover}) and the decay constant of the buffer capacitor's discharching current ($\tau_{\text{discharge}}$) being almostly equal are dominated by the RC-element composed of the T-filter. The capacitor is discharged over the parallel circuit of both resistors. This results in a time constant of

$$\tau_{recover,discharge} = C_{buf} \cdot R_{buf} || R_{term} = \frac{C_{buf}}{1/R_{term} + 1/R_{buf}} \tag{6.26}$$

With a capacitance of $C_{\text{buf}} = 100\text{nF}$, and the known relation between R_{buf} and R_{term}, both time constants could be observed in data.

The sensor current decay time constant also is dominated by the T-filter resistors, but its quantity is not understood yet. A discussion on this can be found in the physics model chapter in Section 6.6.3 on Page 82.

The dielectric voltage's time decay constants ($\tau\{V_{diel\,n}\}$) can be understood assuming that the coupling capacitors ($C_c = 500pF$) are discharged over the parallel circuit of poly silicon resistor ($R_{poly} = 1.76M\Omega$) and measurement resistor ($R_{meas} = 2M\Omega$). This results in $\tau\{V_{diel\,n}\} = 470\mu s$ fitting approximately to the measured value of $720\mu s$ plotted in Fig. 6.23 on the previous page. The discrepancy can be explained with the assumption, that other discharching effects overlay the described one, so that the decay cannot be expressed by a pure exponential function. But there is no dependence on T-filter and bias voltage, as expected. Tests with other sensors having different values of poly silicon resistors, show an appropriate behaviour in dielectric voltage decay.

6.5.4 Impact of Power Supply

6.5.4.1 Terminal Voltage

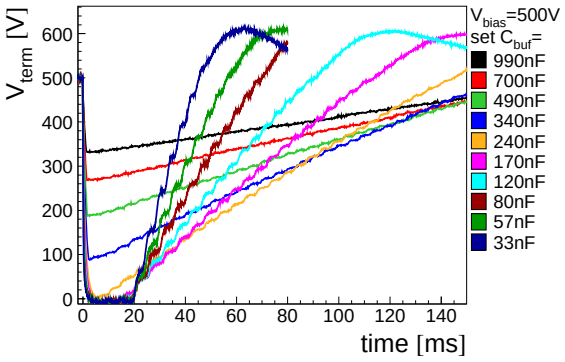

Figure 6.24: Terminal voltage with CAEN high voltage supply. *This data has been taken from the buffer capacitance scan of sensor F at a bias voltage of 500V. Above 240nF ($\approx 100 \times C_{Sensor}$), the capacitor provides enough charge to avoid a complete breakdown. Compare this to the CMS design value for the buffer capacitance of 100nF.*

The terminal voltage of the sensor circuit is an indicator of the power supplies regulation behaviour in case of a short-circuit. As mentioned before, almost all tests have been done with the Oltronix power supply, keeping the terminal voltage constant at any bias voltage value and any incident pulse energy (Fig. B.1 in the Appendix on Page 122). This can be regarded as the worst case scenario for sensor and circuit components. And as described in Section 6.2.6 on Page 62, it simplifies much the modelling of such a circuit.

On the other hand, during the first tests and for all capacitance scans, an other high voltage supply (manufactured by CAEN) has been used. Its maximum rated constant current of 1mA at 500V is far below the specified value of 300mA for the Oltronix device. This leads to a complete different short-circuit behaviour, displayed in Fig. 6.24. The plot shows the terminal voltage vs. time at 500V and a pulse energy of about $550\mu J$ for several buffer capacitances between 30nF and $1\mu F$. The normal buffer capacitance of 100nF is not sufficient to avoid a complete breakdown.

6.5.4.2 Influence on Sensor Parameters

Terminal voltage breakdown and the regulation characteristic afterwards, also seen in Fig. 6.24 as increasing and slightly oscillating signal, has significant influence on the sensors behaviour and all related voltages and currents. Figure 6.25 on Page 78 demonstrates the differences between the two high voltage supplies seen in data. All shots had an energy of about $500\mu J$

and were done at a bias voltage of 500V. The standard buffer capacitance of 100nF and a preliminary T-filter of $R_{buf} = 3.3k\Omega$, $R_{term} = 1k\Omega$ has been used during all tests.

The backplane voltage deadtime and recovery time are much longer with the CAEN device (Fig. 6.25a on the next page). But there is an overshoot (not shown) after voltage recovery starting at about 100ms and lasting for several ms coming from the voltage regulation characteristic. Fortunately, this overshoot is only about 20% at a maximum bias of 500V, seen in Fig. 6.24, and therefore will not endanger the sensor. On the other hand, it is unprobable, that devices with such a short-circuit regulation characteristic will be used in the experiment. The specification for CMS high voltage supplies [FP04] does not give any hint on the regulation details of the demanded short-circuit protection.

The shape of the backplane voltage and the duration of its breakdown have a direct influence on dielectric voltage and bulk current. Figures 6.25c and 6.25e show a complete different behaviour. This makes it impossible to apply the simple electrical model on runs, where an other than the Oltronix supply has been used.

Some evaluated values are displayed in Figs. 6.25b, 6.25d and 6.25f all showing the results from shots at an energy of about $500\mu J$. The flowed charge significantly is reduced, when the CAEN supply is used. This can be understood considering that a few charges are delivered by the voltage supply at the beginning of the breakdown phase (fig 6.25e). Most of the charge has to be provided by the T-filter capacitor. But this is not enough to drain off the total charge (Fig. 6.25b). Nevertheless, the maximum dielectric voltage (Fig. 6.25d) does not depend on the used power supply. The large differences come from different bulk resistivities. This issue is discussed in Section 6.6.5 on Page 84. The maximum sensor current (Fig. 6.25f on the next page) also shows no significant deviation with respect to different tests. This is due to the fact that the current is limited by the T-filter resistors and can be provided also for a short period of time from the discharging of the buffer capacitor, when the CAEN supply is used.

One can conclude that the exposure to a sensors is independent of the used high voltage supply. The Oltronix keeps the terminal voltage constant even in the short-circuit case, applying the maximum voltage to the sensor circuit and therefore stressing its components or the sensor. The CAEN supply voltage breaks immediately but has remarkable overshoots at recovery. However so far, after hundreds of shots, there is no evidence on any damage to sensor or componentes whichever voltage supply is used.

6.5.4.3 Electrical Energy Dissipation

The electrical energy dissipated by the sensor, its circuit and its components depend on the voltage source and the capacitive load on the high voltage line. All relevant formulas are listed in Table 6.2 on Page 65. The total energy flowing through the device during a shot comes from two sources, the power supply and the buffer capacitor. When using a power supply (Fig. 6.26a on Page 79), the fraction coming from the buffer capacitor (E_{buf} in the plot) is low. Thus, most of the energy is delivered by the voltage source. This assumption fits nicely with the simple model of the sensor current given for the Oltronix power supply in Section 6.5.1 on Page 70 and Eq. 6.18 on Page 71. The terminal voltage stays constant and the sensor current is defined by the T-filter resistors. Then, the total dissipated energy is as follows.

$$E_{total} \approx \frac{{V_{bias}}^2}{R_{Tfilter}} \cdot T_{\text{length}} \overset{Eq.\ 6.21}{\approx} Q_{sensor} \cdot V_{bias} \tag{6.27}$$

This formula represents exactly the voltage definition. E is the energy loss the flowed charge experiences when travelling from circuit terminal to ground. The increase in Fig. 6.26a on

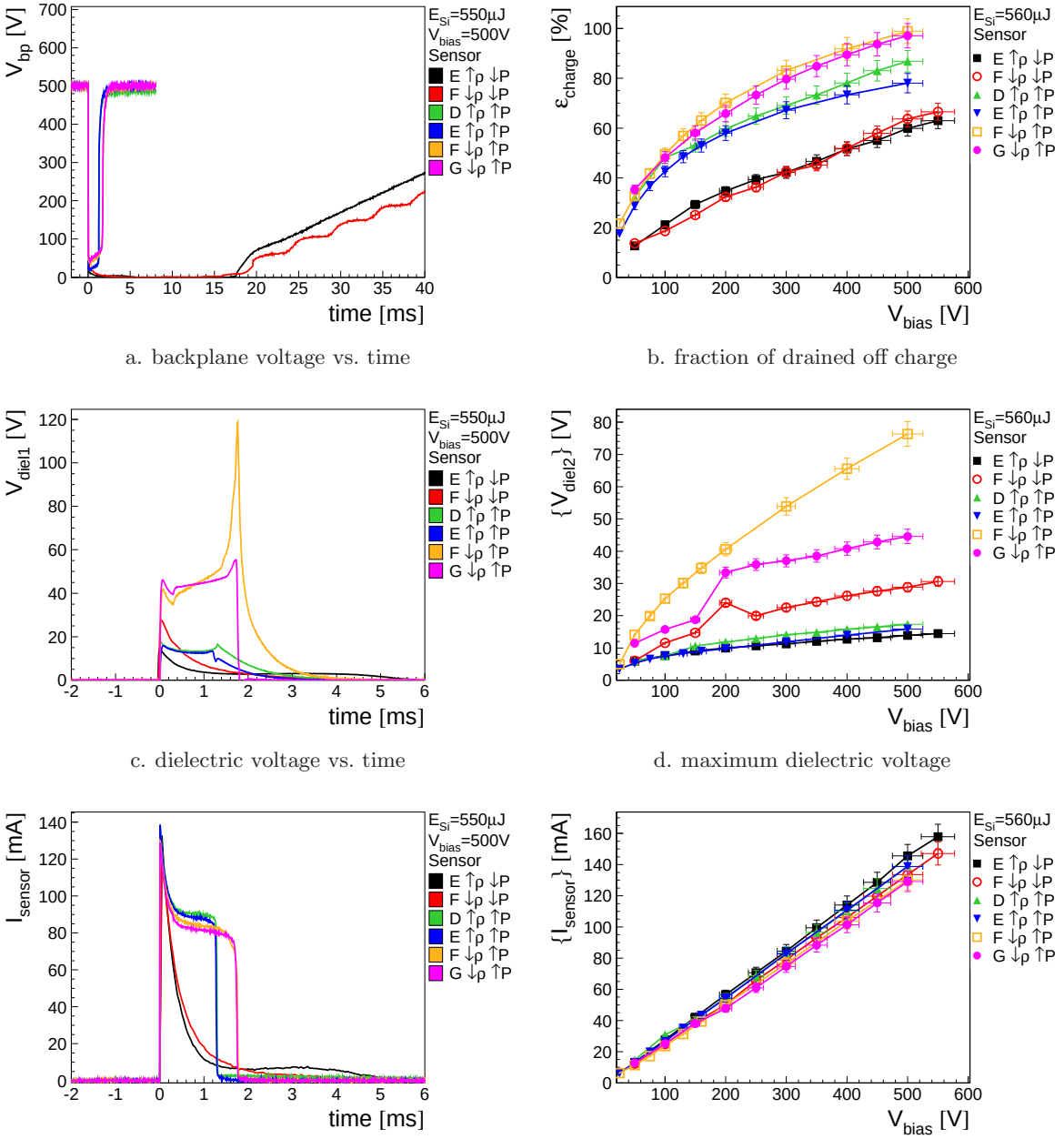

a. backplane voltage vs. time

b. fraction of drained off charge

c. dielectric voltage vs. time

d. maximum dielectric voltage

e. sensor current vs. time

f. maximum sensor current

Figure 6.25: Data taken with different power supplies. *The sensors marked with ↑ P (high power) were tested using the Oltronix high power supply, whereas the other two ones, marked with ↓ P (low power), were biased by a CAEN high voltage supply. The time behaviour of all measured parameters (Figs. a, c and e) differ very, as the CAEN supply starts regulation not until all charge carriers are drained off. The backplane voltage recovers completely not before 100ms (Fig. a). Low resistivity sensors are marked with ↓ ρ and such ones with a high resistivity with ↑ ρ.*

Page 79 is steeper than a straight line as the flowed charge also depends on the bias voltage. See Section 6.6.1 on Page 80 for more details.

When using a low power supply (Fig. 6.26b), the total energy is less than in the latter case, and as expected, it is almost completely provided by the buffer capacitor, that is loaded

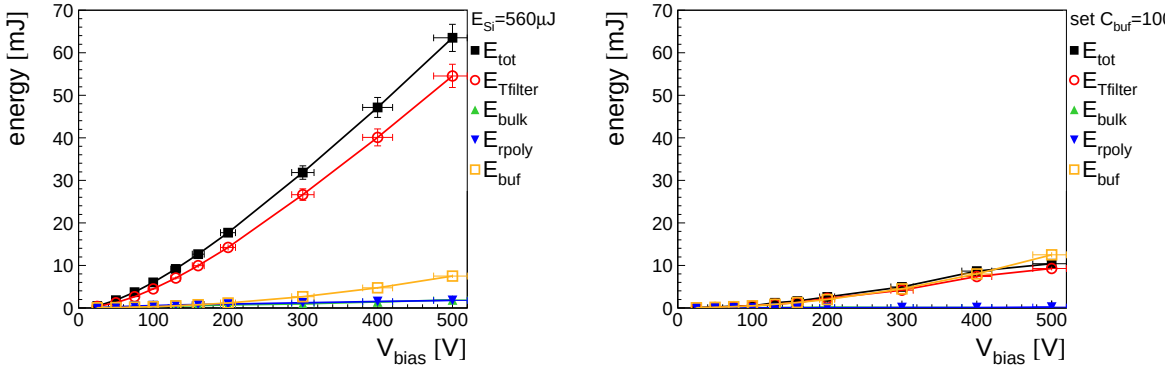

a. Oltronix power supply

b. CAEN high voltage supply

Figure 6.26: Electrical energy dissipation with different voltage supplies. *The total energy dissipation of the device* E_{tot} *is compared to the dissipation of different parts of sensor* (E_{bulk}, E_{rpoly}) *and circuit* ($E_{Tfilter}$, E_{buf}). *Both tests have been done with the same sensor F, the same T-filter* ($R_{term} = 1k\Omega$, $R_{buf} = 3.3k\Omega$, $C_{buf} = 100nF$), *and the same energy per shot of* $550\mu J$ *but different power supplies. The Oltronix power supply delivers most of the energy (Fig.* a) *while the energy at most is provided by the buffer capacitor when using a low power supply (Fig.* b).

by the power supply.

The protection of the sensor by the T-filter resistors is proven also for the energetic point of view. Almost all energy is absorbed by them in both cases. The energy flowing through the poly silicon resistors is neglectible and thus non destructive. Furthermore, the energy conservation relation is valid. Small deviations from this equation seen in data are caused by minor simplifications in the energy calculations.

$$E_{total} \approx E_{Tfilter} + E_{bulk} + E_{R_{poly}} \tag{6.28}$$

6.6 Physical Model of measured Sensor Parameters

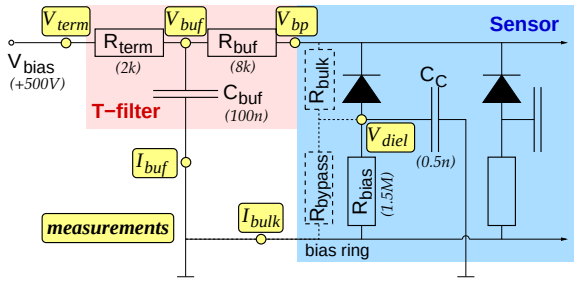

Figure 6.27: Equivalent circuit of a silicon sensor and its electical components. *Although the physical modelling of a sensor and its electrical circuit can be reduced to the discussion of only two measured parameters (see text), this values also strongly depend on the dimensioning of the circuit. The equivalent bulk resistor and the resistor bypassing the* R_{bias} *(dashed) represent a simple model for the whole sensor during voltage breakdown:* $R_{sensor} = R_{bulk} + R_{bypass}$. *The proof of the latter one is given in Section 6.6.4 on Page 83.*

All measured and calculated parameters (see Tables 6.1 on Page 64 and 6.2 on Page 65) depend on each other and on the sensor circuit dimensioning. But only two parameters are sufficient to explain the behaviour of the other parameters, so that the physical modelling of a sensor and its electrical circuit can be reduced to the discussion of those two measured parameters: The collected (or drained off/total/flowed) charge ($\int I_{sensor}\, dt$) and the dielectric voltage (V_{diel}). The collected charge is - together with the sensor setup - the only input parameter for the simulation of the whole device (Sections 6.2.6 on Page 62 and 6.5.1 on

Page 70). The dielectric voltage is not considered in the simulation and explained widely independently of the sensor circuit.

A *qualitative* physical model tries to explain the dependence of the collected charge on the bulk field resp. bulk voltage and the deposed energy. This leads to a better understanding of the fraction of drained off charge. The sensor current decay, starting after the light is switched off, is shown and compared with models presented in textbooks. The behaviour of both items total charge and sensor current decay cannot be studied *quantitatively* with the used setup. The reason for this is, that an equilibrium state - strongly necessary for such studies - has not been reached during any measurement.

Finally, the impact of the bulk resistivity, which determines the depletion voltage, is described. This knowledge provides explanations of differences in behaviour between low and high resistivity sensors hence having very different depletion voltages.

6.6.1 Flowed Charge vs. Bulk Field and Energy

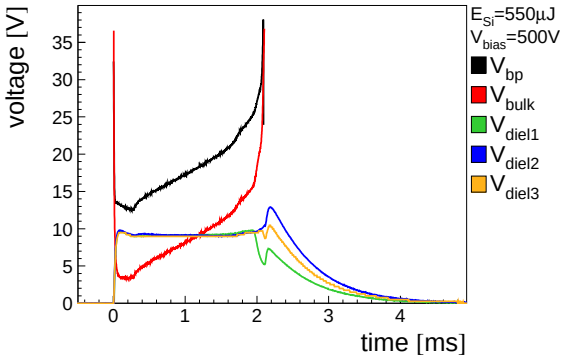

Figure 6.28: Raw data sample of different voltages. *A focus on backplane (V_{bp}) and bulk voltage ($V_{bulk} = V_{bp} - V_{diel}$) is shown here as well as the comparison to the voltages over the dielectric layer (V_{diel}). V_{bp} and V_{bulk} reach the value of 500V before t=0 and after recovery but are cut here at a level of 35V.*

An overview of recombination processes is given in Section 2.4.4 on Page 28 and a detailed discussion of the impact of an electrical field to recombination rates in [Lan91]. Unfortunately, the ideal model described there is not applicable in the present case. Figure 6.28 shows, that the estimated voltage drop over the silicon bulk respectively the electrical field are not constant during dead time. The same is true for the backplane voltage seen in the same figure. Both plots lead to the conclusion, that a simple analytical calculation of field dependent capture and emission of charge carriers (see [Lan91]) is not possible. The reason is, that no equilibrium between charge carrier creation and recombination is reached due to the limitation of the bulk current. Relatively short light pulses of 100ns up to some 100μs face a long phase (some ms) of charge carrier drain off. During this phase, the charge carrier concentration decreases, the resistivity increases and therefore the voltage drop over the bulk. A proof of the electrical limitation of the sensor current is given in Section 6.5.1 on Page 70.

Nevertheless, the dependencies of the flowed charge can be understood qualitatively. Figure 6.29a shows, that at higher energies, the collected charge increases with the bias voltage resp. the remaining bulk field. A higher field prevents more electron-hole pairs (EHPs) from recombining. They are then available for charge transport and photoconductivity. An introduction into this topic (photoconductivity under ideal resp. equilibrium conditions) is given in Section 2.4.3 on Page 27. Figure 6.29a gives reason to the assumption that an analytical expression for the voltage dependence of the charge flowed through the sensor Q_{sensor} can be found. In a double logarithmic scale, all graphs are straight lines. This gives

$$Q_{sensor} = (k\ V_{bias})^p \ with\ p \in [0, 1) \tag{6.29}$$

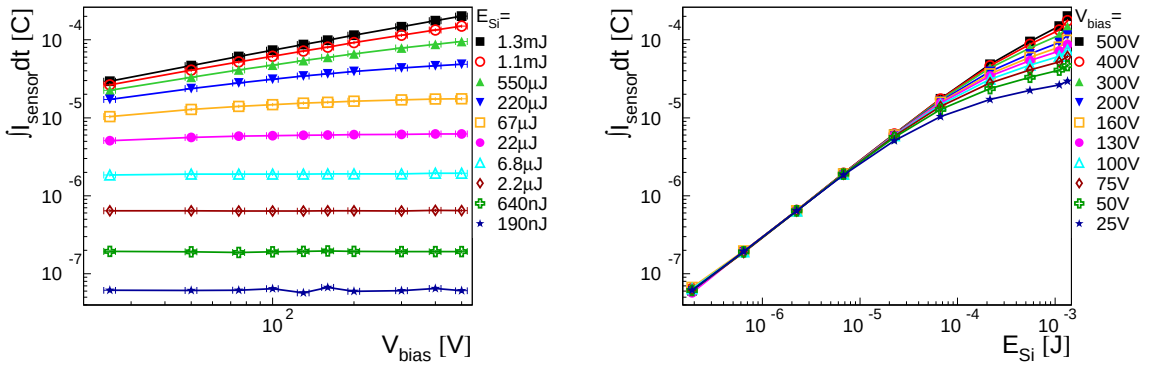

a. Flowed charge vs. V_{bias}

b. Flowed charge vs. E_{Si}

Figure 6.29: Flowed charge. *The high ρ sensor E received the standard scan under optimal conditions (official T-filter: $8k\Omega, 2.2k\Omega, 100nF$, Oltronix power supply, no current-meter in HV line). The total integrated charge flowed through the bulk during and after the shot is displayed vs. bias voltage (V_{bias}) and energy per shot (E_{Si}). Both plots show the same data in transposed protraction to disentangle the dependency of the charge on the two mentioned parameters.*

where k is a constant with an adequate unit and p is the dimensionless exponent. The reason for this behaviour is not understood and cannot be reproduced in all tests.

The charge depends on the energy over a large range as expected (Fig. 6.29b). The amount of generated EHPs is proportional to the incident energy. Up to about 10^{-4}J all charge carriers are drained off. From then on, the limited sensor current is not capable to drain them off before they recombine. So, a saturation effect becomes visible.

6.6.2 Discussion on drained off Charge Fraction

As seen in the previous chapter, not all created charge carriers are drained off as some of them recombine. The amount of the drained off charge is one of the measures for the electrical stress a sensor and its circuit suffer from during and after the shot. In particular, the fraction of created and drained off charge carriers at large shot energies gives information on the sensibility of the sensor under such abnormal conditions. One has to consider, that the following discussion does not reflect the reality of normal sensor operation. The sensors are not designed to be exposed to such a large amount of incident (light) energy within such short time periods!

As the quantum efficiency is 0.3 at 1050nm (1.18eV), it is assumed, that for the creation of an EHP 3.3 photons are needed in average and thus an absorbed light energy of 3.9eV. If the EHP does not recombine and is separated by the remaining electrical field and drained off, it contributes to the flowed charge Q_{sensor}. So, it is a direct measure of the detected light. This concludes to the definition of the drained off charge fraction ϵ_{charge}: It is the fraction of detected to incident light energy being equivalent to the fraction of created and drained off charge carriers.

$$\epsilon_{charge} = \frac{Q_{sensor} \cdot 3.9V}{E_{Si}} \tag{6.30}$$

Incomplete charge collection always is caused by recombination. There are two reasons leading to this.

First, a sensor is not capable to detect the whole incident light when it is not fully depleted. Figure 6.30b on the next page demonstrates this fact. The drained off charge fraction is near

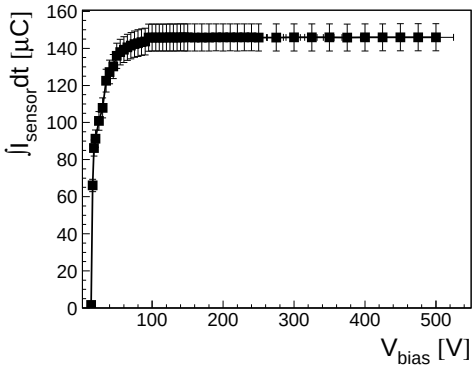

a. charge without T-filter

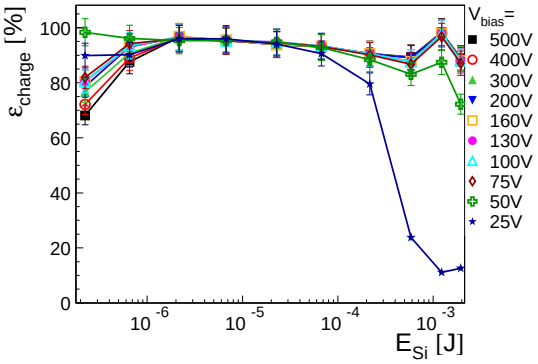

b. charge fraction without T-filter

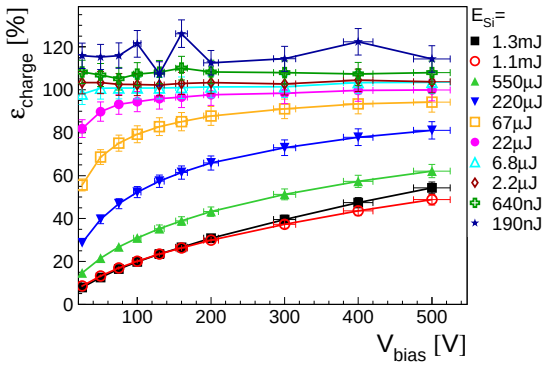

c. charge fraction with T-filter

Figure 6.30: Drained off charge fraction measured with and without T-filter resistors. *Figures a and b show results from sensor D and Fig. c from the standard test of sensor E (both high ρ). Almost the total charge is drained off, when the sensor is over-depleted. Unfortunately, the correct charge fraction could not be evaluated for Fig. a due to calibration problems, so that the total flowed charge is shown instead. The fraction in plot c is above 100% for low energies due to systematical energy calibration problems, that haven't been evaluated and considered during error calculation. Errors shown in all plots are of statistical nature.*

100% at lower deposited energies and decreases with higher energies at voltages below full depletion.

The second reason is the limitation of the sensor current by the T-filter resistors. The higher the resistance the lower the sensor current. Charge carriers recombine before being drained off. Figure 6.30c shows results from a test with the use of nominal T-filter resistors. A smaller fraction of the charge is drained off at medial and larger energies for *all* voltages, not only at those below full depletion, as it has been the case without T-filter. Figure 6.31a demonstrates the fraction of the drained off charge decreasing with larger T-filter resistances at high energies.

When increasing the buffer capacitance, the collected charge gains (Fig. 6.31b). The power supply used in this test has a weak buffering and a very careful regulation behaviour in case of a short-circuit. That means, that the high voltage *at the terminal* breaks down immediately, and the bias voltage buffering mainly is done by the T-filter capacitor.

6.6.3 Sensor Current Decay

The time dynamics of an ideal photo conductor with a defined relaxation of conductivity when light is switched on and off and an equilibrium at constant illumination [See02] could not be reproduced. There are several reasons disturbing the ideal behaviour of a semiconductor crystal irradiated with light.

First of all, a CMS silicon sensor is no pure photo conductor at all. With its p-n-junction,

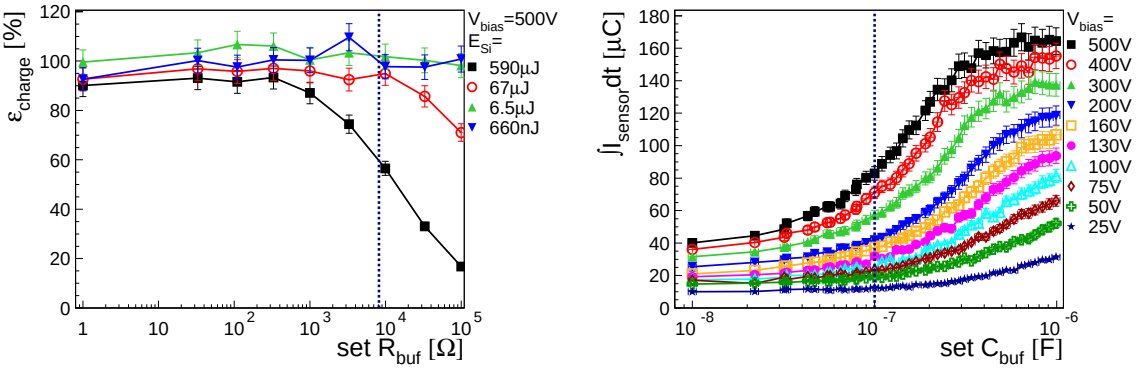

a. charge fraction vs. R_{buf}

b. drained-off charge vs. C_{buf}

Figure 6.31: Charge fraction scan over T-filter components. *The plots show measurements done with sensor D (Fig. a) and sensor F (Fig. b). Energy calibration failed in the latter case so that the collected charge is presented instead. The total created charge is drained off at lower resistances even for large incident light energies. A larger T-filter capacitance bufferes the high voltage and therefore improves charge carrier drain-off. The dashed lines mark the CMS design values for buffer resistor and buffer capacitor respectively.*

it behaves like a photo diode! Next, the T-filter in the HV line contains a capacitor that is partially discharged at voltage breakdown and recharged at voltage recovery. The time constant of the re-charging depends on the T-filter capacitance and resistances and dominates the sensor current decay as well as the bias voltage recovery dynamics. But both are needed to calculate the time dependence of the photo conductivity. The knowledge of its decay time constant would allow conclusions on the quantum yield, the incident light power or the photo generated charge carrier concentration. Figure 6.23 on Page 75 shows the data obtained from the T-filter scan of sensor D (high ρ) and proves the dominance of the T-filter on the sensor current decay constant. This fact also is seen in Fig. B.6 in the Appendix on Page 123. The measured sensor current signal with the simple circuit simulation is compared there. The simulation data shows the same decay behaviour.

A further argument of the non-applicability of the simple photo conductivity model is the large intensity of the incident light. An equilibrium of charge carrier creation and recombination respectively drain-off has not been reached at any time due to saturation effects, and even more important, the pulse intensity is not stable. The pulse power starts decreasing instantaneously in the way the buffer capacitors on the LED array are discharged.

6.6.4 Poly Silicon Resistor Current

An estimation of the current flowing through all poly silicon (bias) resistors is given in Section 5.4.3 on Page 49 but repeated here. The current through a poly silicon resistor is defined by its value and its voltage drop, that is the p^+-potential resp. voltage over the dielectric layer.

$$I_{R_{poly,i}} = \frac{V_{diel,i}}{R_{poly,i}} \tag{6.31}$$

This equation is true, because the bias current return line resistor has not been considered on any sensor circuit in this test. The total poly resistor current is then the sum over the

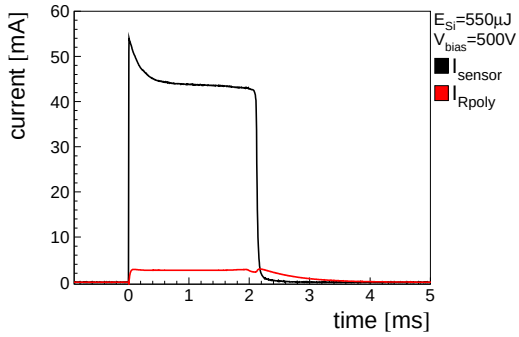

Figure 6.32: Comparison of sensor current with poly silicon (bias) resistor current. I_{Rpoly} *is an estimation gained from the measured dielectric voltage and is limited by the poly silicon resistors* R_{poly} *and therefore much smaller than the total sensor current* I_{sensor}. *The data comes from the standard test of sensor E.*

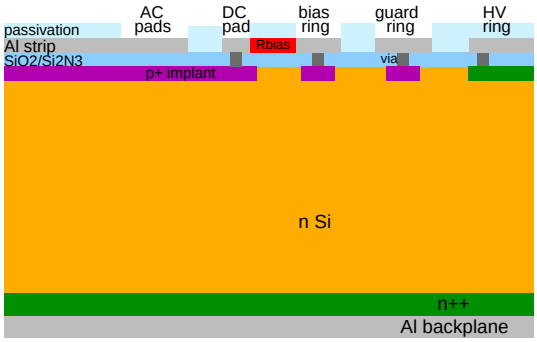

Figure 6.33: Sidelong view of a sensor. *There are possibilities for the current to bypass the poly silicon resistors. While the bulk is* short-circuited, *charges can for example directly flow from the HV ring to bias ring implant and bias ring or underneath the bias resistors from the DC pad to the bias ring.*

currents through all 512 resistors. Their values are approximately equal.

$$I_{R_{poly}} = \sum_{i=1}^{512} I_{R_{poly,i}} \approx 512 \cdot \frac{V_{diel}}{R_{poly}} \tag{6.32}$$

The dielectric voltage is measured and the result of this calculation is presented in Fig. 6.32. In the same plot, a comparison to the measured sensor current shows a large discrepany. There is a large leak of current. The sensor current is not totally explainable with the current flowing through the poly resistors. Figure 6.33 allows the explanation of some effects occuring during the short-circuit of the silicon bulk: The edge of the sensor allows a bypass of the poly resistors. The appropriate equivalent resistor within the scope of the simple model is called R_{bypass} in Fig. 6.27 on Page 79. *Most* of the current chooses the way of minimum resistance and therefore flows from the HV ring through the bulk directly to the bias ring implant and from there on to ground. This is the reason why the sensor current really is dominated by the T-filter resistors and why the sensor can be considered as short-circuited.

In normal sensor operation, the total resistance of a sensor and its circuit is by far dominated from the silicon bulk (several 100MΩ) and not from the parallel circuit of all poly resistors (some kΩ). So, normally there is only a neglectible fraction of the current bypassing them.

6.6.5 Impact of Bulk Resistivity

The resistivity ρ of the n-doped silicon bulk is directly related to the depletion voltage V_d via Eq. 2.10 on Page 26. Assuming a dielectric constant of $\epsilon_r = 11.9$, a mobility of $\mu_n = 1450\ cm^2/Vs$ (n-dominated conduction before irradiation) and a thickness of $D = 500\mu m$ for all sensors used in this test, one obtains the resistivity from the (measured) depletion voltage by means of the following equation.

$$\rho(V_d) = \frac{D^2}{2V_d\epsilon_0\epsilon_r\mu_n} = \frac{820\ k\Omega cm}{V_d/Volts} \tag{6.33}$$

There are significant differences in the depletion voltages seen during pre- and postqualification (Table E.1 in the Appendix on Page 131). According to Eq. 6.33, a typical pre-series depletion

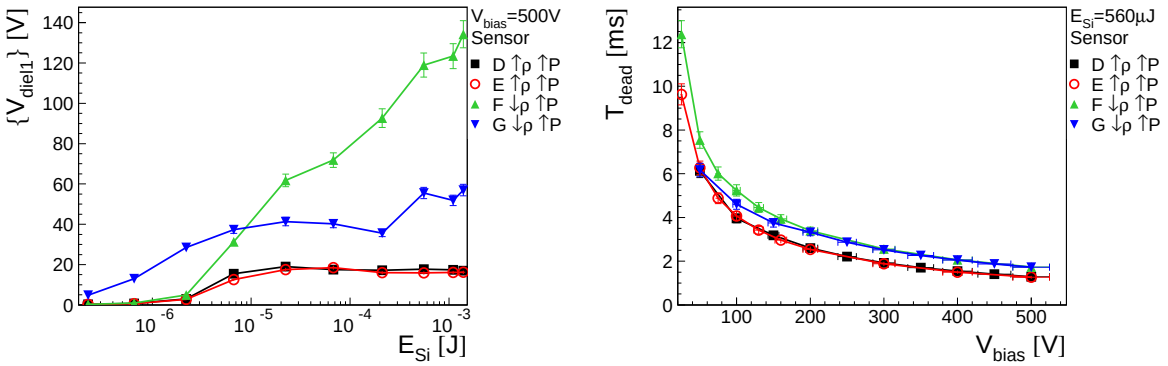

a. dielectric voltage vs. E_{Si}

b. bias voltage dead time vs. V_{bias}

Figure 6.34: Bulk resistivity dependence of test results. *Some results obtained from two high resistivity sensors (D and E, marked with ↑ ρ) and from two ones with low resistivity (F and G, ↓ ρ) are compared to each other. The four tests have been performed under same conditions (preliminary T-filter: 3.3kΩ, 1kΩ and Oltronix power supply). The dielectric voltage (Fig. a) is critical for pinhole creation and therefore from great importance in this comparison: low ρ sensors are affected most! The bias voltage deadtime (Fig. b) is shown here to demonstrate the effect of the resistivity to the* electrical *behaviour of the sensor's circuit.*

voltage of 40V corresponds to a very high resistivity of 20.5kΩcm far above specification, and 150V complies with 5.5kΩcm being in the specification of $3.5 - 7.5$kΩcm for the outermost modules in the tracker tested here (Section 3.1 on Page 30). Low resistivity changes the field configuration of the sensor and the distribution of voltage drops over the different sensor components. The bulk voltage will be lower causing the voltage over the dielectric layer to increase. On this basis, some effects are understood *qualitatively*. But only sensor simulations would enable a *quantitative* investigation of this problem.

The expected excess dielectric voltage for low resistivity sensors is obvious as seen in Fig. 6.34a. This is potentially destructive for the dielectric layer. Furthermore, the dielectric voltage is limited at large pulse energies *only* for high resistivity sensors. This is critical for low resistivity sensors under the present condition of too small T-filter resistors (3.3kΩ,1kΩ). Using the official one reduces the peak voltage far below 120V.

There are deeper studies on the endangerment of this critical part of the sensor in Section 6.7 and within the scope of the laser test.

A lower resistivity resp. higher conductivity leads to a better charge collection. With an almost equal sensor current, the time necessary to collect the separated charge carrier pairs is longer for low-ρ sensors (Fig. 6.34b).

6.7 Robustness Tests

Tests with modified T-filter resistors and capacitors have been done to obtain knowledge on the damage mechanisms to a sensor and its components. The damage threshold for the finally used module design has been determined within the scope of the laser test (Section 7.6 on Page 103).

6.7.1 Dielectric Voltage

The dielectric layer enabling the capacitive signal coupling is the most sensitive part of the sensor. The silicon dioxide layer has a thickness in the order of several 100nm and must stand a voltage of up to 120V. During normal operation at a bias voltage of 500V and using the official T-filter with the following dimensions

$$R_{buf} = 9\ k\Omega,\ R_{term} = 2.2\ k\Omega,\ C_{buf} = 100nF$$

the maximum voltage drop over the dielectric layer after a high intensive IR light shot is about 10V for a high resistivity sensor (Fig. 6.13a on Page 69). As the sensor current and some of the time constants mostly are defined by the T-filter resistors, it is mandatory to study the effect of a modified T-filter on the dielectric voltage. The results of this evaluation are

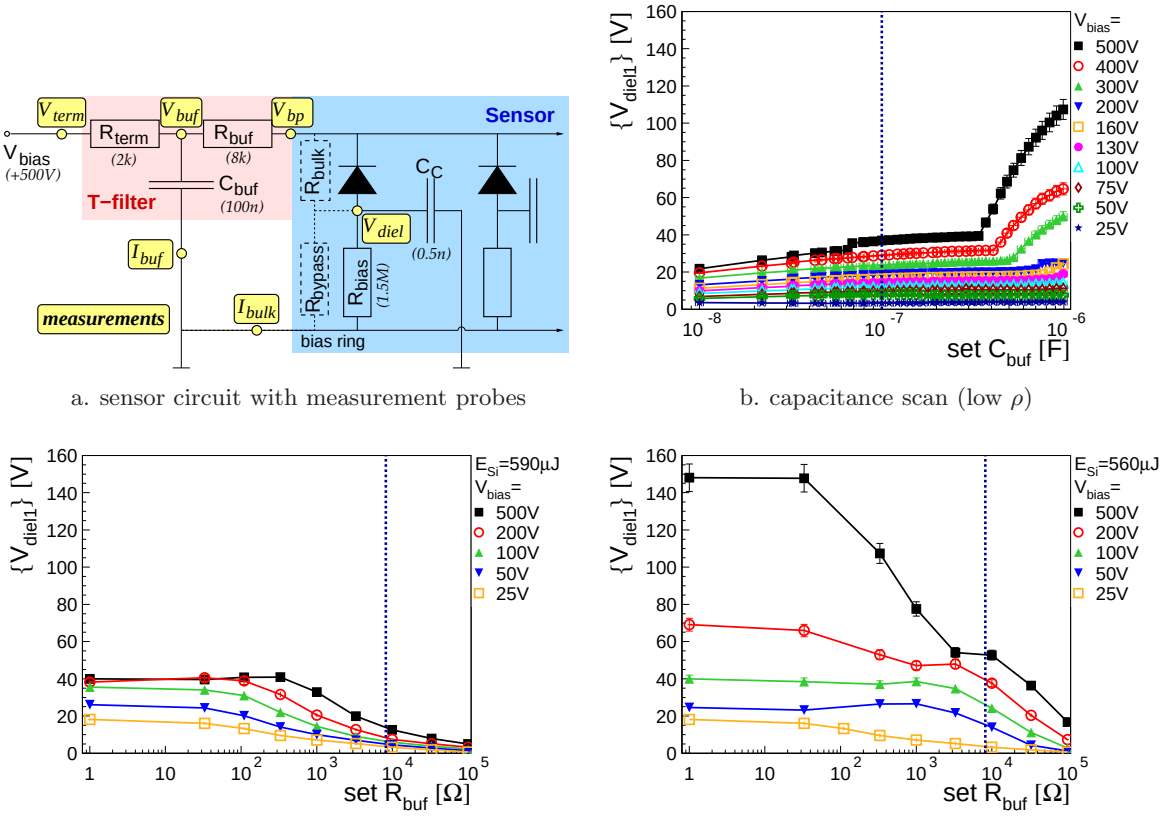

a. sensor circuit with measurement probes

b. capacitance scan (low ρ)

c. resistance scan (high ρ)

d. resistance scan (low ρ)

Figure 6.35: Endangerment of dielectric layer when modifying T-filter. *The schematic of the sensor circuit with T-filter and measurement probes is repeated here (Fig. a). Two resistors scans have been performed, one with a low-ρ (G) and the other with a high-ρ (D) sensor. The only capacitance scan has been done with an other low-ρ sensor (F). The dielectric layer of a low-ρ sensor is endangered when reducing the T-filter's resistances (Fig. d) and increasing the capacitances (Fig. b), but not so for a high-ρ sensor (Fig. c). The dielectric voltage does not exceed 40V. The dashed lines in the plots mark the CMS design values for buffer resistor and buffer capacitor respectively.*

summarised in Fig. 6.35. Figures 6.35c and 6.35d compare the dielectric voltage behaviour when modifying the T-filter resistances between a low-ρ and high-ρ sensor. Both plots show an increase with reduced resistance. But only in the low-ρ case, the voltage exceeds the critical level of 120V when going below 100Ω. The increased dielectric voltage of low-ρ sensors in

comparison to high-ρ sensors already has been understood in Section 6.6.5 on Page 84. But the shown dependence on the resistance will be explained in the following Section 6.7.2. The consequences of those tests at maximum load on the sensor's quality are shown in the qualification Chapter 6.10 on Page 92. Figure 6.35b proves an endangerment of the dielectric layer when increasing the buffer capacitance up to 1μF. The T-filter used in this test had the preliminary dimensioning of

$$R_{buf} = 3.3\ k\Omega,\ R_{term} = 1\ k\Omega,\ C_{buf} = 100nF$$

The CAEN high voltage supply has almost no output buffer. But a setup with the CAEN supply and an *increased* buffer capacitance should behave similar to a setup with a *normal* capacitor and a well buffered power supply. Such a test with the Oltronix power supply and the same T-filter resistors has been done. The result shown in Fig. 6.34a on Page 85 shows, that the dielectric voltage of sensor F reaches 120V at a pulse energy of 500μJ and a bias voltage of 500V. During the previously described capacitance scan of the same sensor F done with a hardly buffered high voltage device (CAEN), approximately the same dielectric voltage of 110V is reached at a bias voltage of 500V and the same shot energy using the *tenfold* buffer capacitance of 1μF.

6.7.2 Sensor Protection

The guess, that the two T-filter resistors protect the sensor, is proven in Fig. 6.36 on the next page. In Fig. 6.36a, increased resistances capture ($\mathrm{V_{Tfilter}}$) most of the bias voltage. The remaining backplane voltage ($\mathrm{V_{dead} = V_{backplane} = V_{sensor}}$) decreases accordingly to a value near zero. A small part of this remainder is responsible for the dielectric voltage drop ($\mathrm{V_{diel,}}_n$). The other part ($\mathrm{V_{bulk}}$) drops over the sensor's bulk. So, one obtains

$$V_{bias} \approx \underbrace{V_{term} + V_{buf}}_{V_{Tfilter}} + \underbrace{V_{bulk} + V_{diel}}_{V_{sensor}} \tag{6.34}$$

$$\Rightarrow R_{total} \approx \underbrace{R_{term} + R_{buf}}_{R_{Tfilter}} + \underbrace{R_{bulk} + R_{bypass}}_{R_{sensor}} \tag{6.35}$$

This voltage and resistor cascade is best illustrated with the sensor circuit schematic in Fig. 6.35a. Reduced resistances caused increased currents flowing through sensor and circuit components (Fig. 6.36b): maximum ($\{\mathrm{I_{sensor}}\}$) and mean ($<\mathrm{I_{sensor}}>$) sensor current, peak currents of buffer capacitor discharging ($\{\mathrm{I_{discharge}}\}$) and recharging $\{\mathrm{I_{recharge}}\}$. Below a buffer resistance of about 300Ω, all currents saturate at some 100mA due to the finite bulk resistance $\mathrm{R_{bulk}}$ of several 100Ω in short-circuited state (compare to Fig. 6.35a). For the exact definition and calculation of all values described here, see Table 6.1 on Page 64. The time needed to drain off all charge carriers (sensor current signal duration $\mathrm{T(I_{sensor})}$) increases with the T-filter resistance (Fig. 6.36c) as the average sensor current is reduced: $\mathrm{T \approx Q_{sensor}/I_{sensor}}$. All other signal durations (bias voltage dead time $\mathrm{T_{dead}}$, distance of buffer capacitors discharge and recharge peaks $\mathrm{\Delta T_{buf}}$, dielectric voltage signal duration $\mathrm{T(V_{diel})}$) show the appropriate behaviour.

6.7.3 Electrical Power Dissipation

It is not astonishing, that large T-filter resistors also limit total dissipated power (Fig. 6.37a on the next page) and energy (Fig. 6.37b). The fraction of the total power catched by the resistors is largest for high resistances. Thus, their protecting capability gets lost when

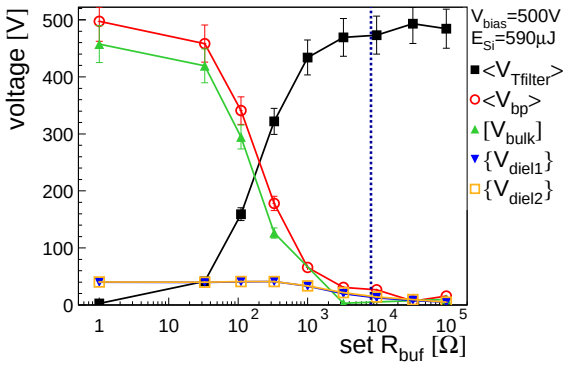

a. sample of voltages

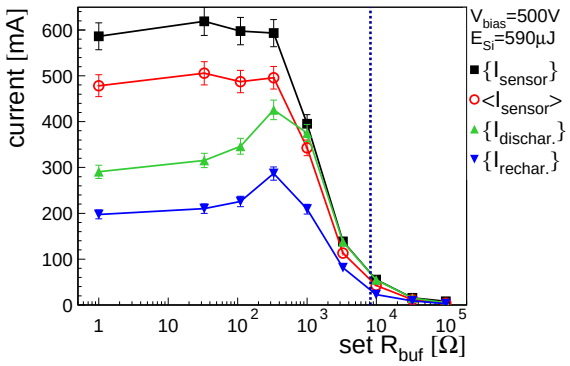

b. sample of currents

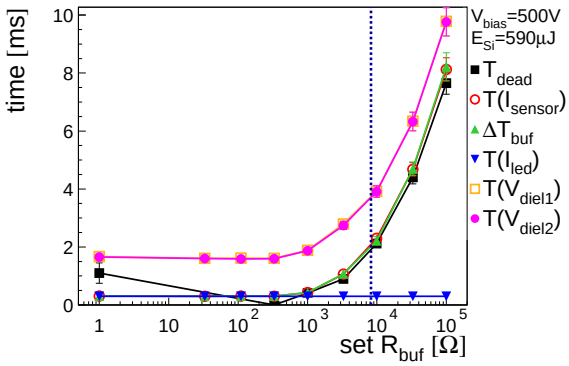

c. sample of time periods

Figure 6.36: Protection of sensor by T-filter resistor. *All presented data has been gained from the resistance scan of high-ρ sensor D. Some voltages are compared to each other in Fig. a. Large T-filter resistances catch the total bias voltage* ($V_{Tfilter}$) *and protect the sensor's components* (V_{diel}, V_{bulk}). *The protection is lost for low T-filter resistances. This behaviour affects the flowing currents (Fig. b) and time constants (Fig. c) in a way explained in the text. The x-scale only shows the buffer resistance* R_{buf}. R_{term} *is choosen so that* $R_{buf} \approx 4 \times R_{term}$ *is fulfilled. The dashed lines mark the CMS design value for the buffer resistor.*

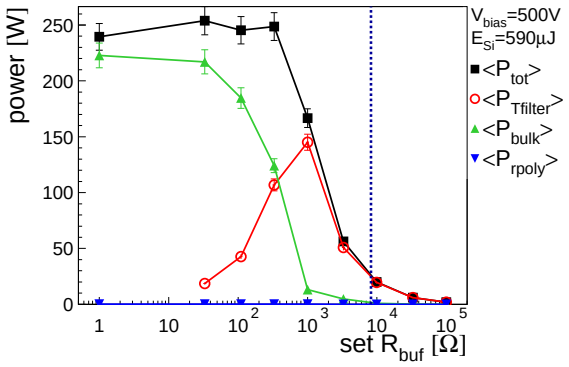

a. Power vs. R_{buf}

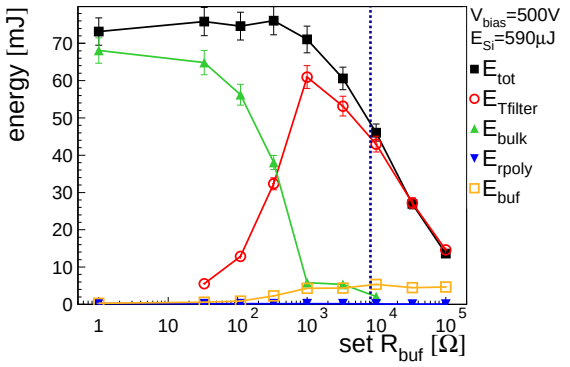

b. Energy vs. R_{buf}

Figure 6.37: T-filter dependence of electrical power dissipation. *The total averaged dissipated electrical power of the device* $< P_{tot} >$ *is compared to the dissipation of different parts of sensor* (P_{bulk}, P_{rpoly}) *and circuit* ($P_{Tfilter}$) *in Fig. a. Both plots show data gained from the test of sensor D (high ρ) using the Oltronix power supply and the standard energy per shot (590µJ). At a low T-filter resistance, the whole device had to stand an extremly large power during the LED pulse (300µs). The dashed lines mark the CMS design value for the buffer resistor.*

decreasing them. Not only the total amount of energy increases but also the *fraction* absorbed by the silicon bulk. At zero resistance, an average power of 220W and an energy of about 70mJ

is deposited there with each shot. This has not been destructive yet. But during the damage studies within the scope of the laser test, it turned out, that the dissipated energy possibly is resposible for damages caused to the whole sensor setup (see Chapter 7.6 on Page 103).

6.7.4 Burned T-filter Resistors

As seen in the previous paragraph, the commonly used T-filters resistors (10kΩ) absorb the total electrical energy. Thus, they have to stand a current of I=50mA at full bias ($V_{bias} = 500V$) during a pulse. This is undangerous in case of single events, like beam losses. But many shots in a sequence will burn the resistors. The reason is the maximum rated *constant* power of $P_{max} = 250mW$, a 1206-resistor[5] can dissipate. Pulses with a duration of T=1ms fired with a frequency of f=10Hz will cause an *averaged* power dissipation in a 10kΩ resistor of $P = f \cdot T \cdot V_{bias}^2/R = 250mW$. This conditions have been surpassed during some LED tests causing the larger one of the resistors being burned out.

6.8 Test of an irradiated Sensor

Sensors, that received an irradiation dose equivalent to the full time period of LHC operation, should behave completely different to unirradiated ones due to their strongly decreased bulk resistivity. Thus, a rough beam loss test with such a sensor has been performed. Sensor H received an irradiation dose equivalent to 15 years of LHC operation. This is 1.5 times the normal dose CMS tracker sensors are exposed to during Irradiation Quality Control (`IQC`). Irradiated sensors cannot be depleted without cooling due to the steep increase of leakage current with temperature. In the used setup, the nominal temperature of $-10°C$ could not be hold, so that the test temperature had been arround $-35°C$.

Only two raw data channels, backplane voltage and sensor current, were taken. The other parameters were either not yet available at this point of time or had to be disabled due to problems with ice causing short-circuits between some bonds and the sensor's high voltage ring.

Figure 6.38 on the next page shows raw data taken at maximum shot energy. The shot duration has been 3ms. A complete different behaviour compared to unirradiated and warm sensors is observed. The backplane voltage dead time and hence the sensor current duration is constant vs. bias voltage.

A model is given in the following paragraphs. As seen in Fig. 6.38b, the maximum sensor current again is limited. The height is calculated in the same way as mentioned in Eq. 6.18 on Page 71 using bias voltage and T-filter resistors. In the present test, $R_{Tfilter}$ is 10kΩ. This fits nicely to the given maximum values. Unusual is the fact that the sensor current signal has the same duration as the incident light signal independently of the bias voltage. The reason for this is a much smaller charge carrier lifetime caused by a concentration of impurities being orders of magnitude larger than in an unirradiated sensor. The current allowed by the T-filter flows as long as the LED pulse is on. Once it is of, the remaining charge carriers start to recombine with a rate proportional to the number of defects in the bulk. The sensor current decays with its characteristic time constant and the number of drained off charge carriers from then on is given by the area of the decay tail. So, a simple relation between flowed charge and bias voltage can be concluded for *large* energies.

$$\int I_{sensor}\, dt \approx I_{sensor} \cdot T_{LED} \approx \frac{V_{bias}}{R_{Tfilter}} \cdot T_{LED} \tag{6.36}$$

[5] package size specification of surface mounted devices (SMD)

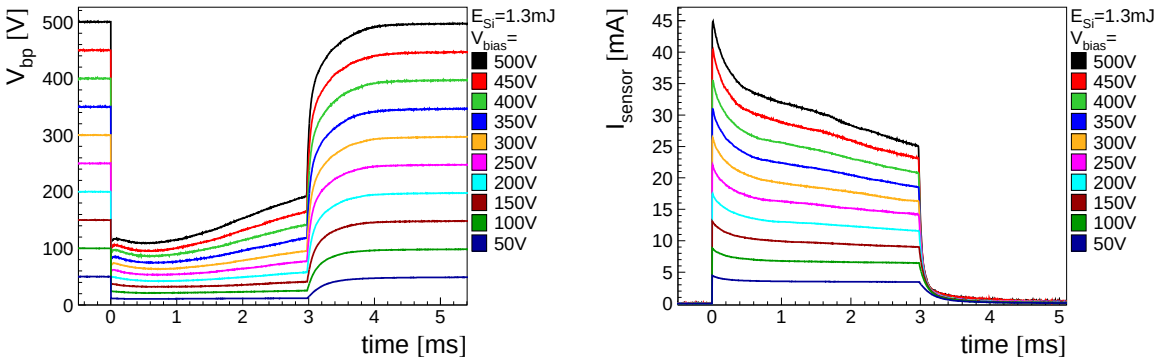

a. backplane voltage b. sensor current

Figure 6.38: Complete set of available raw data. *The behaviour of this sensor, that has been tested cold, differs completely from this of non-irradiated and warm sensors studied up to now.*

Thus, the total flowed charge is proportional to the bias voltage with a factor depending on energy resp. pulse duration. An example straight line fit for 1.3mJ corresponding to a pulse length of 3ms is given in Fig. 6.39a. Its slope P2 is about 0.2μC/V fitting quite well to the expected value of $T_{LED}/R_{Tfilter} = 3ms/10k\Omega = 0.3\mu C/V$.

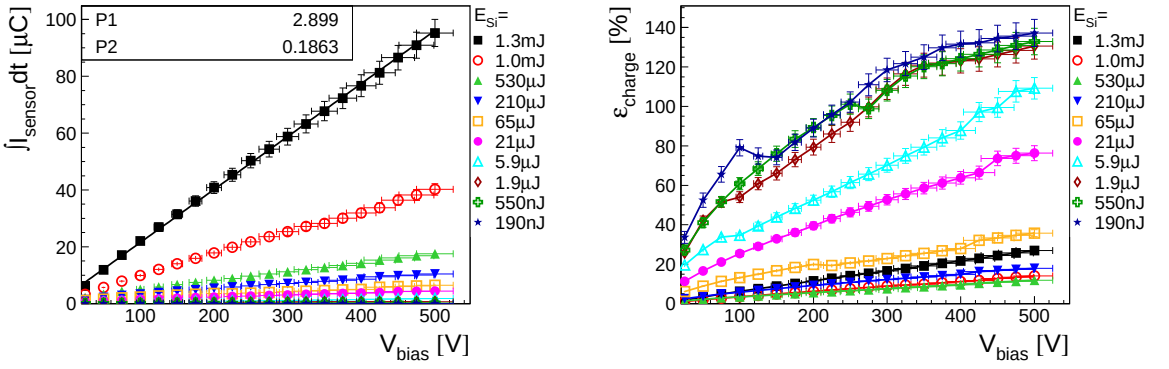

a. total charge b. fraction of drained off charge

Figure 6.39: Total flowed charge and charge fraction. *In contrast to an unirradiated sensor, the dependency of the total charge on bias voltage and energy can be almost completetly understood. The charge is proportional to the bias voltage. An example straight line fit for 1.3mJ corresponding to a pulse length of 3ms is given in Fig. a. Its slope P2 is about* 0.2μC/V *and fits quite well to the formula given in the text. The fraction of drained off charges (Fig. b) increases with decreasing energy. The rise above 100% at low energies is due to energy calibration problems.*

Figure 6.40 shows the sensor current and the appropriate LED pulse for three different energies at full bias. So, at a pulse length of 3ms (6.40a), Eq. 6.36 on the previous page is true. For lower durations (100μs, Fig. 6.40b and 3μs, Fig. 6.40c), the decay tail of the sensor current dominates the area of the signal, as the decay time constant does not decrease in the same proportion than the energy does. So, a much larger fraction of the created charge is drained-off (Fig. 6.39b) and reaches 100% at lowest energies. The proportionality of total flowed charge and bias voltage remains anyway (Fig. 6.39a) as the maximum sensor current remains proportional to the bias voltage.

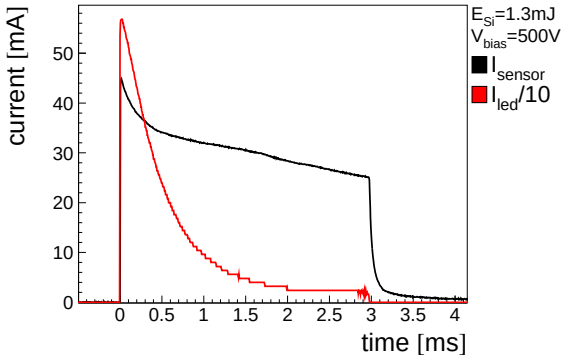

a. $T_{led} = 3ms$

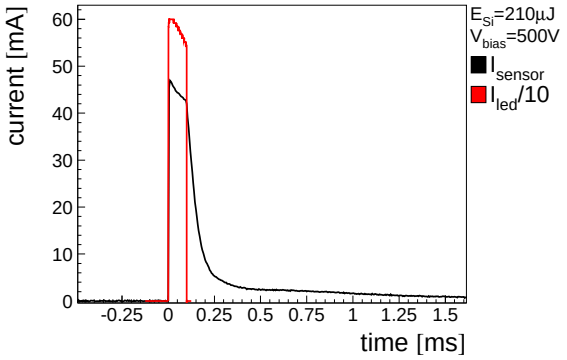

b. $T_{led} = 100\mu s$

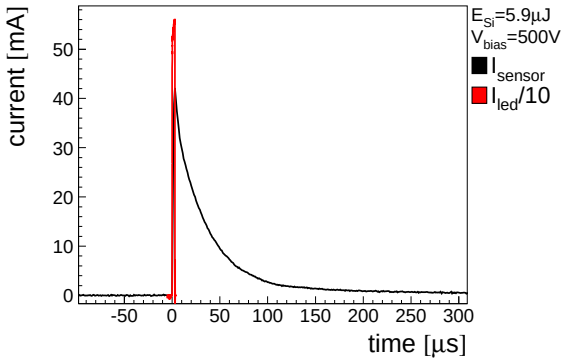

c. $T_{led} = 3\mu s$

Figure 6.40: Evolution of sensor current with pulse duration. *The time behaviour of the sensor current is compared to the LED current. At large LED pulse durations (Fig. a), the sensors respone signal is simply dominated by the LED pulse. But the contribution of the sensor current's tail to total charge and sensor current signal length dominates at lower enegies (Figs. b and c).*

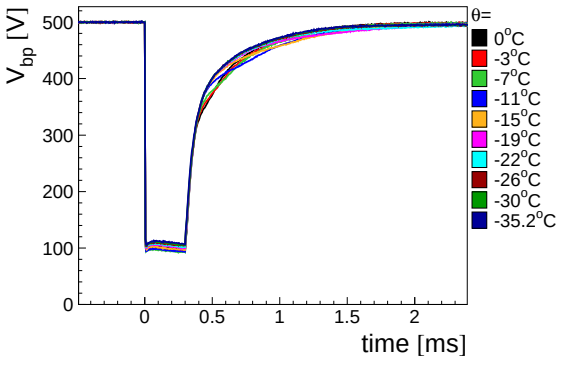

a. raw data

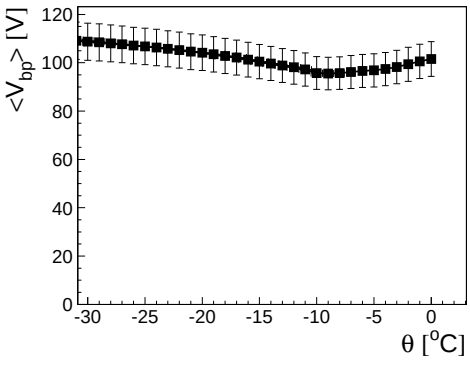

b. breakdown voltage

Figure 6.41: Backplane voltage vs. temperature. *There are slight variations observable in the temperature interval of 35K. The level of backplane voltage breakdown differes by some V. Unfortunately, the dependence on temperature is not monotone: there is a minimum at* $-10°C$.

During the warm-up phase, a temperature scan has been done starting at $-35°C$ and ending with $0°C$. The dependence of the backplane voltage on temperature is presented in Fig. 6.41. In total, a slight decrease of the breakown voltage is observed when getting warmer. This can be explained with an increased conductivity and therefore a reduced resistivity at higher temperatures. Thus, the voltage drop over the lower resistivity bulk decreases when

warming up. Unfortunately, the slight increase from $-10°C$ on cannot be explained with last surance. Probably, there was a change in handling the setup from this temperature on.

6.9 Test of a Module

A module's sensor and its front end hybrid (FEH) have been separately exposed to shots of different lengths under full bias and with running readout. The APVs were triggered by the same pulser as used for the LED array. It has been possible to readout out the hybrid directly after the shot! The signal respectively baseline dissortion of each APV has been defined in the same way as it is done for noise calculations. Pedestal and common mode of the undisturbed data are subtracted from the signal. The corrected signal's root mean square over all channels of one APV is plotted (Fig. 6.42).

$$\sigma_{baseline} = \sqrt{\frac{1}{128}\sum_{k=0}^{127}(S_k - \mathrm{Ped}_k - \mathrm{CMM})^2} \tag{6.37}$$

The duration of baseline dissortion is of the same size as for HIP-events. The reaction of APVs on highly ionizing particles (HIPs) has been studied in [A+05]. The dead-time of an APV has been measured there to be several 100ns. This value has been reproduced in the present test. Shots directly on hybrids have a slight increased effect on the baseline (Fig. 6.42a) in comparison to shots on sensors (Fig. 6.42b).

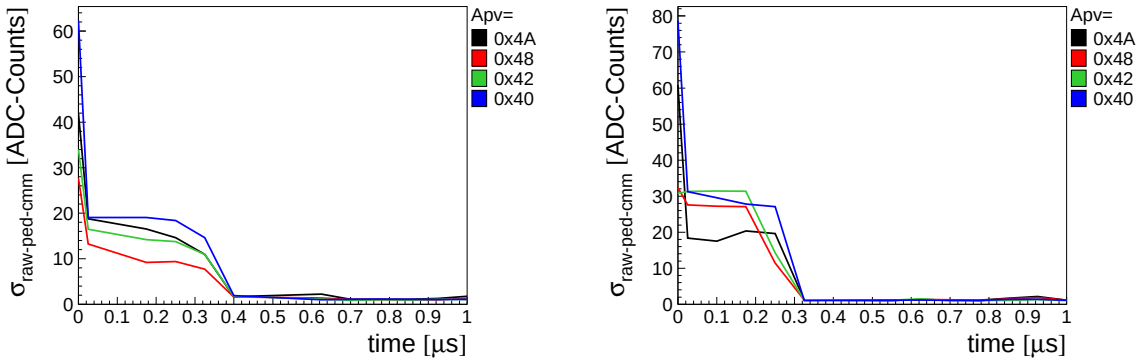

a. hybrid b. sensor

Figure 6.42: Baseline dissortion after shot. *There is a slight difference in duration between the pulsed illumination of a sensor and a hybrid. The presented data results from shots of 10ns length. Tests at much longer pulse lengths show the same behaviour. This is not astonishing as the APV reacts on a fast signal* edge.

6.10 Before and after Test Qualificaiton

All qualification data is presented in Section C.2 in the Appendix on Page 127. Five sensors have been tested with the LED array in total, four unirradiated ones (D, E, F, G) and one irradiated (H). Two have a high resistivity (D, E) and three a low resistivity (F, G, H). All unirradiated sensors received a full qualification before the tests. But for sensors D and H, no full post-qualification is available, so that they are not considered here. Sensors E and F got

a full qualification after the first LED runs with a CAEN high voltage supply. As proven in Section 6.5.4 on Page 76, the stress to the coupling capacitors is comparable with the use of the Oltronix power supply. So, this qualification data is presented. The data shown for sensor G refers to the lab qualification after all destructive tests. Sensor H has not been qualified afterwards, so it is not considered in this section.

When evaluating the post-qualification data, one has to consider, that all sensors were glued on a circuit and bonded on it. During the tests, they received many thousands of shots and were dismounted and mounted into the setup several times. Afterwards, the sensor had to be detached from its carrier circuit against some remnants of (conductive) glue and sticking rubber pads. It is remarkable, that none of the sensors suffered from mechanical damages indicated by an absence of any electrical breakdown even at voltages above 500V.

Sensors E and F behaved almost perfect after the first LED tests. Their IV curves (Fig. C.9 in the Appendix on Page 127) stayed below the specified maximum of 10μA at 450V [CMS00b]. The behaviour of the global capacitance is good (Fig. C.11). The voltages of full depletion are summarised and explained in Table E.1 in the Appendix on Page 131. They should be between 100V and 300V [CMS00b]. Only slight deviances are observed before and after. Sensor E generally being out of specification has been taken from a pre-series and is accepted for special purposes.

No additional strip errors appeared on sensors E and F. Channel 451 on sensor F has been a pinhole already before all tests (Fig. C.13). This channel sometimes is suspicious in the other tests and therefore is not considered any more in further discussions. The maximum allowed current per strip is 100nA at $V_{bias} = 450V$ [CMS00b]. Both sensors do not show additional leaky strips after the tests (Fig. C.10). For the coupling capacities, values arround 500pF are expected [CMS00b]. They do not show additional defect coupling capacitors afterwards. No pinholes appeared during the LED tests (Fig. C.13) and there has not been observed any damaged poly silicon resistor during both qualification tasks (see Fig. C.14).

Sensor G received a complete T-filter scan and a standard scan with the Oltronix power supply and without any protecting resistors in its HV line. As mentioned in Section 6.7 on Page 85, the dielectric layers of low resistivity sensors are affected most when reducing the T-filter resistances. This now is seen in post-qualification data. Some strips are bonded from their AC-pad to ground to be able to measure the voltage over the dielectric layer. Those channels are marked in each qualification plot. For sensor G, a good correlation between bonded regions and new faulty strips can be observed. That are in detail leaky strips (Fig. C.10), new pinholes (Fig. C.13), damaged coupling capacitors (Fig. C.12) and defective poly resistors (Fig. C.14). Together with its IV-curve reaching 1mA (Fig. C.9) and a stronly increased depletion voltage (Fig. C.11 and Table E.1), one has to conclude, that sensor G has been heavily damaged during the LED tests.

6.11 Conclusion and Outlook

The single shot testbeam results could be reproduced largely. New parameters related to the sensor and its circuit (I_{sensor}, I_{buf}, V_{buf}, V_{term}) have been measured to obtain a deep comprehension of the processes taking place during a high intensive particle or light shot. A quantitative electrical model has been developed. It needs only one measured physical input parameter, the total flowed charge $\int I_{sensor}\, dt$, and predicts all values related to the sensor circuit. The presented physical model has been able to forecast one of the physical parameters, the total flowed charge, only in case of irradiated sensors. For the other sensors and for an other measured parameter, namely the dielectric voltage, a qualitative understanding has been given.

The sensor is protected from beam losses by its T-filter resistors. The presently used T-filter capacitance does not endanger the sensor as well. But the sensor can be damaged when reducing the T-filter resistances even with the usage of *low power* supplies and a normal T-filter capacitance.

So, with the use of a normal T-filter, the sensor is not the critical part but the resistors are. Very long pulses or a sequence of many shots dissipate too much average power in the resistors and causes them being burned. Single shots do not damage both the resistors and the sensor. This fact gives some margin and information of running at high irradiation load (concerning intensity and pulse duration)) due to an unforseen beam condition!

The LED pulse duration needed to apply an energy in the order of magnitude of the beam loss energy is some ms and hence much longer than a beam loss lasting some 100ns. Therefore, a further study with a high energetic and pulsed IR laser has been performed representing a more realistic test scenario.

Furthermore, a study of the short-circuit behaviour of the official CMS high voltage supplies is proposed to rule out any damages to the resistors due to long lasting particle pulses or to the sensor due to large overshoots during voltage recovery.

7 Lab Test with a Laser

7.1 Motivation

In order to investigate the impact of a beam loss at the LHC under lab conditions, a pulsed laser of high luminosity can be used. Although the pulse length of 7ns, which is the longest, one could obtain in laser technique, is one to two orders of magnitude shorter than in the beam loss case (260ns), it is a more realistic situation than using ms-pulses like it has been done in the LED test. Furthermore, the maximum available energy per pulse is much higher than the energy deposited in a sensor during a beam loss. Thus the safety margins of the survival of a sensor can be tested.

As the LED test reveals the sensor circuit's components as critical, one aimed to pin down the damage threshold by the laser test.

The bandwidth limit of the analogue data acquisition setup (signal lines and signal termination) being in the order of 10MHz is not sufficient for the usage of the transient current technique (TCT) (see Fig. 7.7b on Page 102).

7.2 Setup

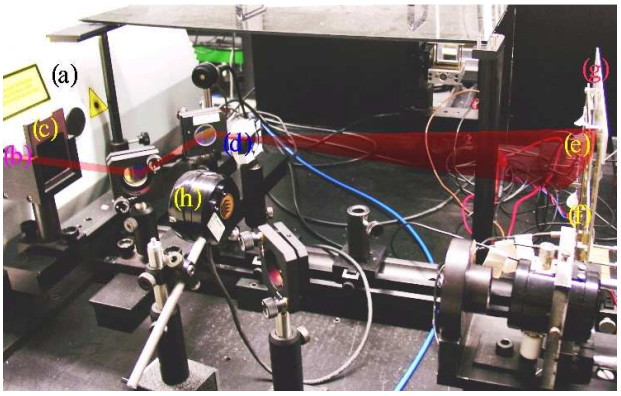

Figure 7.1: Test setup with optical path. *(a) cooled Nd:YAG laser, (b) IR light beam, (c) green filter in its mounting for 6 furthers filters, (d) two divergent lenses glued together, (e) beam spot:* $d \approx 8$cm *(almost homogeneus illumination), (f) sensor, (g) sensor circuit transport frame, (h) light power calibration device (heat detector)*

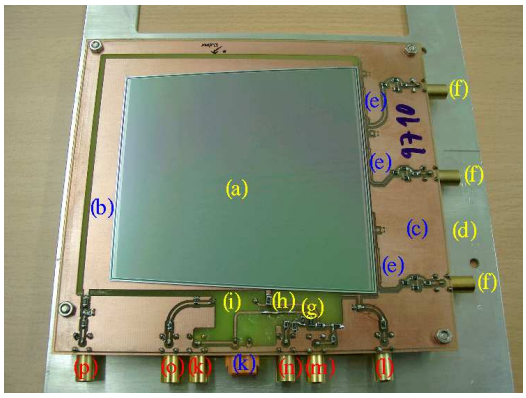

Figure 7.2: Sensor mounted on its carrier circuit. *(a) sensor, (b) high voltage plane, (c) ground plane, (d) transport frame, (e)* V_{diel} *measurement groups, (f)* V_{diel} *out, (g)* R_{term}*, (h)* R_{buf}*, (i)* C_{buf} *(underneath), (k) HV in (2×), (l)* I_{sensor} *out, (m)* V_{buf} *out, (n)* V_{term} *out, (o)* I_{buf} *out, (p)* V_{bp} *out*

Except for the light source, the setup is identical to the LED test. A photo of one sensor setup used in the laser test is shown and explained in Fig. 7.2. The test setup with some explanations can be seen in Fig. 7.1.

7.2.1 Nd:YAG Laser

A Nd:YAG laser has been used for the following test. It has been provided by the *Institut ür Angewandte Physik* at the *Universität Karlsruhe (TH)*.

In a Neodymium-doped Yttrium Aluminium Granat monochrystal (Nd:YAG), up to 1% of the Y^{3+} are replaced by Nd^{3+}-ions [RW95]. Its energetic states are modified by the YAG-crystal, the so called host-crystal. This enables the inversion of population by optical pumping, e.g. with use of a strong flashbulb. The light flash emitted by the long shaped lamp is focused to the laser pole by an elliptical reflector. The pole becomes a laser resonator by evaporating its ends with reflective layers or by mounting external mirrors. The use of flashbulbs enables pulsed operation and very high pulse energies. But it requires a good cooling facility as most of the white light is converted into heat. Laserdiodes with their narrow and best adapted spectrum are more efficient for optical pumping and enable constant operation but are much less luminent.

The laser had a pulse length of 7ns. The primary mode has a wavelength of 1064nm. The other modes available are the half and fourth wavelength of 532nm and 266nm. The latter one stayed in the laser's case. The second mode is unwanted in this test and has been filtered during any shot. Only the near infrared (NIR) component (1064nm) is used as the penetration depth in silicon of 435 μm at this wavelength fits very well to a sensor depth of 500 μm. The conditions of NIR light absorption in CMS silicon sensors have been extensively discussed in Section 6.2.2 on Page 54. In the present case, 90% of the light entering the sensor is absorbed. With the known strip covering, one obtains an absorption efficieny of 68% of the incident light energy. The total pulse energy provided by the laser at the interesting wavelength is 85 mJ. This results in an absorbed energy of 57mJ per pulse! The pulse repetition frequency is at maximum 20Hz but only the single shot mode realised by a mechanical shutter within the laser case has been used.

7.2.2 Energy Calibration

The maximum pulse energy of 85mJ has been measured in pulsed operation at 20Hz with a heat detector. The incoming light is completely absorbed, and the rise of the temperature is registered. The displayed physical value is then the long term averaged thermal power. The energy per shot could be adjusted quite exactly over many orders of magnitude. For this purpose, a large sample of gray filters with attenuation factors between 43% and 1.1% - measured with the power detector - has been available. With the possibility of arranging up to six of them in one row, one could adjust almost any desired attenuation between 43% and 10^{-5}. This results in a pulse energy range from 85mJ down to 850nJ according to a deposited energy in the silicon between 57mJ and 570nJ. Those values one has to compare to the 2.2mJ in 260ns during a beam loss.

The relative systematic error in detecting the attenuation factor of each filter is estimated to be about 20%. The total attenuation factor is the product of the single ones. Thus, according to Eq. 6.10 on Page 59, the whole relative systematic error of the beam energy adds up and may exceed 100% when using six filters. Accordingly, the error decreases at larger energies and fewer filters and should be arround 20% at maximum energy without filter, corresponding to the estimated error of one energy calibration procedure.

The alignment of the sensor with respect to the beam spot has been done by removing the green filter. The laser beam became visible by eye and the sensor's position could be fine-tuned to obtain an optimal illumination. Anyway, after re-installing the green filter, a night-vision device has been used to cross check the IR light spot.

7.3 Measurement Program

7.3.1 Measured Parameters

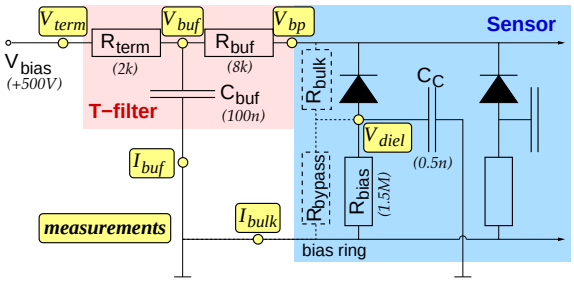

Figure 7.3: Equivalent circuit of a silicon sensor and its electical components. *The measurement setup equals to this one used in the LED tests and is repeated here. See Fig. 6.8 on Page 61 for detailed explanations. The dashed resistors* R_{bulk} *and* R_{bypass} *represent a very simple model of the short-circuited sensor. The proof of the latter one is given in Section 6.6.4 on Page 83.*

The same parameters are measured as in the LED test (Section 6.3.1 on Page 63). Figure 7.3 repeats the equivalent sensor and measurement circuit used during all laser tests. The obtained results are in agreement. A comprehensive description is given in Section 6.3.2 on Page 64. There are minor extensions with respect to fast recording of backplane voltage and sensor current and the analysis of their decay constant. The differences are mentioned when they occur in the results chapters 7.4 on Page 99 to 7.6 on Page 103.

7.3.2 Sensors under Test

thesis ID	database ID	geometry	V_{dep} [V] before	V_{dep} [V] after	resistivity (ρ)
D	30221116053219	W6A	44	?	high
E	30221116053220	W6A	42	?	high
F	30210431112924	OB2	165	268	low
K	30211132911721	W6A	202	?	low
L	30211133509710	W6A	?	192	low

Table 7.1: Sensors under Test. *Geometric data can be looked up in Table E.2 in the Appendix on Page 132. The thesis identifier (ID) is used in plot legends and descriptions.*

Five sensors have been tested (Table 7.1). Three of them have been taken from the LED tests. The new ones (K and L) had an interstrip resistance below specification. But no relevance of this problem was expected for the laser test.

Diversification with respect to manufacturer and silicon bulk resistivity has been realised again. But 4 out of 5 sensors are of type W6A. This is no problem since it came out during the LED test that the geometry does not play any role for the behaviour under pulsed illumination.

Several test runs with multidimensional parameter space were done. See Section 6.3.4 on Page 64 for explanations on test runs, parameters and their variation during a run. Beyond the findings in the LED study, one wanted to study the damage threshold by playing with the T-filter. Some scans with an increased density of measurement points also were done. A summary of all sensors, runs and their multiplicities is given in Table 7.2 on the next page.

test run	measurement points	sensor's thesis ID D	E	F	K	L
$V_{bias} \otimes E_{Si}$	$10 \otimes 6$	1	1		1	1
E_{Si}	31		1			1
V_{bias}	32		1			1
$V_{bias} \otimes C_{buf}$	$10 \otimes 10$			1		
$R_{buf} \otimes V_{bias} \otimes E_{Si}$	$5 \otimes 5 \otimes 5$				1	
	Σ_{shots} (estimated)	**120**	**246**	**200**	**370**	**246**

Table 7.2: Summary of laser test runs. *Several tests with one, two or even three-dimensional parameter space were performed. For each measurement point, about two shots were needed in average to aqcuire nicely fitting data.*

7.3.3 Test Runs

7.3.3.1 Bias Voltage and Energy Scans

The standard test for all sensors was a combined energy and bias voltage scan (two-dimensional parameter space). Six pulse energies with an increase by a factor of 10 per step were used to scan over a large energy scale from 570nJ to 57mJ. The energies are then: 570nJ, 5.7μJ, 59μJ, 540μJ, 5.4mJ and 57mJ. This standard scan contained the standard set of voltages (Section 6.3.4 on Page 64): 25V, 50V, 75V, 100V, 130V, 160V, 200V, 300V, 400V, 500V. All tests have been done under identical experimental conditions. Example plots are seen in Figs. 7.5a, 7.5b and 7.5c on Page 101, 7.8b on Page 102 and 7.14 on Page 105. For deeper studies, pure bias voltage and energy scans were done using an increased density of measurement points with and without T-filter resistors (e.g. Fig. 7.8a).

7.3.3.2 T-filter Resistance Scans

The *decisive test* for the determination of the damage threshold was the T-filter scan. For each of the 5 resistor-configurations, a small energy and bias voltage scan has been done (three-dimensional parameter space): 25V, 50V, 100V, 200V, 500V and 5.7μJ, 59μJ, 540μJ, 5.4mJ, 57mJ. Both resistances R_{term} and R_{buf} were changed in the same way as it has been done in the LED test. See the appropriate Section 6.3.4 on Page 64 for more details. The following pairs of T-filter resistances were used. The configuration in the box is nearest to

R_{buf}	100 kΩ	10 kΩ	1 kΩ	100 Ω	1 Ω
R_{term}	27 kΩ	2.7 kΩ	270 Ω	27 Ω	1 Ω

the officially used T-filter. See Figs. 7.11 on Page 104 and 7.13b on Page 105 for some results of this test.

7.3.3.3 T-filter Capacitance Scan

The scan over the T-filter capacitance covered again the 10 standard voltages but only 10 capacitances from 10nF to 1μF almost exponentially increasing from step to step (two-dimensional parameter space). The same circuit for capacitance adjustment has been used. See Section 6.3.4 on Page 64 for a more detailed explanation. One result of this test is shown in Fig. 7.9 on Page 103.

Results and Interpretation

The electrical and physical model for high intensive light shots have been developed in the previous chapter. Their successful reproductions during the laser tests are not mentioned particularly. The focus in this section lays on the different behaviour coming up when increasing the incident energy by a factor of 30 while decreasing the pulse duration by six orders of magnitude! But first of all, a minor overview on the commonalities to the LED test is given in Section 7.4. A special problem on the short-term behaviour of the sensor current is briefly discussed in Section 7.5 on Page 101. The main outcome of this tests is the determination of the damage threshold for sensors deposed to high energetic pulses. Section 7.6 on Page 103 summarises the results gained from two stress tests. The after test qualification compiled in Section 7.7 on Page 105 is from great importance to verify their assumed impact on the sensor.

7.4 Comparison to LED Test

7.4.1 Raw Data

Figure 7.4 on the next page displays data from the standard test of a high-ρ sensor already used during the LED tests. A comparison with the data taken from the same sensor with the same circuit and high voltage supply (Figs. B.2 in the Appendix on Page 122, B.5, B.6 and B.7 in the Appendix on Page 123) shows the *shapes* being equal. This is not astonishing as the same electrical model, defining the signal shapes, is valid. But signal durations, like breakdown time and sensor current signal length, differ. As already proven in LED tests, they do not depend on the duration of the light pulse being orders of magnitude smaller, but from the amount of incident light and hence the collected charge. And this values completely differ in laser tests.

There is a special point to mention that did not rise in LED tests. The backplane voltage had a slight undershoot below zero during breakdown (Fig. 7.4a on the next page). The reason for this is the very large sensor current of some Amperes during the first μs after the shot. Figure 7.7b on Page 102 shows an example without T-filter resistors. But this fact also is true for the present test. An unstable ground reference will be rised due to its ohmic parts when confronted with such a large return current. The same reference is used for all measurements, especially the backplane voltage. The effective measured voltage is below 1V as a voltage devider is used. So, a rised ground by some mV, being higher than the voltage to measure during backplane voltage breakdown, will result in a negative value. Unfortunately, it is impossible to disentangle a floating ground from the data.

7.4.2 Flowed Charge

The T-filter again protects the sensor from large currents. See Fig. 7.3 on Page 97 for a schematic of the sensor and its circuit. The sensor current is limited according to Eq. 6.18 on Page 71. Figure 7.5a on Page 101 shows, that it does not rise above the electrical limit for a large energy range. The consequence is an increase of time needed to drain off the created electron-hole pairs (EHPs). For example, at the maximum energy of $E_{Si} = 57\text{mJ}$ and a bias voltage of $V_{bias} = 500\text{V}$, the required time T_{dead} to free the sensor from all charge carriers *would be* $T_{dead} = \frac{Q_{sensor}}{I_{sensor}} = \frac{E_{Si}}{3.9\text{eV}} \cdot \frac{V_{bias}}{R_{Tfilter}} \approx 290\text{ms}$. During this time, almost all EHPs recombine, so that only a small fraction contributes to the total flowed charge. Figure 7.5b on Page 101 clearly demonstrates this fact: An increase of energy by a factor of 10 (from 5.4mJ up to 57mJ) results into a gain in flowed charge of only 10%. The plot in Fig. 7.5c

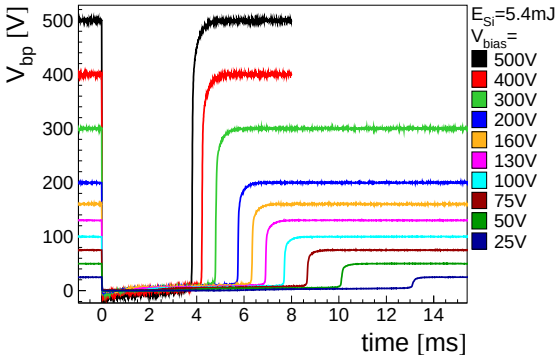

a. backplane voltage vs. V_{bias}. Compare to Fig. B.5

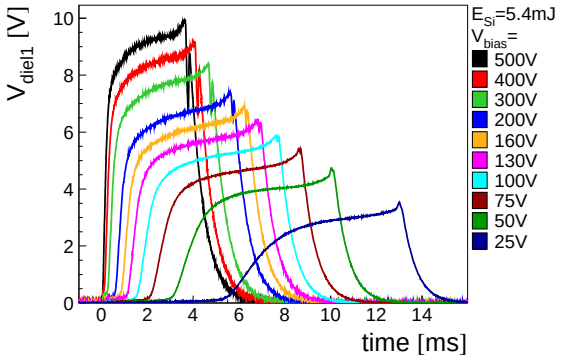

b. dielectric voltage vs. V_{bias}. Compare to Fig. B.2

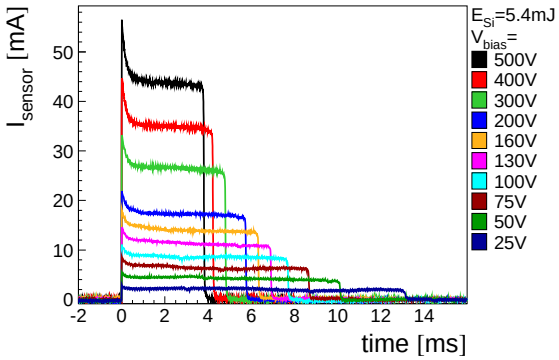

c. sensor current vs. V_{bias}. Compare to Fig. B.6

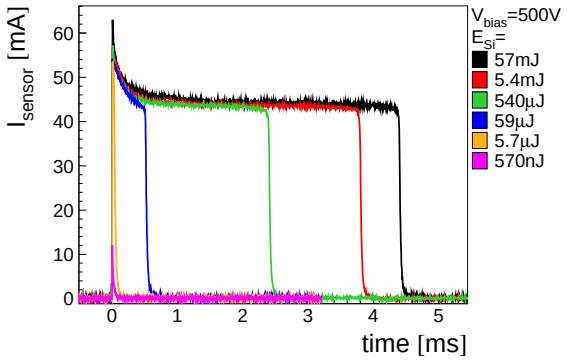

d. sensor current vs. E_{Si}. Compare to Fig. B.7

Figure 7.4: Some raw data. *All plots have been gained from the standard test of sensor E (high ρ). The graphs are exponentially smoothed with a weight of 0.1. This is the reason why the dielectric voltage is slightly delayed at $V_{bias} = 500$ V. The plots match well with the LED test data presented in Chapter B in the Appendix on Page 122.*

expresses this in terms of drained off charge fraction. At the tenth of energy (5.4mJ), this fraction increases tenfold. At maximum energy and full bias, only 1% of the created charges are drained off. This number fits well to the fraction of the sensor current signal length calculated above with the actual duration of about 3ms.

Figure 7.4d confirms the described saturation effect at large energies in raw data. A pulse length of 4.5ms is not exceeded. This allows the conclusion, that the charge carrier life time ranges in the ms-order of magnitude at a (remaining breakdown) bulk field of about 20V/500μm.

7.4.3 Impact of Silicon Resistivity

Four sensors, two with low resistivity ($\downarrow \rho$) and two with high resistivity ($\uparrow \rho$) underwent the standard laser test. The same differences have been observed (see Fig. 7.6). The reader is reminded of Section 6.6.5 on Page 84 showing the LED test results and explanations on this issue. A special result, that is from great importance must be repeated here. The dielectric voltage is limited with increasing energy only for high-ρ sensors. There is no evidence of a saturation when using low-ρ sensors. This fact has been reproduced within the laser test (Fig. 7.6a).

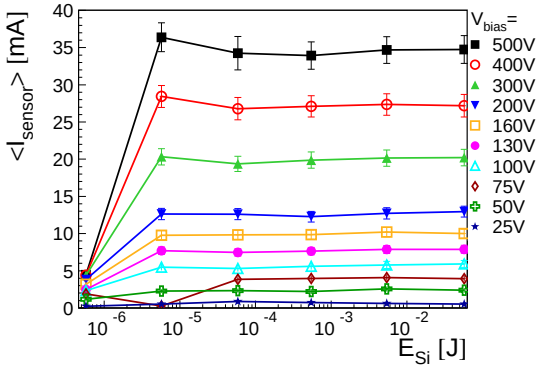

a. mean sensor current

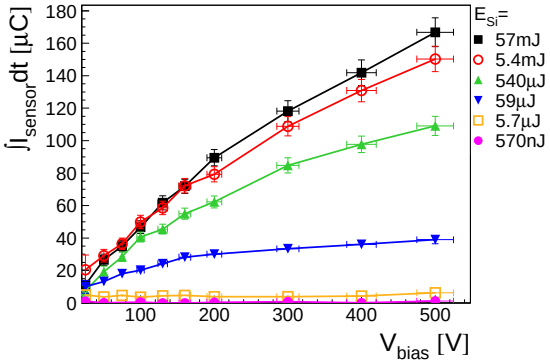

b. flowed charge

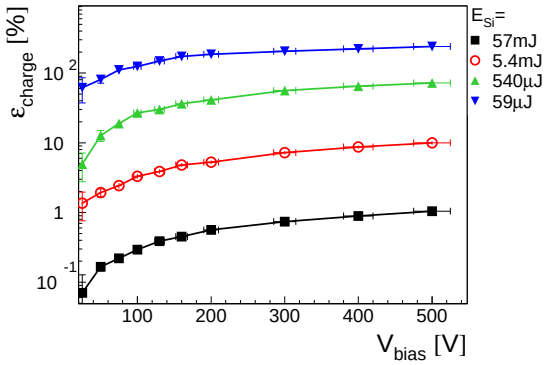

c. fraction of drained off charge

Figure 7.5: Protection of sensor. *The T-filter limits the sensor current (Fig. a). The required time to drain off all created charge carriers therefore would be much too long, so that most of the created* EHPs *recombine at higher incident energies (Figs. b and c). The charge fraction (Fig. c) rises above 100% at low energies due to energy calibration problems (Section 7.2.2 on Page 96): Several gray filters are necessary to attenuate the light to the desired intensity. The relative uncertainities in their attenuation factors add up to errors of 100% and more.*

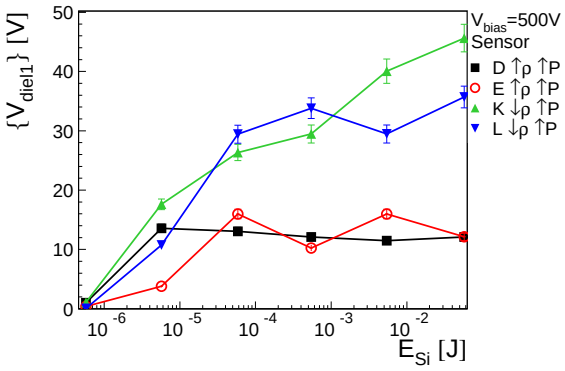

a. dielectric voltage vs. E_{Si}

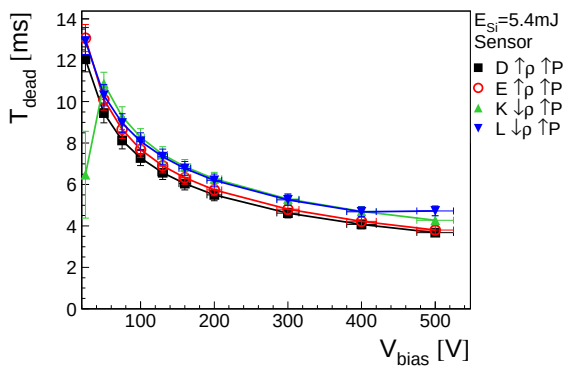

b. bias voltage dead time vs. V_{bias}

Figure 7.6: Bulk resistivity dependence of test results. *Some results obtained from two high resistivity sensors (D and E, marked with ↑ ρ) and from two ones with low resistivity (K and L, ↓ ρ) are compared to each other. The four tests have been performed under same conditions (official T-filter and Oltronix high power supply: ↑ P). The low ρ sensors show an strongly increased dielectric voltage (Fig. a) but only a slightly increased dead time (Fig. b).*

7.5 Short-term Behaviour

The sensor current behaviour has been investigated on the ms-scale up to now. But a large sensor current peak up to 40A directly after the shot has been discovered on the µs-scale

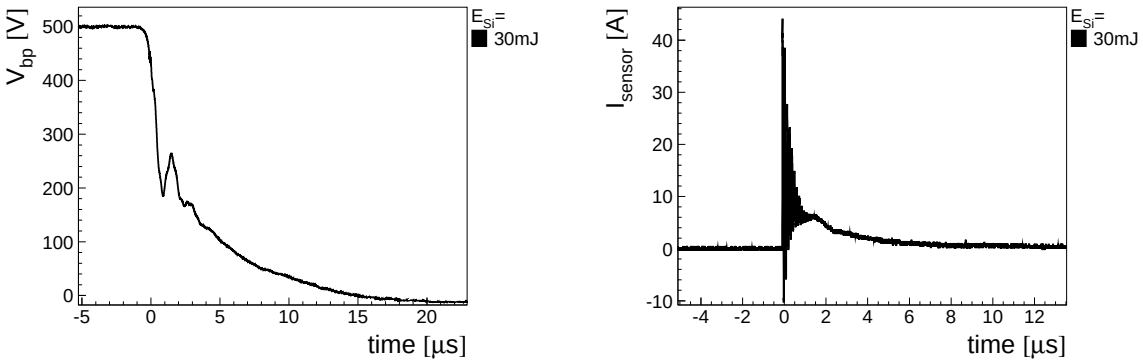

a. backplane voltage vs. time

b. current vs. time

Figure 7.7: Short-term behaviour (raw data). *This data has been taken with sensor E (high ρ) without resistor protection under full bias and applying almost the maximum energy.*

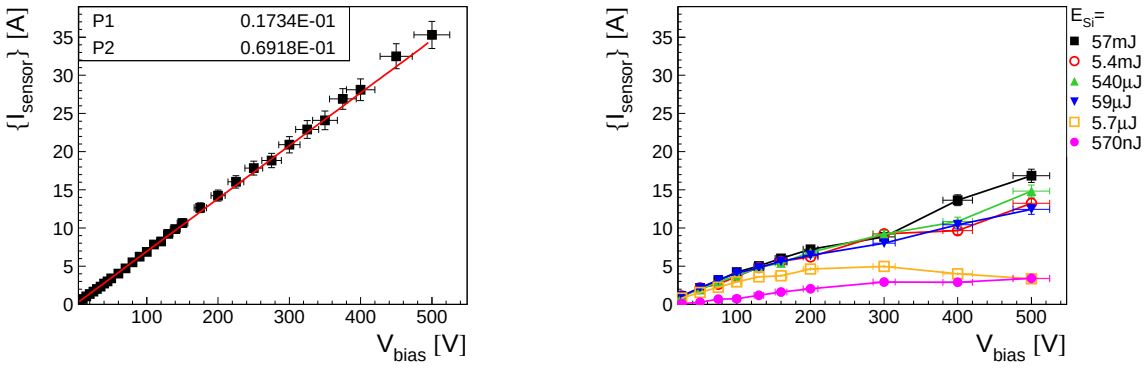

a. maximum current vs. V_{bias} (zero T-filter)

b. maximum current vs. E_{Si} and V_{bias} (usual T-filter)

Figure 7.8: Maximum sensor current. *Sensor E (high ρ) received a voltage scan without resistor protection and biased by a Keithley high voltage supply. The maximum current of this test is shown in Fig. a. It is proportional to the bias voltage with a slope of P2=0.07A/V. The maximum current measured during the standard test of the other high-ρ sensor (D) with official T-filter resistors is plotted in Fig. b.*

(Fig. 7.7b). The peak decays to a normal value and oscillates at the same time. Such oscillations (f ≈ 10MHz) are caused by the limited maximum signal transfer frequency of the used electrical setup mainly given by length and capacitance of the signal cables.

This large current can be explained with the finite duration of backplane voltage breakdown (Fig. 7.7a). The fast decay of the backplane voltage must be considered as a high frequent signal. It sees the parallel circuit of the measurement resistor (1Ω to 10Ω) on the ground side and the T-filter resistors (10kΩ) on the high voltage side. This results in an effective resistance of some Ω. As a consequence, the stepply decaying backplane voltage is able to drive an accordingly decaying sensor current of many A. This is far above the constant current limit required by the T-filter resistances (Fig. 7.8). The ohmic character of this discharging process is proven in Fig. 7.8a. The linear fit of the current against the voltage results in a slope of 0.07A/V corresponding to a resistance of only 14Ω.

Two problems could come up with this concerning the bias bonds. First, they have to stand the ohmic heat caused by the large current. But none of the tests showed any evidence

for burned bonds. The second problem is related to the magnetic field of 4T the bonds will be exposed to. Five bias bonds share the maximum observed sensor current of about 50A. Assuming the worst case of flat bonds with 1cm length and 10A flowing through each of them, they have to stand a shear force of 0.4N $\approx$ 40g for some μs. This is an abnormal large force for a bond in this direction. But they will not be deviated at all during this short period of time the force takes effect. So, no problems are expected. A lab test with bonds exposed to a magnetic field while driving a large, pulsed current through them, has been in preparation and could have given last assurance. But this project has been canceled.

7.6 Damage Studies

Tests with modified T-filter resistors and capacitors have been done to determine the damage threshold of the T-filter in the final module design.

7.6.1 Destruction of Coupling Capacitors

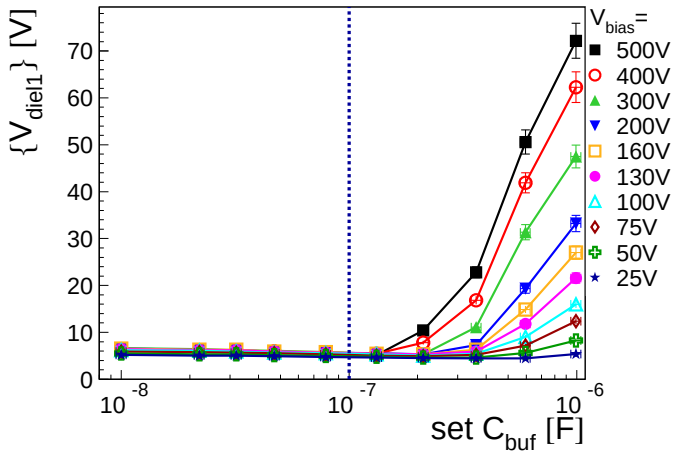

Figure 7.9: Dielectric voltage vs. C_{buf} . *Sensor F (low ρ) received a T-filter capacitance scan while biased with a Keithley high voltage supply and protected by the usual T-filter resistors $R_{buf} = 8k\Omega$ and $R_{term} = 2.2k\Omega$. The coupling capacitors sustained! The dashed line denotes the CMS design value for the buffer capacitor.*

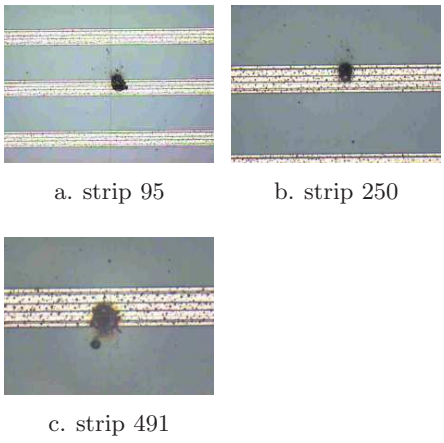

a. strip 95 b. strip 250

c. strip 491

Figure 7.10: Microscope pictures of destructed strips. *In this test, Sensor F was operated* without *T-filter resistors and with C_{buf} of of only 20nF. But this was sufficient to generate three new pinholes!*

A T-filter capacitance scan of sensor F (low ρ) has been done. All shots had an energy of about 20mJ. The sensor was biased by the Keithley high voltage supply, and the official T-filter resistors have been used. The test result is presented in Fig. 7.9. The dielectric layer again is endangered when increasing the T-filter capacitance. It has to be noted, that this sensor already received the same kind of test with the same strips bonded during the LED studies. But nevertheless, the coupling capacitors sustained this test! The same conclusions can be drawn on the height of the dielectric voltage peaks as seen in Section 6.7 on Page 85.

Afterwards, the T-filter resistors have been set to zero ($R_{buf} = R_{term} = 0\Omega$), and the Keithley high voltage supply stayed in use. One has to remind, that the Keithley is a low power device with a terminal voltage breaking down instantaneously at currents far above 1mA. With this setup, the lowest capacitance of 20nF has been anyhow sufficient to kill the coupling capacitors of the bonded strips. This fact could been verified, as sparks at three points were *visible by eye* on the sensor during the shots! The optical inspection showed defects

right on the bonded strips (Fig. 7.10 on the previous page). The sensor's post-qualification (Section 7.7) confirms major damages there. The conclusion on this test is, that although a low power supply and a small buffer capacitance is used, one can kill an *unprotected* sensor.

7.6.2 Destruction of whole Sensor

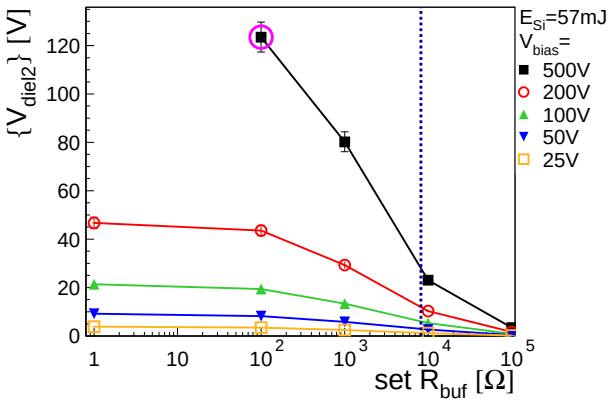

Figure 7.11: Dielectric voltage vs. R_{buf}. *A T-filter resistance scan has been performed with sensor K (low ρ) using the Oltronix power supply and buffering with the normal T-filter capacitance of 100nF. At 1Ω and 500V, the sensor has been destroyed. The dashed line denotes the CMS design value for the buffer resistor.*

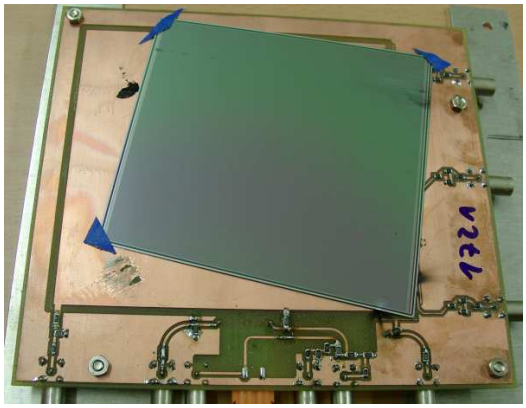

Figure 7.12: Destroyed sensor. *During this scan, at the lowest resistane, sensor K has been destroyed probably by thermal stress caused from the heat dissipated by the sensor and drained off via glue, that melted or broke.*

A T-filter resistance scan has been done with sensor K (low ρ). Figure 7.11 shows, that the dielectric layer is endangered under full bias at a T-filter resistance below 100Ω. Some shots at minimum resistance and maximum energy finally destroyed the sensor (Fig. 7.12). So, the appropriate data point is missing in the plots. The destruction happenened as follows. The sensor, vertically mounted, glided down and short-circuited the sensor circuit's high voltage layer with the ground layer. This burned the edges of the sensor. Afterwards, the conductive glue pads holding the sensor looked as if they melted. The AC-bonded strips showed damages along their length. The reasons for this event are disentangled in the following paragraphs.

As already mentioned in the setup chapters, in normal module operation, the AC-strips are connected to the appropriate preamplifier input defining their potential to 0.85V. Thus, in this test, the AC-strips of some channels were bonded to ground to reflect the stress on the coupling capacitor due to an abnormally rised p^+-potential. But voltage peaks over the dielectric layer do not exceed the values observed in LED tests. So, only the same type of destruction is expected, namely broken coupling capacitors visible afterwards. (Compare with damaged sensor G in Section 6.10 on Page 92.) The heat deposition in the dielectric layer, caused by sparks, *cannot* justify melted glue pads.

A possible explanation can be found looking at the electrical energy dissipated by the bulk. Figures 7.13a and 7.13b prove, that the protection of the sensor from a large energy deposition gets lost when decreasing the T-filter resistances. This has already been observed within the LED tests (see Section 6.7.3 on Page 87). But now, the electrical energy dissipation is by a factor of three larger. The deposited heat is drained off via backplane and glue pads possibly melting them or via the conducting silver glue, that is also used in the official module setup to fix the sensors, probably degenerating and destroying it. Breaking silver glue is a known problem in the collaboration. A further stress study of this glue under large pulsed thermal stress is recommended.

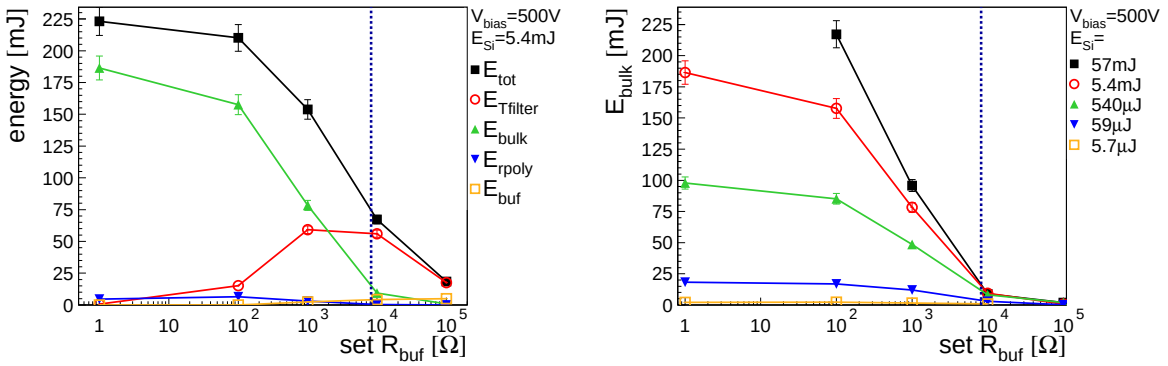

a. Energies vs. R_{buf}

b. Bulk Energy vs. E_{Si} and R_{buf}

Figure 7.13: T-filter dependence of electrical power dissipation. *The energetic analysis of the T-filter resistance scan is shown. The data in Fig. a has been taken at a shot energy of 5.4mJ. Figure b displays the energy dissipated by the bulk for different shot energies at maximum bias (500V). The last point taken at 1Ω and 57mJ is missing due to the destruction of the sensor! The dashed lines denote the CMS design value for the buffer resistor.*

As this happened at first below a resistance of 100Ω, one can conclude, that the safety margin of the officially used T-filter resistors (10kΩ) is 100! Of course, no post-qualification of this sensor has been tried.

It has to be pointed out, that the discussed electrical energies are a multiple of the incident light energy (57mJ). The reason for this is clear. The light energy only is used to separate electrons from holes. The electrical energy is provided by power supply and buffer capacitor to keep the current flowing through all (ohmic) resistors in the sensor circuit.

7.6.3 Protection of Critical Parts

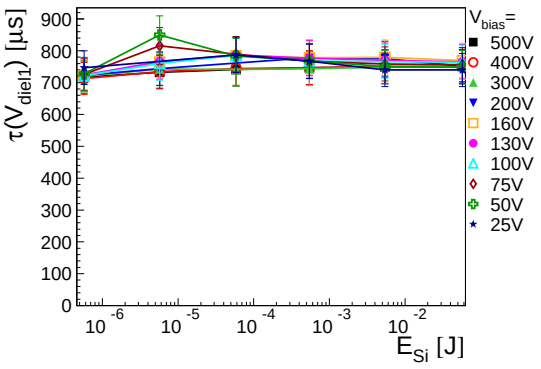

Figure 7.14: Dielectric voltage decay constant. *Depending on the bias resistance and the coupling capacitance, the dielectric voltage decay is a good measure for the constant quality of both sensor properties during a whole test. The two peaks obviously denote a failed analysis as the values return to the baseline afterwards.*

During backplane voltage recovery, the coupling capacitor discharges over the bias resistor. The decay time of the dielectric voltage therefore is $\tau_{diel} = R_{bias}C_C$. The observation of a constant decay time being near the expected value, proves the robustness of the poly-silicon resistors and coupling capacitors during normal resp. protected operation (Fig. 7.14).

7.7 Before and after Test Qualification

The post-qualification of two sensors is available.

Sensor L (low ρ) never has been operated unprotected. It has been perfect after the laser test (see Section C.3 in the Appendix on Page 128) even though it received more than 200 shots (Table 7.2 on Page 98)!

Sensor F (low ρ) showed sparks near the bonded strips. This fact can be disentangeled from its post-qualification data. Three pinholes were created exactly at the bond positions (Fig. C.19 in the Appendix on Page 128). The consequence is a decreased coupling capacitance (Fig. C.18). This figure shows that the whole region arround the bonded strips is affected, probably destroyed! In addition, this can be seen in the strip leakage current (Fig. C.16) and bias resistance (Fig. C.20) measurements.

7.8 Conclusion

The LED test results could be reproduced widely even though pulse duration and energy differ by orders of magnitude.

A low-ρ sensor survived more than 200 shots. 120 were above beam loss energy and 20 of them under full bias. A normally circuited sensor is protected at large energies by the limitation of sensor current and energy and by recombinations.

So, the sensor can stand an energy of $\mathrm{E_{max}} = 57\mathrm{mJ}$ when protected by the correct T-filter-resistors. With a quantum efficiency of about 0.3 [RS 02] and a photon energy of 1.17eV at 1064nm, the average energy needed to create an `EHP` is $\mathrm{E} = 1.17\mathrm{eV}/0.3 = 3.9\mathrm{eV}$. Thus, the number of minimum ionizing particles (`MIP`s) per area unit $\mathrm{T_{max}}$ the sensor can stand at least in one shot is then

$$T_{\max} = E_{\max} / \frac{3.9\mathrm{eV}}{\mathrm{EHP}} / \frac{38000\ \mathrm{EHPs}}{\mathrm{MIP}} / 100\mathrm{cm}^2 = 2.4 \cdot 10^{10} \frac{\mathrm{MIPs}}{\mathrm{cm}^2} \tag{7.1}$$

$$\frac{T_{\max}}{T_{\mathrm{beamloss}}} = \frac{E_{\max}}{E_{\mathrm{beamloss}}} = 24 \tag{7.2}$$

A sensor and its circuit at least can stand single and short pulses with an energy that is 24 times the beam loss energy.

The safety margin of the module design is at least 100!

8 Conclusions on Beam Loss Studies

The robustness of the design of CMS silicon strip tracker modules against likely beam loss scenarios caused by LHC beam dump failures has been demonstrated in three scrutinizing experiments.

The first one has been done at CERN PS by dumping the fast-extracted beam on several modules and their components.[1] Two different types of measurements independently of each other gave the evidence that all the devices under test remained undamaged. All important operational parameters were recorded during the beam impact and showed no indication of any damage. Also lab tests of the devices before and after this experiment confirm this result.

Four problems going beyond the basic question of the robustness of the module design against beam losses were not answered by this test. Firstly, one wanted to be sure that other types of modules also will survive beam losses. Next, the physical and electrical conditions during such an event were not clear. Furthermore, the safety margin of the used design was unknown. And finally, there was no evidence of the robustness of the module design against shots of higher damage potential.

The questions of the robustness of different sensor types againts beam losses and of the conditions in the device during such events have been answered within the scope of a lab test using high intensive IR light from LEDs. Four silicon sensors of different type and one module survived several thousand shots each. By improving the dynamic measurement of operational parameters, a deep comprehension on the mechanisms has been gained. In particular it came out that one part of the module design plays an outstanding role in protecting sensors from beam losses, although this part is not intended for this. Additionally, all measured values have been understood quantitatively by means of a simulation.

The questions concerning safety margin and robustness against higher energies per shot could be answered with the help of a high intensive IR laser. Several laser shots have been applied to modified modules. Components belonging to the design have been exchanged or even removed before yielding to a very comfortable safety margin for the presently used module design. The energy of the laser complied with 24 times the beam loss energy. Thus, a safety margin also has been found on the energy scale.

Finally one can conclude that the design of the CMS silicon strip tracker modules is robust and will survive likely accidental beam losses during LHC-operation.

[1] This experiment had been an LHCC milestone.

A Software for Quality Assurance during Module Production

A.1 Introduction and Motivation

The CMS silicon strip tracker (SST) will consist of about 16000 detector modules. The production of such a large amount requires mass production techniques. Therefore, several collaborating institutes in Europe and the USA are specialised in performing dedicated production tasks. The CMS group in Karlsruhe is involved in *bonding* and qualifying about 1000 tracker end-cap (TEC) modules of Ring5 geometries as well as in repairing and testing TEC modules of all types.

Bonding is a common industrial process to make an electrical connection with reduced space available. One procedure is the so called *ultrasonic welding*, where the ends of a thin Aluminium wire, called *bond*, are melted into metallised surfaces. In the case of Ring5 modules, two bonds have to be placed for each channel, one to join the AC-coupled strips of both sensors and the other one to connect them to the pitch-adapter (PA), that leads the signal to the front end hybrid (FEH). Furthermore, for each module, some bonds are required to connect the sensor's bias ring with the bias current return line. This adds up to about 1550 bond wires to set for each module of Ring5 type requiring a fail-safe, fast and well operable bonding machine as well as experienced technicians.

A module is tested and optically inspected before bonding to detect damages occured during transportation. After bonding, it is qualified, and the technician is instructed in doing eventual improvements. The final qualification is stored in the local and central database.

This test procedure requires an extensive automatisation in finding faults, qualifying modules on the basis of detected faults and in communication with operator and database. Deadlocks during the production process are avoided by reducing user interaction to a minimum.

A further demand has been the ease of maintenance. An expert is able to configure the test software without knowledge of higher programming languages. For example, a very simple script language has been developed to allow the expert to implement his own test procedures. Data tagging and the fault finding process is configurable without modification of the data analysis code.

During the development phase, that started in 2000 and has been finished only a few months ago, sticking to the concept of modularity eased much the extension and debugging of the software.

A.2 Detection and Handling of Module Faults

There are several types of module faults such as strips with a high noise, shorted channels, open bond connections, loss of the capacitive signal coupling by shorting the AC strip with the p^+-implant (so called *pinholes*) and conspicuous channels due to unknown reasons. Module faults have been studied in detail in [Dir03]. Thus, the following paragraphs focus on the application of the gained knowledge and the implementation of the presented methods in a general and automatic module qualification software.

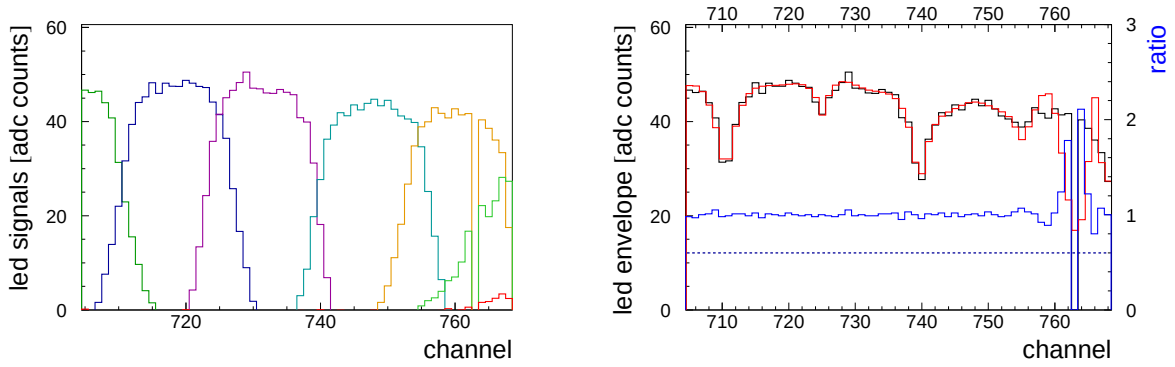

a. LED signals (zoom on affected region)

b. open bond

Figure A.1: Detection of open bonds. *Raw LED signals (Fig. a) are envelopped as well as their fits. The ratio of both gives a good tag on a missing signal connection (Fig. b). The dashed line denotes the cut limit.*

A.2.1 Missing Signal Connection

Incident particles or light are optimal to detect failures in signal transfer. Light emission of fast LEDs was chosen to create reproducable signals in a sensor with respect to intensity and location. About 50 light cones are sufficient to cover the whole width of a sensor. The pitch between two LEDs is such that the overlap of their light cones avoids dead regions. Figure A.1a shows some LED signals near a missing bond connection. All signal shapes are fitted to a polynomial function of higher order. The ratio of envelope respectively maximum value of the raw and fitted shapes gives a failsafe tag on missing signal connections. Figure A.1b displays the envelopes of both raw and fitted data as well as their ratio, detecting that strip 762 is not responding to incident light.

The location of a missing connection can be partially disentangled by illuminating both sensors separately. A signal on the near sensor, while the far sensor is blind, surely is caused by an open bond between both sensors. But a missing signal on both sensors does not stringently point to an open `PA` sensor bond. In some cases, no bond failure or broken AC strip can be detected there optically, so that the reason is supposed to be in the bonded connection between `APV`s and `PA` or within the `APV`'s channel itself. In this case, the channel is lost. But the first mentioned problem can be solved by other dedicated repair centers in the collaboration. In all other cases, the operator is instructed to renew the damaged bond connection and to test the module again.

A.2.2 Pinhole

In case of a *pinhole*, a channel looses its coupling capacitance by developping an ohmic connection between p^+-implant and the Aluminium strip leading to the readout. The preamplifier tries to hold its input potential at a value of $V_{in} = 0.85V$. The strip leakage current I_N flowing from p^+ strip over bias resistor $R_{poly} \approx 1.5M\Omega$, bias ring and the `FEH`'s return line resistor $R_{return} \approx 3k\Omega$ to ground raises on his part the p^+-potential to a defined value. This causes a current I_{PH} flowing into the `APV`'s preamplifier (Fig. A.2 on the next page) driving it into saturation and hence disabling it. Several pinholes assigned to one `APV` may affect the proper operation of the whole readout chip. Therefore, it is important to identify all pinhole channels and remove their electrical connection to the readout.

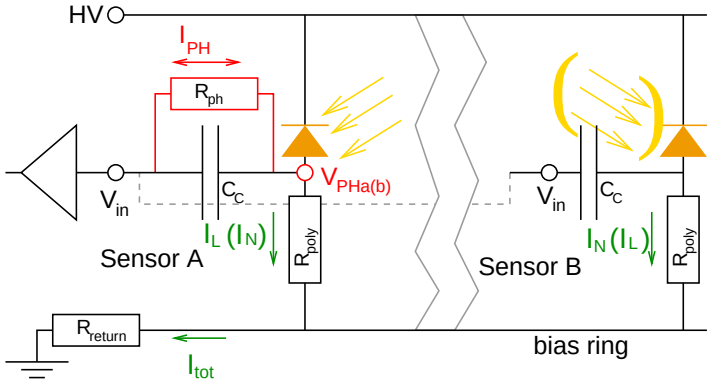

Figure A.2: Schematic of pinhole finding. *In case of a pinhole, the coupling capacitor* C_C *is shunted with a resistor* R_{ph}. *The affected sensor can be disentangled by illuminating both sensors separately (with and without parentheses) Then, different artifical leakage currents are needed to rise the* p^+*-potential at the pinhole* (V_{PH}) *to the preamplifier's input voltage* V_{In}.

Pinhole-identification is done by applying `APV` internal calibration pulses on all channels at different leakage currents created by means of constant LED illumination. The artificial leakage current can be adjusted such that the current flowing through the pinhole is zero and the channel operates undisturbed leading to the maximal calibration gain. Figure A.2 shows currents and voltages for a pinhole on sensor A when illuminating sensor A and B separately. The current flowing through a bias resistor when illuminating the appropriate sensor is I_L. I_N is the current without illumination and is much smaller than I_L ($I_N \ll I_L$). As the number of channels of a Ring5 module is $N_{ch} = 768$, the total current flowing through the bias return line I_{tot} sums up to

$$I_{tot} = N_{ch}\ (I_L + I_N) \approx N_{ch}\ I_L \tag{A.1}$$

The illuminations of sensor A (index a) and sensor B (index b) respectively result in different pinhole potentials $V_{PH_{a(b)}}$.

$$V_{PH_a} = I_{tot}\ R_{return} + I_L\ R_{poly} \approx I_L\ (N_{ch} \cdot R_{return} + R_{poly}) \tag{A.2}$$

$$V_{PH_b} = I_{tot}\ R_{return} + I_N\ R_{poly} \approx I_L \cdot N_{ch} \cdot R_{return} \tag{A.3}$$

If the pinhole potential equals the preamplifier input voltage, no current flows through the pinhole resistor R_{ph} into the preamplifier. This is the case, when the artificially created currents *per strip* ($I_{L_{a(b)}}$) respectively *per sensor* ($I_{tot_{a(b)}}$) fulfill the following relations.

$$V_{PH_a} \stackrel{!}{=} V_{in} \quad \Rightarrow \quad I_{L_a} = \frac{V_{in}}{N_{ch} \cdot R_{return} + R_{poly}} \stackrel{Eq.\ A.1}{\Rightarrow} I_{tot_a} = \frac{V_{in}}{R_{return} + R_{poly}/N_{ch}} \tag{A.4}$$

$$V_{PH_b} \stackrel{!}{=} V_{in} \quad \Rightarrow \quad I_{L_b} = \frac{V_{in}}{N_{ch} \cdot R_{return}} \stackrel{Eq.\ A.1}{\Rightarrow} I_{tot_b} = \frac{V_{in}}{R_{return}} > I_{tot_a} \tag{A.5}$$

$$\tag{A.6}$$

Thus, the evaluation of the calibration gain at different leakage currents gives a clear pinhole signature (Fig. A.3) peaking *roughly* when Eqns. A.4 and A.5 are valid. Comparing the peaking currents of both sensor illuminations gives evidence on the pinhole's location. The gain characteristic peaks at a smaller leakage current when illuminating the affected sensor (Eq. A.5 and Figs. A.3a and A.3b). The typical peaking current for the illumination of the not affected sensor is $I_{tot_b} = \frac{V_{in}}{R_{return}} = \frac{0.85V}{3k\Omega} \approx 300\mu A$. This value is *roughly* verified in Fig. A.3.

Known pinholes from sensor Quality Control Centre (`QTC`) are not bonded at all, and new pinholes are unbonded by the operator. Therefore, all pinholes are reported as open bonds in final module qualification.

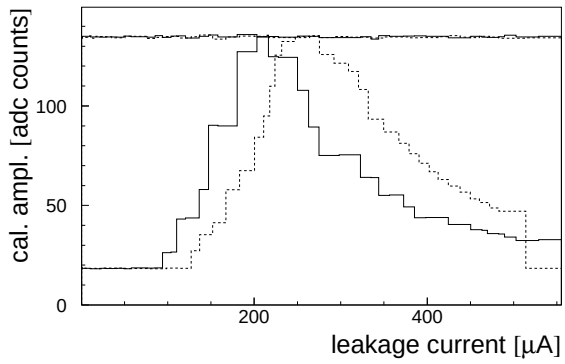

a. pinhole on sensor A and good channel

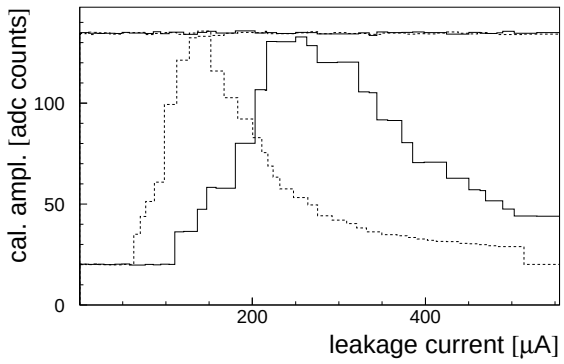

b. pinhole on sensor B and good channel

Figure A.3: Pinhole finding. *Good channels do not show any dependence of their calibration signal height on the leakage current, but so does a pinhole. It can be identified by comparing the calibration signal at different artificial leakage currents. In addition, illuminating both sensors separately gives information on the pinhole's location. (solid line: illumination of sensor A, dashed line: illumination of sensor B)*

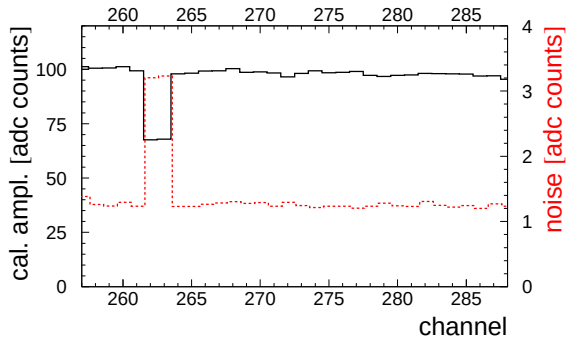

Figure A.4: Detection of shorted strips. *Their signature is clear. Neighboured strips showing a decreased calibration gain (solid line) together with a higher noise (dashed line) are shorted. In the presented example, this is the case for strips 262 and 263.*

A.2.3 Shorted Strips

It is possible that neighboured or next to neighboured channels are shorted by their p^+-strips or their AC-strips. Both give a clear signature but cannot be distinguished. Shorted strips have the double effective coupling capacitance. The total strip capacitance dominates by far the channel noise for not-irradiated modules as the leakage current contribution is neglectible at the beginning of LHC operation [CMS98, CMS00a, Dir03, Wei04]. Therefore, the noise of each shorted channel approximately doubles (solid line in Fig. A.4).

Furthermore, the calibration signal is applied to only each 8^{th} channel amplifier input at the same time [Jon01]. Thus, the charge provided for one channel is distributed over two shorted strips lowering their gain (dashed line in Fig. A.4).

Strips sometimes are shorted by dirt on the sensor's surface. If a short does not dissapear after cleaning, one of the two affected strips is disconnected from the `PA` to reduce the number of module faults by one.

A.2.4 Noisy Channel

Open bonds, shorted strips and pinholes show conspicuousnesses also in the noise spectrum. As mentioned in the previous sections, clearance on the actual fault type give the calibration and light tests. In some cases, the noise of a channel is increased without any evidence from

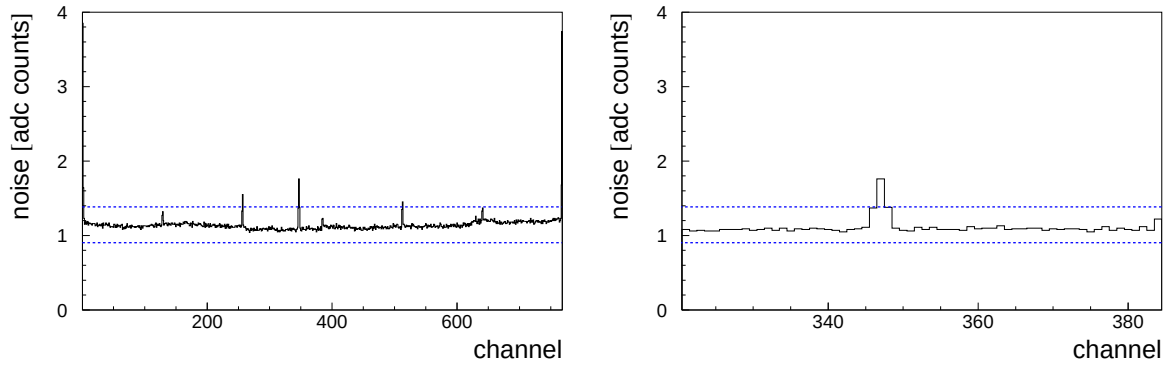

a. view on all channels

b. zoom on critical region

Figure A.5: Error detection with noise. *The chip edges allways show a slightly increased noise and therefore are neglected in this analysis. A noisy region is seen between 346 and 348. No reason for this problem could be found on the basis of module qualification. The straight lines show the low and high cut for fault identification.*

other tests (Fig. A.5). It is likely, that this strip either has a strongly increased leakage current or a damaged amplifying, pipelining or multiplexing stage within the APV. Both cannot be disentangled by the described standard tests on module basis. Thus, this channel is marked as *noisy* but its bond connection is kept.

In rare cases, there are some further faults occuring due to unknown reasons. Channels with a too low noise or a calibration amplitude out of range without showing any problems in the light tests are denoted as *unknown* and count to the total number of module faults as well.

A.2.5 Alternative Fault Detection Methode

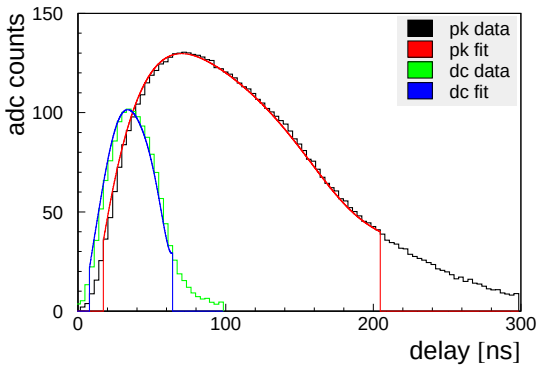

Figure A.6: Calibration pulseshape. *Scanning over the delay time between the calibration signal trigger and the sampling point of time gives the response function of the APV's amplifying stage. The shape of this function differs significantly for both readout modi (peak and deconvolution mode). The fits to both functions used for fault finding is drawn in this plot as well.*

Scanning over the delay time between the calibration trigger and the sampling time of point gives the response function of the APV's shaping stage (Fig. A.6). The shape of this function differs significantly for both readout modes (peak and deconvolution). In peak mode, sampling is done by simply taking the contents of the tagged pipeline cell. In deconvolution mode, the values of three consecutive pipeline cells are convoluted by weighting them. The resulting response function is narrower enabling the discrimination of two consecutive hits on the same channel.

The time of maximum calibration gain, called *peaking time* in this context, can give in-

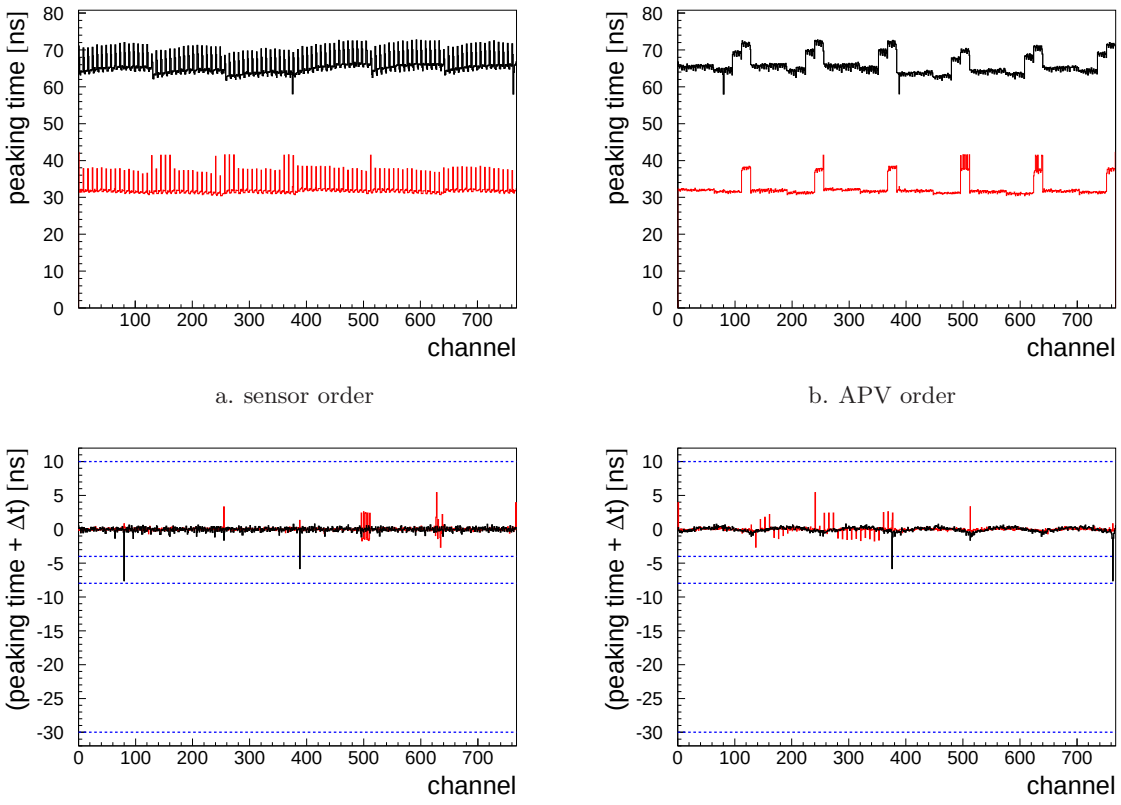

a. sensor order

b. APV order

c. APV order, corrected and cut

d. sensor order, corrected and cut

Figure A.7: Detection of peaking time cut. *In order to be able to detect variances in the calibration pulseshape's peaking time (Fig. a), the data has to be ordered in a special way (Fig. b), corrected (Fig. c) and sorted back to normal order (Fig. d). The two strips out of range (376 and 763) show the pinholes in Fig. A.3 on Page 111. But with this cuts, one cannot disentangle surely wether the pinhole is on sensor A or B. Data from peak and deconvolution mode (smaller peaking time) is shown.*

formation on module faults. The peaking time plotted for each channel (Fig. A.7a) shows periodic deviations comming from different multiplexing stages within the APV. Thus, the data must be firstly sorted back to the so called APV *order* to be able to correct for groups of 16 channels (Fig. A.7c). The data sorted back to the physical sensor order is cut to tag faults (Fig. A.7d).

For example, pinholes and open bonds cause a reduced input capacitance to the amplifier making the channel's signal response faster and the gain curve peaking earlier. The two pinholes shown in a previous chapter are identified in this way (Fig. A.7d). But it is hardly possible to detect the pinhole's location with this methode. Not only therefore, the Karlsruhe Teststations gain most evidence on module faults from the light test results.

A.3 The Karlsruhe Teststations

In the beginning of 2000, the CMS group in Karlsruhe started to develope two stations for module and FEH testing. Various theses cover their electronical and mechanical setup in detail [Hei01, Sch02, Wal03, Dir03, Wei04]. Thus, just a brief overview of components, setup and capabilities is given here.

The so called *Fasttest Station* has been built for automatised, easy and fast module and hybrid tests during preseries qualification and mass production. The *Diagnostic Station* is on the one hand a backup system, on the other hand, its original purpose has been deep module tests in case of problems arising during production.

Both stations have an identical hardware basis consisting of readout and control chain for data acquisition (Section 3.3 on Page 34), high voltage supply for module bias, LED system for fast fault finding and a coincidence setup for signal to noise ratio (`SNR`) studies with cosmic rays. In addition, the *fasttest station* controls the temperature and acquires the module's leakage current enabling automatised IV-curves. An interlock system forbids the operation at open lid to avoid damages to the biased sensor caused by incident light. The *diagnostic station* provides in addition a laser system enabling a better detection of local defects and a stepping motor to allow the movement of a radioactive source or the laser fiber with lid closed. Furthermore, a passive cooling setup, based on cold and dry air, enables tests of irradiated modules. Probe needles enable simple sensor related measurements on-site.

The software has been developped to run on both stations. This requirement only could be fulfilled by means of strict modularity. This enabled the developer to easily disable not needed respectively not running software modules on the appropriate station.

A.4 Software for Karlsruhe Teststations

An extremly detailed technical documentation is given in [Fah05]. Only software aspects of general interest are covered in this section.

A.4.1 Layout

Figure A.8 shows a block diagram of the whole software package for both test stations. Each *separate* block is an independently running process, called *thread*. Each block is one module, eventually embedded into a thread, being either a C++ – or virtual instrument (`VI`)-library, a (perl-) script or a special C-function. LabView [Nat03] is a graphical and data flow oriented programming language used here to provide a graphical user front-end, to visualise data and to control all processes.

The software deals with six different tasks: graphical user interface (`GUI`), run control, communication services, data acquisition (called *readout*), data analysis and environment control (called *slow control*). It is obvious that a large amount of data is exchanged between the processes, namely status and environment information for logging processes and displaying `VI`s, commands from various servers and raw, analysed and qualified module data. There are also a lot of possibilities for the user to interact via user interfaces and configuration files.

Many interprocess communication techniques are applied. Three *Internet sockets* are needed to transfer commands from the run control, implemented in LabView, to the three low level modules readout, analysis and slow control, implemented in C and C++. The analysis task sends plots and qualified data back to the `GUI`. Ping threads keep the sockets alive. Before each module test, a socket connection has to be established with the central tracker database in Lyon to get sensor data needed for module qualification. *Queues* and *notifications* (a kind of one-element queue) synchronise the data flow between threads and are needed here to exchange commands and logging data within the various LabView processes. *Semaphores* coordinate the sequence of different threads and are mainly used to synchronise the readout with the analysis task that are both active during a module test run. A *shared memory* interface cares for a smooth raw data transfer from the data acquisition task (readout) to the only consumer (analysis) by portioning the data in blocks and buffering several of them.

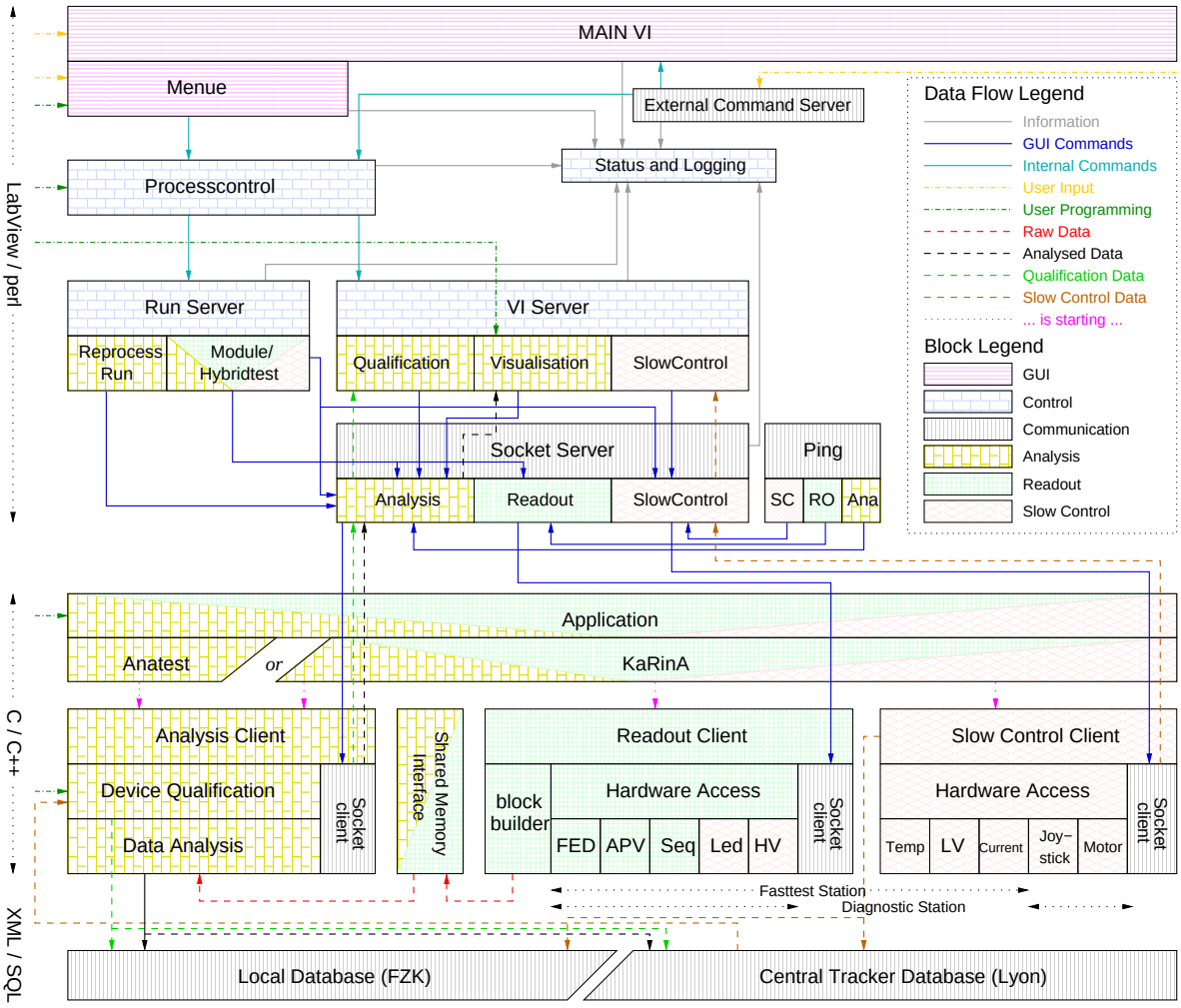

Figure A.8: Block diagram. *Each separate block is an independently running process, called* thread. *Each block (embedded into a* thread*) can be considered as software module being either a C++ –library or a collection of encapsulated LabView-*`VI`*. The failsafe setup of inter-process communication and data flow has been one of the most difficult tasks during software development.*

System signals must be carefully handled since unhandled signals interrupt the software and possibly cause damages to the hardware. An implemented signal handler enabled a first possibility for the user to interact with the running software without access to the `GUI`. This task has been upgraded by installing a *system queue* enabling the submission of commands to the software from a distant computer.

A.4.2 Data Processing

In this section, the complete data path, implemented in the two tasks called *readout* and *analysis* and consisting of acquisition, analysis and qualification, is described. The focus lies on the software aspects after data digitisation and not on the analogue signal chain.

The digitised raw data is read out from the front end driver (`FED`) by the block builder. It collects about 100 events into a higher structure, called *block*, and stores them in the shared memory interface capable of hosting five blocks. The analysis consumer accesses the interface, reads the blocks in the correct order, analyses them and releases the memory afterwards. This can be denoted as a five element queue or first in first out (`FIFO`).

Data analysis is done in several steps. First of all, the raw data is averaged, and the basic corrections like pedestal[1] and common mode[2] subtraction are done.

Afterwards, user defined cuts are applied to the analysed data. The currently used cut definition file is shown below.

```
[TAGS]
# tag = ModTypeList dataid printstatus(print/noprint) cutlevel cuttype cutdirection
#       grouping breakingIdx tag_letter1...tag_letterN cut1...cutN
tag = "" HIS_PED    noprint ABS ABS  HIGH    0 -1 PED 9999. # never tag pedestal
tag = ""               HIS_NOISE print ABS P0  MULTI  128  1 NL  NH  0.79 1.21
tag = H4H6             HIS_NOISE print ABS ABS MULTI    0  1 ANL ANH 0.35 0.90 0.60 1.30
tag = R1nR1sR2nR2sR3R4 HIS_NOISE print ABS ABS MULTI    0  1 ANL ANH 0.75 1.50 1.00 2.20
tag = R5nR5sR6R7OB1OB2 HIS_NOISE print ABS ABS MULTI    0  1 ANL ANH 0.80 2.00 1.20 2.40
tag = "" HIS_CALA      print P1  P1   LOW   128 -1 CL 0.2
tag = "" HIS_CALA      print ABS ABS  LOW     0 -1 ACL -60. -30.
tag = "" HIS_PHMAX0    print P1  P1   LOW   128 -1 PCL0 0.2
tag = "" HIS_PHMAX1    print P1  P1   LOW   128 -1 PCL1 0.2
tag = "" HIS_PHMAX0    print ABS ABS  LOW     0 -1 PACL0 -60. -30.
tag = "" HIS_PHMAX1    print ABS ABS  LOW     0 -1 PACL1 -60. -30.
tag = "" HIS_PEAKAMPL  print P1  P1   LOW   128 -1 PL 0.2
tag = "" HIS_PEAKAMPL  print ABS ABS  LOW     0 -1 APL -60. -30.
tag = "" HIS_LED0      print P0  ABS  LOW     0 -1 L0 0.4
tag = "" HIS_LED1      print P0  ABS  LOW     0 -1 L1 0.4
tag = "" HIS_PHTAG     print ABS ABS  MULTI   0  1 PH1 PH0 -0.05 0.05
tag = "" HIS_LEAK0     print ABS ABS  HIGH    0 -1 HPH0 0.1
tag = "" HIS_LEAK1     print ABS ABS  HIGH    0 -1 HPH1 0.1
tag = "" HIS_NOTBONDED print ABS ABS  MULTI   0  0 PS SS  0.5 1.5
tag = "" HIS_SENSDBPH  print ABS ABS  MULTI   0  0 S0 S1  0.5 1.5
# ##### tags that are supported but not used in fault finding
tag = "" HIS_CALSHAPE noprint ABS ABS  SYM   0 -1 SP 0.03
tag = "" HIS_PLPED     print P0  RMS  SYM     0 -1 PP 5.0
tag = "" HIS_PLNOISE   print P0  RMS  SYM     0 -1 PN 5.0
tag = "" HIS_PLCAL     print P0  RMS  SYM     0 -1 PC 5.0
# ##### task force tags
# tag = "" HIS_NOISE    print ABS ABS MULTI 128 3 NPH NTSO NOSO NNOIS 0.6 1.0 1.3 2.0 0.95 1.4 1.7 2.4
# tag = "" HIS_CALA     print ABS P0  MULTI 128 1 CLOW CHIGH 0.85 1.15 0.8 1.2
tag = "" HIS_PEAKTIME noprint P1  ABS MULTI 16  3 TPH TTSO TOSO TNOIS -30. -8. -4. 10. -30. -4. -2. 10.
# tag = "" HIS_PHTP     print MAX ABS LOW    0 -1 TF_PH 40.0
```

Cuts may be configured for each data array by specifying the cut parameters, the grouping for corrections and an arbitrary amount of tags together with their appropriate thresholds even for all four basic APV modes separately. Three properties must be given for each cut. The cut level specifies wether and how the data should be corrected before applying the threshold(s). The cut type specifies the meaning of the threshold value. It is either an absolute value, a multiple of the mean (polynomial fit of 0^{th} order) or a multiple of the root mean square (RMS). The cut direction is either low, high or multiple. Multiple tags and thresholds are defined together with a multiple cut to specify ranges for the appropriate tag. Cut levels and types may also be polynomial fits of higher order. The straight line fit is used frequently to correct for large scale shapes in data. This analysis step results in a map, containing all tags that have been found for each channel.

Correlations between tags of different channels can be evaluated. The corresponding definition file is seen below.

```
[CORRELATED_TAGS]
# correlated = moduletype_list tag_letter center_expression neighbour_letter neighbour_expression
# neighbour_list neighbour_operator neighbour_mode(override/true/false) printstatus(print/noprint)
correlated = "" calmisstag CL calmisstag CL 8 1008 120 & override print
correlated = R1nR1sR2nR2sR5nR5sOB1H6 veto T veto T 1 766 0 1128 768 127 1128 768 & false noprint
correlated = R3R4R6R7OB2H4           veto T veto T 1 510 0 1128 512 127 1128 512 & false noprint
correlated = H4H6 CLcl "(CL|ACL)&!calmisstag" "" T -1 1 | override print
correlated = R1nR1sR2nR2sR3R4R5nR5sR6R7 CLcl <PL|APL>|{PCL0|PCL1|PACL0|PACL1} "" T -1 1 | override print
correlated = "" SH !H4&!H6&CLcl&(!L0&!L1) "" CLcl -2 -1 1 2 | override print
correlated = "" AND_L1 L1|R4|R3|R2n|R2s|R1n|R1s      "" T -1 1 | override noprint
correlated = "" noika !veto&(NH|ANH)     "" !{(L0&AND_L1)} -1 1 & override print
correlated = "" noidb !veto&NH           "" !{(L0&AND_L1)} -1 1 & override print
correlated = "" TSO L0&AND_L1 "" T -1 1 | override print
correlated = R5nR5sR6R7OB2 MSO !L0&L1 "" T -1 1 | override print
correlated = R1nR1sR2nR2sR3R4H4H6 MSO F "" T -1 1 | override noprint
```

A Logical expression combines the tags, and a pattern defines the channels to correlate. For example, the detection of shorted channels is possible with this feature as well as the

[1] event independent offset different for all channels

[2] event dependent offset equal for all channels of an APV

rejection of the strip edges in noise analysis. Each correlation gives a new tag in the channel map. The interested reader is referred to the manual for more details.

The hence obtained tags (e.g. "high noise", "missing LED signal on sensor B", "pinhole characteristic", "neighboured strip has also a low calibration gain", etc.) are logically combined to module faults. The fault definition is listed below.

```
[FAULTS]
# fault= ModTypeList dbflag faultid description "logical fault expression"
fault = H4H6                        2048 NOI+ "noise problem"       "(NL | NH | ANL | ANH)&!veto"
fault = H4H6                        4096 CAL+ "cal problem"      CLcl
fault = R1nR1sR2nR2sR3R4R5nR5sR6R7OB2    0 ???? unknown NL|ANL|noika|PL|CLcl|L0|L1|PH0|PH1|HPH0|HPH1
fault = R1nR1sR2nR2sR3R4R5nR5sR6R7OB2 1024 ???? unknown NL|    noidb|PL|CLcl|L0|L1|PH0|PH1|HPH0|HPH1
fault = R1nR1sR2nR2sR3R4R5nR5sR6R7OB2    0 NOIS noisy     noika
fault = R1nR1sR2nR2sR3R4R5nR5sR6R7OB2   64 NOIS noisy     noidb
fault = "" 128 SHT+ "short"        SH
fault = ""   0 PSMI "pa sensor bond set by mistake"     "!TSO & PS"
fault = ""   0 SSMI "sensor sensor bond set by mistake" "(!MSO&!TSO) & SS"
fault = ""   0 PDB0 "ph on sensor0 in db but no ph found" S0
fault = ""   0 PDB1 "ph on sensor1 in db but no ph found" S1
fault = ""   0 PHH0 "high leak problem on sensor0" HPH0
fault = ""   0 PHH1 "high leak problem on sensor1" HPH1
fault = ""   0 PHH2 "high leak problem on both sensors" HPH0&HPH1
fault = ""   2 PSO+ "pa sensor open"                    "TSO&!PS&!SO"
fault = ""   2 PSNB "pa sensor open (not bonded!)"      " TSO & PS"
fault = ""   2 PSDB "pa sensor open (ph in sensor db)"  " TSO & S0"
fault = ""   8 SSO+ "sensor sensor open"                " MSO&!SS&!S1"
fault = ""   8 SSNB "sensor sensor open (not bonded!)"  " MSO & SS"
fault = ""   8 SSDB "sensor sensor open (ph in sensor db)" "MSO&S1"
fault = "" 256 PHL0 "pinhole on sensor0 (not present in sensor db)"      PH0
fault = "" 256 PHL0 "pinhole on sensor0 (sensor db confirmed)"           PH0&S0
fault = "" 256 PHL0 "pinhole on sensor0 (sensor db missmatch)"           PH0&S1
fault = "" 256 PHL1 "pinhole on sensor1 (not present in sensor db)"      PH1
fault = "" 256 PHL1 "pinhole on sensor1 (sensor db confirmed)"           PH1&S1
fault = "" 256 PHL1 "pinhole on sensor1 (sensor db missmatch)"           PH1&S0
fault = "" 256 PHL2 "pinhole on both sensors (not present in sensor db)" PH0&PH1
fault = "" 256 PHL2 "pinhole on both sensors (sensor db confirmed)"      PH0&PH1&S0&S1
fault = "" 256 PHL2 "pinhole on both sensors (sensor db missmatch)"      PH0&PH1&((S0&!S1)|(!S0&S1))
```

This file is processed top down for each channel allowing the expert to give the faults a priority, since a channel may have several tags but only one fault, e.g. "noisy", "pinhole", "open bond" etc.

Instructions for the bonding operator are assigned to faults. For example, a detected pinhole on channel 12 will cause the operator to be instructed to remove its PA-bond.

The final step leads to the module's qualification. The number of all faults determines the grade of the module together with the leakage current measured at a bias voltage of 450V. The criteria of all five grades are summarised in Table A.1. Modules of grades A and AF are

grade	fraction ϵ of faulty channels		leakage current I at 450V
A	$\epsilon < 1\%$	*and*	$I \leq 5 \times I_{DB}$
AF	$\epsilon < 1\%$	*and*	$5 \times I_{DB} < I \leq 10\mu A$
B	$1\% \leq \epsilon \leq 2\%$	*and*	$I \leq 5 \times I_{DB}$
BF	$1\% \leq \epsilon \leq 2\%$	*and*	$5 \times I_{DB} < I \leq 10\mu A$
C	$\epsilon > 2\%$	*or*	$I > 10\mu A$

Table A.1: Module grading [Dir03]. *The module's leakage current I is compared with the sensor's leakage current* I_{DB} *measured during* QTC *and obtained from the central tracker database before and during the module test.*

built into the tracker for sure. Grade B and BF modules are spares. When using them, they should be uniformly distributed on all *petals*, the next larger structure in the SST. Grade C modules are rejects.

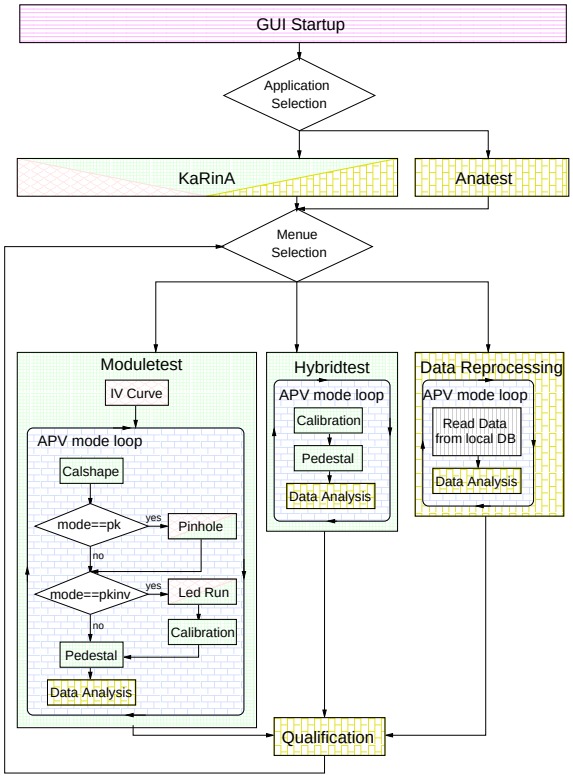

Figure A.9: Flow chart of test processes. *The color convention is equal to Fig. A.8 on Page 115. Starting the main readout application* KaRinA *allows the call of module and hybrid tests, whereas* anatest *is for data reprocessing purposes only. But the analysis module is the same in both applications.*

A.4.3 Test Procedure

This section describes all test capabilities of the software, in particlar all three standard test procedures, the module and hybrid test and the data reprocessing. See Fig. A.9 for all relevant facts.

First of all, the operator must decide wether he wants to test a device or reprocess any old data by either starting the application *KaRinA* or *anatest*. The analysis code is the same in both applications having eased much maintenance and debugging. After this selection, the `GUI` main window becomes operable (Fig. A.10). Test runs are started from a user programmable menue. Menue items and up to two parameters may be configured for each entry as well as the section in the central run control file that should be triggered after clicking the item. This file, also called *process control*, has its own and very simple language allowing the user to implement his own test runs. Loops, conditioned execution, function calls, variables and the invokation of external commands are possible. All settings configured in the settings definition file may be changed within a run script or outside a run by means of a dedicated `VI` (Fig. A.11). The reader again is referred to the manual to obtain a comprehensive documentation of all language elements. The implementations of the module test is given below and can be verified in the flow chart (Fig. A.9).

```
[moduletest]
cleandb
SET = runname "module test run:"
SHOWLOG = $runname initialising
INIT
changedevice = "with settings"
begintest
SET = cal cal
IF "$1" == "pk dc pkinv dcinv"
  totalevents = 90000
ELSE
  totalevents = 30000
FI
IF $STATION == fasttest
  ivcurve = 1
  writedb
ELSE
  SHOWLOG = won't do IV curve: we are at $STATION station
FI
hv_voltage = 400
hyb_pow = 1
FOR withoutcal = $1
  SHOWLOG = $runname mode $withoutcal: begin of mode
  SET = withcal $withoutcal$cal
  submitsettings = APV
  apvmode_withcuts = $$withcal
  apv_ical      =  120 # 2 MIPs
  blocks        =    1
  events        =  500
  beginmode
```

```
  # cal shape run
  SHOWLOG = $runname mode $withcal: begin of cal shape run
  setlatency
  eventsperblock = 118
  start = RUN_PED
  eventsperblock = 20
  start = RUN_CALSHAPE
  writedb
  SHOWLOG = $runname mode $withcal: end of cal shape run
  IF ph_mode == $$withcal
    # pinhole run
    SHOWLOG = $runname mode $withcal: begin of pinhole run
    ilum_start =  30
    ilum_end   = 150
    ilum_step  =   2
    start = RUN_PINHOLE
    eventsperblock = 118
    SHOWLOG = $runname mode $withcal: high leak pedestal run
    led_ilum_sensor1 = 130
    led_ilum_sensor2 = 130
    start = RUN_PED 2
/* obsolete pinhole run
    beginpinholerun = 60 130 2
    FOR ilum = 60 ... 130 2
      SHOWLOG = doing led illumination $ilum (step $INDEX_ilum/36)
      led_ilum_sensor1 = $ilum
      led_ilum_sensor2 = $ilum
      # submit = readout CMD_DCU_MEASURE
      eventsperblock = 118
      start = RUN_PED
      eventsperblock = 20
      start = RUN_CAL
#     writedb
    ROF
    endpinholerun
*/
    SHOWLOG = $runname mode $withcal: end of pinhole run
  FI
  apv_mode = $$withoutcal
  IF led_mode == $$withoutcal
    SHOWLOG = $runname mode $withoutcal: begin of led run
    # led run
    seq_led_latency     =  131
    led_activate        =    1
    disable_led_array   =    0
    led_ilum_sensor1    =   50
    led_ilum_sensor2    =   50
    apv_vpsp            =   17
    # led_array         =    2
    led_voltage         =  180
    events              = 1000
    eventsperblock = 118
    start = RUN_PED
    eventsperblock = 20
    start = RUN_LED
    writedb
    led_ilum_sensor1 = 0
    led_ilum_sensor2 = 0
    apv_vpsp         = $DEFAULT
    SHOWLOG = $runname mode $withoutcal: end of led run
  FI
  led_ilum_sensor1 = 0
  led_ilum_sensor2 = 0
  # cal run
  IF cal_mode == $$withcal
    SHOWLOG = $runname mode $withcal: begin of calibration run
    events = 500
    eventsperblock = 118
    apv_mode = $$withcal
    start = RUN_PED
    # put this cal run into db
    start = RUN_CAL 1
    writedb
    SHOWLOG = $runname mode $withcal: end of calibration run
  FI
  # ped run
  SHOWLOG = $runname mode $withoutcal: begin of pedestal run
  events = 5000
  eventsperblock = 118
  apv_mode = $$withoutcal
  # put this ped run into db
  start = RUN_PED 1
  writedb
  SHOWLOG = $runname mode $withoutcal: end of pedestal run
  endmode = $$withoutcal $INDEX_withoutcal
  # save all histograms of this mode
  histo_write
  SHOWLOG = $runname mode $withoutcal: end of mode
ROF
SHOWLOG = $runname entering qualification
endtest
finishdb
JUMPONSTOP
IF $STOPPED == TRUE
  SHOWLOG = $runname stopped by user or exception
  cleandb
FI
SHOWLOG = $runname resetting #$
DEFAULT
hv_voltage = 0
hyb_pow = 0
```

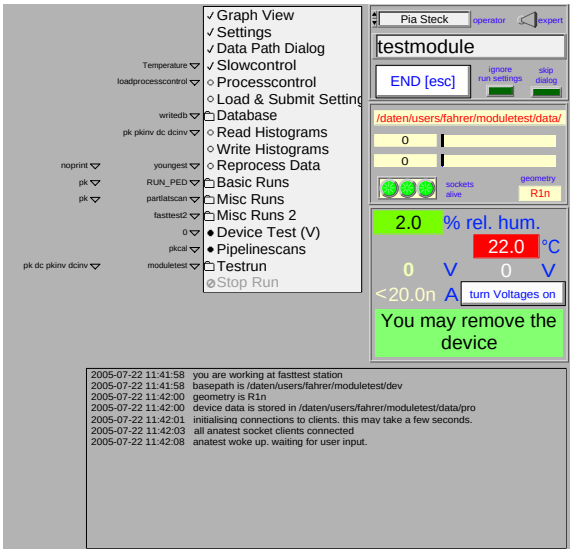

Figure A.10: `GUI` main window. *All relevant user controls and displays are placed there, namely menue, log and environment and readout information. The menue is user programmable and is directly connected to the processcontrol code.*

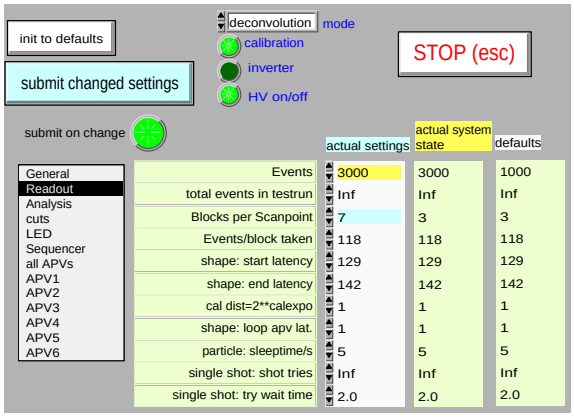

Figure A.11: Settings window. *All default settings as well as their description printed here, their ranges, increment and precission can be configured without knowledge of LabView programming.*

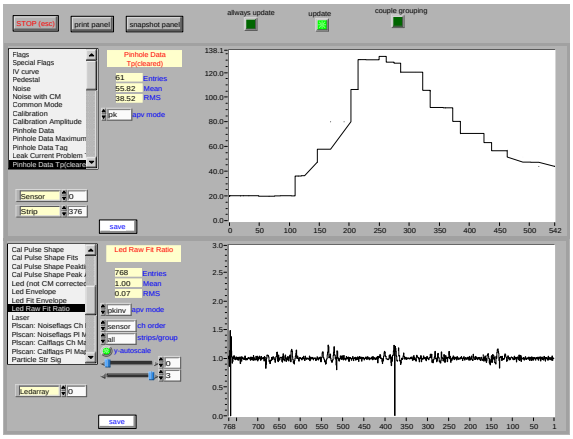

Figure A.12: Data viewer. *Two plots can be viewed and processed independently at the same time. Type, dimensions and simple scaling properties are configurable without modification of this* `VI`.

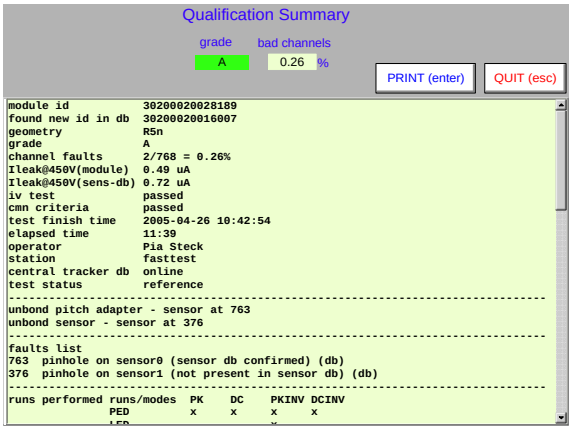

Figure A.13: Qualification window. *This window pops up at the end of a device test and shows the grading result and the test report in text format.*

During a module and hybrid test, the basic runs (pedestal and calibration run) are done for each of the four APV modes (peak and deconvolution mode each with inverter stage on and off). The light runs in case of a module test are done only at one mode. During and after a test, all taken and analysed data can be viewed (Fig. A.12). All device tests as well as data reprocessing use the same data qualification module. According to the analysis procedure developped in Section A.4.2 on Page 115, the device is qualified and the test report is displayed (Fig. A.13) and sent per e-mail to all involved persons. An example report follows.

```
module id           30200020028385
geometry            R5s
grade               A
channel faults      3/768 = 0.39%
Ileak@450V(module)  0.77 uA
Ileak@450V(sens-db) 1.13 uA
iv test             passed
cmn criteria        passed
test finish time    2005-12-05 15:16:41
elapsed time        08:19
operator            Pia Steck
central tracker db  online
------------------------------------------------------------
check pa-sensor and apv-bond at 696 657
check sensor - sensor at 231
------------------------------------------------------------
faults list
696  pa sensor open (db)
657  pa sensor open (db)
231  sensor sensor open (db)
------------------------------------------------------------
runs performed runs/modes  PK    DC    PKINV DCINV
               PED         x     x     x     x
               LED                     x
               CAL                     x
               PINHOLE     x
               CALSHAPE    x     x     x     x
               IVCURVE     x     x     x     x
------------------------------------------------------------
Noise          apvs/modes  PK    DC    PKINV DCINV
               all         1.33  1.72  1.33  1.75
               0x40        1.32  1.70  1.32  1.74
               0x42        1.29  1.68  1.30  1.70
               0x44        1.32  1.73  1.32  1.76
               0x46        1.31  1.68  1.31  1.72
               0x48        1.35  1.71  1.34  1.74
               0x4a        1.41  1.81  1.41  1.84
------------------------------------------------------------
Common mode    apvs/modes  PK    DC    PKINV DCINV
               all         0.32  0.47  0.28  0.40
               0x40        0.28  0.44  0.27  0.39
               0x42        0.34  0.51  0.29  0.43
               0x44        0.30  0.46  0.26  0.38
               0x46        0.32  0.47  0.28  0.40
               0x48        0.31  0.46  0.27  0.39
               0x4a        0.34  0.51  0.30  0.43
------------------------------------------------------------
Calibration    apvs/modes  PK    DC    PKINV DCINV
               all         78.4  55.3  77.7  55.8
               0x40        78.0  55.3  77.2  55.8
               0x42        77.7  54.9  77.1  55.4
               0x44        77.6  55.7  77.0  56.2
               0x46        77.2  54.4  76.4  55.1
               0x48        75.0  52.1  74.2  52.7
               0x4a        85.0  59.3  84.1  59.6
------------------------------------------------------------
bad channel list for PK(p) DC(d) PKINV(P) DCINV(D)
sensor_order (daq_order db_order) fault_type [db] flag_list
768 (  0   1)           NH:pdP
696 ( 72  73) PSO+ db   NL ANL:pP L0:P L1:P po:P
657 (111 112) PSO+ db   NL ANL:pP L0:P L1:P po:P
640 (128 129)           NH:pP
512 (256 257)           NH:pP
256 (512 513)           NH:pP
231 (537 538) SSO+ db   NL:pP ANL:pP L1:P so:P
  1 (767 768)           NH:p
```

A template file in extended markup language (`XML`) [TRK02, ARC06] is prepared to report the test results to the central tracker database and stored locally until its upload. The test data is automatically stored while carefully keeping old tests of the same module or hybrid in an attic file structure.

A.5 Conclusion

	A	AF	B	BF	C	Σ
H4	51		1		7	59
H6	759				28	787
R1n	2	1				3
R1s	1					1
R2n	8		1		1	10
R2s	3				1	4
R3	87		1		6	94
R4	12				2	14
R5n	502	8	16	1	6	533
R5s	360		15	1	8	384
R6	18				4	22
R7	25		1	1	1	28
OB2	1				2	3
Σ	1829	9	35	3	66	1942

Table A.2: Summary of tested modules. *All tested geometries and the multiplicities of obtained grades is listed.* H4 *and* H6 *denote hybrids with four and six* APVs *respectively. The large amount of grade C hybrids is due to hardware problems arised during production phase. The effect of this failure on the data could be ironed out by means of software extensions. The numbers are as of June,* 14^{th} *2006.*

The mass production of Ring5 modules finishes in Karlsruhe in Autumn 2006. Up to now, about 790 modules of this type have been bonded and tested together with the same amount of hybrids (see Table A.2). A production and test rate of five per day has been reached almost throughout. The test of a module consisting of two sensors lasts only 8 minutes. So, this task is never the bottleneck during production. The aim of wide automatisation has been achieved, thus few interactions between operator and expert were necessary within the second production phase. Devices of other geometries were tested within the scope of pre-series, irradiation studies, R&D and repairs.

B LED Test Raw Data

All data in this chapter comes from the standard LED test of sensor E (HPK) under usual conditions, namely biased by the Oltronix power supply and protected by the normal T-filter.

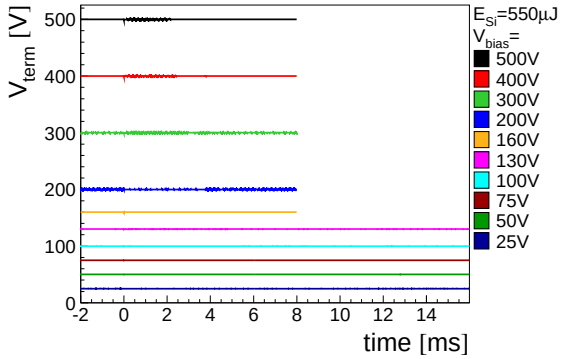

Figure B.1: Terminal voltage vs. time and V_{bias}. *Its perfect permanence is used in the simulation.*

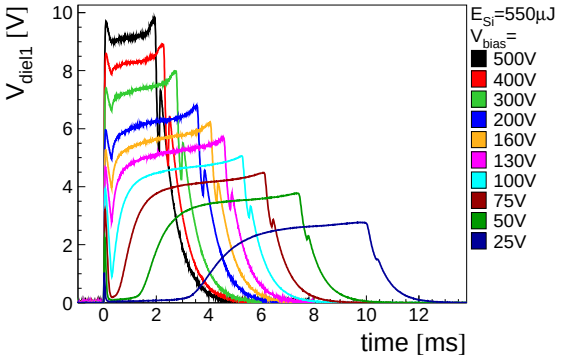

Figure B.2: Voltage over the dielectric layer vs. time and V_{bias}. *There is no simulation available.*

measurement **SPICE simulation**

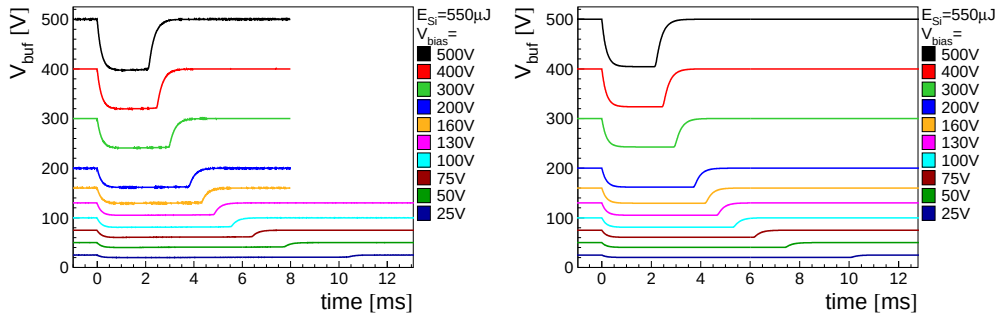

Figure B.3: *Voltage drop over buffer capacitor vs time and* V_{bias}.

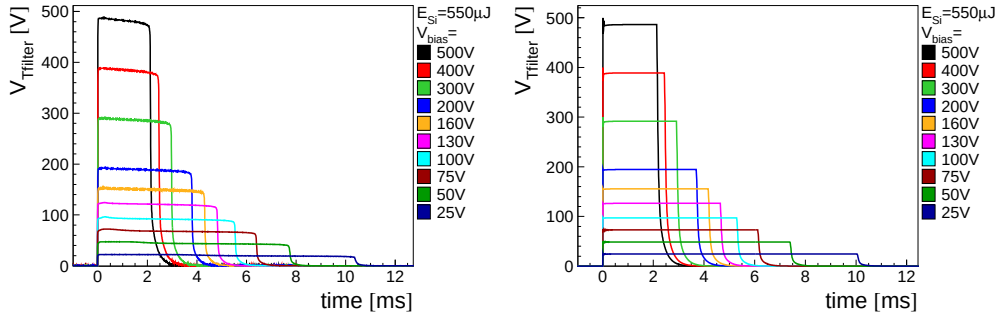

Figure B.4: *Voltage drop over T-filter resistors vs time and* V_{bias}.

measurement **SPICE simulation**

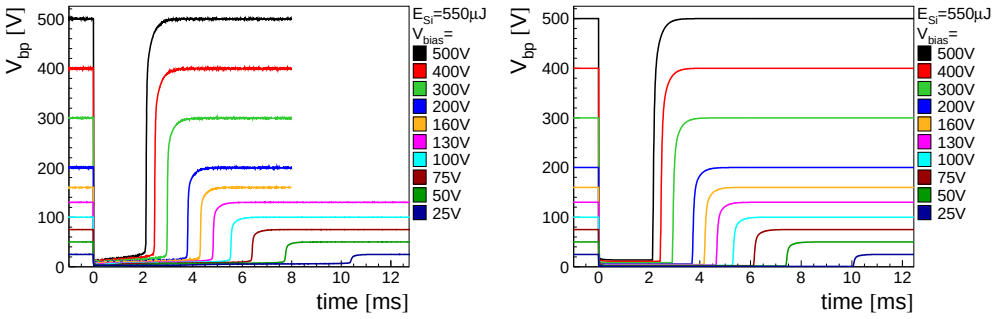

Figure B.5: *Backplane voltage vs time and* V_{bias}.

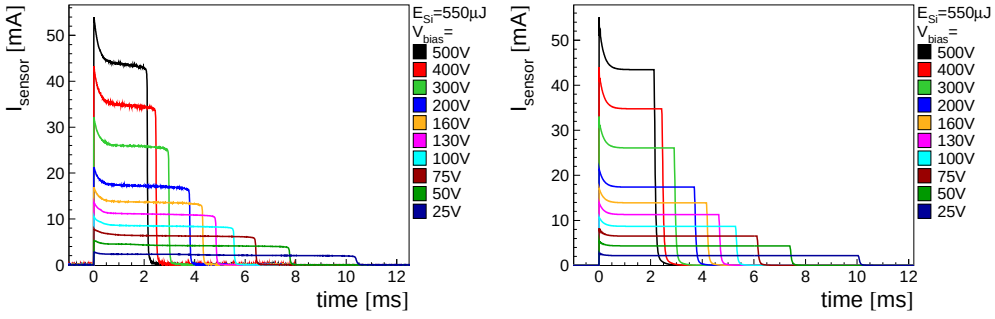

Figure B.6: *Bulk current vs time and* V_{bias}.

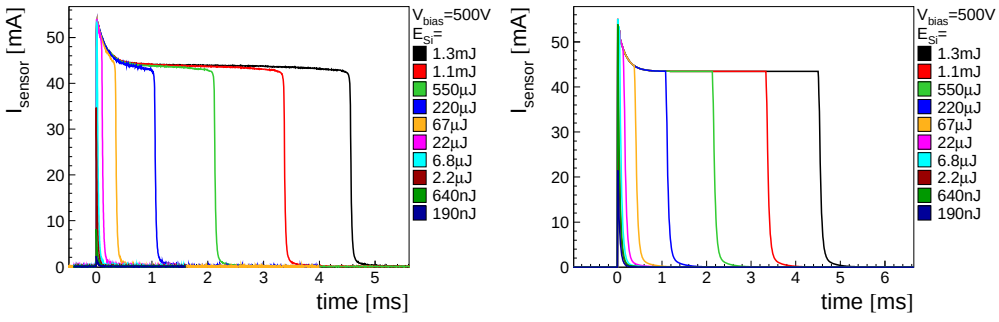

Figure B.7: *Bulk current vs. time and* E_{Si}.

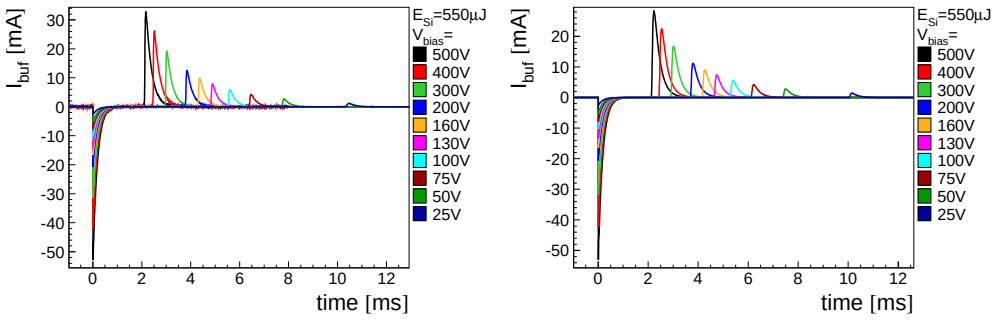

Figure B.8: *(Dis-) charging current of buffer capacitor vs time and* V_{bias}.

C Qualification Data

C.1 Testbeam Qualification

C.1.1 Hybrid Qualification

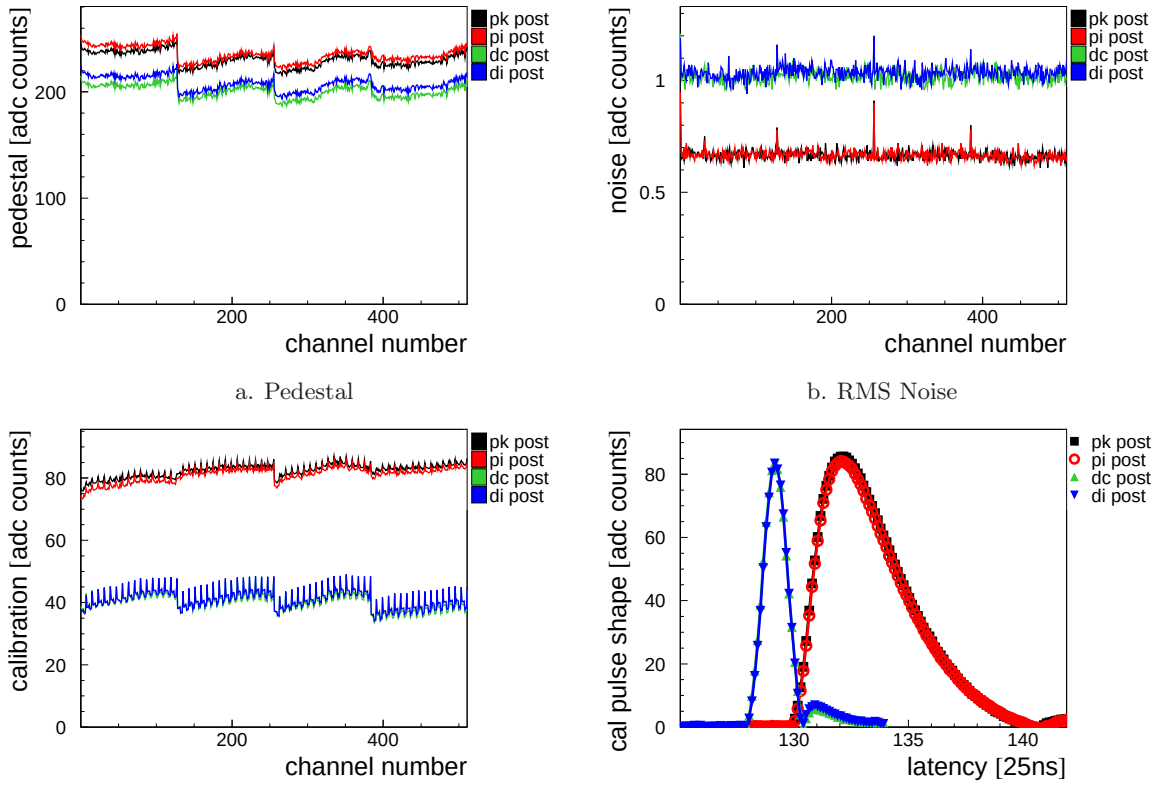

a. Pedestal

b. RMS Noise

c. Calibration Amplitude

d. Calibration Pulseshape

Figure C.1: After beam FEH qualification in all four APV modes *Pedestal, RMS noise, calibration signal amplitude and preamplifier signal shape of the hybrid during post-qualification in the lab. The hybrid was fine before the test and shows appropriate behavior afterwards. The four APV modes are abbreviated as follows: peak (pk), deconvolution (dc), peak with inverter on (pi), deconvolution with inverter on (di).*

C.1.2 Module Qualification

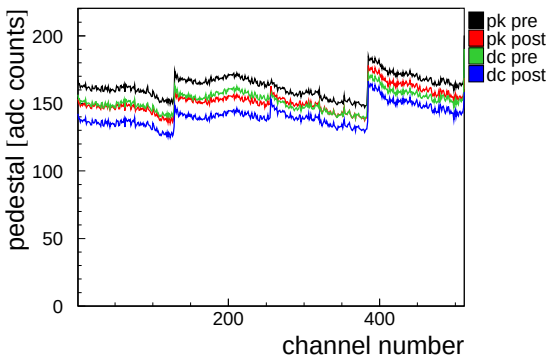

a. Pedestal

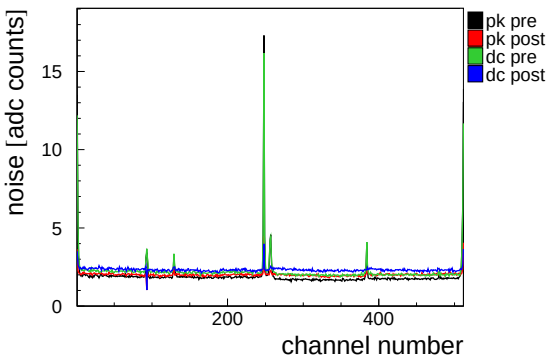

b. RMS Noise

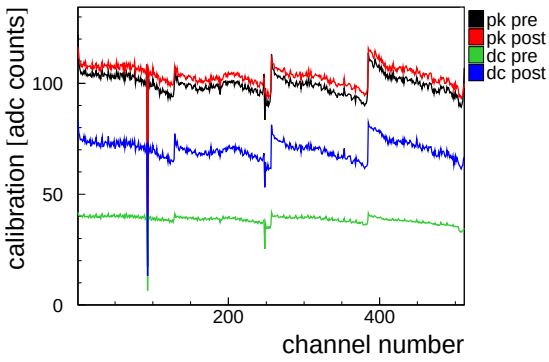

c. Calibration Amplitude

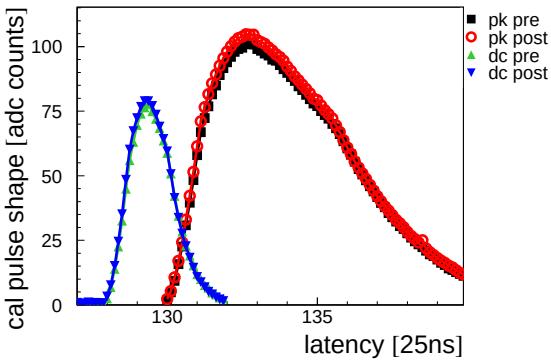

d. Calibration Pulseshape

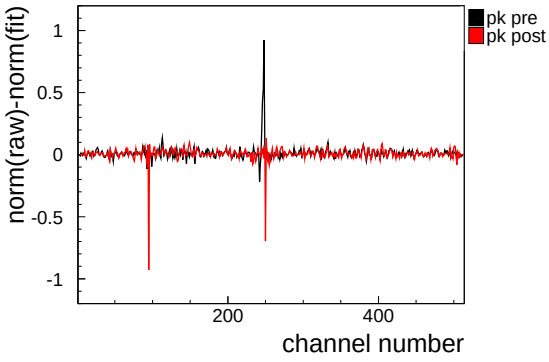

e. LED test of 1st sensor

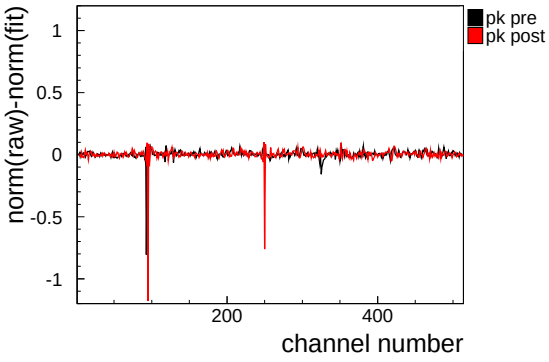

f. LED test of 2nd sensor

Figure C.2: Before and after beam module qualification. *Module M is of* `TEC` *geometry. No additional errors appeared after the beam. The basic test data has been taken in peak (pk) and deconvolution mode (dc): Pedestal (fig. a), noise (fig. b), calibration signal amplitude (fig. c) and calibration pulse shape (fig. d). The pulsed LED test has been done in peak mode (figs. e and f). The plots show the difference between LED signal and polynomial fit in units of maximum led signal amplitude taken with four infrared LED arrays placed at different positions along the strips in increasing distance to the pitch adapter. Two positions are shown: near sensor (fig e) and far sensor (fig f). They indicate sensor failures like open bonds, shorts and pinholes. Postqualification data is plotted with a slight x-offset.*

C.1.3 Sensor Qualification

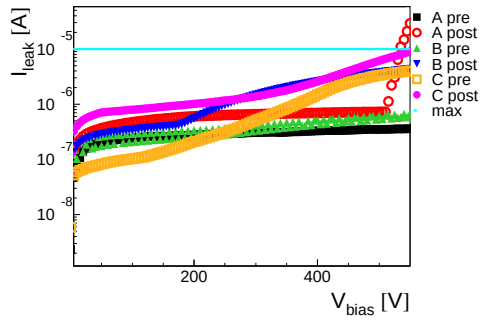

Figure C.3: Global leakage current. *The maximum allowed current of 10μA at 450V [CMS00b] is drawn. All curves stayed below this threshold after the testbeam. The starting break-through at 550V for Sensor A can be explained with careless handling.*

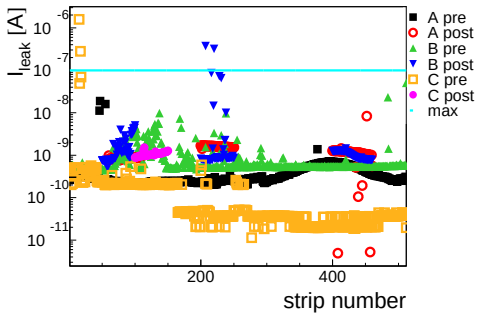

Figure C.4: Strip leakage currents. *The maximum allowed current per strip is 100nA at $V_{bias} = 450V$ [CMS00b]. The problems of Sensor B afterwards are due to silicon from old production.*

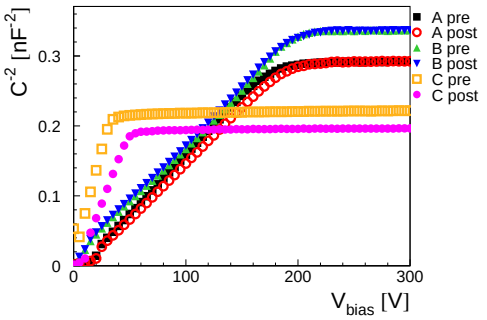

Figure C.5: Global capacitance. *Resulting depletion voltages (listed in Appendix E.1) should be between 100V and 300V [CMS00b]. Only slight deviances are observed before and after. Sensor C generally being out of specification has been taken from a pre-series and is accepted for special purposes.*

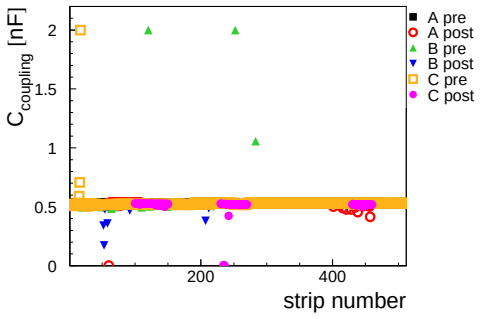

Figure C.6: Coupling capacitances. *Values around 500pF are expected [CMS00b]. The values 0,1 and 2nF are artificially set by the* `QTC` *indicating strip failures. The problems of Sensor B could be explained with a bad contact during measurement. Only the regions arround the bonded strips have been measured at post-qualification.*

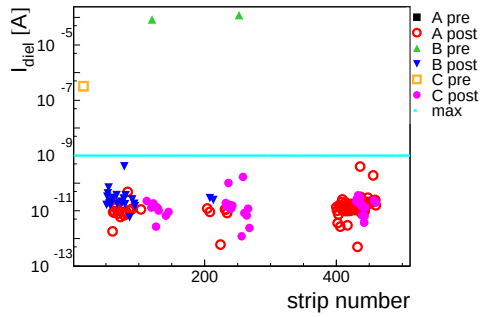

Figure C.7: Pinhole measurement. *The threshold for the dielectric current at a constant voltage of $V_{diel} = 120V$ is 1nA [CMS00b]. The pre-beam measurements only show those channels with a dielectric current exceeding this limit indicating pinholes. No pinholes were found after the beam arround the bonded regions.*

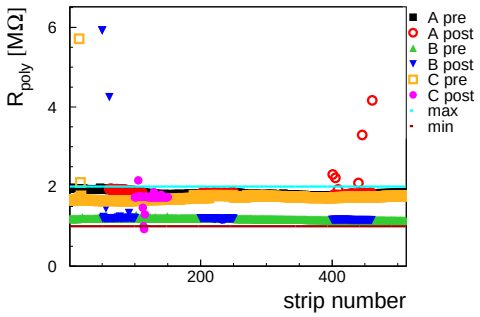

Figure C.8: Bias resistances. *The expected range is between 1 and 2MΩ [CMS00b]. Problems of Sensor A afterwards again can be explained with bad handling of the sensor. Values of above 3MΩ most likely are failed measurements.*

C.2 LED Test Qualification

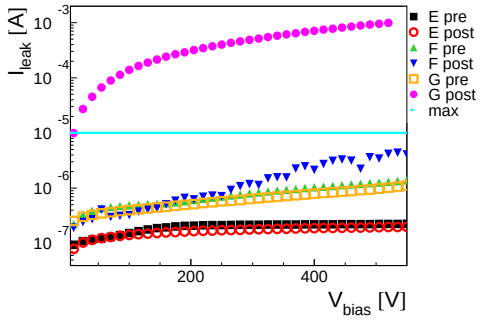

Figure C.9: Global leakage current. *The maximum allowed current of 10μA at 450V [CMS00b] is drawn. The currents of Sensors E and F stayed below this threshold after the tests. Sensor G got a destructive LED test and can be considered as defective.*

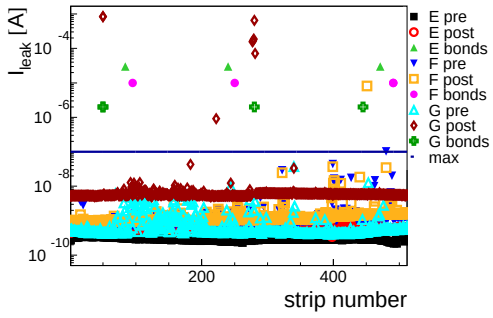

Figure C.10: Strip leakage currents. *The maximum allowed current per strip is 100nA at $V_{bias} = 450V$. Bonded regions are marked at arbitrary y-positions. Sensor E doesn't show any additional leaky strips afterwards. Channel 451 on Sensor F is a pinhole already before. Sensor G developped leaky strips arround its bonded strips.*

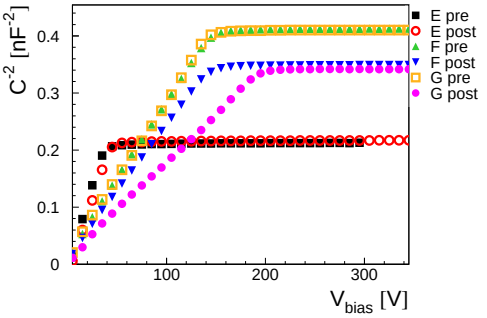

Figure C.11: Global capacitance. *The behaviour of the global capacitance is perfect afterwards for all sensors. The resulting depletion voltages should be between 100V and 300V and are listed in Appendix E.1. Only slight deviances are observed before and after for Sensors E and F. Sensor G is defective and thus shows a strong deviance.*

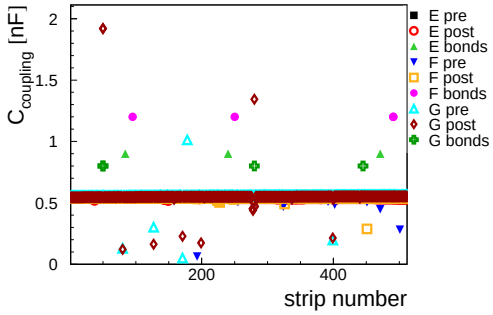

Figure C.12: Coupling capacitances. *Values around 500pF are expected [CMS00b]. The bonded strips are marked at arbitrary y-positions. Sensor E doesn't show additional problems afterwards. Strip 451 of Sensor F already is a pinhole before. Sensor G has new defect coupling capacitors arround two bonded regions.*

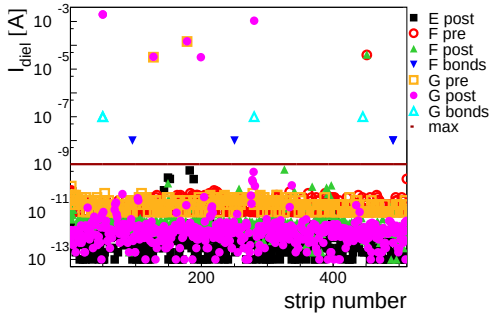

Figure C.13: Pinhole measurement. *The threshold for the dielectric current at a constant voltage of $V_{diel} = 120V$ is 1nA. Bonded strips are marked at arbitrary y-positions. Sensor E doesn't show pinholes afterwards. Strip 451 on Sensor F is a pinhole before. Three pinholes appeared on Sensor G, two at bonded positions.*

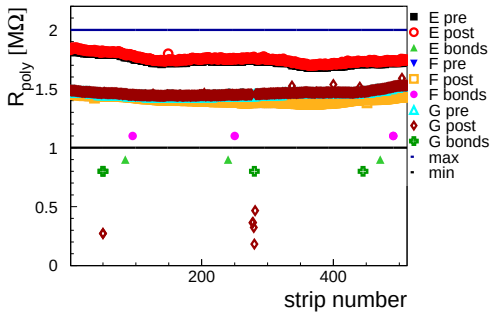

Figure C.14: Bias resistances. *The expected range is between 1 and 2MΩ [CMS00b]. Bonded strips are marked at arbitrary y-positions. The Sensors E and F behave perfect. Sensor G shows destructions arround two bonded strips.*

C.3 Laser Test Qualification

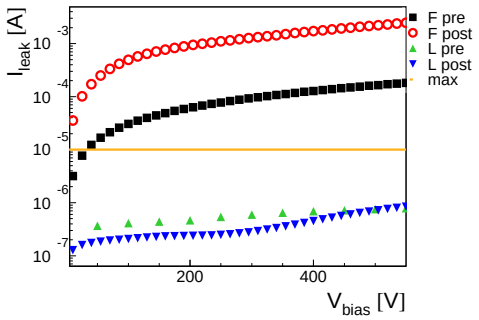

Figure C.15: Global leakage current. *Sensor L behaves perfect after the laser test. Sensor F already was damaged before and has been completely destructed afterwards.*

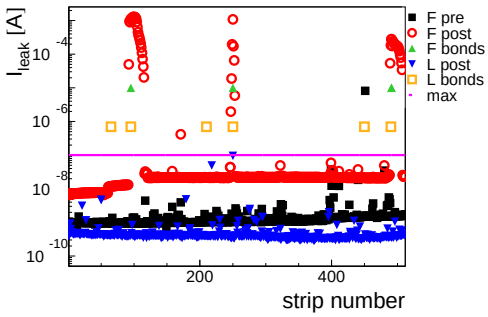

Figure C.16: Strip leakage current. *The bonded regions are marked at arbitrary y-positions. No prequalification is available for sensor L, but it behaves perfectly afterwards. Only the bonded strip 250 is near the limit. Sensor F is destroyed near its bonded channels.*

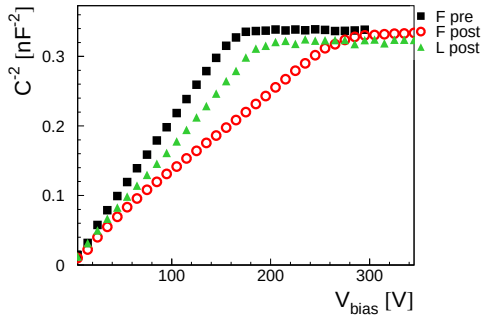

Figure C.17: Global capacitance. *A prequalification of Sensor L is not available. But it has a perfect CV curve afterwards. Resulting depletion voltages should be between 100V and 300V. As expected, the depletion voltage of destroyed Sensor F increased dramatically. Sensor L depletes at a voltage in range.*

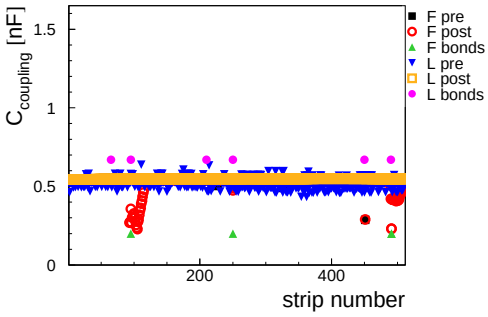

Figure C.18: Coupling capacitances. *Bonded strips are marked at an arbitrary y-position. Sensor L is perfect afterwards. Sensor F developped many destructed coupling capacitors arround the bonded regions.*

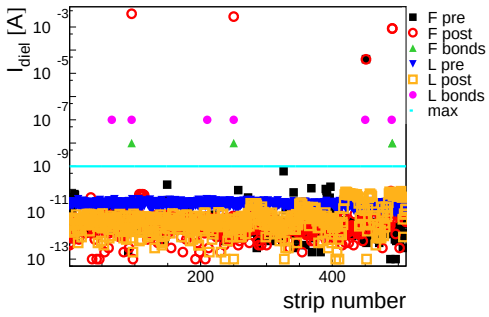

Figure C.19: Pinhole measurement. *The bonded regions are marked at arbitrary y-positions. Sensor L is perfect with respect to the pinhole measurement. Sensor F developped three of its four pinholes exactly at the bonded channels.*

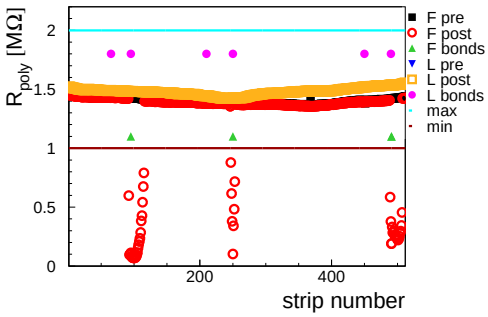

Figure C.20: Bias resistances. *The bonded regions are marked at arbitrary y-positions. Sensor L again is perfect with respect to this measurement. Sensor F shows extensive destructions arround its bonded channels.*

D Schematics

D.1 LED Test

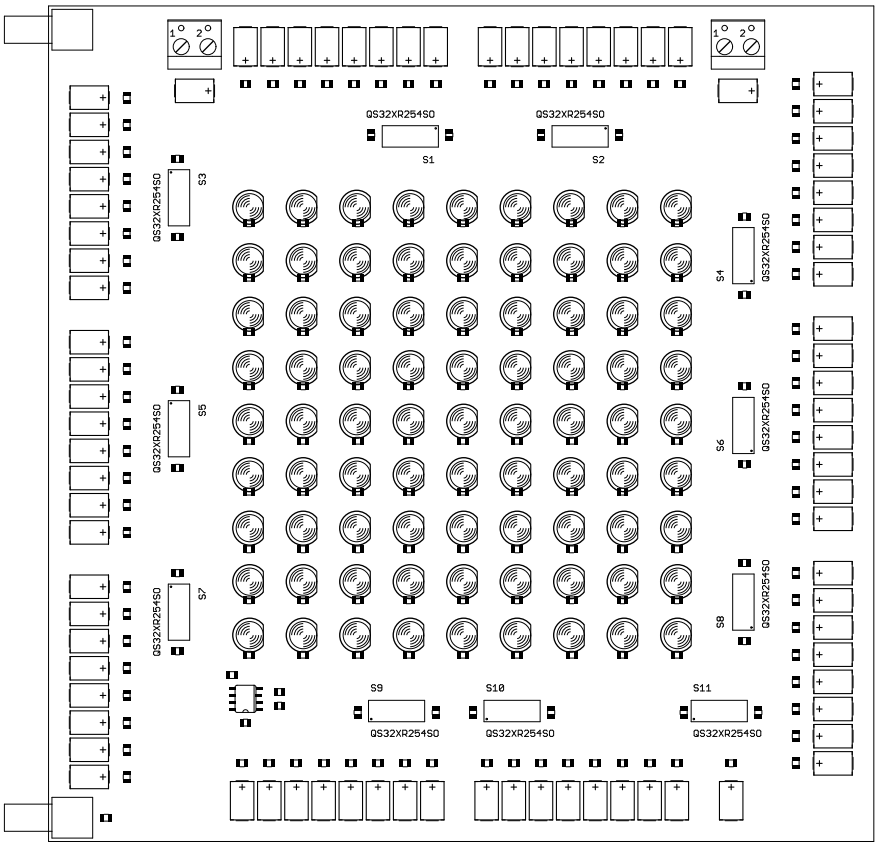

Figure D.1: Layout of the LED array [Hei04]. *Each of the 81 LEDs center were powered by* 150μF*-capacitors (outer border) summing up to a total capacitance of 12mF! A trigger (Lemo input in the upper left) opens the* IC*-Quickswitches (inner border, back side) to discharge the capacitors via impedance dimensioning resistors and the LEDs. A peak current of 48A is flowing for some* 10μs*.*

D.2 Test Beam

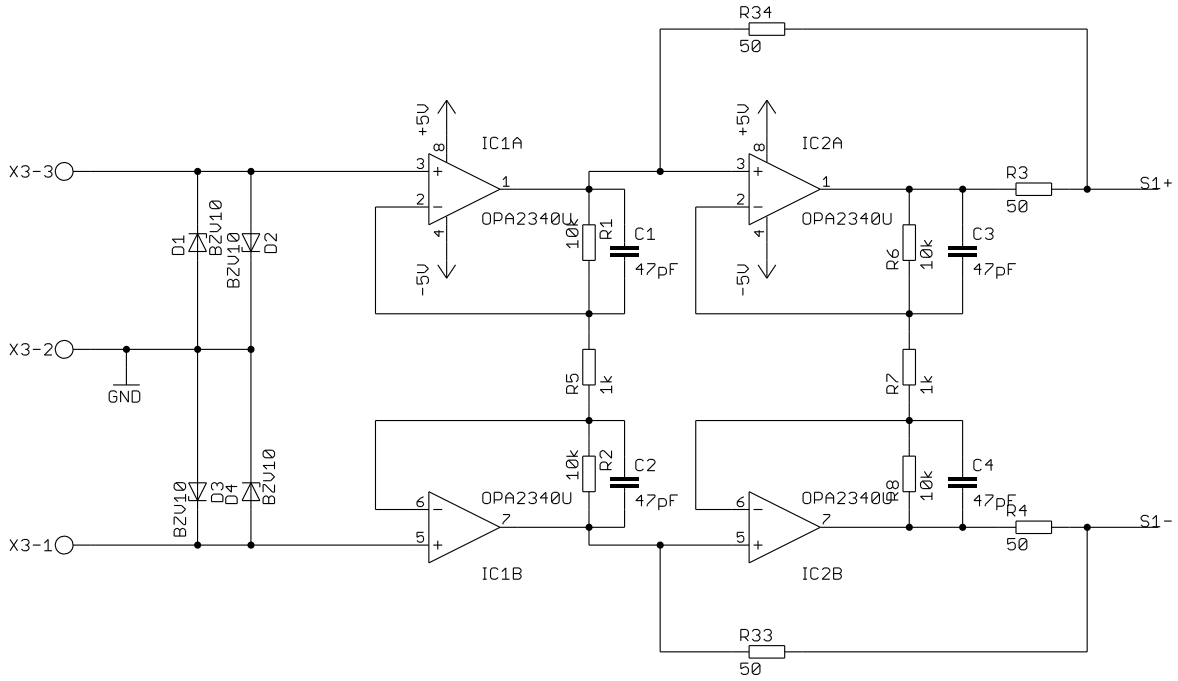

Figure D.2: Schematic of differential amplifier electronics [Hei02]. *Raw signals are amplified, impedance-changed and converted into differential signals (S1+, S1-) to be able to drive them over a very long distance with minimized injections of disturbances. There are two signal inputs for the amplification of differences of signals, e.g. voltage drops over resistors. For unipolar signals, the negative input is connected with the local ground.*

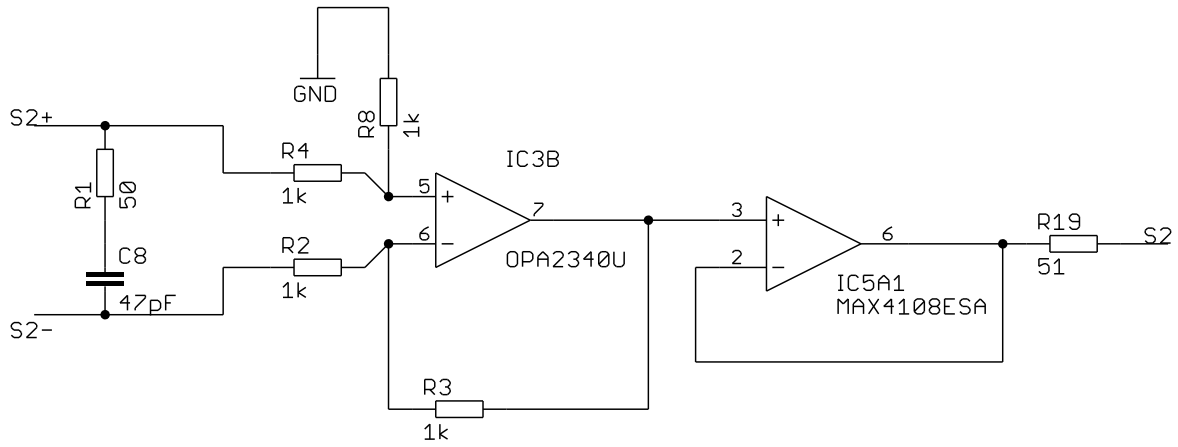

Figure D.3: Schematic of receiver electronics [Hei02]. *Differential signals are received, amplified and converted into unipolar signals referenced to the ground in the control room. This allows the data acquisition with oscilloscopes.*

E Tables

E.1 Devices under Test

thesis ID	database ID	type	geometry	V_{dep}[V] before	V_{dep}[V] after	resistivity (ρ)
Testbeam						
A	30221116054840	sensor	W6A	176	187	low
B	30210414739617	sensor	OB2	204	197	low
C	30221216053316	sensor	W6B	33	50	high
M	30216630200027	module	R6	-		-
-	?	module	TOB	-		-
-	?	hybrid	-	-		-
LED Test						
D	30221116053219	sensor	W6A	40	44	high
E	30221116053220	sensor	W6A	37	42	high
F	30210431112924	sensor	OB2	148	165	low
G	30210433608620	sensor	OB2	148	200	low
H	30211434603447	sensor	W7B	?		[irradiated]
-	?	module	R6	-		-
Laser Test						
D	30221116053219	sensor	W6A	44	?	high
E	30221116053220	sensor	W6A	42	?	high
F	30210431112924	sensor	OB2	165	268	low
K	30211132911721	sensor	W6A	202	?	low
L	30211133509710	sensor	W6A	?	192	low

Table E.1: All devices under Test. *This table repeats the characteristic data of the 14 devices that have been tested in total during testbeam, LED test and laser test. Geometric data can be looked up in Table E.2 on the next page. The thesis identifier (ID) is used in plot legends and descriptions e.g. in the qualification chapter C on Page 124.*

E.2 CMS Silicon Strip Sensors

type	shape	width [mm]	length [mm]	area [cm^2]	pitch [μm]	thickn. [μm]	strips	prod.
W1 TEC	wedge	64.6 - 87.9	87.2	66.5	81-112	320	768	288
W1 TID	wedge	63.6 - 93.8	112.9	88.9	80.5-119	320	768	288
W2	wedge	112.2 - 112.2	90.2	101.2	113-143	320	768	864
W3	wedge	64.9 - 83.0	112.7	83.3	123-158	320	512	880
W4	wedge	59.7 - 73.2	117.2	77.9	113-139	320	512	1008
W5a	wedge	98.9 - 112.3	84.0	88.7	126-142	500	768	1440
W5b	wedge	112.5 - 122.8	66.0	77.6	143-156	500	768	1440
W6a	wedge	86.1 - 97.4	99.0	90.8	163-185	500	512	1008
W6b	wedge	97.5 - 107.5	87.8	90.0	185-205	500	512	1008
W7a	wedge	74.0 - 82.9	109.8	86.1	140-156	500	512	1440
W7b	wedge	82.9 - 90.8	90.8	78.9	156-172	500	512	1440
IB1	rectangle	63.3	119.0	75.3	80	320	768	1536
IB2	rectangle	63.3	119.0	75.3	120	320	512	1188
OB1	rectangle	96.4	94.4	91.0	122	500	768	3360
OB2	rectangle	96.4	94.4	91.0	183	500	512	7056

Table E.2: CMS silicon strip tracker sensors. *W-sensors belong to the Tracker End Cap (*`TEC`*), I-senosrs to the Inner Barrel (*`IB`*) and O-sensors to the Outer Barrel (*`OB`*). W1, W2 and W5 will be assembled in double-sided modules, the other* `TEC`*-geometries in single-sided modules. All data except the area has been gathered from [A$^+$04, Kra04].*

E.3 Acronyms and Abbreviations

`ADC`	analogue to digital converter
`CMOS`	Complementary MOS
`EHP`	electron-hole pair
`FEH`	front end hybrid
`GPIB`	General Purpose Interface Bus
`HIP`	highly ionizing particle
`IC`	integrated circuit
`IQC`	Irradiation Quality Control
`MIP`	minimum ionizing particle
`MSSM`	Minimal Supersymmetric Standard Model
`NIR`	near infrared
`OPA`	operational amplifier
`PAW`	Physics Analysis Workstation
`PS`	Proton Synchrotron
`RMS`	root mean square
`SMD`	surface mounted device
`SST`	silicon strip tracker
`TTL`	transistor-transistor logic
`XML`	extended markup language
`APV`	analogue pipeline voltage type
`CMS`	Compact Muon Solenoid
`FED`	front end driver
`FIFO`	first in first out
`GUI`	graphical user interface
`IB`	inner barrel
`IP`	interaction point
`LHC`	Large Hadron Collider
`MOS`	metal oxide semiconductor
`Nd:YAG`	Neodymium-doped Yttrium Aluminium Granat monochrystal
`OB`	outer barrel
`PA`	pitch-adapter
`PCB`	printed circuit board
`QTC`	Quality Control Centre
`SM`	Standard Model
`SNR`	signal to noise ratio
`TOB`	tracker outer barrel
`VI`	virtual instrument

List of Figures

List of Tables

Bibliography

[A+02] Ralph Aßmann et al. The Consequences of abnormal Beam Dump Actions on the LHC Collimation System. *LHC Project Note*, (293), May 2002.

[A+04] J.-L. Agram et al. The silicon sensors for the Compact Muon Solenoid tracker - design and qualification procedure. *Nuclear Instruments and Methods*, A(517):77–93, 2004.

[A+05] Wolfgang Adam et al. The Effect of highly ionising Particles on the CMS Silicon Strip Tracker. *Nuclear Instruments and Methods*, A(543):463–482, 2005.

[ABS80] R. C. Alig, S. Bloom, and C. W. Struck. Scattering by ionization and phonon emission in semiconductors. *Phys. Rev. B*, 22(12):5565–5582, Dec 1980.

[ARC06] Aachen Readout and Control System. Technical report, RWTH Aachen, 2006. http://www.physik.rwth-aachen.de/group/IIIphys/CMS/tracker/software/Arcs8.1.zip.

[B+03] M. Battaglia et al. The CKM matrix and the unitarity triangle. 2003. arXiv:hep-ph/0304132.

[Brü01] Oliver Brüning. Mechanisms for Beam Losses and their Time Constants. In *Proceedings of the LHC Workshop, Chamonix, France*, pages 264–269, 2001.

[CMS94] The CMS Colaboration. Technical Proposal of the Compact Muon Solenoid. Technical Report CERN-LHCC-1994-38, 1994.

[CMS97a] The CMS Collaboration. The electromagnetic calorimeter project. Technical Report CERN-LHCC-1997-33, 1997.

[CMS97b] The CMS Collaboration. The hadronic calorimeter project. Technical Report CERN-LHCC-1997-31, 1997.

[CMS97c] The CMS Collaboration. The magnet project. Technical Report CERN-LHCC-1997-10, 1997.

[CMS97d] The CMS Collaboration. The muon project. Technical Report CERN-LHCC-1997-32, 1997.

[CMS98] The CMS Colaboration. The tracker project. Technical Report CERN-LHCC-1998-6, 1998.

[CMS00a] The CMS Collaboration. Addendum to the Tracker TDR. Technical Report CERN-LHCC-2000-16, 2000.

[CMS00b] CMS Tracker Sensor Working Group. *Specifications for the Quality Control & Assurance of the CMS Silicon Sensors, Version 5*, April 2000. email: hartmann@iekp.fzk.de.

[CMS06] CMS plots and drawings. http://cmsinfo.cern.ch/Welcome.html/CMSdocuments/CMSdocuments.html, 2006.

[D+00] T. Dubbs et al. Voltages On Silicon Microstrip Detectors In High Radiation Fields. *IEEE Trans. Nucl. Sci.*, (47):1902–1906, 2000.

[Die03] Alexander Dierlamm. *Studies on the Radiation Hardness of Silicon Detectors*. PhD thesis, Universität Karlsruhe (TH), October 2003. IEKP-KA/2003-23.

[Dir03] Guido Dirkes. *Development and Implementation of Quality Control Strategies for CMS Silicon Strip Tracker Modules*. PhD thesis, Universität Karlsruhe (TH), July 2003. IEKP-KA/2003-18.

[E+04] Simon Eidelman et al. Review of Particle Physics. *Physics Letters B*, 592:10, 2004. http://pdg.lbl.gov/2005/reviews/contents_sports.html.

[Ege03] Ulrik Egede. CKM reach at hadronic colliders. *ECONF*, C0304052:FO002, 2003. arXiv:hep-ex/0307022.

[F+04] Manuel Fahrer et al. Beam Loss Induced Electrical Stress Test on CMS Silicon Strip Modules. *Nuclear Instruments and Methods*, A(518):328–330, 2004.

[Fah05] Manuel Fahrer. *Karlsruhe Readout for CMS Strip Tracker Modules (Version 1.7.12)*. Universität Karlsruhe (TH), December 2005. http://www-ekp.physik.uni-karlsruhe.de/∼weiler/readout/datasheets/readout/doc/documentation.pdf.

[FP04] Ettore Focardi and Giuliano Parrini. Supply of Voltage Power Supplies for the CMS Si Tracker Detector. Technical report, INFN, January 2004.

[Fri01] Markus Friedl. *The CMS silicon strip tracker and its electronic readout*. PhD thesis, Vienna University of Technology, 2001.

[Fur06] Alexander Furgeri. *Irradiation Studies on CMS Silicon Strip Modules*. PhD thesis, Universität Karlsruhe (TH), May 2006. to be published.

[Gia02] Paolo Giacomelli. The CMS muon detector. *Nuclear Instruments and Methods*, A(478):147–152, 2002.

[Gri00] Chris Grigson. The ATLAS SCT irradiation facility at T7, East Hall, PS/CERN. http://atlas-sct-irradiation.web.cern.ch/atlas-sct-irradiation/default.htm, 2000.

[H+98] C.M. Herzinger et al. Ellipsometric determination of optical constants for silicon and thermally grown silicon dioxide via a multi-sample, multi-wavelength, multi-angle investigation. *Journal of Applied Physics*, 83(6):3323–3336, March 1998.

[H+99] Mika Huhtinen et al. Accidental Beam Losses at LHC and Impact on CMS Tracker. Talk given at CMS Tracker General Meeting, March 1999.

[Har02] Frank Hartmann. The CMS All-Silicon Tracker - Strategies to ensure a high quality and radiation hard Silicon Detector. *Nuclear Instruments and Methods*, A(478), 2002.

[Har05] Frank Hartmann. CMS Silicon Strip Sensors Qualification Procedure. private communication, 2005.

[Hei01] Stefan Heier. Entwicklung einer Teststation für CMS Mikrostreifendetektoren. Master's thesis, Universität Karlsruhe (TH), 2001. IEKP-KA/2001-18.

[Hei02] Stefan Heier. Amplifier and Receiver Electronics for the Single Shot Test Beam at PS/CERN. private communication, September 2002.

[Hei04] Stefan Heier. Circuit Layout of an IR LED array for Pulsed and High Intensive Stimulation of CMS Silicon Sensors. private communication, April 2004.

[Int99] Integrated Device Technology, Santa Clara, CA, USA. *IDTQS32XR245: High-Speed CMOS 16-bit Bus Switch data sheet*, November 1999. http://www.datasheetarchive.com/datasheet.php?article=1785857.

[Int04] Integrated Photomatrix. *IPL 10020-60 Series, PIN Photodiodes data sheet*, 2004. http://documents.rs-components.com/itc_paging_off.htm?id=0900766b80318e05.

[Jon01] L. L. Jones. *APV25-S1 user's guide, version 2.2*. Rutherford Appleton Laboratory, 2001.

[KM04] N. V. Krasnikov and V. A. Matveev. Search for new physics at LHC. *Phys. Usp.*, 47:643–670, 2004. arXiv:hep-ph/0309200.

[Kot01] Danek Kotlinski. The CMS pixel detector. *Nuclear Instruments and Methods*, A(465):46–50, 2001.

[Kra01] Gregor Kramberger. *Signal development in irradiated silicon detectors*. PhD thesis, University of Ljubljana, Slovenia, 2001.

[Kra04] Manfred Krammer. The silicon sensors for the Inner Tracker of the Compact Muon Solenoid experiment. *Nuclear Instruments and Methods*, A(531):238–245, 2004.

[Kvi04] Jurana Kvietkova. Ellipsometric Calculation of optical Properties for Silicon. Private communication: use of software package, December 2004.

[Lan91] Peter Theodore Landsberg. *Recombination in Semiconductors*. Cambridge University Press, 1991.

[Len01] Michela Lenzi. Performance of the all-silicon CMS tracker. *Nuclear Instruments and Methods*, A(473):31–38, 2001.

[LHC05] The LHC Project Group. LHC Design Report. Technical report, CERN, 2005. http://ab-div.web.cern.ch/ab-div/Publications/LHC-DesignReport.html.

[Lut99] Gerhard Lutz, editor. *Semiconductor Radiation Detectors*. Springer, 1999.

[M+99] N. V. Mokhov et al. Impact of the LHC beam abort kicker pre-fire on high luminosity insertion and CMS detector performance. In *Proceedings of the Particle Accelerator Conference, New York*, pages 1231–1233, 1999.

[M+01] N. V. Mokhov et al. Protecting LHC Components against Radiation resulting from an Unsynchronized Beam Abort. In *Proceedings of the Particle Accelerator Conference, Chicago*, pages 3168–3170, 2001.

[Mac05] Philipp Mack. Beam Losses at Tevatron and their handling at CDF II. Private communication, October 2005.

[Mer98] Jean-Pierre Merlo. CMS hadronic forward calorimeter. *Nuclear Physics (Proc. Suppl.)*, B(61):41–46, 1998.

[Nat03] National Instruments. *Labview - a graphical programming language*, April 2003. http://www.ni.com/pdf/manuals/320999e.pdf.

[Olt04] Oltronix. *B 605 DPM Users Manual*, 2004. http://www.oltronix.nl/∼german/datasheet/b605dpm.pdf.

[paw01] CERN, Geneva, Switzerland. *Physics Analysis Workstation*, May 2001. http://paw.web.cern.ch/paw/reference_manual.

[Pia01] Christian Piasecki. Studien an Siliziumstreifendetektoren und deren Qualitätssicherung für CMS. Master's thesis, Universität Karlsruhe (TH), 2001. IEKP-KA/2001-12.

[Roi04] Roithner Lasertechnik, Vienna. *LED1050-03 Infrared LED Lamp data sheet*, 2004. http://www.roithner-laser.com/All_Datasheets/LEDs/LED1050-03.pdf.

[Roy03] D. P. Roy. Higgs and SUSY searches at LHC: An overview. *Acta Phys. Polon.*, B34:3417–3440, 2003. arXiv:hep-ph/0303106.

[RS 02] RS Components. *RS Photodiodes data sheet*, September 2002. http://documents.rs-components.com/itc_paging_off.htm?id=0900766b8065f7c9.

[RW95] M.N. Rudden and J. Wilson. *Elementare Festkörperphysik und Halbleiterelektronik*. Spektrum Akademischer Verlag, 1995.

[S+02] Rüdiger Schmidt et al. Equipment Failure and Beam Losses in the LHC. In *Proceedings of the* 8^{th} *European Particle Accelerator Conference, Paris*, pages 362–364, June 2002.

[Sch02] Wolfgang Schwerdtfeger. Entwicklung von Systemkomponenten zur Qualitätssicherung von CMS-Silizium-Streifen-Detektoren. Master's thesis, Universität Karlsruhe (TH), 2002. IEKP-KA/2002-09.

[Sch03] Rüdiger Schmidt. How can we lose the beam? Beam loss scenarios and strategies for the design of the protection systems. In *Proceedings of the* 12^{th} *LHC Performance Workshop, Chamonix, France*, pages 150–156, March 2003.

[See02] Karheinz Seeger. *Semiconductor Physics*. Springer, 2^{nd} edition, 2002.

[Sgu04] Giacomo Sguazzoni. The CMS Si-strip tracker. 2004. physics/0402009.

[spi02] Spice Opus 2.22 Circuit Simulation Software, April 2002. http://www.fe.uni-lj.si/spice.

[SSZ00] H. Spiesberger, M. Spira, and P. M. Zerwas. The standard model: Physical basis and scattering experiments. 2000. arXiv:hep-ph/0011255.

[Sze81] S.M. Sze. *Physics of semiconductor devices*. John Willey & Sons, 1981.

[Sze94] S.M. Sze, editor. *Semiconductor Sensors*. John Willey & Sons, 1994.

[Sze02] S.M. Sze. *Semiconductor Devices, Physics and Technology*. John Willey & Sons, 2^{nd} edition, 2002.

[Tol03] Alexei Tolmatchev. New Semiconductor Materials. Characteristics and Properties (Electronic archive). http://www.ioffe.rssi.ru/SVA/NSM/Semicond/Si/bandstr.html, 2003.

[TOT04] The TOTEM Collaboration. The TOTEM Experiment. Technical Report CERN-LHCC-2004-4, 2004.

[Tri04] Alessia Tricomi. Performances of the atlas and cms silicon tracker. *Eur. Phys. J.*, C33:1023–1025, 2004.

[TRK02] CMS Central Tracker Database Action XML file format. http://cmsdoc.cern.ch/%7Ecmstrkdb/xml_file_format/new_XML_file_format.html, 2002.

[Wal03] Markus Waldschmitt. Fertigstellung einer Teststation zur Qualifikation von CMS Siliziumstreifendetektormodulen. Master's thesis, Universität Karlsruhe (TH), 2003. IEKP-KA/2003-02.

[Wei04] Thomas Weiler. *Studies on Silicon Strip Detectors for the CMS Experiment*. PhD thesis, Universität Karlsruhe (TH), June 2004. IEKP-KA/2004-15.

Acknowledgements

Writing this section is the most enjoyable task of this thesis. This work would not have been successful without the help and the engagement of many people which I want to thank now.

First of all, I'm grateful to my supervisor Prof. Dr. Thomas Müller for giving me the opportunity to work on this issue, for supporting this thesis both scientifically and financially over such a long period of time and for the possibility to take part in a very nice conference, in an autumn school and in several workshops. I kindly thank Prof. Dr. Günter Quast for taking over at short notice the co-reference of this work.

Many thanks to Dr. Peter Blüm, Dr. Guido Dirkes, Dr. Frank Hartmann and Stefan Heier for constructive corrections and hints in writing this thesis.

I sincerely thank Peter, Fr. Fellner-Thedens and Frank for their advices, encouragement and motivation during the last months.

I thank Frank for finding research topics and for his ideas related with the subject of this thesis.

A special thank goes to Stefan, who significantly contributed in the success of this work by doing circuit layouts for the LED and lasertest, and during the preparation of the testbeam under heavy pressure of time. Furthermore, he patiently answered most of my questions concerning technical problems.

I want to thank all people involved in the preparation of the testbeam for their ideas, for organizing things at CERN, for providing a fast extracted PS beam, for doing circuit layouts, soldering and assembling circuits and device carriers: Robert Hammastrøm (CERN), Alick Macpherson (CERN and PSI), Maurice Glaser (CERN), the PS crew, Frank, Guido, Stefan, Dr. Thomas Weiler and Tobias Barvich.

The lasertest would not have been possible without the help of Prof. Dr. Klingshirn's team, especially Dr. Jurana Hetterich (now Lichttechnisches Institut, University of Karlsruhe) and Dr. Michael Hetterich (Institut für Angewandte Physik, University of Karlsruhe). They provided me their lab and the laser and solved any optical problem arised during this test.

I thank all technicians at my home institute for contributing in the LED and lasertest by soldering circuits, preparing mechanics, bonding and being patient with me in spite of my advanced demands: Tobias, Felix Bögelspacher, Pia Steck and the members of the electrical and mechanical workshop.

Thanks to the persons in charge and the testers in our sensor lab for qualifying the sensors: Frank, Alexander Furgeri, Cedric Menge, Thomas Punz and Pia.

For good discussions not only during the preparation of the defense, I would like to thank all colleagues, especially Hannes Bol, Dr. Achim Denig, Stefan, Bernhard Ledermann and Christian Piasecki. Thanks to Achim for organizing the PhD students seminars.

I thank Dr. Hans-Jürgen Simonis for his help on computer and network problems.

For their administrative work concerning travelling, orders, payment, arranging dates etc., I kindly thank Fr. Fellner-Thedens, Fr. Haas, Fr. Schulz, Fr. Weißmann, and Hrn. Fuchs.

For their patience, encouragements and other manifold support, I'm very grateful to my family and my friends!